UNIVERSITY OF OKLAHOMA

GRADUATE COLLEGE

APPLICATION OF COMPRESSIVE SENSING TO WEATHER RADARS

A DISSERTATION

SUBMITTED TO THE GRADUATE FACULTY

in partial fulfillment of the requirements for the

Degree of

DOCTOR OF PHILOSOPHY

By

SERKAN OZTURK
Norman, Oklahoma
2016

APPLICATION OF COMPRESSIVE SENSING TO WEATHER RADARS

A DISSERTATION APPROVED FOR THE
SCHOOL OF ELECTRICAL AND COMPUTER ENGINEERING

BY

_____
Dr. Tian-You Yu, Chair

_____
Dr. Lei Ding, Co-Chair

_____
Dr. Robert Palmer

_____
Dr. Boon Leng Cheong

_____
Dr. Ming Xue

Dedication

For my family: Mesude, Munibe Ipek, Isa, Melehat, Cihan, Suzan, Nazan.

Acknowledgements

I would like to express my sincere gratitude to all people and Allah who have helped, supported and inspired me during my doctoral study.

I want to show my deepest appreciation to my advisors and committee chairs, Profs. Tian-You Yu and Lei Ding, for their guidance for my research and supervision of my dissertation. Their advices and invaluable comments greatly directed my research. I truly appreciate their consistent instruction, help and patience. Their perpetual energy and enthusiasm in work deeply motivated me and will continuously inspire me in my carreer.

I would like to acknowledge my committee members, Profs. Robert Palmer, Boon Leng Cheong and Ming Xue, who generously contributed their time and efforts to my study at the University of Oklahoma. I am very grateful for their support and help.

I also would like to thank all the professors and friends in the Advanced Radar Research Center (ARRC) for their help. I would like to acknowledge the support by Turkish Ministry of Education.

This dissertation would be simply impossible without my family's support. I would not have the opportunity for the education of a doctoral degree without their unlimited love and encouragement. The last and surely the most, I want to acknowledge my wonderful wife Mesude for her love, support, encouragement and understanding in dealing with all the challenges I have faced, for always giving me strength and hope.

Table of Contents

List Of Tables

List Of Figures

Abstract

The capability and importance of weather radar are proven for hazardous weathers detection, monitoring, and prediction in both research and operations. Continuous efforts have been made in improving radar performance in terms of spatial and temporal resolutions, data quality, new capabilities, etc. On the other hand, compressive sensing (CS) theory has been developed for solving underdetermined problems using l1-norm minimization. It has been shown that CS is capable of reconstructing the sparse images from a limited number of measurements. In this work, CS is specifically applied to two weather radar problems of (1) refractivity retrieval using a network of radars, and (2) retrieving reflectivity and velocity from an imaging radar.

In the first study, CS is proposed to improve the refractivity retrieval since the performance of a conventional constraint least squares method can be degraded significantly by the measurement noise and the limited number of high-quality ground returns. The application of CS to refractivity retrieval is formulated using a linear model and subsequently the feasibility is demonstrated and verified using simulations. In the second study, the problem of digital beamforming (DBF) is posed as an inverse problem and formulated using a linear model for both reflectivity and velocity estimation for CS. The application of CS is investigated using both simulation and real data. In simulations, the performance of CS is quantified and compared to the traditional Fourier beamforming and high resolution Capon beamforming for

various conditions. The feasibility of CS to weather observations is further demonstrated using the data collected by the Atmospheric Imaging Radar (AIR), developed at the Advanced Radar Research Center (ARRC) of the University of Oklahoma, on 15 April 2012.

Chapter 1

Introduction

1.1 Introduction

The impact of severe weather and weather-related hazards is considerable. Human injury, loss of life and property damage alone account for an average cost of $1 billion per year in the United States (Baer and Company 1978; Bunting and Smith 1993). As such, the economic and humanitarian value of studying and predicting such weather phenomena is immense. It has been shown that weather radars can improve operationally the warning lead time of severe and hazardous weather, and provide researchers with important atmospheric information to advance the understanding of these phenomena (National Research Council 2002; Polger et al. 1994). For example, Doppler radars have been used to detect and monitor storms and understand their structure and formation (Davies-Jones et al. 2001; Metzger et al. 2011). Moreover, polarimetric weather radars provide additional information, such as differential reflectivity, the differential phase, and the co-polar cross-correlation coefficient. This additional information allows for a hydrometeor classification (Park and Fabry 2010; Snyder et al. 2010), improves quantitative precipitation estimation (Brandes

et al. 2002; Ryzhkov et al. 2005; Giangrande and Ryzhkov 2008), and provides a better estimation of drop size distributions (Zhang et al. 2001).

In addition to the two milestones of Doppler and polarimetric capabilities in the history of weather radar development, efforts in improvement of radar performance such as resolution, data quality, functionality, etc. have never stopped. For example, the spatial resolution of weather radar is typically defined by the size of radar resolution volume, which is determined from the two-way beam pattern (in angle) and range resolution (in radial direction). Additionally, the temporal resolution is defined by the revisit time. For instance, the revisit time of mechanically scanned radar such as Weather Surveillance Radar -1988 Doppler (WSR-88D) is defined by the time it takes to complete a Volume Coverage Pattern (VCP). In order to improve angular resolution of conventional radar, the radar beamwidth can be decreased by increasing antenna aperture size. Cross-range resolution can be improved with mobile radars by simply locating the radar at a close but safe range from severe weather. Moreover, range resolution can be improved without sacrificing radar sensitivity by employing pulse compression, where a coded or frequency-modulated long pulse is used (e.g. Kurdzo et al. 2014). However, neither of the refinement can be achieved easily or economically. On the other hand, high temporal resolution of weather radars is required to observe the dynamics and structure of rapidly evolving severe weather storms, particularly considering that the development time for a tornado can be faster than the typical radar update time (Zrnic et al. 2007; Bluestein et al. 2003; Carbone et al.

1985). Moreover, radar observed high resolution structures potentially improve the understanding of storm formation and lead to improvements in numerical weather prediction models (Gasperoni et al. 2009; Sun 2005).

Further, temporal resolution can potentially be improved by using phased array radars (PAR) and imaging radars. PAR scans the atmosphere electronically as opposed to the mechanical scanning in conventional radar. Electronic beam steering makes it possible for PAR to rapidly update the beam position (Zrnic et al. 2007). Further, the temporal resolution can be improved by increasing the rotational rate of a mechanically scanned radar to complete the VCP more rapidly. However, increasing the antenna rotational rate reduces the number of samples and dwell time and thus leads to poor data quality. However, the beam multiplexing technique was developed to increase the update time and maintain data quality by exploiting PAR's beam agility to collect independent samples (Yu et al. 2007).

Moreover, high temporal resolution can be achieved by using an imaging radar by transmitting a large beamwidth and simultaneously receiving returned signals from all angles with a number of spatially separated receivers (or subarrays) (Isom et al. 2013). For example, the Atmospheric Imaging Radar (AIR) developed at the Advanced Radar Research Center (ARRC) at the University of Oklahoma allows an update time of approximately 6 seconds for a $20^o \times 90^o$ volumetric scan in the range-height indicator (RHI) (Isom et al. 2013; Kurdzo et al. 2016). Note that an imaging radar exploits digital beamforming (DBF) to obtain reflectivity and velocity fields

within the wide transmitted beam simultaneously. As a result, the fast update time offered by an imaging radar allows for improved flash-flooding detection and forecast (Wada et al. 2013) and warning time for hazardous weather, including tornadoes and hailstorms.

There have also been continuous efforts to explore new weather radar capabilities. For example, it has been shown that crossbeam wind can be estimated using a PAR system (Zhang and Doviak 2007). Additionally, the near-surface refractive index can be measured with weather radars which can be used as a proxy for humidity field. Radar-derived refractivity applications can be found related to cold fronts, boundary layer process (Weckwerth et al. 2008), operational forecasting (Weckwerth et al. 2005; Bodine et al. 2008), etc.

1.2 Radar refractivity retrieval

Many studies have shown that one of the main limitations for convective forecasting is the lack of high-resolution moisture observations (Emanuel et al. 1995; National Research Council 1998). 3D high spatial and temporal resolution observations of moisture fields are desired for accurate weather prediction (Gasperoni et al. 2009). In situ measurements such as radiosonde, weather surface station, and balloons provide direct point measurements typically with good accuracy, but exhibit low spatial and/or temporal resolution and coverage. Even a network of high density surface stations, such as mesonet, the spatial resolution provided might not be sufficient

in many applications. Weckwerth et al. (2005) reported that a high density of networked stations cannot be achieved easily and economically since 100-meter spatial and 10-minute temporal resolution may be needed to observe convection initiation. Radar-derived refractivity is currently the only available method to estimate moisture content with relatively high spatial resolution and reasonable temporal resolution and coverage, since at warm temperatures, moisture variations in the atmosphere are the dominant factor on the change of refractive index (Bean and Dutton 1968; Bodine et al. 2008; Fabry et al. 1997; Weckwerth et al. 2004). It has been reported that radar-derived refractivity has a high correlation with moisture measured from surface observations (Bodine et al. 2011).

Radar-derived refractivity exploits the phases of signals from ground clutter. Refractivity retrieval was initially implemented using a single radar (Fabry et al. 1997; Cheong et al. 2008a). Later on, a network of radars was proposed to improve the resolution and accuracy of refractivity estimation (Hao et al. 2006; Fritz and Chandrasekar 2009). In refractivity retrieval, only signals from high quality ground clutter with strong returns and stable phases should be used. Additionally, the quality and resolution of the retrieval depends on the available number of high quality clutter. In other words, the number of high quality ground clutter targets can be limited, especially when only a single radar is used. Refractivity measurements from a network of radars can be approximated by a linear model, and the problem of refractivity

retrieval is postulated as an inverse problem. This inverse problem is typically underdetermined due to the large number of refractivity pixels (to achieve desirable spatial resolution) to be reconstructed and a relatively small number of measurements. However, high resolution and accurate refractivity estimation is still a challenge for weather radars due to the limited number of measurements they produce. Therefore, this dissertation studies the estimation problem of high resolution refractivity by using a network of radars.

A constrained least square (CLS) method was proposed to estimate refractivity by using an assumption of smoothness (Fritz and Chandrasekar 2009). Compressive sensing (CS) theory is introduced as a technique to obtain accurate and high-resolution refractivity estimation from a limited number of measurements for a network of weather radars (Ozturk et al. 2014). Because CS has the potential to recover sparse images from the limited number of measurements, the sparsity of refractivity can be obtained in a transform domain by considering the low coherence. The CS theory will be briefly reviewed in Chapter 2, and specifically the refractivity retrieval with CS will be discussed in detail in Chapter 3. It is also known that as CS is robust to noise, it is expected that CS can provide reliable estimation under noisy conditions.

1.3 Digital beamforming

A fast update time is required to observe rapidly evolving severe weather (Bluestein et al. 2003; Carbone et al. 1985). The radar update time can be reduced by decreasing the number of samples, decreasing the pulse repetition period (PRT), and by changing the scanning strategy in elevation angles. Simply reducing the number of samples and PRT leads to the degradation of data quality (Zrnic et al. 2007). For example, the variance of the moment estimators (such as radar reflectivity, differential reflectivity, velocity, etc.) will increase by the reduction of dwell time. In addition, clutter filtering can be challenging if the number of samples is too small. Moreover, reducing PRT leads to a shorter maximum unambiguous range and results in range folding. Changing the scanning strategy by reducing the number of scanning angles in elevation is a sound approach (Torres et al. 2013a,b). However, fully exploiting this capability requires a sophisticated and adaptive radar. Pencil-beam PAR has capabilities to provide fast adaptive scanning by using a scan processing module for the region of interest without compromising the data quality while improving the temporal time (Zrnic et al. 2007). Meteorological Weather Radar 2005 X-Band (MWR-05XP) uses both phase and frequency scanning to steer the beam in elevation and azimuth, respectively, for limited sectors, then requires a mechanical scan to have a complete azimuth coverage (Bluestein et al. 2009). Additionally, the rapid scanning X-band polarimetric radar (RaXPol) can provide update time by a fast

rotating pedestal (180^o/s) and frequency-hopping techniques to maintain data quality (Pazmany et al. 2013).

An imaging radar, which is a subset of phased array radars, employs a wide transmitted beam and a number of receivers. This removes the need of phase shifters for electronic beam steering by transmitting a large beamwidth and receiving returned signals simultaneously from all angles (Isom et al. 2013). DBF techniques are used to estimate atmospheric reflectivity in angle using signals from spatially distributed receivers. As such, high temporal resolution has been achieved by using imaging radar with DBF. Several DBF methods have been applied to observations of the atmosphere using profiler radars. For example, Fourier beamforming (FB) has been used for reflectivity and velocity estimation, but it has a resolution limitation due to high sidelobes (Palmer et al. 1998; Yu et al. 2000). Capon beamforming (CB) achieves higher resolution, but is difficult to calibrate to obtain the absolute reflectivity estimates. Spatial amplitude and phase estimation (APES) provides reliable reflectivity estimation, but the spectral resolution is poorer than CB (Isom et al. 2013). Recently, an adaptive beamspace algorithm has been proposed for accurate and calibrated weather observations (Nai et al. 2016). Moreover, CS is used for observations of irregularities in equatorial ionosphere by using Jicamarca radar, but the velocity estimation did not performed (Harding and Milla 2013). Furthermore, reliable reflectivity and velocity estimation with high angular resolution are still a challenge for DBF using imaging radars due to calibration, noise, receiver configurations, etc.

Recently, radar imaging has been considered as an inverse problem for the spatial map of reflectivity and velocity. In this work, CS is proposed as an alternative reconstruction method to DBF to estimate reflectivity and velocity structure of the atmosphere. The investigation of CS for an imaging radar AIR is conducted in Chapter 4.

1.4 Inverse problems

Inverse problems can be categorized as linear and nonlinear inverse problems. In this work, we are interested in linear inverse problems. Hadamard (1923) defines inverse problems as well-posed problems if the solutions exist, unique and continuously dependent on the data. Otherwise, the problem is called an ill-posed. In other words, ill-posed problems arise approximating the continuous function by discretization it into a finite dimension. Furthermore, when the discretization is applied, if the number of measurements is higher than the number of unknown variables, the problem is called overdetermined. Accordingly, the problem is called underdetermined if the number of measurements is smaller than the number of unknown variables. Subsequently, both underdetermined and overdetermined problems can be considered as ill-posed problem, since the solution is not unique. Further, it is noted that ill-posed problems are extremely sensitive to measurement noise and modeling errors (Tikhonov et al. 1995; Müller and Siltanen 2012).

Regularizations are needed for ill-posed inverse problems to stabilize the problem due to sensitivity to the measurement noise (Tikhonov et al. 1995; Müller and Siltanen 2012). Tikhonov regularization and singular value decomposition (SVD) are commonly used in inverse problems (Hansen 1987; Müller and Siltanen 2012). However, standard methods, such as least square and SVD, are highly sensitive to perturbations in the data and do not provide the unique solution for underdetermined problems. In order to obtain numerically a stable solution, a regularization function based on a priori assumption is needed as a constraint. The regularization function in the constraint such as smoothness, sparsity, etc. may vary with the regularization method. Consequently, the accuracy and quality of the estimation will be limited with the regularization method.

1.5 Compressive sensing

In the last decade, CS theory has been studied as a new framework for solving underdetermined problems using l_1-norm minimization and a priori assumption of sparsity. l_1-norm is defined as the sum of magnitude of the variables and causes the solution to be sparse. It has been shown that CS guarantees the exact solution using l_1-norm minimization from a limited number of measurements if the solution is sparse (Candès 2006; Donoho 2006). In other words, CS requires that the image to be reconstructed has to be sparse in an original domain or transform domain and the measurements should be obtained incoherently.

The CS theory has been applied to improve the quality of the reconstructed image in many different engineering fields such as optical imaging (Baraniuk 2007), magnetic resonance imaging (Lustig et al. 2007), computer tomographic imaging (Aybat and Chakraborty 2008), ultrasound imaging (Eldar and Kutyniok 2012), etc. Further, the application of CS can be found in the radar field, such as observations of equatorial ionosphere by using Jicamarca radar (Harding and Milla 2013), directions of arrivals for multiple point targets (Liu et al. 2013), ground-penetrating radar (Gurbuz et al. 2007), wideband spectrum radio signal sampling (Polo et al. 2009), radio interferometry for astrophysical objects (Wiaux et al. 2009), pulse compression (Potter et al. June 2010; Naini et al. 2009), and synthetic aperture radar imaging (Potter et al. June 2010). As such, CS has been widely used in radar applications and has potential for atmospheric observations in weather radars.

In this dissertation, the problem of refractivity estimation by networked radars is formulated as an inverse problem (Hao et al. 2006; Fritz and Chandrasekar 2009). Since the number of measurements are limited, CS is proposed to retrieve radar refractivity with improved reconstruction accuracy.

In the second study, the problem of DBF is considered as an inverse problem and formulated in a linear model (Gurbuz et al. 2007; Edelmann and Gaumond 2011). CS is applied to reconstruct high resolution reflectivity and velocity from a limited number of receivers from an imaging radar

1.6 Scope of research and organization of dissertation

The main purpose of this study is to explore the application of CS to radar refractivity retrieval from a network of radars and to an imaging radar to estimate reflectivity and velocity from spatially distributed receivers. First, CS is applied to solve the inverse problem of refractivity retrieval from radar phase measurements, where the number of measurements can be small due to the lack of high quality ground clutter. Second, CS is applied to imaging radar to obtain high-resolution reflectivity and velocity profiles from the limited number of receivers. Subsequently, CS is tested and verified through numerical simulations. Because the parameters are known and controllable in simulations, statistical comparisons of estimation methods are made by varying the signal-to-noise ratio (SNR), number of measurements, and receiver configurations. Experimental results of FB, CB, and CS from AIR are provided. This dissertation is organized as follows:

- Chapter 2: The theory of CS is briefly introduced. The necessary conditions for CS estimation are briefly reviewed. Different minimization algorithms with different regularization parameters are discussed.

- Chapter 3: The refractivity retrieval is made by using CS from networked weather radars. The CS algorithm is developed and an extensive simulation environment is developed. The time-evolving moisture fields associated with refractivity are obtained from the Advanced Regional Prediction System (ARPS)

models. The performance of CS is statistically analyzed by using numerical simulations and is compared to the conventional CLS method.. The impacts of the number of measurements and the amount of noise on the estimation are also examined.

- Chapter 4: The application of CS to estimate reflectivity and velocity from imaging radar is introduced as an alternative to DBF methods. The DBF problem is formulated for CS estimation for both reflectivity and velocity from the correlation of signals from multiple receivers. Wavelet and second order difference transforms are used for reflectivity and velocity estimation in CS minimization algorithm. The performance of CS is statistically analyzed using numerical simulation and compared to FB and CB in simulation and real experimental cases.

- Chapter 5: A summary of this research is presented. Future work is proposed and discussed.

Chapter 2

Compressive Sensing

2.1 Introduction

The recently developed compressive sensing theory offers the reconstruction of signals/images from a relatively low sample rate compared with the requirement of the Nyquist sampling theorem. The Nyquist sampling theorem states that the sampling rate has to be twice the maximum frequency in order to recover signal the accurately. Based on the compressive sensing theory, the Nyquist sampling rate is not required, and the signals or images can be exactly recovered from a limited number of measurements (Candès 2006; Eldar and Kutyniok 2012). The CS theory requires that the signal/image has to be sparse either in original domain or in a transform domain such as discrete cosine transform (DCT), Fourier transform, or wavelet. (Donoho 2006; Candès and Wakin 2008). Therefore, a priori assumption about the signal/image is needed in a transform domain. Secondly, the measurements should be obtained incoherently. Consequently, the signal/image can be reconstructed from small incoherent measurements via nonlinear l_1-norm minimization (Candès and Romberg 2006; Donoho 2006).

2.2 Theory

In CS, the measurements are obtained as inner products of a signal, and the measurement matrix is in linear form,

$$\mathbf{y} = \mathbf{H}\mathbf{x} \tag{2.1}$$

where $\mathbf{y}$ is the measurements with size of $M \times 1$, $\mathbf{H}$ is $M \times P$ measurement matrix, and $\mathbf{x}$ is $P \times 1$ signal. Typically in CS, the number of measurements M is less than the number of pixels P. In underdetermined problems, the measurement $\mathbf{H}$ matrix is rank deficient because either M is smaller than P or the high condition number of $\mathbf{H}$ due to the large gap between the large and small singular values (Hansen 1987). In other words, the sorted singular values decay gradually to zero. This implies that one or more rows and columns of $\mathbf{H}$ can be expressed approximately as a linear combination of others. Therefore, the matrix $\mathbf{H}$ contains almost redundant information. As a result, there are an infinite number of solutions for underdetermined problems, and without a priori information about the underlying source field, the exact solution cannot be found. In CS, the sparsity assumption of the image and incoherent measurements make the reconstruction possible by using the l_1-norm minimization. The key elements required in CS to produce satisfactory reconstructions are sparsity, incoherency, restricted isometry property, and l_1-norm minimization. These will be discussed in the following subsections.

2.2.1 Sparsity

A sparse image means that the image can be represented by only a few nonzero coefficients either in the original domain or in its transform domain (Candès and Romberg 2006; Donoho 2006; Candès and Wakin 2008). For example, even if an image has all pixels of nonzero values, it might only contain a few nonzero coefficients after a linear transformation, such as DCT, Fourier transform, or wavelet. A linear transformation of an image $\mathbf{x}$ is given as

$$\mathbf{s} = \mathbf{\Psi}\mathbf{x}, \tag{2.2}$$

where $\mathbf{s}$ is $P \times 1$ transformed image coefficients and $\mathbf{\Psi}$ is $P \times P$ transformation matrix. If the image is sparse in a transform domain and the number of nonzero coefficients is K, then it is called K-sparse image.

In practice, the condition of sparsity might not be met, but most natural images can be compressible in transform domains (Eldar and Kutyniok 2012; Candès and Wakin 2008). An image is said to be compressible if it can be well approximated by a few large coefficients in the transform domain, while the rest of the coefficients have relatively small values and only contribute negligible content to the original image. In other words, if the coefficients for a compressible image are sorted, they decay rapidly. In this dissertation, the level of compressibility for a given image is defined based on the root-mean-square error (RMSE) between the image and the approximation (derived using a portion of large coefficients) of that image. The RMSE is set to 6.32 for this case. It will be explained in more detail in Section

3.6.3. An example of the “Lena" image is used to demonstrate compressibility of the image in DCT and wavelet in Fig. 2.1. Note that the sparsity level K of the

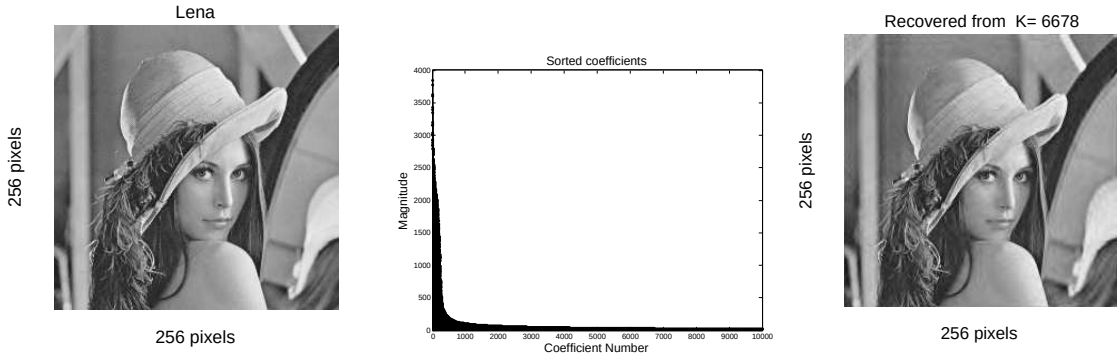

(a) Wavelet

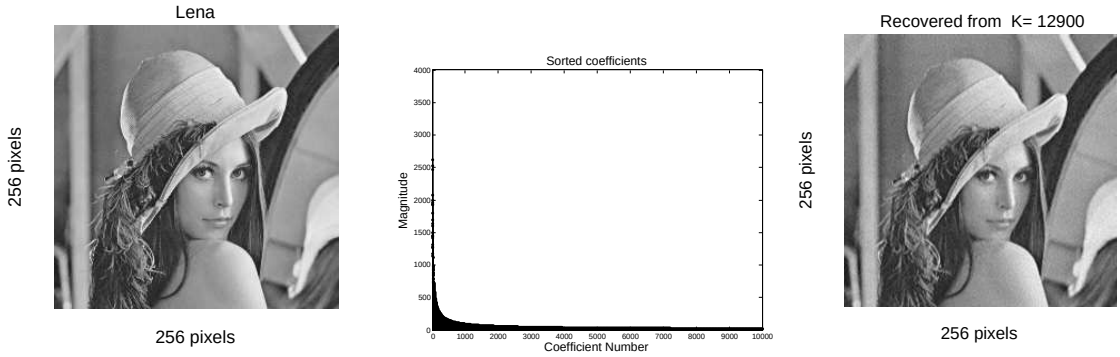

(b) DCT

Figure 2.1: Lena image (left panels) is shown with 65536 pixels (256 by 256) and the first 10,000 sorted transform coefficients are shown for better demonstration after wavelet and DCT in the middle panels. The recovered images (right panels) are obtained by inverse wavelet and DCT using 10% and 19.7% of largest coefficients, respectively, to achieve RMSE =6.32.

recovered image can be different in different transformation domains to achieve the same RMSE. For this case, wavelet is capable of recovering the image using only 10.2% of the largest coefficients, whereas DCT uses 19.7% of the largest coefficients for the given RMSE. In other words, the image is more compressible in wavelet

than DCT. Therefore, in order to take advantage of sparsity for efficient recovery, an appropriate transformation should be chosen.

DCT and wavelet are linear orthogonal transformations that have the property $\mathbf{\Psi}^{-1}\mathbf{\Psi} = \mathbf{I}$. DCT expresses as a sum of cosine functions at different frequencies and is equivalent to the real part of the discrete Fourier transform. Wavelet has various transform bases including Haar and Daubechies, which are commonly used in applications. Wavelet requires the size of the signal power to be 2, and in this work, Daubechies basis functions are used for the wavelet transform. It is worth mentioning that sparsity could be considered in the spatial and temporal variations of an image. Total variation (TV), which performs the first order difference of the image, has been widely used to obtain gradient sparsity of a signal (Rudin et al. 1992; Ding and Selesnick 2015). Additionally, the second order difference operator (Laplace) has been used for signal smoothing (Boyd and Vandenberghe 2004) but can be used to obtain signal sparsity as well. The Laplace operator can lead to sparser representation of the image compared to TV when the image has linear variations.

2.2.2 Incoherence

To reconstruct sparse or compressible images using CS, the second important element is that the measurements should be incoherent with the sparse representation of basis functions (Donoho and Elad 2003; Candès and Romberg 2006). Coherence is

mathematically defined as the maximum value of inner products between the transformation basis $\mathbf{\Psi}$ and the measurement matrix $\mathbf{H}$ in the following equation (Candès and Wakin 2008):

$$\mu = \sqrt{P}\max(|\langle \boldsymbol{h}_i, \boldsymbol{\psi}_j \rangle|) \quad 1 \le i \le L, \quad 1 \le j \le P, \tag{2.3}$$

where $\boldsymbol{\psi}_j$ is the j^{th} column of $\mathbf{\Psi}$ and $\boldsymbol{h}_i$ is the normalized i^{th} row of $\mathbf{H}$. Coherence is a measure of how these two bases are similar to each other and has a theoretical range of $[1, \sqrt{P}]$ (Candès and Romberg 2006). If each measurement vector $\boldsymbol{h}_i$ spread out in the $\mathbf{\Psi}$, μ approaches 1, indicating maximal incoherence. If one $\boldsymbol{h}_i$ from $\mathbf{H}$ and one $\boldsymbol{\psi}_j$ from $\mathbf{\Psi}$ are exactly same, μ is $\sqrt{P}$, indicating maximal coherence. Large coherence values indicate that some measurements are only sensitive to certain coefficients. In other words, a few relatively large values in the measurement basis dominate the contribution from remaining small values by amplifying certain coefficients more than others in the forward and inverse operation. This can lead to poor reconstructions since missed information might be important.

On the contrary, incoherent measurements receive contributions from a significant portion of all coefficients. While these contributions are linearly mixed in measurements, the possibility of accurate reconstruction is increased. Therefore, coherence needs to be as low as possible for better recovery. From another point of view, if the coherence becomes low, the minimal number of measurements needed for exact reconstructions decreases (Candès and Romberg 2006; Candès and Wakin 2008). Decreasing the required minimum number of measurements will lead to reduce the cost

of the system and computational time of the solver. It is also worth noting that the condition of incoherence can be further improved by designing a transformation matrix. For the same given number of measurements, reducing the coherence will also help to recover low sparse images (non-compressible), since the required number of measurements is a multiplication of μ and sparsity K. As a result, better sparsity of signals in the transformed domain with incoherent measurement matrices is likely to increase the possibility of exact reconstruction.

2.2.3 Restricted isometry property

The restricted isometry property (RIP) was derived and guarantees the exact solution (Candès 2006; Baraniuk et al. 2010; Duarte and Eldar 2011). Theoretically, the condition of the restricted isometry property (RIP) has been shown and satisfied for special cases such as random Gaussian matrices, but it is hard to prove in engineering applications (Candès 2006; Eldar and Kutyniok 2012). An M x P measurement matrix $\mathbf{H}$ allows the reconstruction of a $K-$sparse signal with size of P x 1, if the following condition is satisfied,

$$(1-\delta_k)||\mathbf{x}||_{l_2}^2 \leq ||\mathbf{H}\mathbf{x}||_{l_2}^2 \leq (1+\delta_k)||\mathbf{x}||_{l_2}^2 \tag{2.4}$$

where δ_k is a constant value between 0 and 1. RIP states that there are no two different $K-$sparse signals which lead to the same measurements (Baraniuk et al. 2010; Eldar and Kutyniok 2012). If we replace the norm term in (2.4) with the inner product,

$$(1-\delta_k)||\mathbf{x}||_{l_2}^2 \leq < \mathbf{H}^\mathbf{T}\mathbf{H}\mathbf{x}, \mathbf{x} > \leq (1+\delta_k)||\mathbf{x}||_{l_2}^2 \tag{2.5}$$

where $\|\mathbf{Hx}\|_{l_2}^2 = \mathbf{x^T H^T Hx} =< \mathbf{H^T Hx}, \mathbf{x} >$. It is clear that if $\delta_k = 0$, then $\mathbf{H^T H} = \mathbf{I}$. It indicates that all the columns of H have to be orthonormal. More specifically, RIP requires that all $M \times K$ submatrices of $\mathbf{H}$ behave like orthonormal system. Therefore, each measurement has a unique representation from each sparse vector for the noiseless case. Note that $\mathbf{H^T H}$ produces cross-correlation between the columns of $\mathbf{H}$. Consequently, coherence is at the minimum level, since the columns of the measurement matrix are orthonormal; so there is no correlation between the columns. As a result of this property and the orthonormality of the measurement matrix, the exact recovery can be obtained.

In order to demonstrate this phenomenon visually in a matrix form, let us assume that we know the locations of the K non-zero values of a sparse signal with the length of P, where $K < P$ and the number of measurements M equals K.

$$\begin{bmatrix} y_1 \\ y_2 \\ \vdots \\ y_M \end{bmatrix} = \begin{bmatrix} h_{11} & h_{12} & \dots & \dots & h_{1P} \\ h_{21} & h_{22} & \dots & \dots & h_{2P} \\ \vdots & \vdots & \dots & \dots & \vdots \\ h_{M1} & h_{M2} & \dots & \dots & h_{MP} \end{bmatrix} \begin{bmatrix} 0 \\ x_1 \\ 0 \\ \vdots \\ x_k \\ 0 \end{bmatrix} \tag{2.6}$$

It is obvious that we can remove the columns associated with 0's in the sparse vector. Then, we obtain $M \times M$ new square $\mathbf{H_M}$ submatrix, where $M = K$.

$$\begin{bmatrix} y_1 \\ y_2 \\ \vdots \\ y_M \end{bmatrix} = \begin{bmatrix} h_{12} & \dots & \dots & h_{1k} \\ h_{22} & \dots & \dots & h_{2k} \\ \vdots & \dots & \dots & \vdots \\ h_{M2} & \dots & \dots & h_{Mk} \end{bmatrix} \begin{bmatrix} x_1 \\ x_2 \\ \vdots \\ x_k \end{bmatrix} \tag{2.7}$$

$\mathbf{H_M}$ matrix is invertible since it is obtained from well-conditioned columns of $\mathbf{H}$, and so the solution is trivial and exact.

As a second example of a high coherence case, let us assume that some of the columns are not independent. As a result, $\mathbf{H_M}$ is rank deficient and the inverse does not exist; exact reconstruction is not guaranteed anymore and an erroneous solution is likely. Note that RIP requires verification in (2.4) for each of the $\binom{P}{K}$ possible combinations of $K-$sparse vector $\mathbf{x}$. Therefore, in practice, coherence has been used to indicate the satisfied condition of CS for stable recovery, since it is hard to show that the RIP condition is sufficient.

2.2.4 l_1-norm minimization

l_1-norm is the sum of the magnitudes of the transform coefficients and is defined as $\|\mathbf{s}\|_1 = \sum_i |s_i|$, where $\mathbf{s}$ is the transform coefficients vector. It has been shown that the l_1-norm minimization supports sparsity as opposed to the conventional methods based on the l_2-norm approach (Donoho and Elad 2003; Candès and Tao 2005). This

is because the l_1-norm penalizes small values heavily compared to the l_2-norm approaches, and thus tends to generate sparse solutions. In other words, sparse signals have a small l_1-norm relative to non-sparse signals for the given same conditions, whereas non-sparse signals have a small l_2-norm relative to sparse signals (Candès and Tao 2005; Donoho and Elad 2003). The unique solution for sparse signals can be found by using the l_1-norm minimization (Donoho and Elad 2003). Consequently, the l_1-norm solution for the noiseless case is obtained by solving the convex optimization problem in the following:

$$\min \ \|\mathbf{\Psi x}\|_{\mathbf{1}} \quad \text{subject to} \quad \mathbf{y} = \mathbf{Hx}, \tag{2.8}$$

Note that if $\mathbf{\Psi}$ is the identity matrix, then $\mathbf{x}$ is sparse in the original domain. For the noisy case, the error in the measurements are constrained with β,

$$\min \ \|\mathbf{\Psi x}\|_{\mathbf{1}} \quad \text{subject to} \quad \|\mathbf{y} - \mathbf{Hx}\|_{\mathbf{2}}^{\mathbf{2}} < \beta, \tag{2.9}$$

where β controls the discrepancy between the measurements and estimation. In order to demonstrate a signal reconstruction from highly limited measurements with l_1-norm reconstruction by using nonlinear sampling, the following example is considered. In a time variant signal from which the samples are obtained randomly in time from a partial Fourier matrix $\mathbf{H}$, then the signal can be expressed as

$$y(t) = \sum_{k=1}^{n} x(k) e^{i2\pi tk/n} \tag{2.10}$$

where x is $K \times 1$-sparse vector and has K nonzero frequency coefficients. For a numerical example, sparsity is chosen as $K = 2$ and the frequency bandwidth as 10

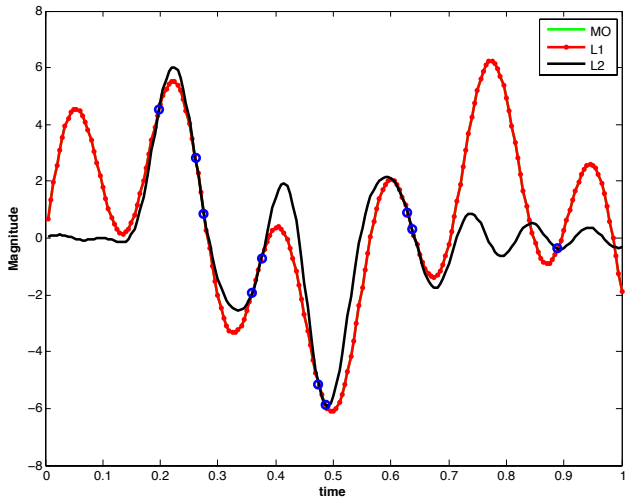

(a) Time (seconds)

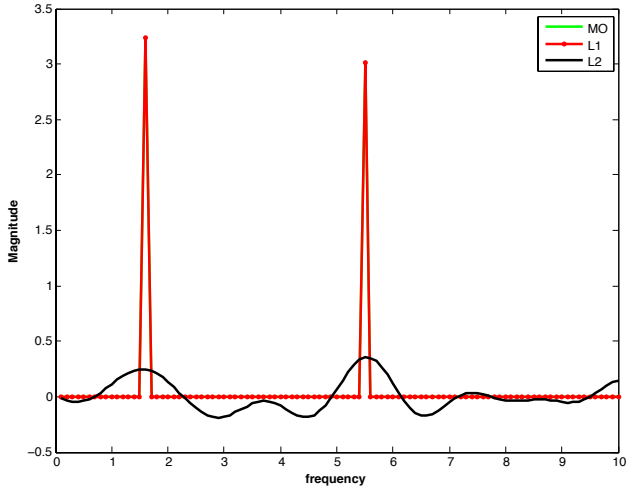

(b) Frequency (Hz)

Figure 2.2: Time variant signal and random samples (blue circles) in time in Fig. 2.2(a). Recovered frequency coefficients from l_1 and l_2-norm in Fig. 2.2(b)

Hz, where we seek the resolution of 0.1 Hz for the reconstruction and assume no additive noise in the measurements. The reconstruction from 10 random samples using l_1-norm minimization is shown in Fig. 2.2. The amplitude recovery using l_1-norm minimization is exact in the frequency content in Fig. 2.2(b), and so the signal is recovered exactly in time domain for the noiseless case in Fig. 2.2(a). It is obvious

that l_2-norm estimation is not sparse in the frequency domain in Fig. 2.2(b) and requires more samples for accurate reconstruction. Additionally, the least square reconstruction ($l_2 - norm$) is matched exactly in the time sampled values, but the estimated model structure is far from the true model in the time domain in Fig. 2.2(a). Note that 200 uniform samples are required based on the Nyquist sampling theorem to recover the signal exactly, but the result is not shown here since it overlaps exactly with l_1-norm reconstruction.

2.2.5 l_1-norm solvers

In the last decade, there has been significant interest in developing l_1-norm minimization solvers to recovery sparse signals from undersampled measurements. Currently, many l_1-norm solvers exist in the literature including l_1-Magic (Emmanuel Candès 2005), the nonlinear conjugate gradient algorithm with backtracking line search (Lustig et al. 2007), second order convex programming (Grant and Boyd 2014), the CoSaMP algorithm (Needell and Tropp 2009), universal Markov chain Monte Carlo (MCMC) algorithm (Zhu et al. 2015). In this dissertation, the nonlinear conjugate gradient method (Lustig et al. 2007) and the convex optimization solver packet (Grant and Boyd 2014) are used to solve the l_1-norm minimization problem.

2.2.5.1 Nonlinear conjugate gradient method

The l_1-norm solver described in Lustig et al. (2007) was used to solve the problem of refractivity estimation in chapter 3. The solver uses the nonlinear conjugate gradient

and error back-projection algorithm to converge on a solution. An initial solution is required to start iteration in the solver and convergence sensitive to the initial value. The solver iteratively solves the problem and allows use of multiple transformation matrices in the minimization. Further, the l_1-norm problem can be designed using multiple transformation matrices in the following, for example.

$$\min \ \ ||\mathbf{\Psi x}||_1 + \alpha||\mathbf{Tx}||_1 \quad \text{subject to} \quad ||\mathbf{y} - \mathbf{Hx}||_\mathbf{2}^\mathbf{2} < \beta, \tag{2.11}$$

where $\mathbf{\Psi}$ and $\mathbf{T}$ are the transformation matrices, such as DCT, wavelet, TV, etc. The constrained convex optimization problem in (2.11) is considered to be an unconstrained problem in Lagrangian form, and the algorithm was derived by rewriting the minimization problem.

$$\min \ \ \gamma||\mathbf{\Psi x}||_1 + \alpha||\mathbf{Tx}||_1 + ||\mathbf{y} - \mathbf{Hx}||_\mathbf{2}^\mathbf{2}, \tag{2.12}$$

where β value is converted to γ and the value is adjusted based on the noise term. γ and α balance the sparsity of reconstruction in $\mathbf{\Psi}$ and $\mathbf{T}$, respectively. Then, the conjugate gradient term is obtained by taking the derivative of the total cost function, which is the sum of the measurement error and sparse coefficients in l_1-norm.

$$\gamma\nabla||\mathbf{\Psi x}||_\mathbf{1} + \alpha\nabla||\mathbf{Tx}||_\mathbf{1} + \mathbf{2H^T(y - Hx)}, \tag{2.13}$$

Note that the absolute value of the transform coefficients is approximated with a smoothing function, $|x| = \sqrt{x * x + \mu}$, where μ is the smoothing parameter and chosen 10^{-12} within the suggested region in (Lustig et al. 2007). The other parameters in the algorithm are the same in the default value. As a result, the minimization problem

was solved by using nonlinear conjugate gradients and a backtracking line search (Lustig et al. 2007; Donoho 2006), where the error term and solution were updated in each iteration.

2.2.5.2 CVX optimization solver

CVX is designed specifically for convex optimization problems so that the convex problems can be constructed and solved (Grant and Boyd 2014; Boyd and Vandenberghe 2004). CVX supports linear and quadratic programs, second-order cone programs, etc. Further, complex convex optimization problems and non-differentiable functions such as l_1-norm can be solved using CVX. CVX also supports and uses Self-Dual minimization (SeDuMi) so that the minimization problem can be converted into an equivalent dual standard form (Grant and Boyd 2014; Boyd and Vandenberghe 2004), where the solution can also be obtained without converting. However, in linear program problems, the solution can be simpler than its dual version in some cases. Moreover, CVX using SeDuMi can provide a more stable and robust solution compared to the fast convergence algorithm, which may suffer from numerical errors.

CVX has a set of rules based on the convex functions and analysis that are explained in more details in (Grant and Boyd 2014). The following example is given for setting up a minimization problem in the CVX packet,

```
cvx_begin
```

```
  variable x(P)
        minimize (norm(Tx, 1))
  subject to
        norm(y - Hx, 2) <= e
cvx_end
```

where P is the number of pixels, x is the unknown variable to estimate, and e is the error bound. l_1 and l_2-norm in the solver interface are expressed by using the degree of norm in the Matlab program convention. Constraints and objectives are expressed relying on the rules and transformed automatically into second order dual minimization form. CVX does not require an initial solution to converge on a solution. In this work, CVX uses the SeDuMi packet to solve the defined problem, where we can directly and explicitly set up the problem in SeDuMi.

Further, if the unknown variable x is complex, the problem can be defined by the following changes,

```
cvx_begin
  variable x(P) complex
        minimize (norm(Tx, 1))
  subject to
        norm(y - Hx, 2) <= e
cvx_end
```

The multiple transformation matrix can be added by using a summation operation in the objective function (“minimize" term). More detailed information about CVX is available in (Grant and Boyd 2014; Boyd and Vandenberghe 2004).

2.3 CS reconstruction challenges in radar problems

2.3.1 Selection of transformation basis

The sparsity level of signals and incoherence between the transformation and measurement basis mainly determine the performance of CS. However, in the engineering applications, the signals can be compressible and not strictly sparse in a chosen transformation basis. Another challenge in the application is the incoherence associated with the selection of the transformation matrix and measurement matrix. In some applications, such as in the radar refractivity problem, when the forward problem is set up and observations are obtained, the measurement matrix cannot be changed. Accordingly, a transformation basis such as the Fourier transformation, DCT, avelet, etc. can be chosen depending on the small coherence value. If one transformation basis makes some images significantly more compressible than the others as having relatively high coherence with the measurement matrix, it makes the selection of transformation more challenging. The selection of transformation basis is currently an open question and requires an intensive analysis for all the possible cases.

2.3.2 Measurement error and noise estimation

In practice, a mismatch problem can arise in the forward measurement setup when approximating to continuous source field with a discretized one (Chi et al. 2011). In order for the reconstruction, the continuous source field is artificially gridded into finite numbers. Commonly we assume that the source targets are located in the center of the grid cells. Even if we finely grid the source space, if the targets may not lie in the center of the grid cells, there will be a mismatch between the assumed and actual measurement basis (Hao et al. 2006). This problem can be observed clearly in the radar refractivity retrieval formulation by reconstructing the refractivity into Cartesian coordinates while the receiving signals from ground targets are based on the polar coordinate system. If the ground clutter targets are not in the center of the Cartesian grid cells, the error in the signal phase will occur due to the two-way path difference.

Measurements for CS in DBF formulation are obtained from cross-correlations of received signals, where the signal sources are uncorrelated. However, in the simulation, by using a small number of samples, this assumption may be violated depending on the degree of correlation, if a correlation exists. Lastly, the commonly used additive white Gaussian noise assumption in the applications may not be valid. Estimating the noise level associated with the mentioned uncertainties in the measurements becomes more difficult. Accordingly, the performance of CS is likely to degrade.

2.3.3 Multiple penalty functions in l_1-norm minimization

It is common in CS applications to use a transformation matrix to obtain sparsity of the signal and additional relaxation terms for stable reconstruction. This is because the single transformation may not be sufficient to obtain a well-approximated solution due to low signal compressibility. The benefit of using multiple transformations in the minimization is to compensate for their individual weakness in order to provide stable solutions. However, there is a risk of degrading their performance in some cases. Further, the complexity of the problem, as well as the difficulty of analysis, increases when using multiple transformations. In this dissertation, TV and the Laplacian operator were used in the l_1-norm minimizations. DCT and TV are used simultaneously in the l_1-norm minimization to solve the refractivity inverse problem. Further, wavelet and Laplace are used in the l_1-norm minimization to solve the reflectivity and velocity inverse problem in DBF. TV and Laplace are used to suppress possible fluctuations in the reconstruction, in addition to DCT and wavelet.

2.3.4 Minimum number of measurements

The required minimum number of measurements was derived theoretically to recover the image exactly in some special cases, such as $\mathbf{H}$ as random Fourier matrix, Gaussian matrices, etc. (Candès 2006; Eldar and Kutyniok 2012). The equation for the

required number of measurements is calculated by using the number of pixels P, coherence, sparsity level, and a constant C value,

$$M \geq C \cdot \mu^2 \cdot K \cdot logP \tag{2.14}$$

where C is a small constant and can be calculated for the special cases. In engineering applications, it is not possible to know it accurately. Moreover, the number of measurements M can be calculated as a function of the C value in the best and worst case of sparsity level K when we determine the transformation matrix and thus the coherence. Consequently, it is difficult to determine the required number of measurements in the applications, because of the unknown sparsity level of the image K and ambiguous C value.

Chapter 3

Refractivity Retrievals with a Network of Radars

3.1 Introduction

It has been shown that high temporal and spatial resolution measurements of the moisture field have the potential to improve the forecast of convection initiation (Crook 1996; Dabberdt and Schlatter 1996; National Research Council 1998; Weckwerth et al. 2004). However, spatial resolution from surface weather stations such as mesonets is often limited to 10 - 100 km (Weckwerth et al. 2004; Roberts et al. 2008). On the other hand, radar-derived refractivity, which can be used as a proxy for the near-surface moisture field, can provide better spatial resolution of a few kilometers and comparable temporal resolution of a few minutes (Fabry et al. 1997). Good agreements can be generally found between refractivity derived from radar measurements and mesonet observations (Fabry 2004; Bodine et al. 2011). Note that the vertical profile of refractivity can be estimated from Global Positioning System (GPS)-based method (Braun et al. 2001) and is complementary to radar measurements. Recently, in order to improve the quality of the retrieved refractivity, the change in the vertical refractivity profile and the varying altitudes of ground targets have been considered (Feng et al. 2016).

Radar-derived refractivity is obtained by exploiting the phase of radar signals from ground targets (Fabry et al. 1997). The refractivity reconstruction using a single radar can be achieved by taking the range derivative of phase measurements and has been implemented on S-, C- and X-band radars (Fabry 2004; Weckwerth et al. 2005; Nicol and Illingworth 2012; Cheong et al. 2008a). However, the resolution can be degraded due to the lack of high-quality ground targets in adjacent range gates. Note that the quality of ground target signals is affected by the changes in targets' shapes, ranges from the radar, variations in the height of targets, and precipitation delays, for example (Fabry 2004; Bodine et al. 2011). An assimilation of simulated radar refractivity for improving forecasting is made by considering the related phase change observations, including the ground target position uncertainty (Shimose et al. 2013). Further, in order to improve the accuracy of phase measurement in operational radar applications, the use of higher altitudes of ground targets (Besson and Parent du Châtelet 2013; Feng et al. 2016) and small time intervals between the measurements are suggested to reduce the phase ambiguity (Besson and Parent du Châtelet 2013). Dual polarization radars can provide additional phase information from ground clutter by using short pulse width and potentially improve the quality of refractivity (Besson and Parent du Châtelet 2013).

On the other hand, a network of weather radars was proposed to address this issue, where phase measurements from multiple radars are represented by a linear model with gridded refractivity field (Hao et al. 2006). Consequently, refractivity retrieval

is postulated as an inverse problem. The issue is that the number of measurements is typically fewer than the number of refractivity pixels to be estimated and the inversion is ill-conditioned. In other words, the commonly used least squares (LS) approach will lead to erroneous refractivity reconstruction. Therefore, a constrained least squares (CLS) method was proposed, where a locally smoothed refractivity field is assumed (Hao et al. 2006). The CLS method was verified using simulation (Hao et al. 2006) and the principles were demonstrated by a field experiment with multiple S-band radars in Colorado (Fritz and Chandrasekar 2009). It is shown that the performance of CLS can be improved by using two radars rather than a single radar for the same number of ground targets and measurements (Hao et al. 2006). Further, CS can be applied to networked radar to reconstruct the refractivity field from a limited number of phase measurements and compared to the CLS method (Ozturk et al. 2014). Theoretically, CS can provide exact solutions via l_1-norm minimization if signals are strictly sparse and acquired with maximum incoherence in the absence of noise (Candès and Romberg 2006; Donoho 2006; Candès and Wakin 2008). The concept of sparsity and compressibility for refractivity field will be discussed in more detail later.

3.2 Formulation of refractivity retrieval with networked radars

Given a stationary ground target located at a distance of R from the radar, the phase difference of radar signals at two observation times of t and t_0, $\delta\phi(R, t-t_0)$, is determined by the integration of refractivity difference along the ray path (Fabry et al. 1997), as shown in the following equation:

$$\delta\phi(R, t-t_0) = \frac{-4\pi 10^{-6}}{\lambda} \int_0^R \delta N(r, t-t_0) dr, \tag{3.1}$$

where λ is the radar wavelength and δN is the refractivity difference between time t and t_0 as a function of range. The refractivity field at time t_0 is termed the reference map and is measured prior to the experiment typically on a calm day, when the meteorological condition is steady with cool temperature that leads to spatially uniform refractivity (Fabry et al. 1997). The introduction of the reference map made refractivity retrieval possible, because otherwise the radar's phases are severely wrapped, i.e., wrapped every half wavelength due to the two-way ray path. For a single radar, the refractivity difference δN can be estimated from the range derivative of smoothed and interpolated phase differences. Consequently, the refractivity field at time t is obtained by adding back the reference map (Fabry 2004; Cheong et al. 2008a). A more detailed description of refractivity retrieval using phase measurements from a single radar can be found in (Fabry 2004; Cheong et al. 2008a).

A linear model was introduced to represent the phase measurements from multiple radars (Hao et al. 2006; Fritz and Chandrasekar 2009) and is briefly reviewed here. Let's assume that the field of refractivity difference to be reconstructed consists

of $M \times N$ pixels and is subsequently arranged into a column vector of $\boldsymbol{\eta}$ with a size of $P \times 1$, where $P = MN$. As a result, the phase difference from a network of K radars and J ground targets can be represented in the following matrix form:

$$\boldsymbol{\Phi} = \frac{-4\pi 10^{-6}}{\lambda} \mathbf{H}\boldsymbol{\eta} + \mathbf{e}, \tag{3.2}$$

where $\boldsymbol{\Phi}$ is a column vector of measured phase differences with a length of $L = KJ$, $\mathbf{e}$ is the measurement errors with size of $L \times 1$, and $\mathbf{H}$ is a measurement matrix with size of $L \times P$. Let $\boldsymbol{h}_i$ be the i^{th} row of $\mathbf{H}$ that represents one measurement from a radar to a ground target. Then (3.1) is approximated by the product of $\boldsymbol{h}_i$ and $\boldsymbol{\eta}$. The values in the $\boldsymbol{h}_i$ are zero, except where the ray passes the pixels and the value is the length of ray path in that pixel. Therefore, the measurement matrix $\mathbf{H}$ is likely sparse. Note that in this work, the first J measured phase differences in $\boldsymbol{\Phi}$ are obtained from the first radar, and the second J measurements are from the second radar, etc. Note that the linear model can also be applied to a single radar ($K = 1$).

Consequently, the refractivity retrieval is posed as an inverse problem to estimate P values of $\boldsymbol{\eta}$ from L measurements of $\boldsymbol{\Phi}$. If L is smaller than P, then (3.2) becomes an underdetermined problem. The LS method is not sufficient to produce a unique solution. Therefore, CLS was developed to reconstruct refractivity from multiple radars by adding the criterion of a smoothed field to constrain the solution space (Hao et al. 2006). In this work, CS is proposed to estimate refractivity from both single and networked radars. These two retrieval approaches are now briefly reviewed.

Additionally, RMSE between the model and recovered images is used to quantify the quality of reconstruction and is defined as,

$$\text{RMSE} = \left\{ \frac{1}{P} \sum_{i=1}^{P} (\eta_i - \hat{\eta}_i)^2 \right\}^{\frac{1}{2}}. \tag{3.3}$$

Note that $\hat{\boldsymbol{\eta}} = [\hat{\eta}_1, \hat{\eta}_2, ..., \hat{\eta}_P]^T$ is the recovered or reconstructed refractivity difference field with size of $P \times 1$. Although the refractivity N is dimensionless, it is often expressed in N-unit.

3.3 A brief overview of the constrained least square method

As mentioned previously, (3.2) is underdetermined due to the limited number of measurements. As a result, no unique solution exists. As such, the commonly used LS solution is often noisy due to the spatial discontinuity on the retrieved refractivity difference field (Hao et al. 2006). In order to improve the LS solution, a smoothness function is proposed to minimize the sharp changes and provide spatial continuity in the refractivity field. The smoothness function is defined as the squared second differences of the image as shown in the following equation (Hao et al. 2006):

$$D^2 = \frac{1}{2} \boldsymbol{\eta}^T \mathbf{Q} \boldsymbol{\eta}, \tag{3.4}$$

where $\mathbf{Q}$ is a $P \times P$ matrix that performs the squared second finite differences of the gridded field in horizontal, vertical and diagonal directions (Hao et al. 2006). In other words, the lower the D^2 value, the smoother the refractivity image is. Moreover,

the refractivity difference using CLS has two minimization processes that can be postulated as follows:

$$\min D^2 \text{ subject to minimize } \quad \|\mathbf{\Phi} - \frac{-4\pi 10^{-6}}{\lambda}\mathbf{H}\hat{\boldsymbol{\eta}}\|_2^2, \tag{3.5}$$

where the squared l_2-norm is defined as $\|\mathbf{x}\|_2^2 = \sum_i |x_i|^2$. In other words, the regularization for the reconstruction of refractivity difference can be performed in two parts by exploiting SVD of $\mathbf{H}$ and the smoothness function D^2. The SVD of $\mathbf{H}$ is written as $\mathbf{H} = \mathbf{U}\mathbf{\Sigma}\mathbf{V}^\mathbf{T}$, where $\mathbf{U}$ and $\mathbf{V}$ are square unitary matrices and $\mathbf{\Sigma}$ represents the diagonal matrix of successively decreasing singular values. Note that the SVD computational time cost of $\mathbf{H}$ can be expensive because the $\mathbf{H}$ matrix is often large. Subsequently, the forward phase difference in 3.2 can be rewritten as, $\mathbf{\Phi} = \frac{-4\pi 10^{-6}}{\lambda}\mathbf{U}\mathbf{\Sigma}\mathbf{V}^\mathbf{T}\boldsymbol{\eta} + \mathbf{e}$. In order to derive successive minimization, we define $\mathbf{V}^\mathbf{T}\boldsymbol{\eta} = \mathbf{z} = \begin{bmatrix} \mathbf{z_t} \\ \\ \mathbf{z_r} \end{bmatrix}$. By multiplying both sides with $\mathbf{V}$, $\boldsymbol{\eta}$ can be formulated as:

$$\boldsymbol{\eta} = \mathbf{V}\mathbf{z} = \mathbf{V_t}\mathbf{z_t} + \mathbf{V_r}\mathbf{z_r}, \tag{3.6}$$

where $\mathbf{z_t}$ is $t \times 1$, $\mathbf{z_r}$ is $(P-t)\times 1$, and $\mathbf{V} = [\mathbf{V_t}\ \mathbf{V_r}]$. Note that the CLS solution in (3.6) has two parts, as $\hat{\boldsymbol{\eta}}_{CLS} = \hat{\boldsymbol{\eta}}_{LS} + \hat{\boldsymbol{\eta}}_m$. The LS solution $\hat{\boldsymbol{\eta}}_{LS}$ is obtained from truncated SVD (TSVD) of $\mathbf{H}$, $\mathbf{H_t} = \mathbf{U_t}\mathbf{\Sigma_t}\mathbf{V_t^T}$. where $\mathbf{U_t}$ is $L \times t$, $\mathbf{V_t}$ is $P \times t$, and $\mathbf{\Sigma_t}$ is a $t \times t$ truncated matrix. t is determined by assuming that the Frobenius norm of the smaller singular values does not exceed a threshold (Hao et al. 2006). Specifically, the LS

solution from (3.2) is obtained by the inverse of the TSVD as shown in the following equation:

$$\hat{\boldsymbol{\eta}}_{LS} = \frac{\lambda}{-4\pi 10^{-6}} \mathbf{V_t} \boldsymbol{\Sigma}_\mathbf{t}^{-1} \mathbf{U}_\mathbf{t}^\mathbf{T} \boldsymbol{\Phi}. \tag{3.7}$$

In other words, $\mathbf{z_t}$ in (3.6) is derived as, $\mathbf{z_t} = \boldsymbol{\Sigma}_\mathbf{t}^{-1} \mathbf{U}_\mathbf{t}^\mathbf{T} \boldsymbol{\Phi}$. As a result, $\mathbf{V_r}$ is also known and has a size of $P \times (P - t)$. The next step is to derive the $\mathbf{z_r}$ in (3.6), which can be used to update the LS solution to meet the requirement of a smoothed field. This can be achieved by substituting (3.6) into (3.4) and minimizing D^2 with respect to $\mathbf{z_r}$. Consequently, the CLS solution can be derived in the following equation:

$$\hat{\boldsymbol{\eta}}_{CLS} = [\mathbf{I} - \mathbf{V_r} (\mathbf{V}_\mathbf{r}^\mathbf{T} \mathbf{Q} \mathbf{V_r})^{-1} \mathbf{V}_\mathbf{r}^\mathbf{T} \mathbf{Q}] \hat{\boldsymbol{\eta}}_{LS}, \tag{3.8}$$

where $\mathbf{I}$ is a $P \times P$ identity matrix. Note that the CLS solution in (3.8) was derived from the LS solution by estimating from a prior assumption, i.e., smoothness. Therefore, the smoothness constraint in the minimization can mitigate sharp and strong variation in the refractivity field and result in smoothed refractivity. It should also be noted that CLS-derived refractivity becomes smoother if the threshold level to determine t is higher.

3.4 Compressive sensing technique

In this work, CS is applied to solve the inverse problem of refractivity retrieval from radar phase measurements in section 3.2, where the number of measurements can be small due to the lack of high quality ground clutter. The key elements required

in CS to produce satisfactory reconstructions include sparsity, incoherency, and l_1-norm minimization, which will be discussed in the following subsections. Note that the discussion of the RIP with relation to sparsity and incoherency is made in section 3.7.

3.4.1 Sparsity

In CS theory, images can be reconstructed with high accuracy from a limited number of measurements if the images are sparse (Candès and Romberg 2006; Donoho 2006; Candès 2006; Baraniuk 2007). In this work, the level of compressibility for a given image is defined based on the RMSE between the image and its approximation by using a portion of large coefficients. When the coefficients for a compressible image are sorted, they decay rapidly into relatively smaller values and only contribute ignorable contents to the original image. This will be explained in more detail in Section 3.6.3.

In this work, the DCT (Jain 1989) was applied to the field of refractivity difference. In other words, the refractivity difference can be represented by $\boldsymbol{\theta} = \boldsymbol{\Psi}\boldsymbol{\eta}$, where $\boldsymbol{\Psi}$ is the DCT transformation basis function with size of $P \times P$ and $\boldsymbol{\theta}$ is the transformation coefficient of $\boldsymbol{\eta}$ with a size of $P \times 1$. Two scenarios of refractivity difference with two different degrees of compressibility are exemplified in Fig. 3.1, where the field of refractivity difference is shown from -12.5 to 12.5 km with a resolution of 0.5 km in both directions (i.e, P=2500). In Scenario I, the refractivity difference is

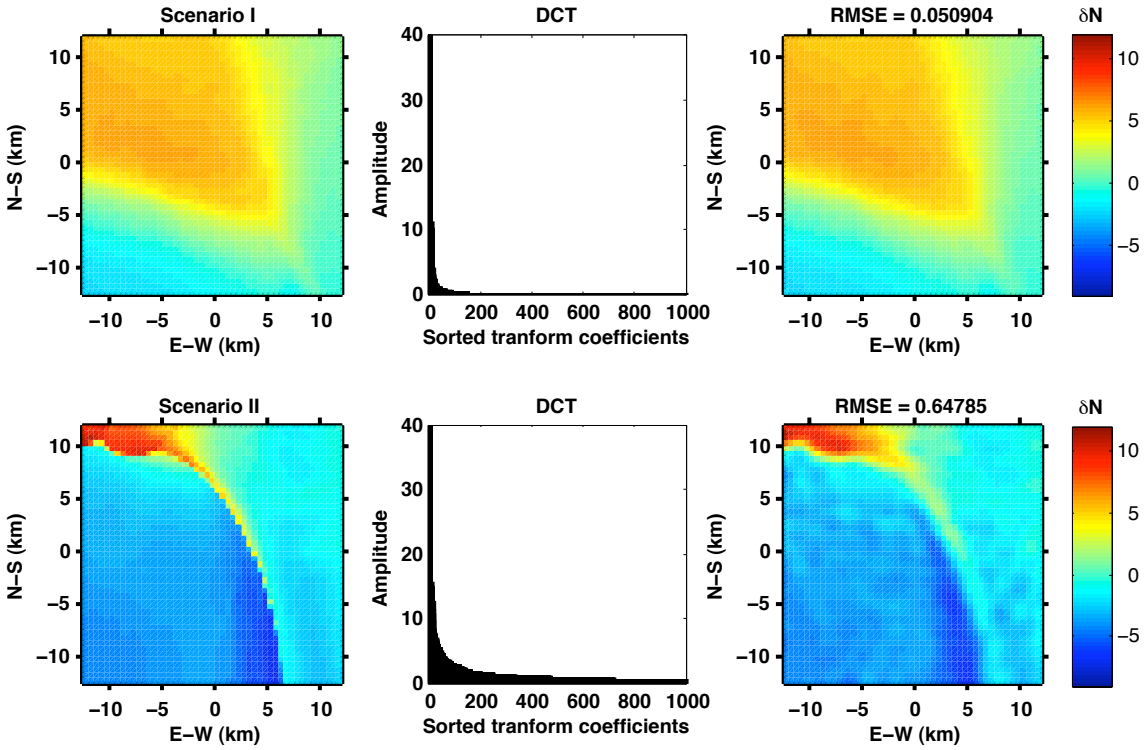

Figure 3.1: The refractivity difference fields (left panels) are shown for both Scenarios I and II with 2500 pixels (25 by 25 km with a 0.5 km grid spacing). The first 1000 sorted transform coefficients for both scenarios after DCT are shown in the middle panels. The recovered refractivity changes (right panels) are obtained by the inverse DCT using 6 % of the largest coefficients.

shown in the upper left panel, and its sorted DCT coefficients are shown in the upper middle panel in a descending order. The rapid decrease of these coefficients suggests that the image is compressible but not sparse, because small values are nonzero. In other words, the image can be well-approximated by a few large coefficients. For example, if only 6% of the largest transform coefficients are used, the approximated image is shown in the upper right panel with a RMSE of 0.051 N-unit. The difference between the original image and the recovered image using a small number of

coefficients is visually almost indistinguishable. In contrast to Scenario I, a less compressible image is shown in the lower panels for Scenario II. The decreasing rate of sorted DCT coefficients is slower than the one in Scenario I. The image recovered using only 6% of the largest coefficients is presented in the bottom right panel with a RMSE of 0.648 N-unit. Although the RMSE value is significantly larger than in Scenario I, the general pattern of the refractivity difference field in Scenario II is still preserved. This indicates both scenarios are compressible, and the degree of compressibility in Scenario I is higher.

The impact of different compressibility factors on CS refractivity retrieval will be discussed in more detail in Section 3.6.3. Additionally, the value of smoothness D^2 for both Scenarios I and II are 35.68 and 6452.06 N-unit/km^2, respectively. In other words, the refractivity difference in Scenario I is smoother than in Scenario II.

3.4.2 Incoherency

To reconstruct sparse or compressible images using CS, the second important element is that the measurements should be obtained as incoherently with the sparse representation basis functions as possible (Donoho and Elad 2003; Candès and Romberg 2006). A theoretical incoherence value range is given between [1, 60] (Candès and Romberg 2006). Incoherence is computed between the measurement matrix $\mathbf{H}$ and DCT $\mathbf{\Psi}$ and obtained as 10. While the computed coherence is relatively low (10 in

a range of 1 to 60), such a value cannot guarantee exact recovery (similar to conditions with unsatisfied RIP) unless the sparsity property of signals to be recovered and transformation matrix are also considered (Candès and Romberg 2006; Duarte and Eldar 2011). It is also worth noting that the condition of incoherence can be further improved by designing a better transformation matrix, which can result in better sparsity of signals in the transformed domain and incoherence to measurement matrices.

3.4.3 l_1-norm minimization

Donoho and Elad (2003) showed that the unique solution for sparse signals can be found by using the l_1-norm minimization, where the l_1-norm penalizes small values heavily compared to the l_2-norm approaches, and thus tends to generate sparse solutions. In this work, another objective function, termed TV norm, was used in the minimization, which is defined by the sum of the magnitudes of gradients of the image (Candès and Romberg 2005). It has been shown that TV in the optimization can mitigate high frequency oscillations in the reconstructed images, which are typically caused by noise (Rudin et al. 1992). Consequently, the refractivity retrieval using CS is obtained by solving the following minimization problem:

$$\begin{aligned} &\min \ \|\boldsymbol{\Psi}\hat{\boldsymbol{\eta}}\|_1 + \alpha \mathrm{TV}(\hat{\boldsymbol{\eta}}) \\ &\text{subject to} \quad \|\boldsymbol{\Phi} - \frac{-4\pi 10^{-6}}{\lambda}\mathbf{H}\hat{\boldsymbol{\eta}}\|_2^2 < \tau, \end{aligned} \tag{3.9}$$

where τ controls the consistency between the estimated data from reconstruction and measured data, and α controls the sparsity in $\boldsymbol{\Psi}$ and total variation of the reconstructed refractivity field. The minimization problem was solved by using nonlinear

conjugate gradients and a backtracking line search (Donoho 2006), where the error term and solution were updated in each iteration.

3.5 Description of numerical simulations

Numerical simulations were developed to demonstrate and verify the feasibility of CS for refractivity retrieval with both single and networked radars. The model refractivity field was generated from the ARPS, a compressible nonhydrostatic storm-scale numerical weather prediction model developed at the Center for Analysis and Prediction of Storms (CAPS) at the University of Oklahoma (Xue et al. 2003). In this work, a numerical simulation was performed for a period of approximately two hours, from 1800 to 1945 UTC May 19, 2010, with 5-minute intervals. The domain used for this refractivity study had a size of 30 by 30 km and resolution of 0.1 by 0.1 km.

The simulation was initialized from a North American Mesoscale Model (NAM) 12-km analysis at 1800 UTC interpolated to the ARPS grids. The interpolated NAM analysis also served as lateral boundary conditions throughout the simulation. Given the high grid resolution (100-m horizontally), the model was configured to run as a large eddy simulation in order to develop more complex structures of the moisture field in the boundary layer. Since the initial conditions for model integration were interpolated from a much coarser 12-km NAM grid, there was a model spin-up period of less than 10 minutes that allowed for these complex structures to fully develop via forward integration. Absolute refractivity was obtained in the model every five

minutes through the use of the classic Bean and Dutton equation (Bean and Dutton 1968).

In this work, the first model refractivity at 1800 UTC was considered to be the reference map, and the subsequent refractivity changes were obtained by the difference between the reference map and the current model refractivity. The resulting refractivity differences vary from approximately -9 to 12 N-units over the simulation period. The model field of refractivity differences is considered to be the truth.

For simplicity, the ground targets were located randomly with uniform distribution within the domain. Further, it was assumed that all the radars are operated at the same frequency of 10 GHz and are able to sense all the ground targets. Each radar range gate is defined by the beamwidth of one degree and a range resolution of 100 m.

For a given radar and ground target location, a row vector in the measurement matrix $\mathbf{H}$, $\boldsymbol{h}_i$, was obtained by gridding the simulation domain (Hao et al. 2006) as shown in section 3.2, and the resultant phase measurements were obtained using (3.2). If multiple targets were presented within one range gate, the phase of radar signal was obtained after the superposition of the complex signals from multiple targets. The measurement errors were simulated by adding random fluctuations, generated from a zero-mean Gaussian random variable with a desirable standard deviation (SD), to the model of refractivity difference. The SD of error is denoted by σ_e.

The maps of simulated phase difference measurements from a radar located at the south-west corner of the domain, (-12.5, -12.5) km, together with 1200 ground target points and σ_e = 1 N-unit are demonstrated in the left and right panels of Fig. 3.2 for the two scenarios discussed in Fig. 3.1. The fields of refractivity for the two scenarios were obtained from the simulation at 1845 UTC and 1920 UTC. In order for better presentation, the phase differences were interpolated to a grid size of 0.1×0.1 km. Although one of the practical and important issues for refractivity retrieval is the phase unwrapping, in this work it is assumed that the same unwrapped phases were to be used by both CLS and CS. The simultaneous phase-unwrapping algorithm proposed for CLS reconstruction can be used for CS retrieval (Hao et al. 2006). The idea is to group the ground targets that are locally close and have similar phase change within $\frac{\pi}{4}$ with respect to 2π and then unwrapping them locally.

In the reconstruction, the grid size of 0.5 by 0.5 km was used for refractivity retrieval within the domain of 25 by 25 km. Without any prior knowledge of the ground target locations, the $\mathbf{H}$ matrix was obtained by assuming only a single ground target located at the center of the gate. Practically, it is highly difficult to determine the number of ground targets and their exact locations within a range gate. In other words, even without noise contamination, errors can exist for model-based refractivity retrieval.

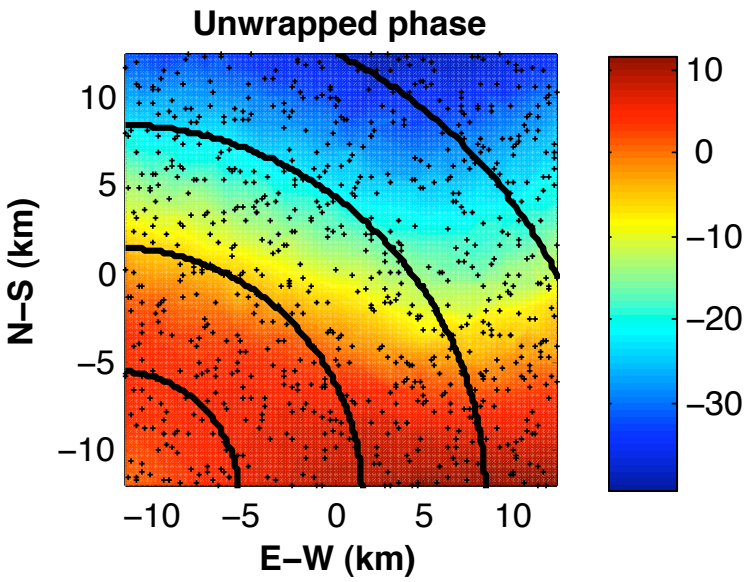

(a) Scenario I

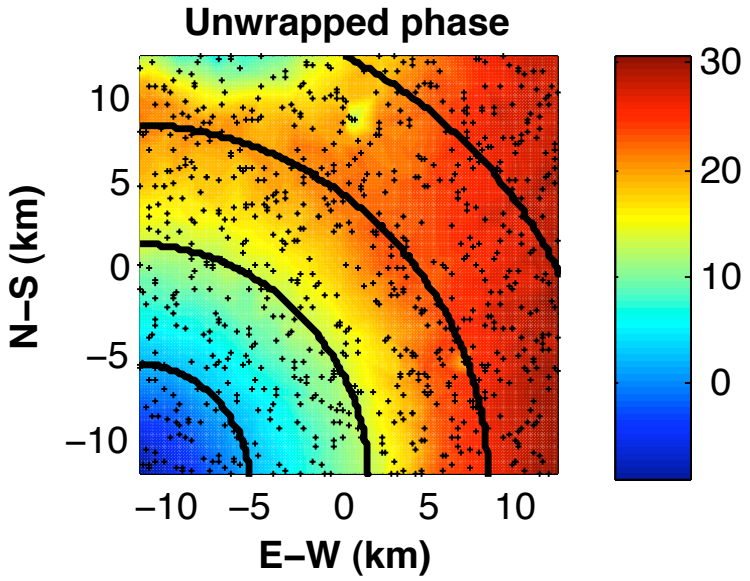

(b) Scenario II

Figure 3.2: Interpolated phase difference measurements for scenario I and scenario II with 1 N-unit noise from one radar located at (-12.5, -12.5) km. The location of 1200 ground target points are denoted by black dots on the panels.

3.6 Numerical results

The goal of this section is to investigate the performance of CS for different amounts of noise, different numbers of radars, and various refractivity structures through statistical analysis. Additionally, the performance of CS will be compared to CLS under these conditions. The performance of both retrieval methods is quantified by the RMSE defined in (3.3). Note that the reconstructed field is the refractivity difference, and the absolute refractivity field can be easily obtained by adding back the reference refractivity field. For each case, 50 realizations were performed, each with independent ground target location and noise sequence. In Section 3.6.1, the SD of measurement errors (σ_e) is varied from 0 to 1.5 N-unit with a step of 0.5 N-unit to study the impact of noise for the two scenarios, given two radars located at (-12.5, -12.5), (-12.5, 12.5) km and 1200 ground targets. In Section 3.6.2, the number of radars is varied from one to four for the two scenarios, given 600 ground targets and σ_e = 1 N-unit. In Section 3.6.3, the evolution of refractivity difference over the simulation period is investigated using three radars, σ_e = 1 N-unit, and 800 ground targets.

3.6.1 Impact of noise

In order to investigate the robustness of CS in refractivity retrieval, various amounts of noise were added, and the mean of RMSE for CLS and CS in both scenarios is shown in Fig. 3.3. The degradation of CS and CLS as a function of noise can be

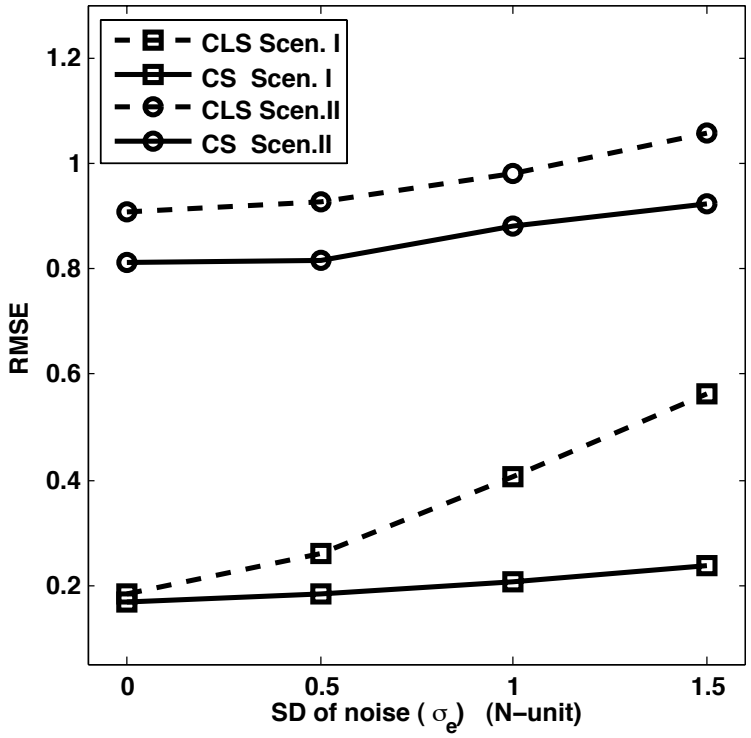

Figure 3.3: The mean of the RMSE as a function of noise for CS (solid line) and CLS (dash line) for both Scenarios I and II. The statistical results were obtained from a network of two radars with 2400 measurements.

observed for both scenarios. Recall that the refractivity difference field in Scenario I is relatively more compressible than the one in Scenario II, as demonstrated in Section 3.4.1 (Fig. 3.1). As a result, CS performs better in Scenario I than Scenario II, for different noise levels, given the same number of measurements, manifested by the lower RMSE. Similar results are observed for CLS because the smoothness of D^2 in Scenario I is relatively low (in Section 3.4.1), and CLS is designed to reconstruct smooth fields. The performance of CS and CLS for different levels of compressibility and smoothness will be discussed in more detail in Section 3.6.3. Moreover, it can be observed that the degree of degradation of CS and CLS with noise also depends

on the corresponding compressibility and smoothness levels. The RMSE from the noiseless case can be thought of as the upper bound of the performance for each algorithm under the given conditions.

It is important to point out that CS performs better than CLS in both scenarios for all noise levels considered. Moreover, in Scenario II the degree of degradation of CS with noise is comparable with CLS's. On the other hand, in Scenario I the degradation of CS is significantly slower than CLS, while CS and CLS have similar RMSE for the noiseless case. In other words, although CLS has better performance for the smoother condition in Scenario I compared to Scenario II, it is more susceptible to noise under such conditions. On the other hand, the degradation of CS with noise is relatively stable for both scenarios. One of the reasons is the use of the TV constraint in CS. The inclusion of TV enforces adjacent pixels in horizontal and vertical dimensions to have similar values. In other words, CS searches for the solution with the minimal value of TV-norm and l_1-norm, based on the parameter of α. On the other hand, it should be noted that the smoothness function D^2 used in CLS also forces adjacent pixels in orthogonal and diagonal dimensions to have similar values based on the LS solution.

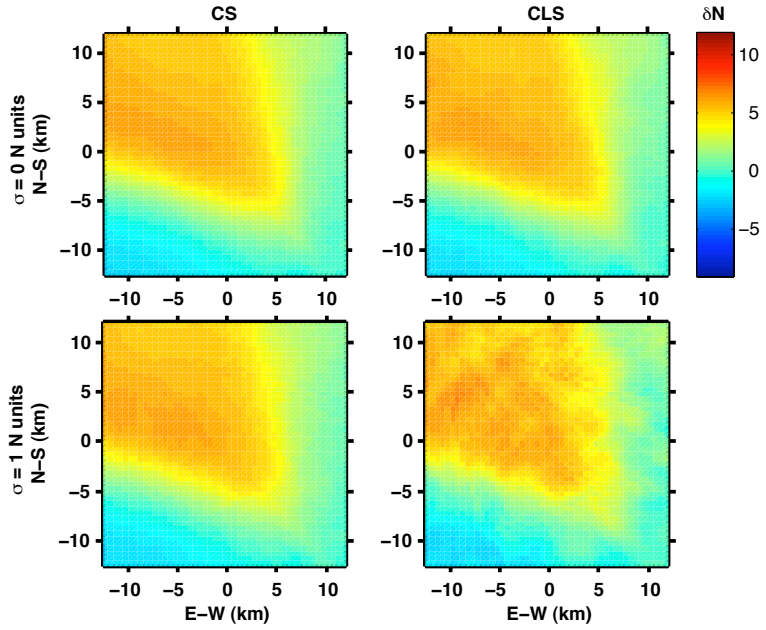

(a) Scenario I

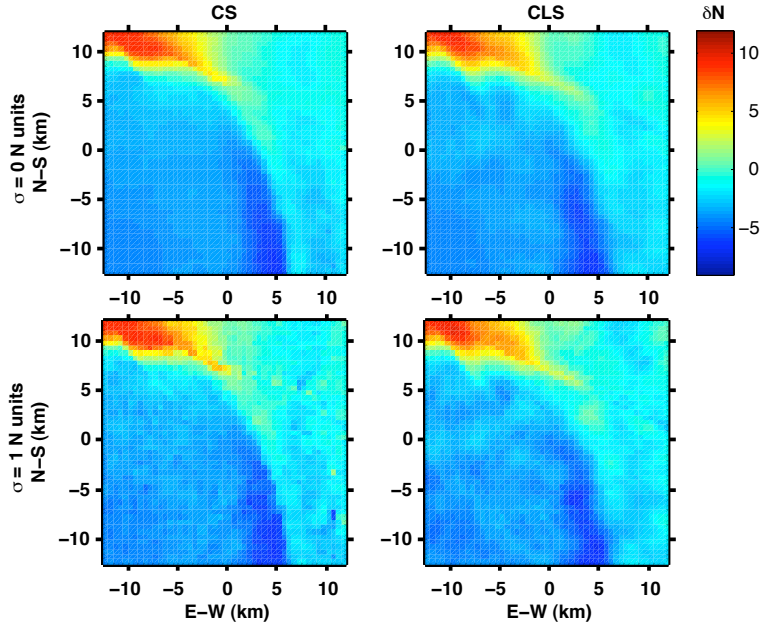

(b) Scenario II

Figure 3.4: CS (left panel) and CLS (right panel) refractivity difference retrieval with noise $\sigma_e = 0$ (1st row) and $\sigma_e = 1$ N-unit (2nd row), using two radars and 2400 measurements. CS is better at preserving the shape of refractivity difference than CLS for both cases in Scenario II and $\sigma_e = 1$ N-unit in Scenario I.

Examples of CS and CLS retrievals from one realization of the noiseless and noisy cases with σ_e = 1 N-unit in Scenarios I and II are provided in left and right panels of Fig. 3.4, respectively. Note that the models of refractivity differences are presented in Fig. 3.1. It is clear that the refractivity differences for Scenarios I and II can be grossly reconstructed using both CS and CLS for both noiseless and noisy cases, but some detailed structures are not recovered accurately. First of all, for both algorithms and scenarios, large errors often occur in the vicinity of regions with strong gradient, such as the V-shaped boundary of the positive refractivity difference in Scenario I, and the north-south oriented arc-shaped boundary in Scenario II. Secondly, in Scenario I, the degradation of CLS from noiseless to noisy case of σ_e = 1 can be clearly observed and is more evident than the degradation of CS, as indicated in Fig. 3.3. Specifically, more fluctuations caused by the noise were produced by CLS for σ_e = 1. Thirdly, the sharp change of the arc-shaped boundary in Scenario II is better resolved using CS than with CLS for both cases. Additionally, the smaller values of negative refractivity change on the southwest side of the domain are not recovered using either of the algorithms.

3.6.2 Impact of the number of radars

Expanding from a single radar to a network of four radars was studied by adding radars at the location in the order of (-12.5, -12.5), (-12.5, 12.5), (12.5, 12.5), and (12.5, -12.5) km. Note that the number of phase measurements is determined by

the product of the numbers of radars and ground targets. In this experiment, a fixed number of 600 ground targets were used for various numbers of radars. It is shown in Fig. 3.5 that for both CLS and CS in the two scenarios, the mean of RMSE decreases as the number of measurements is increased by adding more radars.

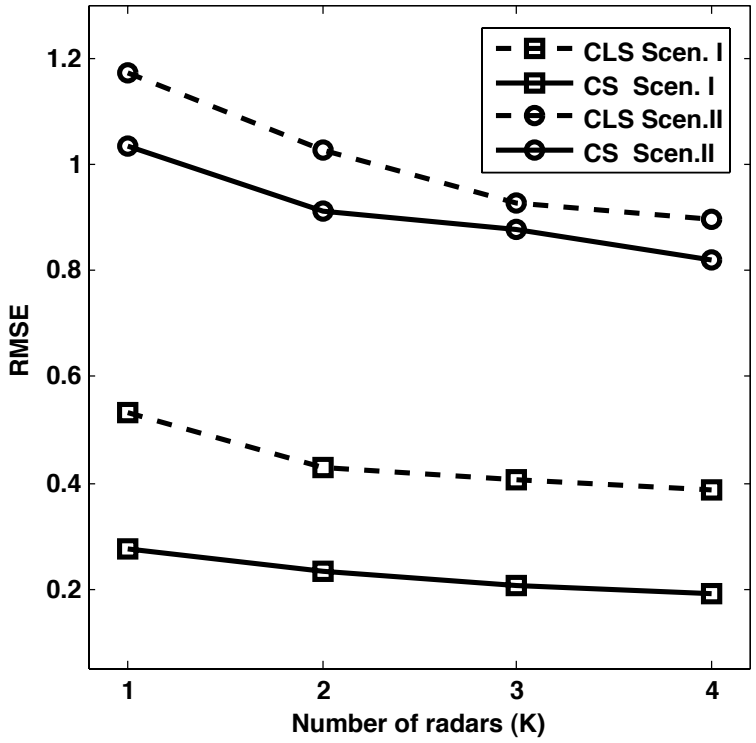

Figure 3.5: The mean of the RMSE as a function of number of radars for CS (solid line) and CLS (dash line) from 1 N-unit noisy measurements for both Scenarios I and II. There are 600 ground targets in the field so the number of measurements increases as the number of radars increases.

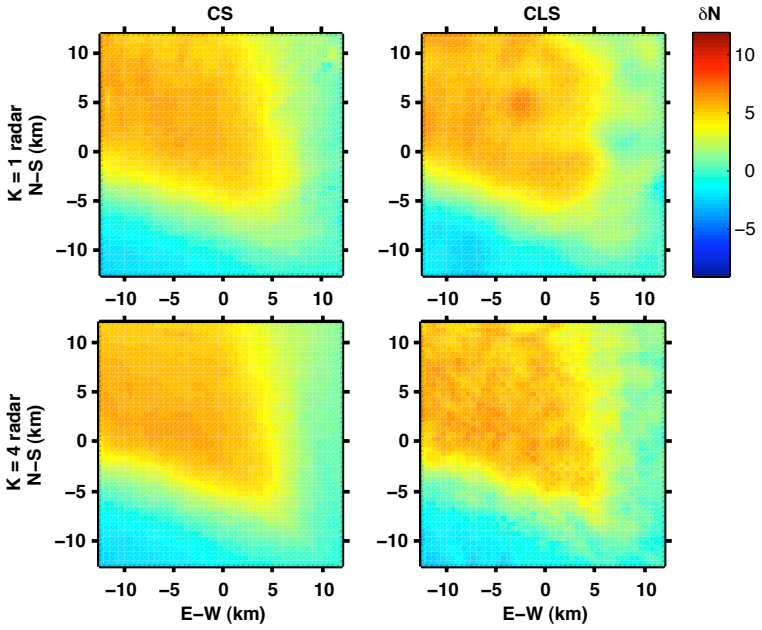

(a) Scenario I

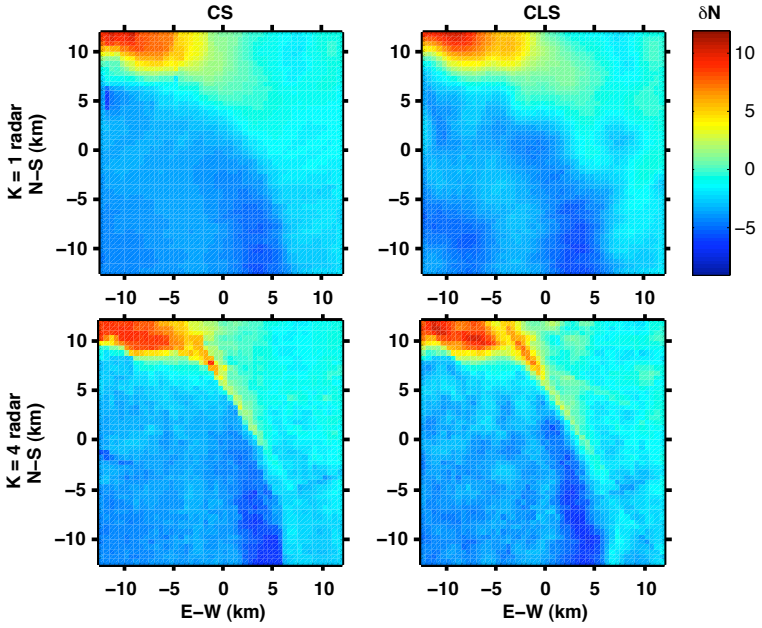

(b) Scenario II

Figure 3.6: CS (left column) and CLS (right column) refractivity difference retrieval with radars K=1 and K=4. There are 600 ground targets in the domain and measurements are with σ_e = 1 N-unit noise.

Note that the mean RMSE of CS is lower than CLS for one to four radars in both scenarios. The impact of the number of radars on CS and CLS reconstructed refractivity difference is exemplified in Fig. 3.6 for σ_e = 1 N-unit for both scenarios. It is evident that for both CS and CLS, additional radars can provide better reconstruction, especially in the region of strong gradient. For example, CS in Scenario I with four radars can provide a better refractivity difference field of the V-shaped boundary than CS with only a single radar located at (-12.5, -12.5) km. Similar results can be observed for CLS. Moreover, both CS and CLS can reconstruct the sharp arc-shaped boundary better using four radars than with a single radar. Additionally, CS can better reconstruct the shape of the structure in the refractivity difference field than CLS does for both scenarios and cases. It is also evident in Fig. 3.6 that the estimation of the refractivity difference using both CS and CLS is improved by using more radars for both scenarios.

It is interesting to compare the lower panels in Figs. 3.4 and 3.6, where the number of measurements and noise level are the same. Note that two radars with 1200 ground targets were used in Fig. 3.4, while four radars with 600 ground targets were used in Fig. 3.6. It is more evident from Scenario II that the combination of four radars with 600 ground targets produce better reconstruction in the upper portion of the arc-shaped boundary, where the refractivity difference of approximately 4 N-units is better recovered. Indeed, for the mean of RMSE using CS and CLS with two radars, 0.88 and 0.98 are reduced to 0.82 and 0.89 with four radars, respectively. For

a given ray path between the radar and clutter, this path could be intercepted more often if additional radars were used.

3.6.3 Evolution of refractivity

To further demonstrate the feasibility of CS for refractivity retrieval, the fields of refractivity difference over the entire simulation period were used with three radars located at (-12.5, -12.5), (-12.5, -12.5), and (12.5, 12.5) km, σ_e = 1N-unit, and 800 ground targets. The smoothness of D^2 from all the 23 models of refractivity difference is denoted by a dashed line in Fig. 3.7(a). Moreover, a compressibility index was introduced in this work to quantify the compressibility of refractivity difference images. Note that higher compressibility index indicates the need of a less number of coefficients for image recovery, which means high compressibility.

The compressibility index is defined by the percentage of the number of the largest DCT coefficients used to reconstruct the image that meets a pre-defined RMSE between the original and recovered images. In this work, a RMSE of 0.051 was set to represent the case where the original image is well-approximated, as shown in the upper panel of Fig 3.1. The compressibility index for the 23 models of refractivity difference is denoted by the solid line in Fig. 3.7(a). Furthermore, the coherences under the conditions of various random target locations and different radar configurations were calculated to be approximately 10 for all the cases, which is considered low, given the theoretical value between 1 and 60. Since the coherence for all conditions

is similar, the performance of CS is expected to largely depend on the compressibility index. Compressibility index decreases and smoothness increase (becoming less compressible and less smooth) with time in the first 75 min. and subsequently become stable at the approximate compressibility level of 30% and smoothness of 6400 N-unit/km^2. The evolution of refractivity difference from the model is exemplified in the first column of Fig. 3.9 for a 15-min. interval.

The mean of RMSE for CS and CLS over 50 realizations is shown in Fig. 3.7(b) for the entire simulation at 5-min intervals. The dependence of CS on the sparsity level and CLS on the smoothness level can be clearly observed. Specifically, the mean RMSE of CS and CLS increases as the values of compressibility index decreases and smoothness increases. Note that CS provides better performance than CLS for the entire simulation period. The difference of the RMSE between CS and CLS is as large as 0.27 at 1805 UTC and decreases to approximately 0.07 at 1915 UTC. It is interesting to note that the degradation of CS is faster than CLS from 1805 – 1900 UTC in Fig. 3.7(b). It indicates that the CS is more sensitive to the level of compressibility than CLS is to smoothness, under the 1 N-unit noise.

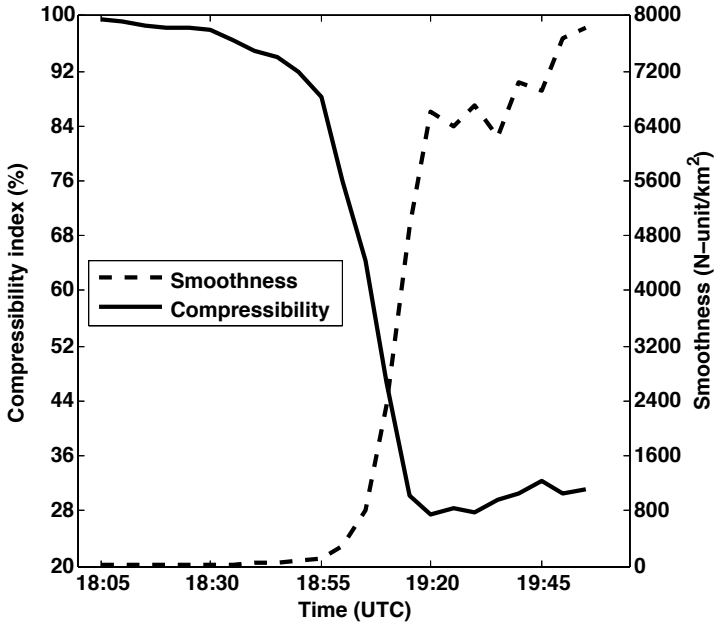

(a) Compressibility index and smoothness

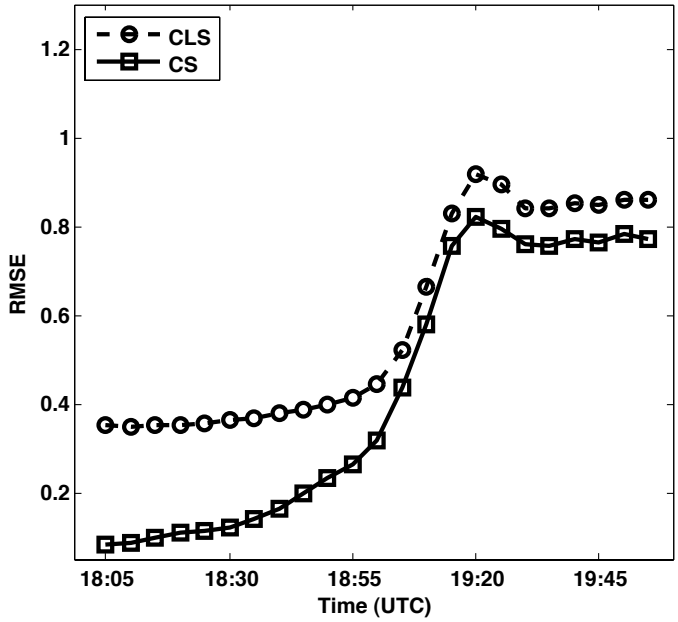

(b) RMSE of CS and CLS

Figure 3.7: a) Compressibility index (solid line) and smoothness (dash line) of the refractivity changes for 2-hr period of simulation time. b) The mean of the RMSE for CS (square-solid line) and CLS (circle-dash line) as a function of time using three radars and 2400 measurements with σ_e = 1 N-unit noise.

Examples of CS and CLS reconstruction are shown in the second and third columns of Fig. 3.9, respectively. The strong gradient in refractivity difference becomes more evident as time evolves, and therefore, the smoothness value increases (becoming less smooth). Generally speaking, both CS and CLS can qualitatively reconstruct the refractivity difference most of the time. This can be observed easily from the results in Fig. 3.9 after 1850 UTC. Moreover, CS provides better reconstructions than CLS especially for the first hour, when the compressibility level is relatively low. Additionally, CLS produces noisier reconstruction than CS over the 2-hr simulation period.

3.7 Summary and conclusions

The performance of conventional refractivity retrieval can be limited by the number of high-quality ground returns. In this work, the emerging technique of CS was proposed to improve the refractivity retrieval using a network of radars. CS has been applied to other fields and has shown promising image reconstruction with much fewer measurements than those used in the conventional sampling scheme. The application of CS to refractivity retrieval was formulated using a linear model and subsequently demonstrated using simulations, where the modeled refractivity fields were obtained from a numerical weather prediction model.

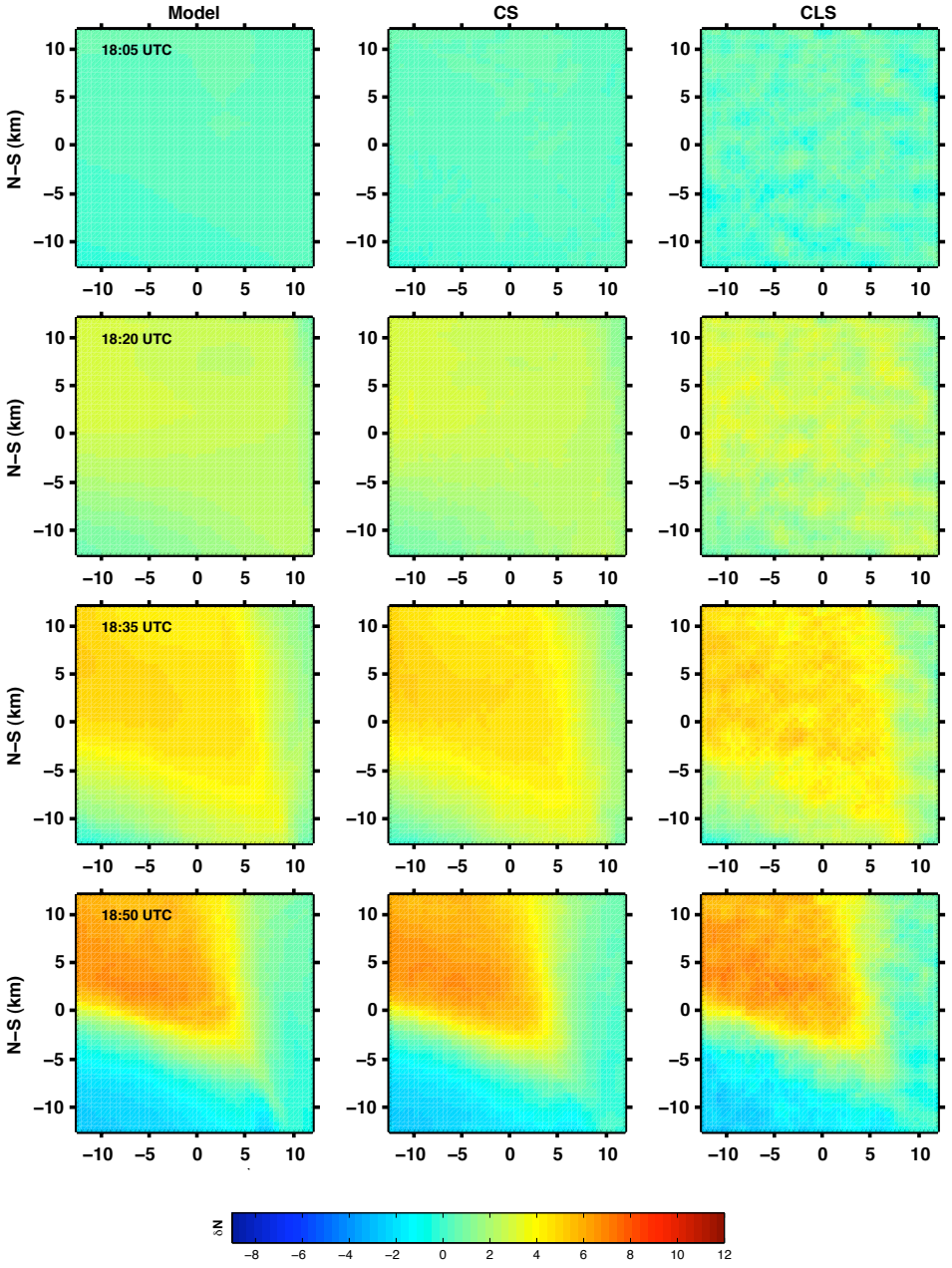

Figure 3.8: Model refractivity differences are on the left panels over the 2-hr simulation period with 15 minute time intervals. CS (middle panels) and CLS (right panels) retrieval of refractivity difference from three radars and 2400 measurements with 1 N-unit noise. The first 1-hr simulation period is demonstrated here due to lack of space; the second 1-hr simulation period is shown on the next page.

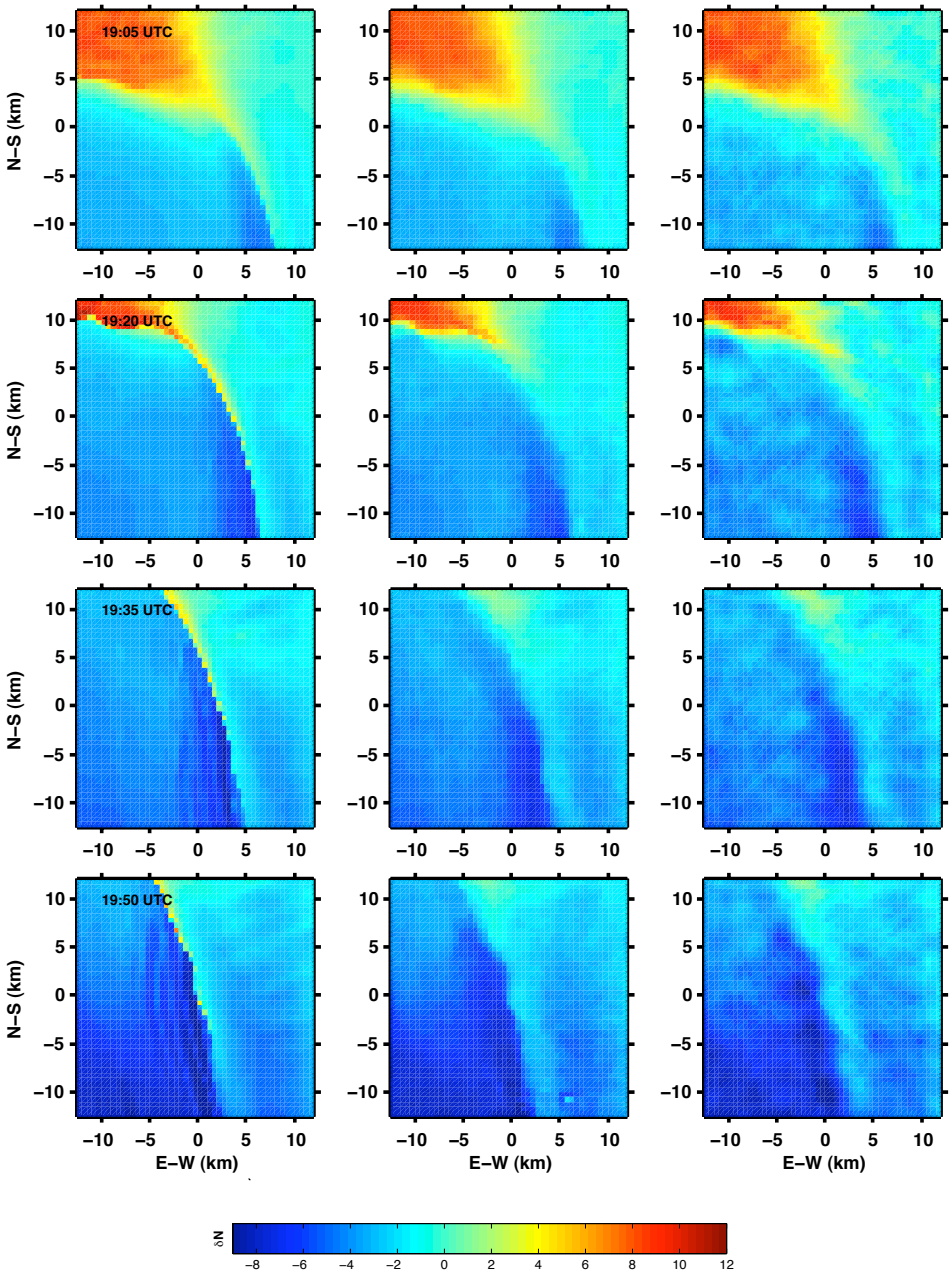

Figure 3.9: The second hour of the simulation period. The model refractivity differences are on the left panels over the 2-hr simulation period with 15 minute time intervals. CS (middle panels) and CLS (right panels) retrieval of refractivity difference from three radars and 2400 measurements with 1 N-unit noise.

The performance of CS and CLS was quantified using RMSE and was tested statistically as a function of noise, number of radars and refractivity models with different compressibility and smoothness. Note that both CS and CLS rely on the same linear model and can be implemented for a single radar. It is evident that both CS and CLS can grossly reconstruct the refractivity difference most of the time. Moreover, from the cases investigated, CS always provides better reconstruction than CLS, manifested by the lower RMSE. In addition, the results have shown that CS is also less susceptible to noise contamination, especially when the image for reconstruction is more compressible.

By taking advantage of networked radars, both CS and CLS performances are improved as the number of measurements and the viewing angles increase. However, the shape of the refractivity difference is better preserved in CS than CLS. The CS algorithm can be further improved by more carefully choosing penalty parameters between the DCT and TV terms. In CLS, the selection of the threshold level for the singular values may not be optimal. Based on the cases presented in this work, CS has the potential to perform better reconstructions than CLS given the same condition such as noise, number of radars, etc.

In the present study, the coherence condition was discussed to assess the probability of exact reconstruction using l_1-norm minimization on sparse images. It is important to note that, while coherency is fundamental in evaluating quality of

sparse approximation, the satisfaction of the RIP enables more robust and stable reconstruction of sparse signals (Duarte and Eldar 2011). RIP ensures that two sparse images with same transform coefficients at different locations cannot produce the same measurement vector and thus guarantees a unique solution (Duarte and Eldar 2011). However, it is computationally expensive to check the RIP condition (Baraniuk et al. 2010). On the other hand, coherency provides an alternative way to check the probability of robust recovery (Tropp 2006). Additionally, coherency can be conservatively used to bound RIP and enables stable recovery via l_1-norm minimization (Potter et al. June 2010). Furthermore, it is also important to note that compressible images can be reconstructed by approximating the most significant transform coefficients, even when RIP is not satisfied (Zhang 2008; Candès and Tao 2007). While, under such conditions, the recovery of images might not be exact, they are still valuable in solving practical problems. In the present study, while the computed mutual coherence is relatively low (10 in a range of 1 to 60), such a value cannot be used to guarantee exact recovery (similar to conditions with unsatisfied RIP) unless the sparsity property of signals to be recovered and transformation matrix are also considered (Candès and Romberg 2006). On the other hand, the present simulation results demonstrate that the proposed method based on the CS theory indicates better performance than CLS in reconstructing refractivity. It is also worth noting that the

condition of incoherence can be further improved by designing a better transformation matrix, which can result in better sparsity of signals in the transformed domain and incoherence to measurement matrices.

Chapter 4

Application of CS to Digital Beamforming

4.1 Introduction

Rapidly evolving severe weather storms require a high temporal resolution for weather radars to observe the dynamics and structures, particularly considering that the development time for a tornado is faster than the radar update time (Zrnic et al. 2007; Bluestein et al. 2003; Carbone et al. 1985). Unlike the conventional pencil-beam radar requiring a longer revisit time, an imaging radar can offer much faster revisit time through DBF techniques, where a wide transmitted beam and a number of receivers are required (Mead et al. 1998; Isom et al. 2013). Imaging radars have been used for clutter suppression (Cheong et al. 2006), for clear air observations in the atmospheric boundary layer (Mead et al. 1998), reflectivity and velocity observations (Cheong et al. 2006; Isom et al. 2013) by exploiting DBF techniques. FB and CB are commonly used for atmospheric observations (Kudeki and Sürücü 1991; Palmer et al. 1998; Cheong et al. 2006; Isom et al. 2013). FB has a resolution limitation and suffers from clutter contamination due to high sidelobes (Palmer et al. 1998; Woodman 1997). CB can adaptively suppress interference from different directions and provide improved resolution compared to FB (Yu et al. 2000; Isom et al. 2013).

Further, robust CB bas been suggested for better power estimation accuracy (Li and Stoica 2006; Isom et al. 2013). Recently, an adaptive beamspace algorithm has been designed to achieve accurate weather observations by suppressing the interference from different directions by utilizing a cluster of simultaneously received beams after a set of beams is formed by using nonadaptive beamforming algorithm (Nai et al. 2016). However, reliable reflectivity and velocity estimation with high angular resolution are still a challenge for DBF using imaging radars with a smaller number of receivers, due to problems associated with calibration, noise, receiver configurations, etc.

In this work, CS is exploited to reconstruct high resolution reflectivity and velocity from various numbers of receivers and different receiver configurations. The problem of beamforming is formulated as a linear model. Consequently, reflectivity and velocity estimation is postulated as an inverse problem. The number of measurements for CS is determined from the number of receiver pairs, which can often result in larger than the number of reflectivities to be estimated. However, the problem is still underdetermined due to poor conditioned of derived measurement matrix. In other words, the number of unique receiver pairs is still much smaller than the number of pixels. As an alternative to DBF, CS has been applied for imaging equatorial ionospheric irregularities (Harding and Milla 2013) and direction of estimations (Liu et al. 2013), etc. However, velocity estimation and different receiver configurations with a different number of receivers and number of samples have not been studied

yet for CS. Moreover, in order to demonstrate the feasibility of CS for reflectivity and velocity estimation, various conditions of SNR, different receiver spacings, and various numbers of receivers are used. The performance of CS with FB and CB are evaluated based on a quality measure of RMSE, resolution, and dynamic range.

4.2 Overview of digital beamforming

For DBF application, let us first consider an imaging radar, which is located at the origin with a wide transmit beam and N (need to check the notation to be consistent) spatially separated receivers. The received signals from the m^{th} receiver can be represented as the summation of backscattered signals from all the scatters within the radar resolution, as shown in (4.1) (Cheong et al. 2008b),

$$V_m(t) = \sqrt{\frac{P_t G_t G_r}{(4\pi)^3}} \sum_{i=1}^{N_s} \sqrt{\frac{Z(i,t) w_{at}(i) w_{ar}(i) w_r(i)}{r_t^2(i,t) r_m^2(i,t)}} e^{-jk(|\vec{r}_t(i,t)|+|\vec{r}_m(i,t)|)} \tag{4.1}$$

where N_s is the total number of scatterers within the radar resolution volume, $|\vec{r}_t|$ is the range from the transmitter to the location of scatterer i and $|\vec{r}_m|$ is the range from the scatter to the m^{th} receiver, and $k = 2\pi/\lambda$ is the wavenumber. P_t is the peak transmitted power, and G_t and G_r are the transmitted and receiving antenna gain respectively. Additionally, the range weighting function (w_r) is, by the Gaussian function, centered at r_0, where the SD $\sigma_r = 0.35\delta r$ and δr represents range resolution.

For DBF operation, all the signals from N receivers are received simultaneously without the need of any phase shifters. Instead, appropriate phases (or generally

weights) can be added to received signals to form a synthesized beam at any desirable angular location. As a result, a snapshot of reflectivity and velocity profiles can be obtained without physically scanning through a number of angular locations as it is done in conventional pencil-beam radar operations. Specifically, the output of the beamformer, $\mathbf{y}(t)$, can be obtained for the desired angular direction by assigning a complex weighting vector, $\mathbf{w}$ with the size of $N \times 1$, to received signals,

$$\mathbf{y}(t) = \mathbf{w}^H \mathbf{V}(t) \tag{4.2}$$

where H is the Hermitian (complex conjugate) operator, $\mathbf{V}(t)$ is the received time series signals from N receivers with the size of $N \times T$. The mean power of the received signals can be derived from the autocorrelation function of $\mathbf{y}(t)$. Then the returned power from a particular direction can be obtained as following (Palmer et al. 1998; Kudeki and Sürücü 1991; Isom et al. 2013):

$$P(\theta) =< \mathbf{y}(t)\mathbf{y}^H(t) >= \frac{1}{N^2}\mathbf{w}^H \mathbf{R}(0)\mathbf{w} \tag{4.3}$$

where $< \cdot >$ denotes the expectation operator and $\mathbf{R}(0) =< \mathbf{V}(t)\mathbf{V}^H(t) >$ is the spatial autocorrelation matrix with a size of N x N in which each element in $\mathbf{R}(0)$ can be expressed as, $R_{m,n}(0) =< V_m(t)V_n^H(t) >$. The radial velocity can be obtained from pulse-pair processing using the cross-correlation matrix of the received signals at lag 1 (Cheong et al. 2004).

$$v(\theta) = \frac{-\lambda}{4\pi T_s} arg[\mathbf{w}^H \mathbf{R}(1)\mathbf{w}] \tag{4.4}$$

where $\mathbf{R}(1) = \mathbf{R}(T_s) =< \mathbf{V}(t)\mathbf{V}^H(t - T_s) >$ with a size of is $N \times N$.

4.2.1 Fourier beamforming

One way to design an array is with equally spaced sampling which allows the use of the fast Fourier transform. The complex weights for Fourier beamforming for N receivers is

$$\mathbf{w}_f = [e^{jk\vec{a}_k \cdot \vec{d}_1} \; e^{jk\vec{a}_k \cdot \vec{d}_2} \; \cdots \; e^{jk\vec{a}_k \cdot \vec{d}_N}] \tag{4.5}$$

where $\vec{a}_k = [\sin\theta\sin\phi \;\; \sin\theta\cos\phi \;\; \cos\theta]$ is a unit vector, θ and ϕ are the zenith and azimuth angles, respectively, and $\vec{d}_m$ is the position vector of receiver m. Fourier weights depends only on the receiver's location, and therefore the resolution is limited. When we substitute (4.5) into (4.3), the Fourier-based estimate of the power is obtained. Similarly, the velocity can be obtained from (4.4) by replacing the Fourier weights.

4.2.2 Capon beamforming

CB was developed to adaptively suppress interference such as ground clutter, which leads to improved resolution (Capon 1969; Palmer et al. 1998). The weights of CB are obtained from minimization of output power in all directions while maintaining the unity gain in the pointing direction (Yu et al. 2000; Palmer et al. 1998). The minimization problem is expressed as

$$\text{minimize} \;\; \mathbf{e}^H \mathbf{R}(0) \mathbf{e} \quad \text{subject to} \quad \mathbf{e}^H \mathbf{w_c} = 1 \tag{4.6}$$

where $\mathbf{e} = [e^{jk\vec{a}_k \cdot \vec{d}_1} \; e^{jk\vec{a}_k \cdot \vec{d}_2} \; \cdots \; e^{jk\vec{a}_k \cdot \vec{d}_N}]^T$. The weighting vector of CB can be obtained by solving the problem using Lagrangian methods.

$$\mathbf{w_c} = \frac{\mathbf{R}(0)^{-1}\mathbf{e}}{\mathbf{e}^H\mathbf{R}(0)^{-1}\mathbf{e}} \tag{4.7}$$

Then, the power estimation for CB is given as following

$$P(\theta) = \frac{1}{\mathbf{e}^H\mathbf{R}(0)^{-1}\mathbf{e}} \tag{4.8}$$

It is obvious from (4.7) that the Capon weights are dependent on the spatial autocorrelation matrix $\mathbf{R}$, which is obtained from the received signals. In contrast to the fixed Fourier receiving pattern given the receiver configuration, the Capon receiving pattern is adaptive. Therefore, the power calibration for CB is extremely difficult and studied in Section 5.2. It has been reported that Capon beamforming can provide higher resolution than the Fourier beamforming (Yu et al. 2000; Palmer et al. 1998).

Similarly to FB, the velocity estimation can be obtained by applying the weights of CB to the spatial autocorrelation matrix at lag 1 (Cheong et al. 2004).

$$v(\theta) = \frac{-\lambda}{4\pi T_s} arg[\mathbf{w_c}^H\mathbf{R}(1)\mathbf{w_c}] \tag{4.9}$$

In contrast to the power estimation in CB, no attempt was made to improve velocity resolution directly. However, the adaptive weights in Capon lead to better velocity estimation (i.e. mitigate the interference of velocity from strong targets).

Consequently, the reflectivity field has a significant effect on Capon velocity estimation and outperforms Fourier velocity for the nonuniform reflectivity, where the resolution is needed.

4.3 Problem formulation of beamforming for compressive sensing

Compressive sensing theory requires that the relationship between measurements and the field to be estimated should be represented in linear form. The received signal at the m^{th} receiver is represented as a superposition of complex signals from all the scatters in (4.1). Further, the received signal at the m^{th} receiver can be expressed by separating scatterers into sub volumes within the radar resolution volume in angle. Note that the received complex signals from P sub-volumes are uncorrelated.

$$V_m(t) = \sqrt{\frac{P_t G_t G_r}{(4\pi)^3}} \sum_{z=1}^{P} \sum_{l=1}^{N_s(z)} \sqrt{\frac{Z(l,z,t) w_{at}(l,z) w_{ar}(l,z) w_r(l,z)}{r^4(l,z,t)}} e^{-jk(|\vec{r}_t(l,z,t)|+|\vec{r}_m(l,z,t)|)} \tag{4.10}$$

The two-way path distance from a scatter to the transmitter and receiver m in (4.25) can be rewritten with the scatter velocity $v(l,z)$.

$$|\vec{r}_t(l,z,t)| + |\vec{r}_m(l,z,t)| = |\vec{r}_t(l,z,t_o)| + |\vec{r}_m(l,z,t_o)| - 2 * |v(l,z)|t \tag{4.11}$$

where t_o is the initial time for the scatter location within the z^{th} sub volume. Here, we assume that the scatterer moves with an average wind velocity $\vec{v}$ and the doppler frequency shift from a scatter with respect to the transmitter and receiver is relatively

similar. Subsequently, the received signal at the receiver m from P angular directions can be derived as:

$$V_m(t) = \sum_{z=1}^{P} A_m(z,t) e^{-jk(|\vec{r}_t(z)|+|\vec{r}_m(z)|)} e^{jk2v(z)t} \tag{4.12}$$

where $A_m(z,t)$ is the complex amplitude at the receiver m^{th} from z^{th} sub-volume and is defined in the following equation.

$$A_m(z,t) = \frac{\sum_{l=1}^{Ns(z)} \sqrt{\frac{Z(l,z,t) w_{at}(l,z) w_{ar}(l,z) w_r(l,z)}{r^4(l,z,t)}} e^{-jk(|\vec{r}_t(l,z,t_o)|+|\vec{r}_m(l,z,t_o)|)} e^{jk2|v(l,z)|t}}{e^{-jk(|\vec{r}_t(z)|+|\vec{r}_m(z)|)} e^{jk2v(z)t}} \tag{4.13}$$

It is assumed that the complex amplitudes $A_m(z,t)$ from different angles are uncorrelated, $< A_m(z,t) A_n^*(y,t) >$. $A_m(z,t)$ is a zero mean random process since scatters within a subvolume move relatively randomly between successive pulses. Moreover, scatter displacements of an order of a wavelength can cause large changes in the second sum and also cause change in the phase of $A_m(z,t)$. Furthermore, the cross-correlation of received signals from the m^{th} and n^{th} receivers at temporal zero lag can be approximated by the following equation.

$$\begin{aligned} R_{m,n}(0) =< V_m(t) V_n^*(t) >= & \sum_{z=1}^{P} < A_m(z,t) A_n^*(z,t) > e^{-jk(|\vec{r}_m(z)|-|\vec{r}_n(z)|)} \\ & + \sum_{z=1}^{P} \sum_{y=1, z\neq y} < A_m(z,t) A_n^*(y,t) > e^{-jk(|\vec{r}_t(z)-|\vec{r}_t(y)+|\vec{r}_m(z)|-|\vec{r}_n(y)|)} \end{aligned} \tag{4.14}$$

The first sum in (4.14) is relatively constant and the second sum represents a rapidly fluctuating contribution to the instantaneous power. Consequently, the second sum in (4.14) will be zero when the expectation is applied, since the expectation of the zero mean random variable is zero. Assuming the process is ergodic, we can approximate the expectation operator with a sum.

The correlation function at zero lag is obtained when the assumptions are applied in the equation (4.14),

$$R_{m,n}(0) = \sum_{z=1}^{P} < |A(z)|^2 > e^{-jk(|\vec{r}_m(z)| - |\vec{r}_n(z)|)} \tag{4.15}$$

Consequently, the correlation function at temporal zero lag of all receiver pairs can be written in matrix form as,

$$\mathbf{R_p} = \mathbf{H_p}|\mathbf{A}|^{\mathbf{2}} \tag{4.16}$$

where $\mathbf{R_p}$ represents the vectorized form of the upper diagonal of $\mathbf{R}(\mathbf{0})$ with the size of $M \times 1$, where $M = N(N-1)/2$. $\mathbf{H_p}$ is $M \times P$ measurement matrix, $|A|^2$ is $P \times 1$. $\mathbf{H_p}$ and $\mathbf{R}(\mathbf{0})$ are displayed in a matrix form, which are created using Eq. 4.15 in the following,

$$\begin{pmatrix} R_{11}(0) \\ R_{12}(0) \\ \vdots \\ R_{22}(0) \\ R_{23}(0) \\ \vdots \\ R_{NN}(0) \end{pmatrix} = \begin{pmatrix} e^{jk(r_1(1)-r_1(1))} & e^{jk(r_1(2)-r_1(2))} & \dots & e^{jk(r_1(P)-r_1(P))} \\ e^{jk(r_1(1)-r_2(1))} & e^{jk(r_1(2)-r_2(2))} & \dots & e^{jk(r_1(P)-r_2(P))} \\ \vdots & \vdots & & \vdots \\ e^{jk(r_2(1)-r_2(1))} & e^{jk(r_2(2)-r_2(2))} & \dots & e^{jk(r_2(P)-r_2(P))} \\ e^{jk(r_2(1)-r_3(1))} & e^{jk(r_2(2)-r_3(2))} & \dots & e^{jk(r_2(P)-r_3(P))} \\ \vdots & \vdots & & \vdots \\ e^{jk(r_N(1)-r_N(1))} & e^{jk(r_N(2)-r_N(2))} & \dots & e^{jk(r_N(P)-r_N(P))} \end{pmatrix} \begin{pmatrix} |A(1)|^2 \\ |A(2)|^2 \\ |A(3)|^2 \\ \vdots \\ \vdots \\ \vdots \\ |A(P)|^2 \end{pmatrix} \tag{4.17}$$

Further, the correlation function at lag 1 can be obtained from the received signal samples in the following,

$$R_{m,n}(1) =< V_m(t)V_n^*(t+\tau) >= \sum_{z=1}^{P} < |A(z)|^2 > e^{-jk(|\vec{r}_m(z)|-|\vec{r}_n(z)|)} e^{jk2v(z)(\tau)} \tag{4.18}$$

where $V_n(t+\tau) = \sum_{z=1}^{P} A_m(z) e^{-jk(|\vec{r}(z)|+|\vec{r}_n(z)|)} e^{jk2v(z)(t+\tau)}$ and τ is equal to the PRT. The correlation of all receiver pairs at lag 1 can be written in matrix form as,

$$\mathbf{R_v} = \mathbf{H_v B} \tag{4.19}$$

where $\mathbf{R_v}$ is the velocity measurements and obtained from the vectorizing $\mathbf{R}(1)$ into $N^2 \times 1$, $\mathbf{H_v}$ is the $N^2 \times P$ measurement matrix for velocity estimation, and $\mathbf{B}$ is $P \times 1$ complex vector where $B(z) = |A(z)|^2 e^{jk2v(z)\tau}$. The size of measurement matrix $\mathbf{H_v}$ is doubled compared to $\mathbf{H_p}$, because all of the values of $\mathbf{R}(1)$ are used as measurements, whereas the half of the number of values are used for $\mathbf{R_p}$. The reason is that $\mathbf{R}(0)$ is a Hermitian matrix and the inclusion of the conjugate values will only increase the redundancy in $\mathbf{H_p}$ matrix and in measurements $\mathbf{R_p}$, since the rows in $\mathbf{H_p}$ will be conjugated too. However, in velocity, $\mathbf{R}(1)$ is not a symmetric matrix and contributes additional information for the estimation even though some of the measurement basis in $\mathbf{H_v}$ matrix is repeated.

4.4 Decreasing number of measurements using SVD

The purpose of this section is to reduce the number of redundant measurements into a smaller size. This is because the number of measurements M in (4.16) are increased

dramatically based on the equation $(N^2 - N)/2$ as the number of receivers N increases. The problem seems to be overdetermined when the number of measurements M is larger than the number of pixels P, for example $N = 36$ receivers like AIR and $P = 128$ to be reconstructed reflectivity,. However, the measurement matrix $\mathbf{H_p}$ and $\mathbf{H_v}$ is rank deficient and does not have full rank because of redundancy in the rows for uniform spacing receivers. Because the receiver spacing is the same for all the adjacent receivers, there are only N different receiver pair spacings. In other words, there will be only N unique rows in $\mathbf{H_p}$ and $\mathbf{H_v}$ and all the others will be repeats. However, even when the rows are repeating exactly, the associated measurements can be different. For non-redundant spacing, there is no repeating spacing for any receiver pairs, but when $\mathbf{H_p}$ is still rank deficient, it is likely due to small angle separations in the column. The condition numbers of $\mathbf{H_p}$ and $\mathbf{H_v}$ after applying SVD are also significantly high based on the ratio of maximum and minimum singular value. The problem is considered underdetermined under these conditions (Hansen 1987). The SVD of $\mathbf{H_p}$ matrix, written as $\mathbf{H_p} = \mathbf{U\Sigma V}^T$, can be applied to (4.16), $\mathbf{R_p} = \mathbf{U\Sigma V}^T|\mathbf{A}|^\mathbf{2}$, where $\mathbf{U}$ is $M \times M$ square unitary matrix and $\mathbf{U^H U} = \mathbf{I}$. Moreover, Σ is $M \times P$ diagonal matrix and $M > P$, therefore, the lower number of $M - P$ rows is zero. When we multiply both side with the $\mathbf{U}^H$ matrix, we obtain $\mathbf{U}^H\mathbf{R_p} = \mathbf{\Sigma V}^T|\mathbf{A}|^\mathbf{2}$. After reducing the $\mathbf{U}$ and $\mathbf{\Sigma}$ matrix to their non-zero columns and rows (or using first P number of columns),

$$\tilde{\mathbf{R}}_\mathbf{p} = \tilde{\mathbf{H}}_\mathbf{p}|\mathbf{A}|^\mathbf{2} \tag{4.20}$$

SVD linearly combines the measurements and all the (redundant) data are maximally utilized in $\tilde{\mathbf{R}}_\mathbf{p}$ (Edelmann and Gaumond 2011; Hansen 1987). Reducing the size of $\mathbf{H_p}$ and $\mathbf{R_p}$ decreases the computational time of the solver significantly.

The same procedure can be applied in (4.19) for velocity estimation, where the number of measurements is increased with the square of the number of receivers. Once the SVD of measurement matrix $\mathbf{H_p}$ is obtained, then $\tilde{\mathbf{H}}_\mathbf{p}$ and $\tilde{\mathbf{U}}$ matrices can be stored for further estimation calculations since the measurement matrix is fixed and only the measurements are updated.

4.5 Compressive sensing

In this work, CS is applied to solve the inverse problem of reflectivity and velocity retrieval from the measurements which are obtained in (4.16) and (4.19) respectively. The sparsity and incoherency will be discussed in Subsections 4.6.1 and 4.6.2. The l_1-norm minimization will be discussed in the following subsection.

4.5.1 l_1-norm minimization

In order to reconstruct reflectivity and velocity structures from the measurements, which are obtained based on correlation of receiver pairs, wavelet and Laplace transforms are used in the l_1 norm minimization. The advantage of multiple transformations in the minimization is that they compensate their weakness, despite the complexity in the minimization increasing. The problem of reflectivity retrieval is solved using the following minimization,

$$\min \ \alpha_p \|\mathbf{\Psi}|\mathbf{A}|^{\mathbf{2}}\|_1 + \|\mathbf{L}|\mathbf{A}|^{\mathbf{2}}\|_1 \quad \text{subject to} \quad \|\tilde{\mathbf{R}}_{\mathbf{p}} - \tilde{\mathbf{H}}_{\mathbf{p}}|\mathbf{A}|^{\mathbf{2}}\|_{\mathbf{2}}^{\mathbf{2}} < \beta_{\mathbf{p}}, \tag{4.21}$$

where $\mathbf{L}$ is the Laplace operator and $\mathbf{\Psi}$ is wavelet transformation. $\alpha_p = 0.2$ is the weights for $\mathbf{\Psi}$. β_p value is obtained by using the norm of measurements by defining a threshold value $th, \beta_p = \|\tilde{R}_p(th : P)\|_2$. The Laplace matrix used in the minimization is given in the following,

$$L = \begin{bmatrix} -1 & 1 & 0 & 0 & \dots & 0 \\ 1 & -2 & 1 & 0 & \dots & 0 \\ 0 & 1 & -2 & 1 & \dots & 0 \\ \vdots & \vdots & \vdots & \ddots & & \vdots \\ 0 & \dots & 0 & 1 & -2 & 1 \\ 0 & \dots & \dots & 0 & -1 & 1 \end{bmatrix} \tag{4.22}$$

The Laplacian performs a second order difference of the image, and allows linear changes in the estimation, unlike TV. Because the reconstruction using only wavelet

transformation has small variation in the linear scale but large in the dB scale, including Laplace in the l_1-norm minimization mitigates possible oscillations in the estimation. These minimization problems were solved by using the CVX optimization solver (Boyd and Vandenberghe 2004), where the error term and solution were updated in each iteration.

Similarly to the reflectivity problem, velocity can be obtained by replacing $\mathbf{R_p}$ with $\mathbf{R_v}$ and $\mathbf{H_p}$ with $\mathbf{H_v}$ in the following,

$$\min \ \alpha_v \|\mathbf{\Psi B}\|_1 + \|\mathbf{LB}\|_1 \quad \text{subject to} \quad \|\tilde{R_v} - \mathbf{\tilde{H}_v B}\|_2^2 < \beta_v, \tag{4.23}$$

Note that $\mathbf{B}$ is complex and the velocity can be obtained by taking the arctangent of the imaginary part divided by the real part in the following,

$$v(\theta) = \frac{-\lambda}{4\pi T_s} arg(\mathbf{B}) \tag{4.24}$$

β_v value is obtained by using the norm of measurements by defining a threshold value thv, $\beta_v = \|\tilde{R_v}(thv : P)\|_2$. Theoretically, there is no noise on the velocity measurements, but statistical fluctuations or any other possible phase errors can be handled by the error tolerance in the l1-minimization routine. $\alpha_v = 0.1$ is the weight for $\mathbf{\Psi}$ for the velocity estimation. It is observed that increasing the value of α_v results in more oscillations in the velocity estimation. This is also true for the reflectivity estimation.

4.6 Numerical simulations

Numerical simulations were developed to demonstrate and verify the feasibility of CS for reflectivity and velocity estimations. To simplify the problem, in this work a receiving aperture of 2 meters is selected to produce an intrinsic angular resolution of one degree. If a half-wavelength spacing is used, a total of 129 receivers are needed. The antenna aperture size is fixed at 2 meters and determined by the total length of uniformly spaced 129 receivers with half-wavelength. Moreover, three receiver configurations of uniformly spaced (US), pseudo-randomly spaced (RS), and non-redundantly spaced (NRS) with different numbers of receivers are considered. Specifically, US is obtained while all the receivers are equally spaced to make up the aperture. In RS, the locations of a given number of receivers are randomly selected out of the locations of 129 receivers, but a minimum spacing of half-wavelength is always maintained. Moreover, NRS is designed to ensure no repeated spacing among any pair of receivers for the given number of receivers, while a minimum spacing of half-wavelength is always employed. The receiver locations are shown in Fig. 4.1 for all three receiver configurations with 17, 33 and 65 receivers.

The time series signals were generated by using the dimensional radar simulator (Cheong et al. 2008b). In the first part of the simulation, user-defined and simplified reflectivity and velocity fields are used to study performance such as resolution, dynamic ranges, etc. For example, single and dual-Gaussian profiles are used for reflectivity, while a linearly varying profile is used for velocity. In the second part

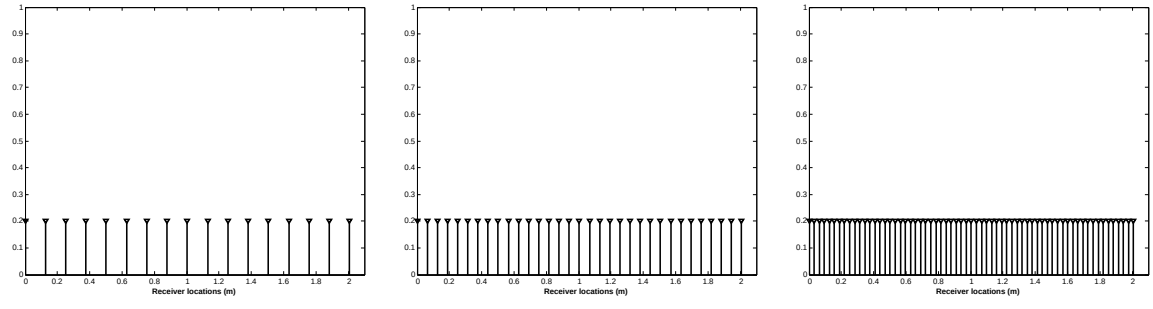

(a) Uniform spacing

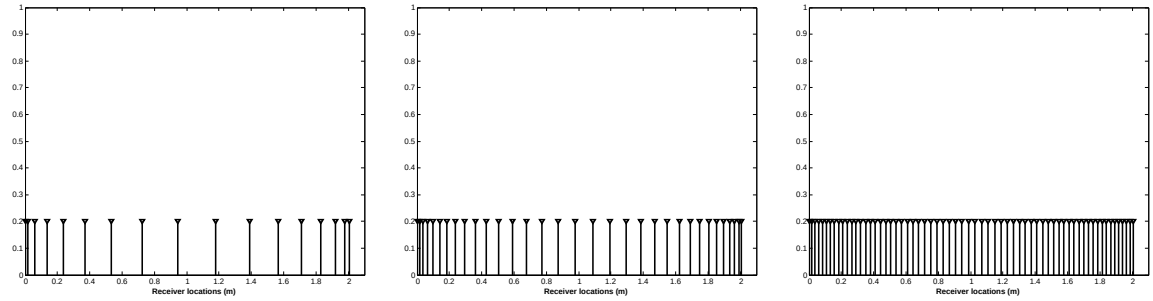

(b) Non-redundant spacing

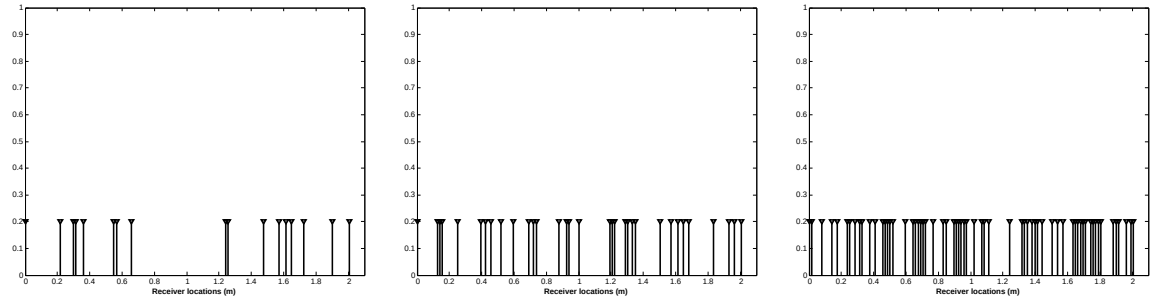

(c) Random spacing

Figure 4.1: Receiver locations are for US, NRS, and RS with 17 (left column), 33 (middle column), and 65 receivers (right column).

of the simulation, realistic reflectivity and velocity profiles derived from the ARPS data (Xue et al. 2003) are used to further demonstrate the feasibility of CS under different conditions such as SNR, number of samples, and number of receivers. The size of the simulator domain is 42 degrees in elevation (-8 to 34 degrees), 1 degree in

azimuth angle and 75 meters in range. The antenna is tilted back 13 degrees. Thousands of scatterers are populated in the simulation domain, and the initial locations of scatterers are positioned randomly with uniform distribution. The scatterers are moved by the assigned three dimensional wind velocity, and their locations are updated for each sample time. Additionally, 3-D turbulent motion is also added to all the scatterers based on the turbulent kinetic energy (TKE), which is set at 2 m^2s^{-2} for the first part of the simulation. The radar is located at 6 km distance from the simulation domain by pointing east for the first part of the simulation and at 3 km for the second part of the simulation. The received complex signals at each receiver are obtained by coherently summing individual returns from all the scatterers within the simulator domain.

$$V_m(t) = \sqrt{\frac{P_t G_t G_r}{(4\pi)^3}} \sum_{z=1}^{P} \sum_{l=1}^{N_s(z)} \sqrt{\frac{Z(l,z,t) w_{at}(l,z) w_{ar}(l,z) w_r(l,z)}{r^4(l,z,t)}} e^{-jk(|\vec{r}_t(l,z,t)|+|\vec{r}_m(l,z,t)|)} \tag{4.25}$$

where $\sqrt{\frac{P_t G_t G_r}{(4\pi)^3}} = 10^8$. The amplitude of the received signal is attenuated by the distance from receiver to simulator domain. The phase of signal is determined by the two-way distance of the scatterer to radar receiver. The range-weighting function and transmitting antenna pattern is considered in the simulator. The normalized antenna transmit weighting function is approximated with a Bessel function centered around the pointing direction in angle ϕ_o, w_{ar} is the receiving antenna beam pattern, and Z is the reflectivity field. Additionally, a spatial and temporal linear interpolation

procedure is used to extract the atmospheric parameters corresponding to individual scatterers for spatial and temporal continuity in the reflectivity (Cheong et al. 2008b).

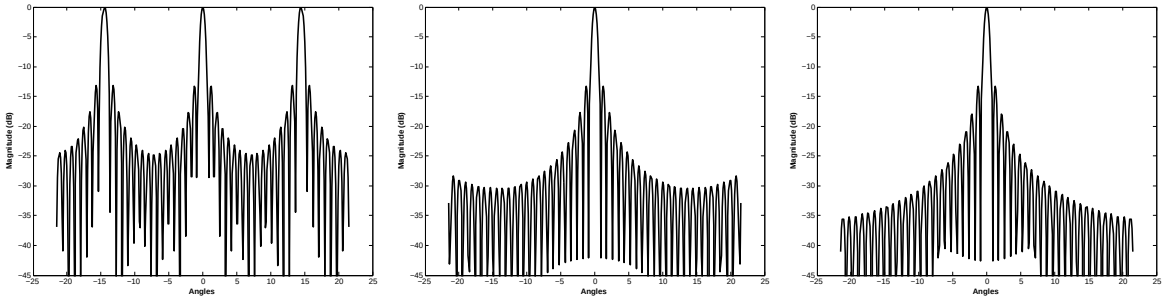

(a) Uniform spacing

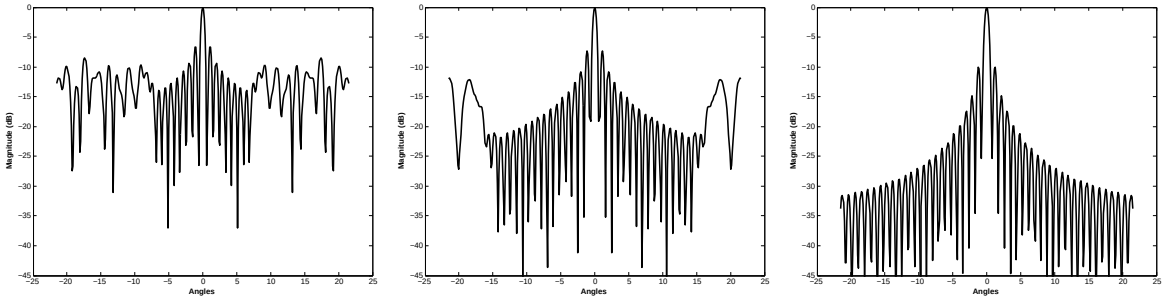

(b) Non-redundant spacing

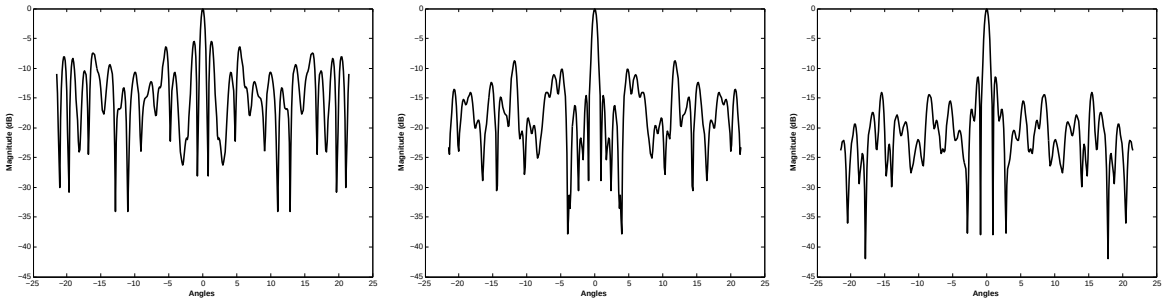

(c) Random spacing

Figure 4.2: Receiving antenna pattern is obtained from spatial Fourier transform of FB weights for US, NRS, and RS with 17 (left column), 33 (middle column), and 65 receivers (right column).

The radar is operated at 10 GHz and 1-D linear array in the vertical direction is considered. The transmitted beamwidth is 25 degrees in elevation but the simulator

size is set to 42 degrees to remove the edge effect of the simulator in the reconstruction. The number of pixels in the reconstruction is chosen to be 128 due to wavelet transformation matrix size, which requires the size to be a power of 2. Then, the angular sampling in the reconstruction field is about 0.2 degree, while 0.9 degree beamwidth is obtained from the aperture. As mentioned previously, three receiver configurations of US, RS, and NRS are considered. Note that the minimum spacing in RS and NRS is set to the half-wavelength to mitigate grating lobes. In this work, receiver numbers of 17, 33, 65, and 129 are considered. A sequence of zero mean additive white Gaussian noise is added to generated time series signals based on the desirable SNR.

The FB receiving pattern, obtained from spatial Fourier transform of FB weights, for the three receiver configurations of 17, 33 and 65 receivers is shown in Fig. 4.2. It is clear that grating lobe occurs at -14.5 and 14.5 degrees in the US configuration with 17 receivers. The highest sidelobe level of receiving pattern is displayed in Table 4.1. The highest sidelobe in NRS is slightly higher than RS for 33 and 65 receivers. The sidelobes in RS are a at similar level, and the sidelobes of NRS decay quickly from the main lobe but then increase again at 17 and 33 receivers. In US, the first sidelobe is the highest one at 33 and 65 receivers.

Table 4.1: The highest sidelobe level (in dB) of the receiving antenna pattern

RX number	US	NRS	RS
17	-13.3	-6.6	-5.4
33	-13.3	-7.2	-8.7
65	-13.3	-10.1	-11.4

4.6.1 Sparsity

The term sparsity and compressibility is defined in Section 2.2.1 as when an image can be well approximated by using a few of its large coefficients in the original or transform domain. In this work, reflectivity models of single and dual Gaussians are used to investigate the CS performance in addition to ARPS model reflectivity. Gaussian models with a fixed base value are usually not sparse in the original domain, nor in DCT and wavelet. In order to demonstrate the compressibility of single and dual Gaussian models in the wavelet domain, the sorted transformed coefficients are presented in the middle column of Fig. 4.3, where each single Gaussian has a std of 1.5^o with a fixed 5 dB base in (4.28). The compressibility level is found to determine the number of coefficients to achieve RMSE of 0.3. The peak separation of two Gaussian models is 8 degrees in angle.

It is clear that the sorted wavelet coefficients of Gaussian models rapidly decrease but do not reach zero, which indicates that the image is compressible but not sparse. For this case, the compressibility level of Gaussian models decreased from the single

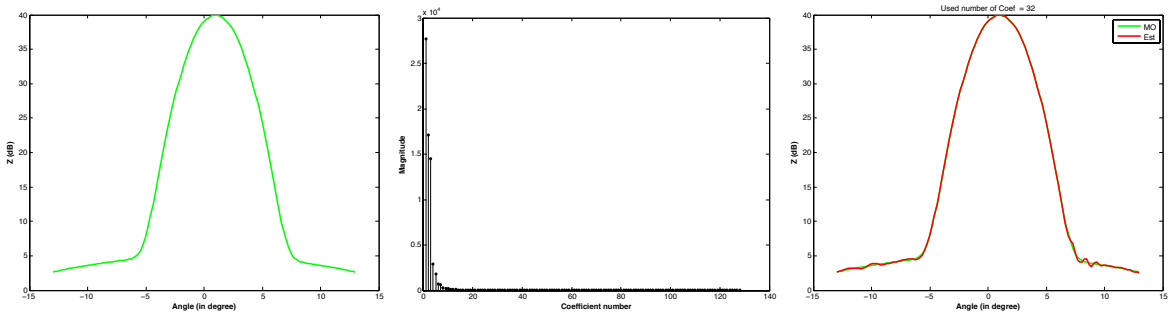

(a) Single Gaussian model with std of 1.5 degree

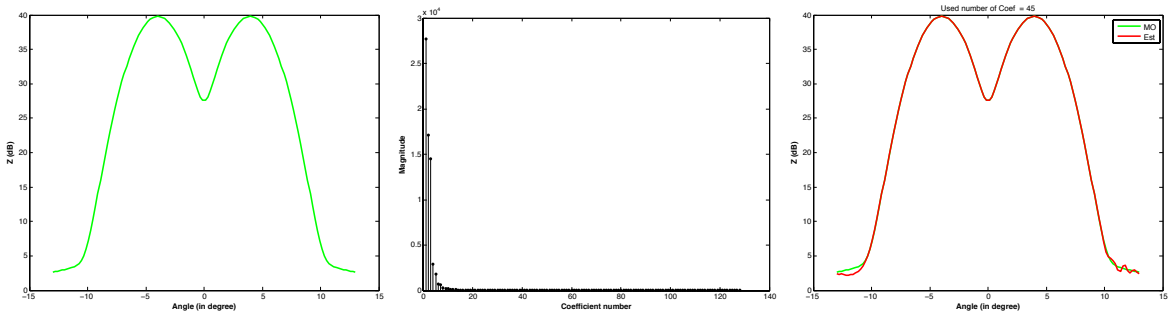

(b) Two Gaussian models with std of 1.5 degree

Figure 4.3: Single and dual Gaussian models (left panels) with std of 1.5 degree with 128 pixels are generated within the 25-degree beamwidth radar FOV. The sorted transform coefficients after wavelet transformation are shown in the middle panels. The recovered single and dual Gaussian models (right panels in red) are obtained by using 25% and 35% of the largest coefficients based on the defined RMSE of 0.3.

to double peaks from 75% to 65%, even though the decaying rate of the coefficients seems to be similar.

Moreover, more realistic reflectivity structures are obtained from ARPS models. The compressibility of reflectivity structures as function of ranges is shown in Fig. 4.4 by using the same RMSE 0.3. The difference between the original image and the recovered image is not visually noticeable. The low compressibility number indicates that the image is less compressible in the wavelet transform. The vertical

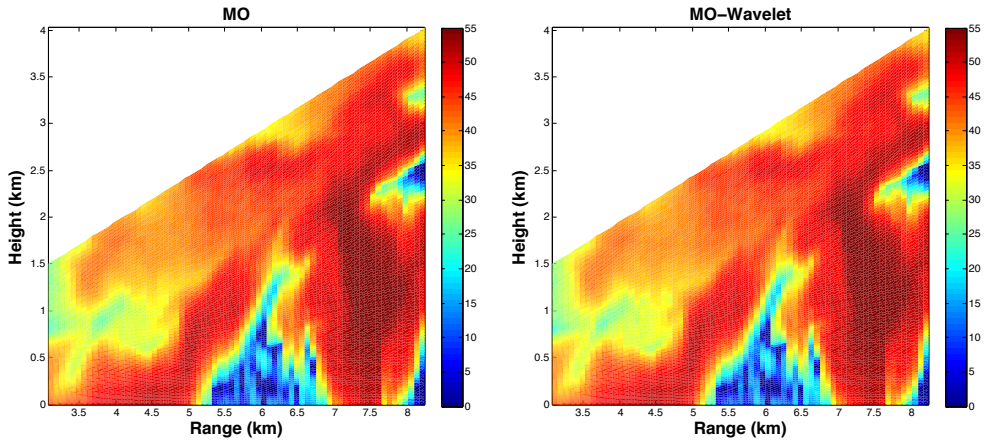

(a) Reflectivity model

(b) Recovered reflectivity

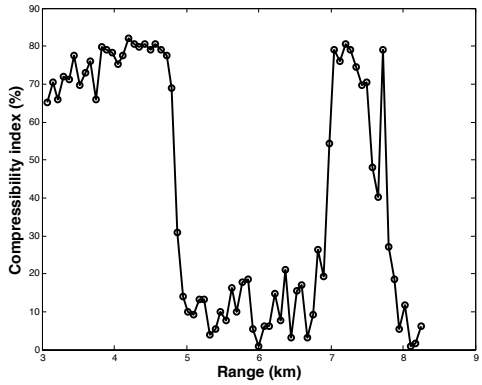

(c) Compressibility of reflectivity structures in range

Figure 4.4: Reflectivity model and recovered reflectivity model by using the largest coefficients based on the defined RMSE of 0.3 after wavelet transformation are display in the upper panels. The compressibility index of reflectivity structures as function of ranges after wavelet transformation are shown in the lower panel.

reflectivity profiles are relatively more compressible up to 5 km in range than the reflectivity models between 5 and 7 km. Reflectivity models between 5-7 km have almost no compressibility. Therefore, a worse performance of CS is expected in this region.

4.6.2 Incoherence

Incoherence of the $\mathbf{H_p}$ and $\mathbf{H_p}$ matrices with wavelet are calculated for three receiver configurations. The incoherence level for different numbers of receivers and three different receiver configurations are shown in Table 4.2 for reflectivity estimation and in Table 4.3 for velocity estimation.

Table 4.2: Incoherence with wavelet for reflectivity estimation

RX number	US	NRS	RS
17	6.78	4.52	5.31
33	5.77	5.43	5.2
65	6.67	6.22	5.54

Table 4.3: Incoherence for velocity estimation

RX number	US	NRS	RS
17	6.78	6.56	6.11
33	6.67	6.1	0.57
65	6.67	5.88	6.33

The calculated average incoherence level is about 5.5 within the range of 1 to 11.3; such a value cannot guarantee exact recovery unless the field is highly compressible. The incoherence value with DCT was about 11 for three receiver configurations for both reflectivity and velocity (the result is not shown here). The incoherence values in Table 4.2 are close for the three receiver configurations and three numbers of receivers. Increasing the number of receivers from 17 to 65 causes incoherence to increase; for example, the incoherence increases 4.52 to 6.22 for the NRS

receiver configuration in Table 4.2 for reflectivity estimation. However, the behavior of the incoherence trend is the opposite in Table 4.3 for velocity estimation; the value is slightly decreased from 6.56 to 5.88. In the velocity estimation, the measurement matrix has measurement vectors two times larger than in the reflectivity estimation, where the only single pair of receiver combinations is considered in the $\mathbf{H_p}$ matrix.

4.7 Numerical results

The goal of this section is to investigate the performance of CS regarding the estimation quality, the dynamic range of reflectivity, the resolution for reflectivity retrieval, the impact of model reflectivity on velocity estimation, the impact of noise on estimation for different numbers of receivers, and various reflectivity and velocity structures through statistical analysis. Additionally, the performance of CS will be compared to Capon and Fourier beamforming methods under these conditions. The performance of these methods is quantified by the RMSE defined in (3.3), dynamic range, and resolution. In this work, the RMSE is calculated in dB scale for the reflectivity. Note that, the reflectivity estimations of CS, CB, and FB are obtained after calibration process from their estimated power, which is explained in Section 5.2. For each case, 30 realizations were performed, each with independent scatterer locations and noise sequence. The default number of samples is 1024 and the default SNR is 30 dB. Moreover, the computational times for CS, CB, and FB are given in Table 4.4 with 17, 33, and 65 receivers using 1024 samples and SNR=30 dB. For a given case, FB

has the lowest computational time, while CS has the highest. The computational time of CS is much higher than CB (about 100 - 200 times), which makes the usage of CS operationally difficult when high temporal resolution is needed.

Table 4.4: Computational time (s) for CS, CB, and FB at SNR=30 dB

RX number	CS	CB	FB
17	2.48	0.011	0.009
33	2.55	0.013	0.01
65	2.62	0.02	0.013

4.7.1 Dynamic range

4.7.1.1 Dynamic range of reflectivity

In order to investigate the sensitivity of CS in reflectivity estimation by using three receiver configurations, a single Gaussian reflectivity model with a std of 2^o is used for dynamic range analysis with a fixed 5-dB reflectivity base. The Gaussian model is generated for different dynamic ranges in the following,

$$Z(\theta) = (A - C)e^{\frac{(\theta-\theta_o)^2}{2\sigma_z^2}} + C, \tag{4.26}$$

where θ_o is the mean location and σ_z^2 is the std of Gaussian structure and θ varies from -13 to 13 degrees. A and C are the amplitudes and determine the dynamic range. Dynamic range of reflectivity is varied from 2 to 37 dB with a step of 5 dB, and uniform velocity is used to mitigate any velocity impact on the reflectivity model estimation. Velocity is set to 5 ms^{-1} in a three dimensional wind field. Initially, the

model dynamic range was set as 0 to 35 dB without transmitter antenna pattern. However, the dynamic ranges increased 2 dB because of the transmitter antenna pattern effect on the edges (far away from the boresight) of the reflectivity.

The dynamic range for reflectivity is defined by the difference between the maximum and minimum values of the reflectivity profile, as shown in the following equation.

$$\mathrm{DR} = Z_{max} - Z_{min}, \tag{4.27}$$

where Z_{max} and Z_{min} are the maximum and minimum values of the model reflectivity and reconstructed reflectivity, respectively. For the estimated reflectivity, Z_{max} is obtained by taking the mean of 5 pixels in the vicinity of θ_o and Z_{min} is obtained by taking the mean of 5 pixels in the vicinity of $\theta = 0$ and $\theta = 25$ degrees. The averaging is necessary because of the fluctuation in the estimation.

The mean of DR for CS, CB, and FB reconstructed reflectivity is shown in Fig. 4.5 by using the three configurations of 33 receivers. It can be observed that generally CS can produce better DR than CB and FB for all the model DRs and receiver configurations. Specifically, CS can provide DR that is consistent with the model DR up to 22 dB. Beyond model DR of 20 dB, the DR from CS estimation using RS and NRS starts to slightly overestimate the DR, while CS with US produces slightly better agreement with the model DR. For both CB and FB, the best DR is achieved by US configuration, then NRS and RS configurations. The sidelobe levels of FB in RS is higher than NRS and US, thus it prevents achieving larger DR. Additionally,

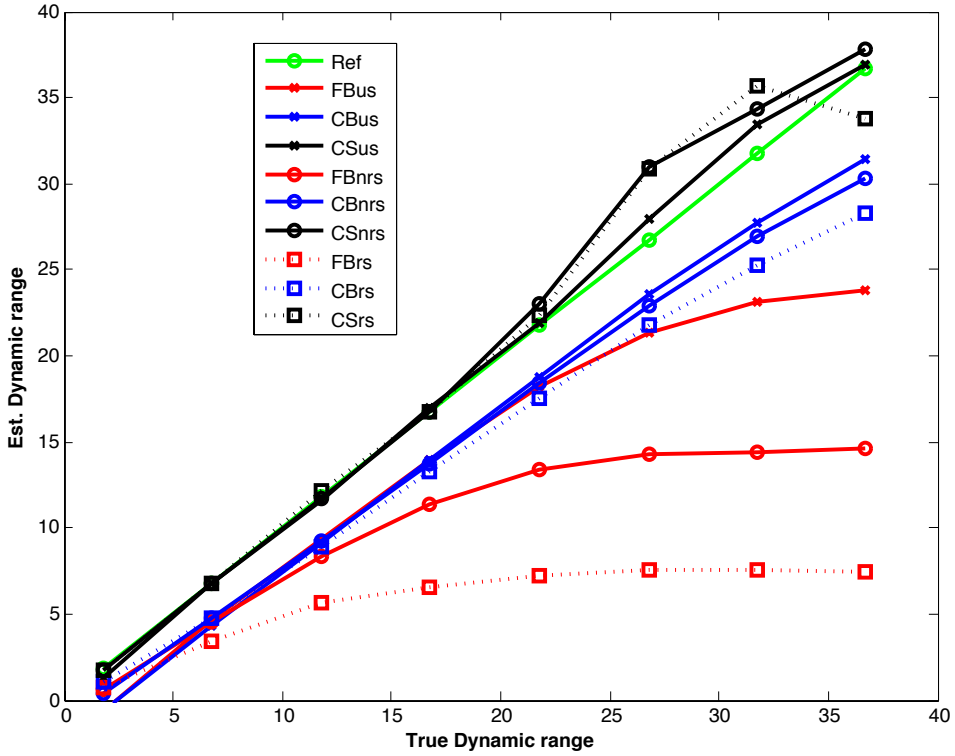

Figure 4.5: The mean of DR for estimation as a function of model DR for CS (black), CB (blue), and FB (red) is shown for US, RS, and NRS. The reference line is shown in green. The number of receivers is 33, the number of samples is 1024, and SNR=30 dB.

CB can generally produce better DR than FB at high model DR. Nevertheless, CS is capable of reconstructing reflectivity to larger DR than both CB and FR.

An example of CS, CB, and FB reconstruction from one realization using 33 receivers with 1024 samples and SNR at 30 dB is shown in Fig. 4.6(b) for the dynamic range of 27 dB. It is clear that CS and FB using US receivers have a better estimation than NRS and RS on the tails below 0.5 km and above 2.5 km in Fig 4.6(b), and thus better DR. It is also true for CB, but the degradation is small when compared to CS and FB.

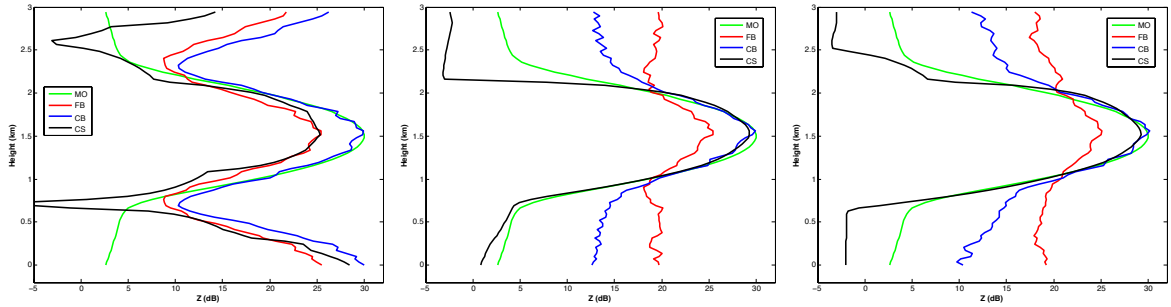

(a) Number of receivers= 17

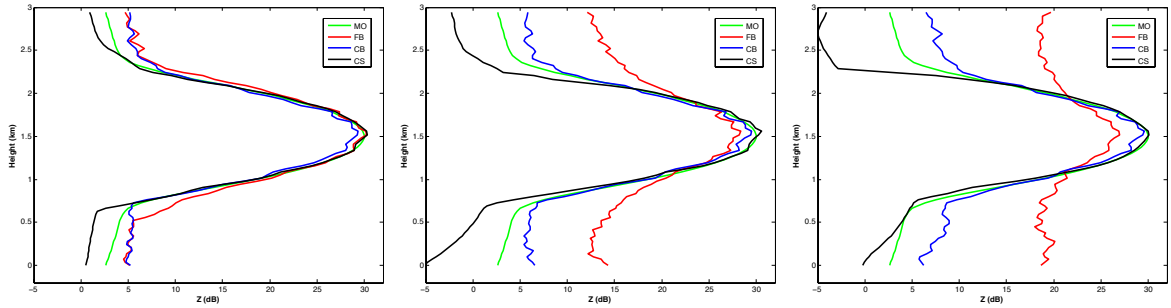

(b) Number of receivers= 33

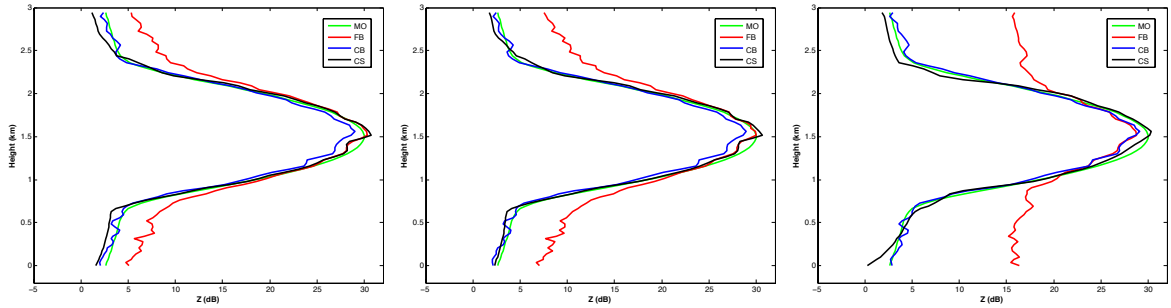

(c) Number of receivers= 65

Figure 4.6: Reconstructed images from CS (black), CB (blue), and FB (red) by using US (the first column), NRS (the second column) and RS (the last columns). Model reflectivity (MO) is shown in green. Dynamic range is 27 dB, SNR= 30 dB.

The impact of the number of receivers on the DR of estimates is investigated using the model DR of 27 dB for the three receiver configurations each with 17, 33, and 65 receivers. The results are shown in Fig. 4.7. In general, the estimated DR is improved with increasing receiver numbers for all the methods and configurations.

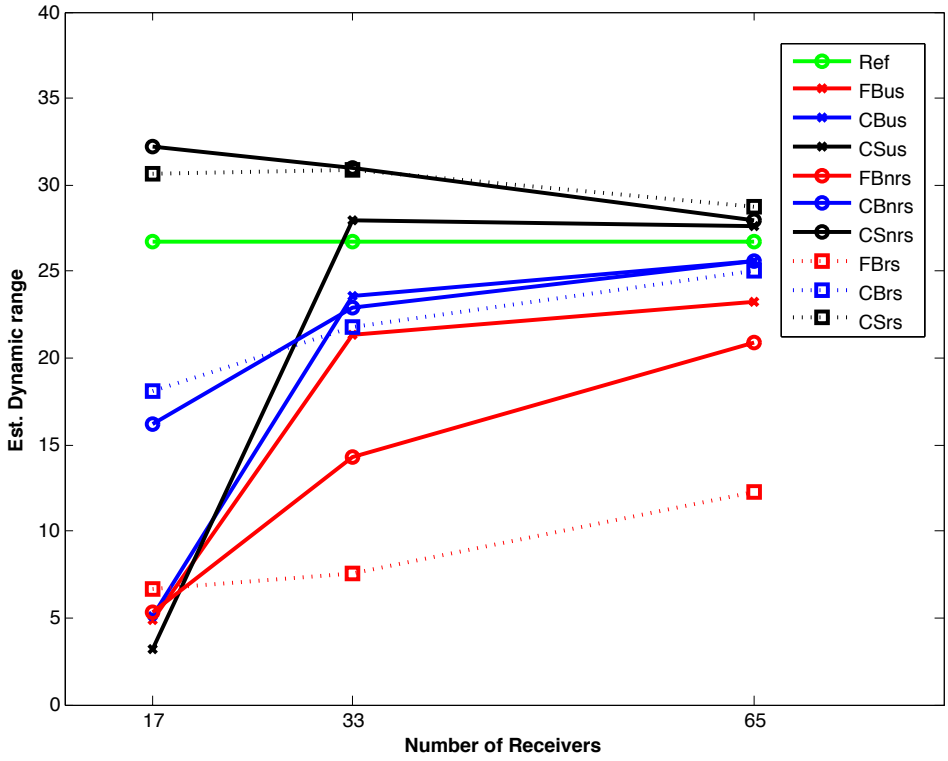

Figure 4.7: The mean of DR for estimation as a function of number of receivers for CS (black), CB (blue), and FB (red) is shown for US, RS, and NRS. The reference line is shown in green. DR=25 dB, the number of samples is 1024, and SNR=30 dB.

The DR for CS, CB, and FB with US configuration is significantly improved by increasing the receiver number from 17 to 33. Examples of DR estimates from all three methods and configurations for 17, 33, and 65 are presented in Fig. 4.6. In FB, the improvement of DR as the receiver number increases is relatively limited for the RS configuration, because the sidelobes in FB with RS are high and did not decrease much by increasing the number of receivers as demonstrated in Fig. 4.2 and Table 4.1. The impact of the sidelobes is evident in Fig. 4.6 where the FB estimation on the tail part above 2 km and below 1 km using RS is higher than 15

dB, which is a high value compared to the US configuration with 33 and 65 receivers. Note that the grating lobes occur at locations of -14.47 and 14.47 degrees in the US configuration of 17 receivers and can lead to much worse DR performance compared to sidelobe effect. The impact of the grating lobe is apparent in Fig. 4.6(a) in US with 17 receivers. It is also worth mentioning that the grating lobe is mitigated in NRS and RS by setting the minimum spacing to half wavelength. Therefore, it has the potential to reduce the number of receivers to achieve a certain performance without a grating lobe in the radar FOV. However, higher sidelobes will result and adaptive processing, such as CB, can be used to mitigate sidelobe impact.

The DR of CB and CS using 65 receivers in the three configurations is comparable. As shown in Fig. 4.7, the reconstructions of CS and CB have better agreement with the model reflectivity than the 17 and 33 receivers. Further, the performance of CS, CB, and FB as the number of receiver increases improves more using NRS than RS and then US receivers, respectively. In order words, the performance of CS is better using RS with 17 receivers than NRS and US configuration.

4.7.1.2 Impact of dynamic range on velocity

The impact of reflectivity DR on the velocity estimation is studied. The same single Gaussian model with the same interval of DR, as shown in Fig. 4.6, is used for the velocity analysis. The model velocity is shown in Fig. 4.9, where the velocity varies

linearly from -2 to 12 ms^{-1} within the 25^o FOV. The quality of velocity reconstruction in this case is quantified by the interval where the estimated velocities have an error smaller than or equal to 3 ms^{-1}. Subsequently, the percentage of the interval to the entire velocity range (ie., twice of Nyquist velocity of 52 ms^{-1}) is computed and shown in Fig. 4.8 for various model DRs. CS is capable of estimating the entire

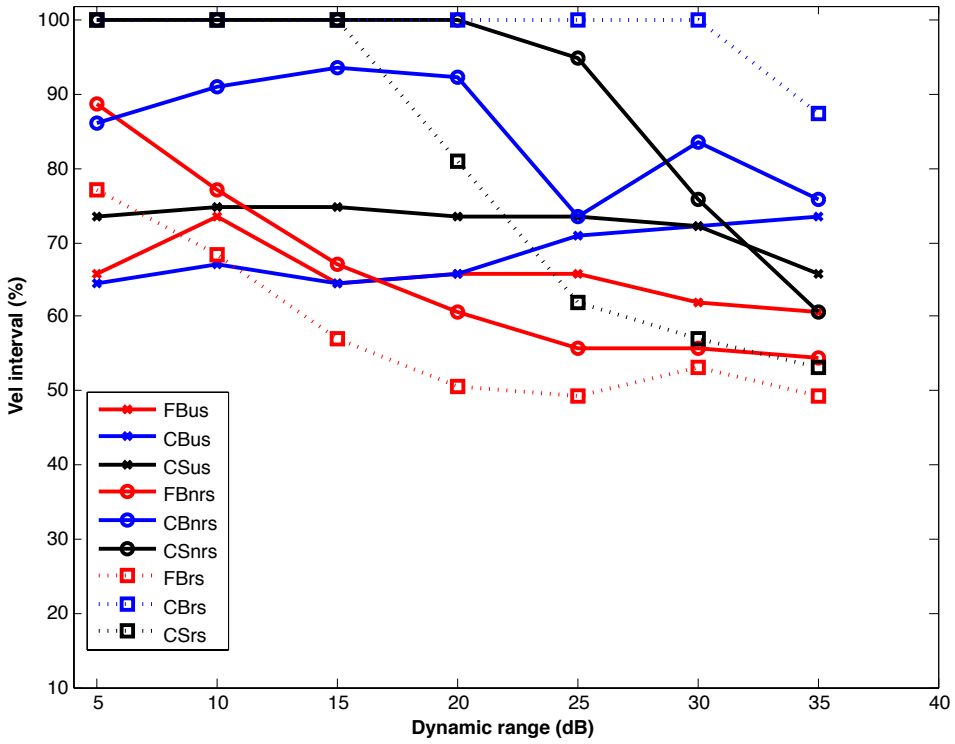

Figure 4.8: Estimated velocity interval as a function of true DR for CS (black), CB (blue), and FB (red) is shown for US, RS, and NRS. The number of receivers is 33, the number of samples is 1024, and SNR=30 dB.

velocity profile accurately (error less than 3 ms^{-1}) for model DR less than 20 dB. Nevertheless, CS can achieve relatively larger velocity interval by using NRS than with RS and US as increasing the DR of reflectivity, except DR = 35 dB with US. CB using RS provides a higher velocity interval compared to NRS and using NRS

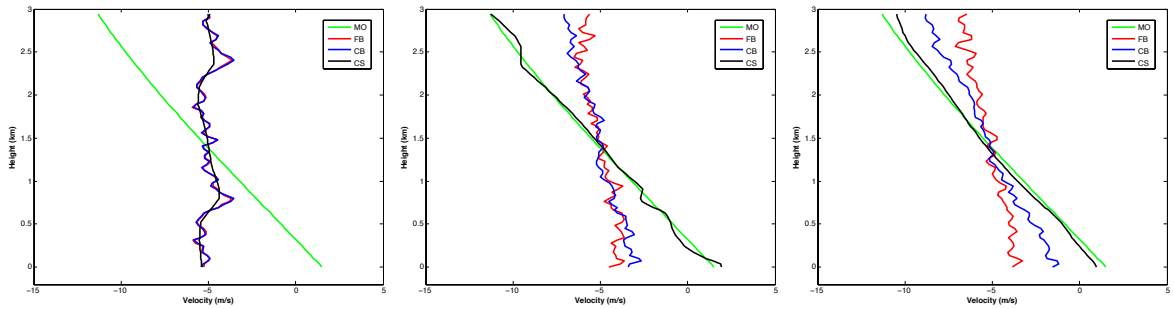

(a) Number of receivers=17

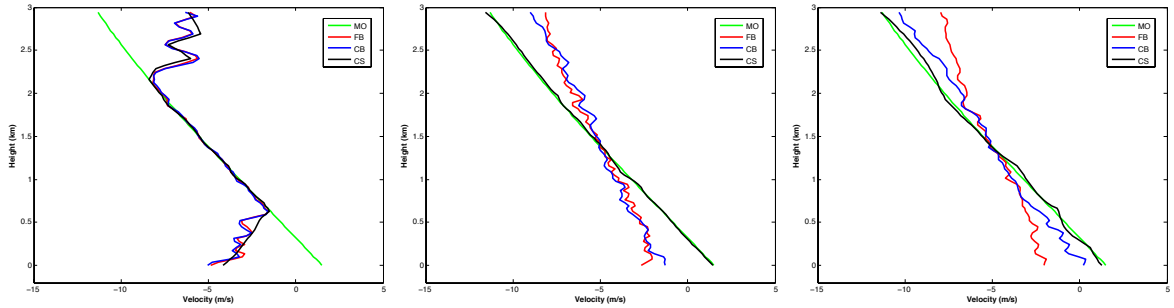

(b) Number of receivers=33

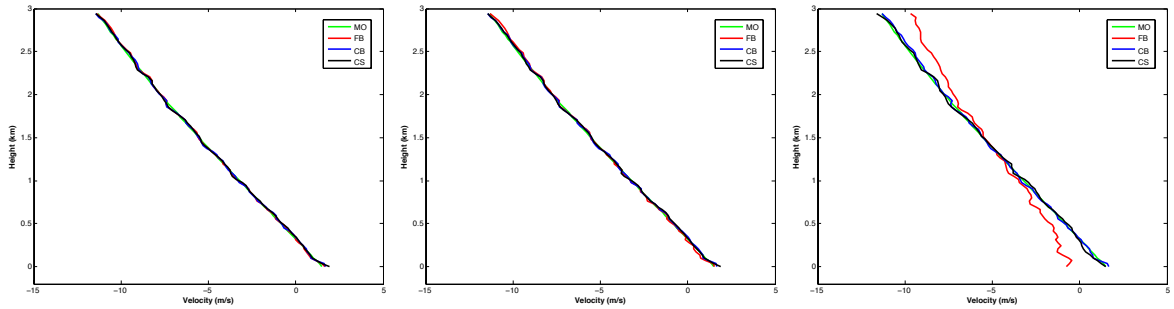

(c) Number of receivers=65

Figure 4.9: Reconstructed velocity profile from CS (black), CB (blue), FB (red) by using US (the first column), NRS (the second column), and RS (the last column) receiver configurations. Model reflectivity (MO) is shown in green. Velocity slope is 4, dynamic range of reflectivity model is 25 dB, SNR=30 dB.

compared to US with 33 receivers for all the DR cases. In contrast, CS provides the higher velocity interval by using NRS when DR is greater than 15 dB. The velocity interval of CS quickly decreased to half by using RS compared to NRS and US. FB

did not estimate the entire velocity profile accurately (error less than 3 ms^{-1}) in any of the cases. The largest velocity interval of FB is obtained as 90% using NRS. The smallest velocity interval is obtained from FB using RS configuration. An example of the reconstructed velocity profile is shown in Fig. 4.9(b) for CS, CB, and FB using 33 receivers and DR of reflectivity as 25 dB. The velocity interval of FB is reduced by changing the receiver configuration from US to RS (left to right, US, NRS, RS). The velocity interval of FB is higher using NRS than RS for all given DR cases. As DR increases, the velocity interval of CB increases in contrast to FB and CS using US configuration. However, CS achieves better performance than CB and FB using US and NRS configuration when DR is less than 30 dB. CB using RS provides the largest velocity interval when DR is greater than 20 dB. As shown in Fig. 4.9(b) that CB velocity profile is closer to model velocity than CS and FB's using 33 receivers. The impact of the receiver number on the velocity interval is investigated using the model reflectivity DR of 27 dB for the three receiver configurations each with 17, 33, and 65 receivers. The results are shown in Fig. 4.10. When the number of receiver increases, the velocity interval from CS increases for all three receiver configurations and reaches the maximum value using NRS and US with 65 receivers. CB with the RS configuration is capable of providing the entire velocity profile accurately (error less than 3 ms^{-1}) for the three receiver numbers. Also, the percentage of valid velocity interval from CB with NRS and US reaches a maximum value of 100% for 65

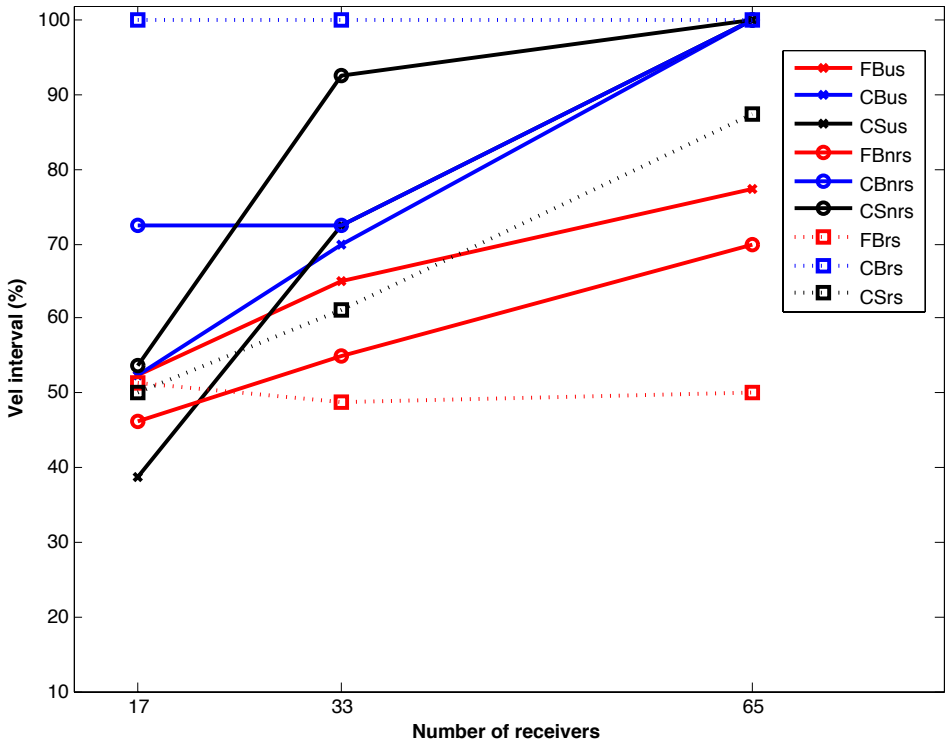

Figure 4.10: The mean estimated velocity interval as a function of number of receivers for CS (black), CB (blue), and FB (red) is shown for US, RS, and NRS. DR=25, the number of samples is 1024, and SNR=30 dB.

receivers. CB takes advantage of RS more than CS and FB and provides the maximum velocity interval using only 17 receivers, whereas CS and FB achieve half of it for DR=25dB.

On the other hand, NRS is more favorable for CS for 17 and 33 receivers than RS and US, even though only approximately 50% of velocities can be reconstructed reasonably if 17 receivers are used. Also, CS usually provides a large velocity interval at a large dynamic range using NRS. Examples of a reconstructed velocity profile are shown in Fig. 4.9 for 17, 33, and 65 recievers. The CB velocity estimate overlaps with the model velocity with small fluctuations using 65 receivers at three

receiver configurations. CS has good agreement with the model velocity using US and NRS with 65 receivers. However, FB has a limited velocity interval around the centered velocity of -5 ms^{-1} for all cases as shown in Fig. 4.9. When the number of receivers decreases, CS, CB, and FB deviate from the model velocity at the edges in three configurations. It can be observed in Fig. 4.9 that the velocity interval between 1 km to 2 km in height can be reconstructed well, and the interval of valid velocity estimates extends as the number of receivers increases for CS with all three configurations. Similar performance can be observed for FB with NRS and US but with a narrower valid velocity interval. Further, the common region for CS, FB, and CB corresponds to the relatively higher values in their reflectivity estimates in Fig. 4.6. The reason for FB is the high sidelobes, which prevent resolving the structure accurately. The weights of CB adaptive to received data and 65 receivers are sufficient to resolve the structure accurately in this case. A possible explanation can be made for CS by using the reconstructed reflectivity profile in Fig. 4.6. The CS reflectivity above 2 km and lower than 1 km in height was not recovered accurately for 17 and 33 receivers. Since the CS velocity estimation is obtained by the reconstructed real and imaginary part of the velocity structure in (4.24), inaccurate estimation of those relatively small values will lead to an inaccurate velocity profile.

4.7.2 Resolution

4.7.2.1 Resolution in reflectivity

The performance of resolution for CS reflectivity estimation is investigated by using dual-Gaussian reflectivity models with varying separations. Specifically, the dual-Gaussian model is defined in the following equation.

$$Z(\theta) = (A - C)(e^{\frac{(\theta-\theta_1)^2}{2\sigma_z^2}} + e^{\frac{(\theta-\theta_2)^2}{2\sigma_z^2}}) + C, \tag{4.28}$$

where $\sigma_z = 1.5^o$, θ_1 and θ_2 are the location of the peaks in the two Gaussian functions. In this work, the separation of the dual Gaussian is defined by $\theta_2 - \theta_1$, which is varied every 0.4^o. Additionally, $C = 5$ dB for a fixed reflectivity base, and DR of the model is 35 dB. The resolution of the reflectivity estimation is defined by how well the two Gaussians can be resolved. Specifically, the resolution in this work is quantified by the peak-to-valley-difference (in dB scale) (e.g., (Mir and Carlson 2012)), as shown in the following.

$$\text{RES} = \frac{Z_{P1} + Z_{P2}}{2Z_V}, \tag{4.29}$$

where Z_{P1} is the maximum reflectivity value at the first peak location and Z_{P2} is the maximum reflectivity value at the second peak location, and Z_V is the minimum reflectivity value between the two peaks. The mean RES for CS, CB and FB is shown in Fig. 4.11 for the three receiver configurations.

The estimated resolution from CS generally agrees better with the model resolution, depicted by the green line, for most of the cases than from both CB and FB for

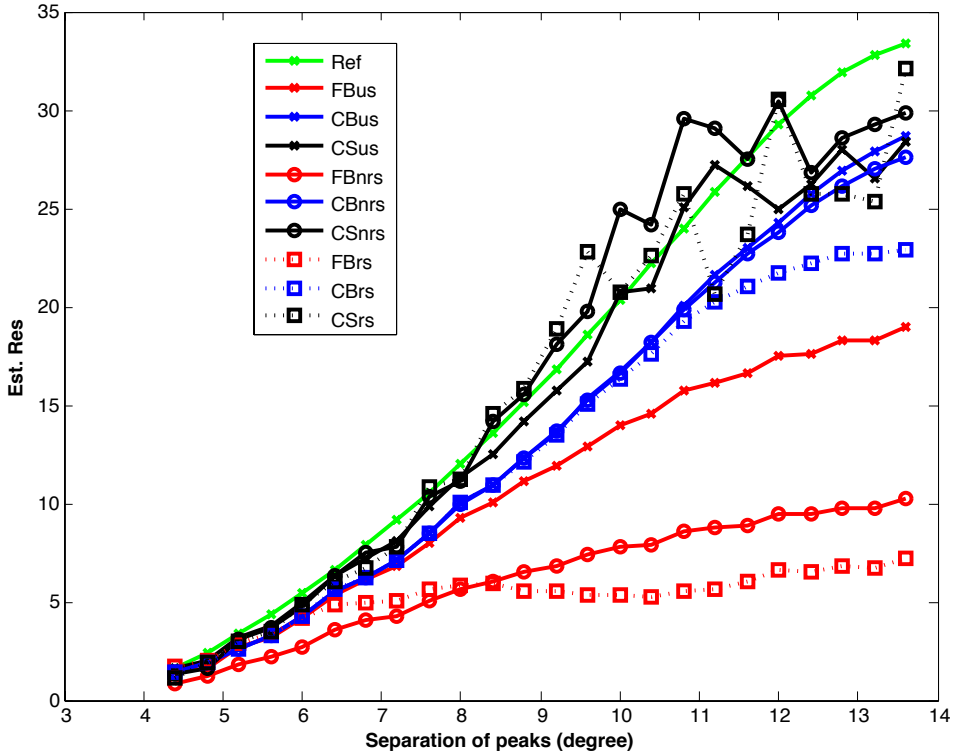

Figure 4.11: The mean resolution of CS (black), CB (blue), and FB (red) as a function peak separation is shown for US, RS, and NRS. The reference line is shown in green. The number of receivers is 33, the number of samples is 1024, and SNR=30 dB.

all three configurations. As the separation of the two Gaussians increases, all three methods can better distinguish the two Gaussian structures for all the configurations, except the FB with RS configuration (red dashed line with square markers), where the larger sidelobes significantly contaminate the estimates. Nevertheless, it should be emphasized that even for large separation (larger than 5.6^o) neither CB or FB can achieve the level of model resolution. Additionally, the difference in resolution from model and estimates from CB and FB increases as the separation increases. On the other hand, CS with all three configurations can produce improved resolution that

is consistent with the model resolution up to a separation of approximately 10^o. It can also be observed that the variation of RES for CS increases as the separation increases. When the values in the valley between the two peaks become relatively small, CS is not able to accurately estimate those values. Similar evidence was observed for CS in DR analysis in Fig. 4.5. Note that CB and FB underestimate the resolution for three receiver configurations using 33 receivers, while CS can overestimate RES using NRS when the separation of the two Gaussians is between 9 and 11.6 degrees, then underestimate it for greater than 11.6 degrees. An example profile of estimation for CS, CB, and FB is shown in Fig. 4.13(b) for 33 receivers. It is obvious that neither method is capable of fully resolving the sharp variation in the valley at 1.5 km, while CS can capture the deep valley slightly better than CB for US and RS configurations. However, CS with NRS produces a valley that is far too deep. It is also evident that the high sidelobes effect the FB, especially with the RS configuration. The mean RES of CB is almost the same for different receiver configurations up to the peak separation of 10^o using 33 receivers.

In order to show the impact of the receiver numbers, a dual Gaussian reflectivity with separation of 11.6^o is used, and the results are shown in Fig. 4.12. An improvement in the RES of CS, CB, and FB estimate can be observed by using the NRS and RS receiver configuration as the number of receivers increases from 17 to 33. In the US configuration, the improvement for CB and FB is indistinguishable from 33 to 65, and CS has some small improvement, where CS has a large improvement from

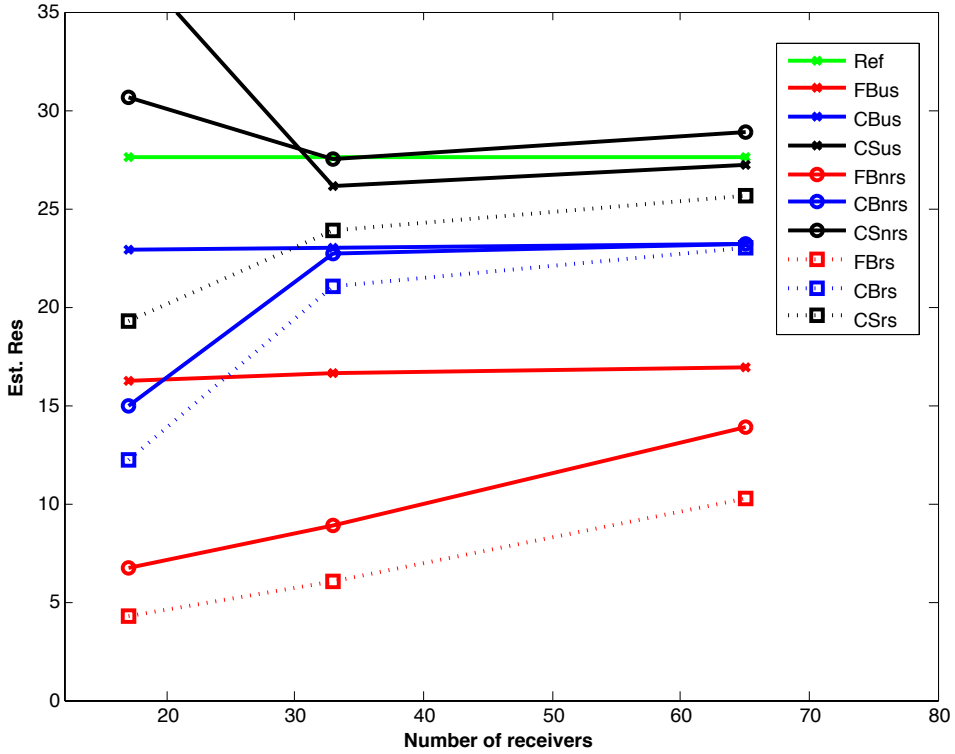

Figure 4.12: The mean resolution of CS (black), CB (blue), and FB (red) as a function of number of receivers for a profile of 11.6-degree peak separation is shown for US, RS, and NRS. The reference line is shown in green. The number of receivers is 33, the number of samples is 1024, and SNR=30 dB.

17 to 33 receivers, in which grating lobes inside the radar FOV. For the NRS and RS configurations, generally, the RES of CS is more consistent with the model resolution than CB and FB for a given number of receivers. FB has the highest resolution by using US receiver configuration based on this profile of reflectivity model with the separation of 11.6 degrees. Moreover, CB produces high resolution with US and NRS configurations using 33 receivers, and the performance of CB with 65 receivers is the same.

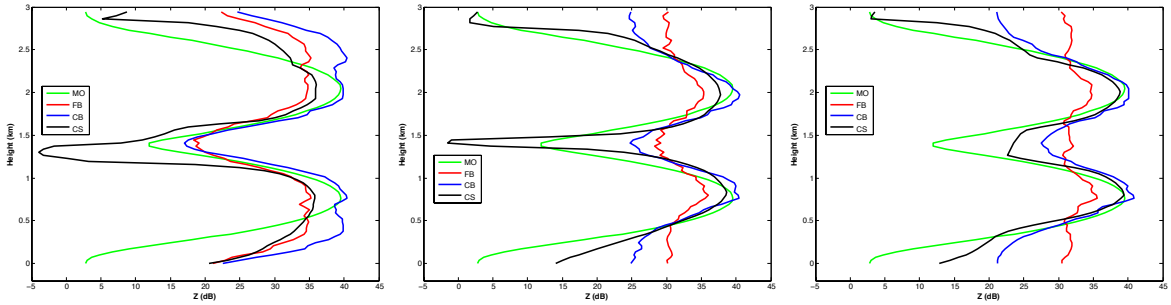

(a) Number of receivers= 17

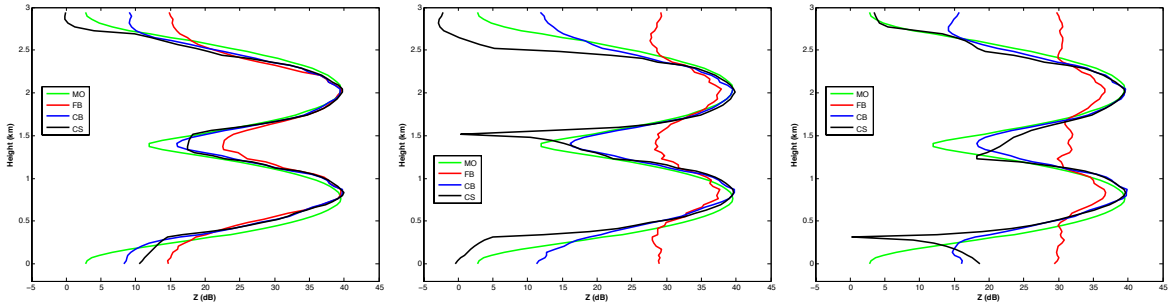

(b) Number of receivers= 33

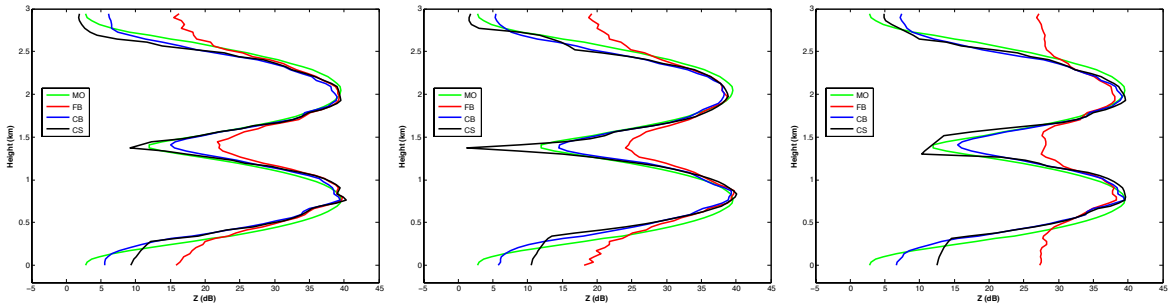

(c) Number of receivers= 65

Figure 4.13: Reconstructed image profile from CS (black), CB (blue), and FB (red) by using US (the first column), NRS (the second column) and RS (the last columns) receiver configurations. Model reflectivity (MO) is shown in green color. Std of Gaussian model is 1.5 degree, peak separation is 11.6 degree, and SNR=30 dB.

Examples of reconstruction from CS, CB, and FB are shown in Fig. 4.13. Generally, it can be observed that the dual Gaussian with various separations can be generally reconstructed by the three estimation methods, while CS and CB provide

better resolvability than FB. It is clear that the CS reflectivity estimation between the two Gaussians improves more than CB and FB as the receiver numbers increase using the US configuration. Similarly, the CS estimation of the valley with RS is progressively improved by increasing the receiver numbers from 17 to 65. The same performance improvement can be observed for CB and FB, but the improvement is more obvious in CS. Interestingly, the two Gaussian peaks are increasingly better reconstructed using FB with NRS and RS as the receiver number increases. In contrast, the improvement in CB and CS resolution is mainly contributed to by better resolving the valley as the receiver number increases in NRS and RS.

4.7.2.2 Resolution of velocity estimation

In this work, the resolution of velocity is characterized by how well a linear velocity profile can be reconstructed given uniform model reflectivity. Specifically, uniform reflectivity of 30 dB is used in the simulation, while the slope of the linear velocity profile varies from 0 to 7 (unit ms^{-1}/deg). The performance of velocity resolution is quantified by the RMSE as a function of velocity slope with various numbers of receivers. RMSE is calculated for the entire range within the Nyquist velocities (i.e., ± 52 ms^{-1}) within the 25-degree beamwidth radar FOV.

As the slope of velocity increases, the mean RMSE from CB and FB increases for all receiver configurations. The mean of RMSE from CS with US configuration increases as the slope increases (except at zero slope), while those with NRS and RS

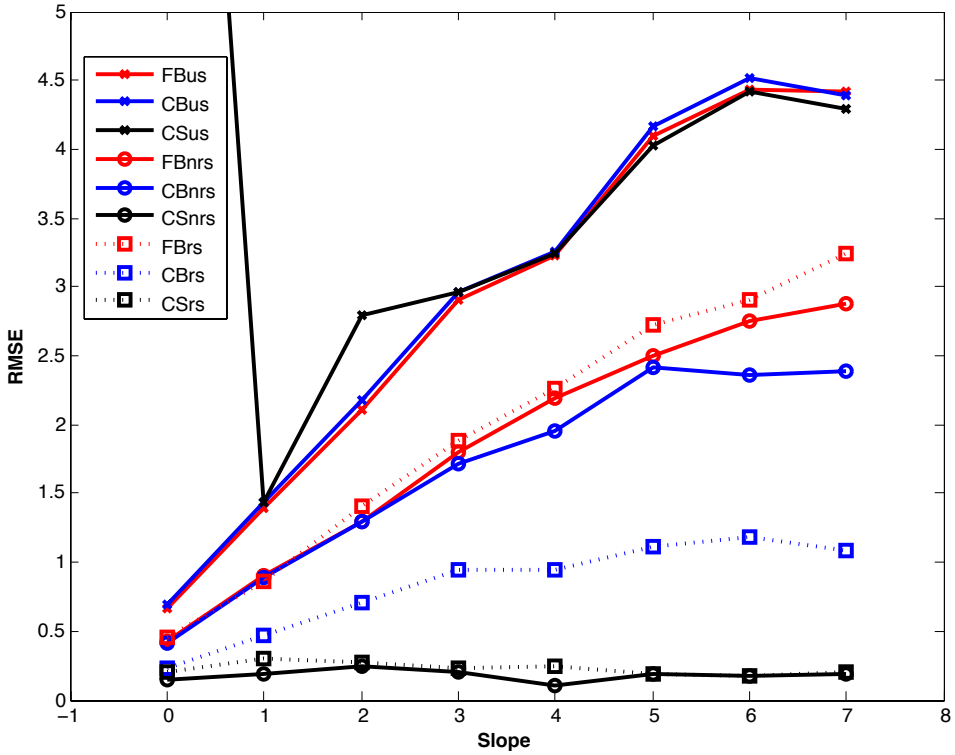

Figure 4.14: The mean RMSE of CS (black), CB (blue), and FB (red) velocity estimation as a function of velocity slope is shown for US, RS, and NRS. The reference line is shown in green. The number of receivers is 33, the number of samples is 1024, and SNR=30 dB.

configurations maintain a relatively low and constant RMSE. For the configurations of NRS and RS, it is evident that CS provides better velocity estimates than CB and FB. As shown in Fig. 4.15 CS can estimate the entire velocity profile with better agreement than CB and FB in NRS and RS configurations. The mean RMSE of CS is less than 0.25 m/s for the given slopes in NRS and RS. However, the performance of CS for velocity estimation is comparable to CB and FB with US configuration of 33 receivers.

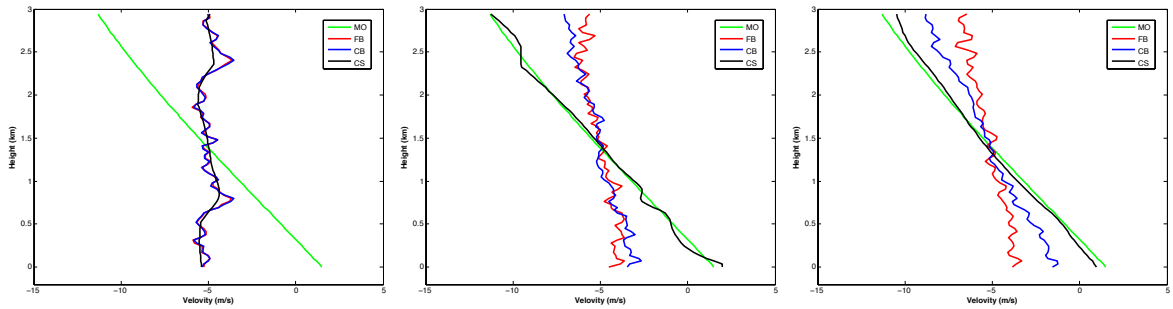

(a) Number of receivers= 17

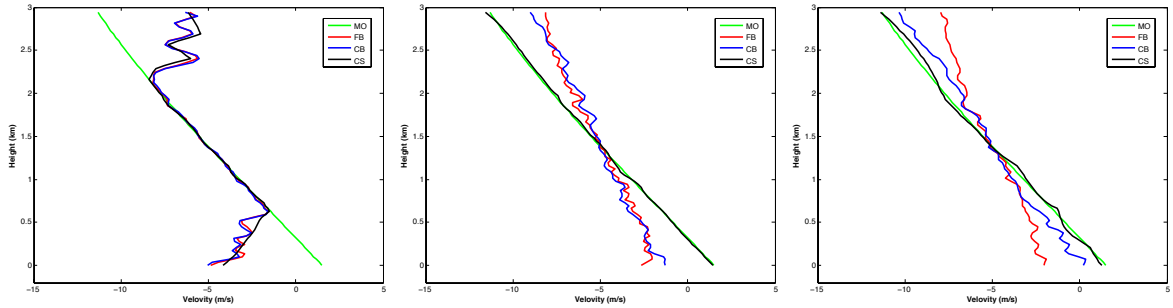

(b) Number of receivers= 33

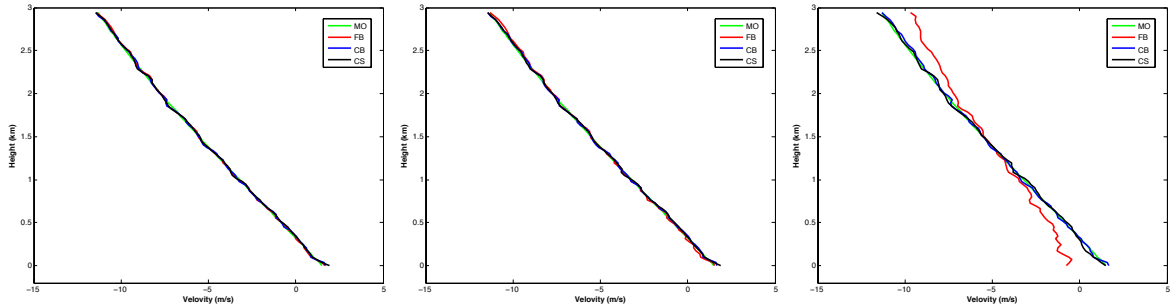

(c) Number of receivers= 65

Figure 4.15: Reconstructed velocity profile of CS (black), CB (blue), FB (red) by using US (the first column), NRS (the second column) and RS (the last columns) receiver configurations. Model reflectivity (MO) is shown in green color and velocity slope is 4. Uniform reflectivity model is at 30 dB, number of samples 1024 and SNR= 30 dB.

In order to show the impact of receiver numbers on velocity estimation, a slope of velocity equal to 4 is used, and the resulting statistics are shown in Fig. 4.16. When the number of receivers increases, the mean RMSE from all three methods

with US configuration decreases. Note that for CS with NRS and RS, even though the estimation is improved as the number of receivers increases, fairly good results (mean RMSE of less than 0.5 ms^{-1}) can be achieved using only 17 receivers. It can be observed clearly in Fig. 4.15, CS, CB, and FB reconstruct the velocity profile accurately using 65 receivers in US and NRS configurations. Further, CS and CB can estimate the entire velocity interval with 65 receivers using the RS configuration as well.

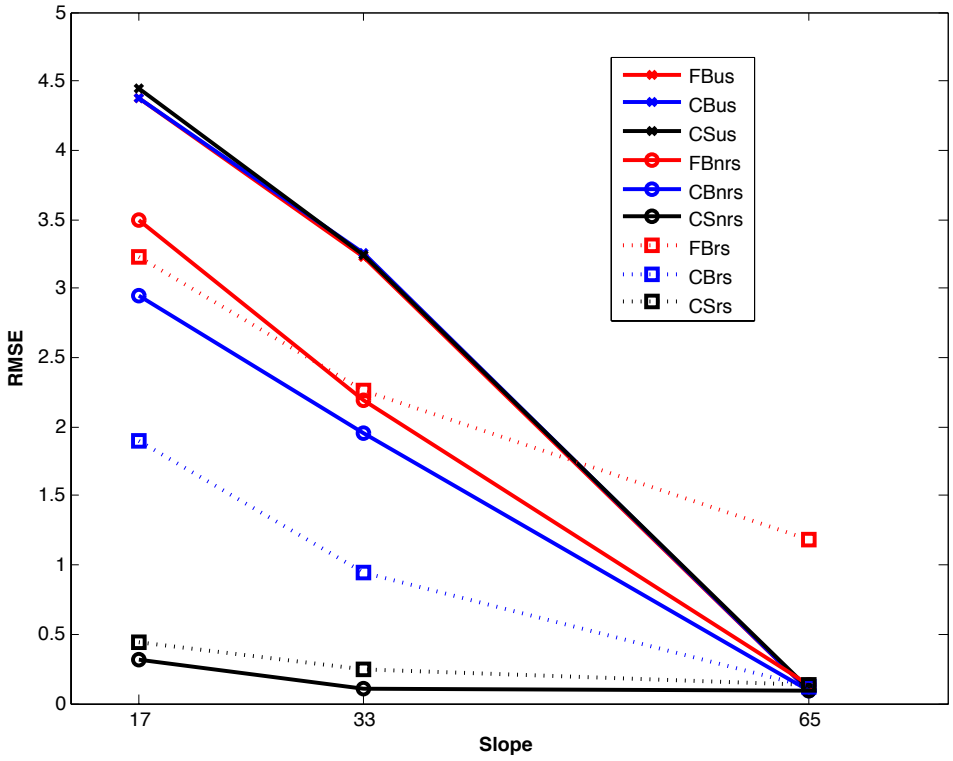

Figure 4.16: The mean RMSE of CS (black), CB (blue), and FB (red) as a function number of receivers is shown for US, RS, and NRS. The velocity slope is 4, the number of samples is 1024, and SNR=30 dB.

Note that none of the three methods can produce satisfactory reconstruction over the entire velocity interval using the US configuration of 17 and 33 receivers. If we compare the result in Fig. 4.15 with the velocity results in Fig. 4.9 in the dynamic range analysis, it can be observed that CS velocity estimation is improved by increasing receiver number for NRS and RS configurations. This improvement also indicates that CS velocity estimation is sensitive to the underlying reflectivity structure. Note that the impact of reflectivity on the velocity estimation is also studied in Section 4.7.1.2. Additionally, CB produced good velocity agreement with model velocity using the RS configuration.

4.7.3 RMSE analysis with ARPS model reflectivity and velocity

To further demonstrate the feasibility of CS for reflectivity and velocity reconstruction, the fields of reflectivity and velocity from ARPS were used with the same three receiver configurations for various SNR, number of samples, and number of receivers. In simulation, the distance between the radar and ARPS model domain is 3 km, and the array is tilted by 13^o. The range time indicator (RHI) of reflectivity and velocity model structures were derived from ARPS variables and is shown are Fig. 4.17. The simulated RHI domain is defined by 3 km to 8.3 km in range and -8 to 34^o in elevation (defined from the 6 dB from the transmitted pattern). There are a total of 70 vertical profiles of reflectivity and velocity within the simulation domain. The reconstruction is performed only between the region of 0 to 26^o (slightly larger

than the 3 dB transmitted beamwidth of 25^o) in elevation. Further, in order to make the discussion clear, five reflectivity regions in the model are selected, where they are also depicted in the upper panel of Fig. 4.17. The reflectivity in Region II is high (larger than 45 dBZ) and in Regions III, IV, and V is low (less than 20 dBZ). Region I has relatively moderate reflectivity between 20 to 38 dBZ. The same region assignment is also applied to the RHI of model velocity as shown on the lower panel of Fig. 4.17.

4.7.3.1 Impact of noise

Noise impact on reflectivity estimation

The performance of CS for reflectivity and velocity reconstruction is studied as a function of SNR. The noise power was fixed at -70 dB and the received signal power was scaled to obtain desirable SNR. Subsequently, a noise sequence was added to the time series of signals for a given SNR. The mean of RMSE of reflectivity estimates from CS, CB, and FB is shown in Fig. 4.18. Specifically, the mean RMSE is computed over 10 realizations, 70 range gates and profiles. The improvement of CS, CB, and FB as a function of SNR can be observed for all three receiver configurations of 33 receivers and 1024 samples. It is important to point out that CS performs better than CB and FB with NRS and RS configurations for all SNR levels. In the US configuration, CS and FB has the same RMSE at SNR=0 dB, which is lower than CB's. Additionally, CS performs better than FB and CB when SNR greater than 10 dB in

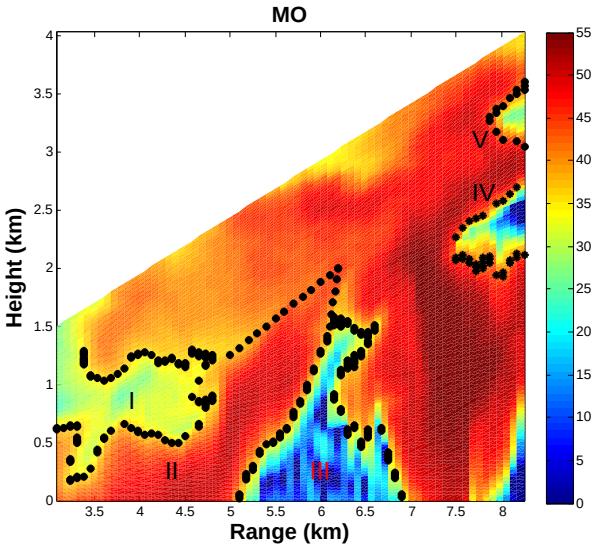

(a) Reflectivity

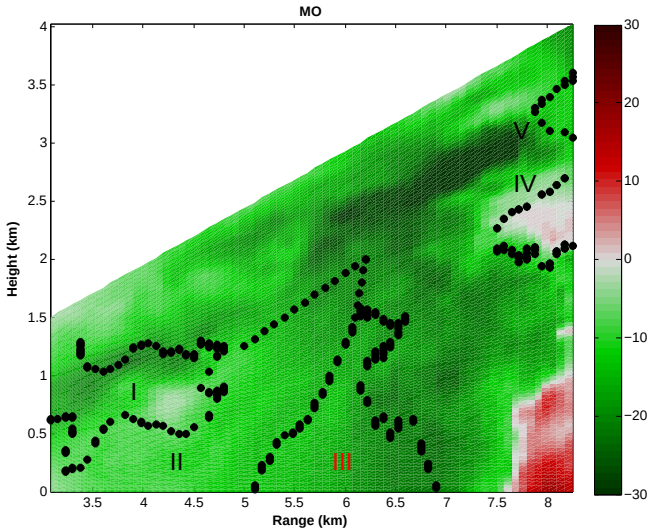

(b) Velocity

Figure 4.17: ARPS reflectivity and velocity model structure in RHI format.

US. On the other hand, FB performs better than CB using the US configuration for all SNR in Fig. 4.18(a) and also with the NRS and RS configurations if SNR is less than 10 dB. CB produces lower RMSE than FB for the NRS receiver configuration if SNR is greater than 10 dB and their performances are comparable at SNR=10 dB.

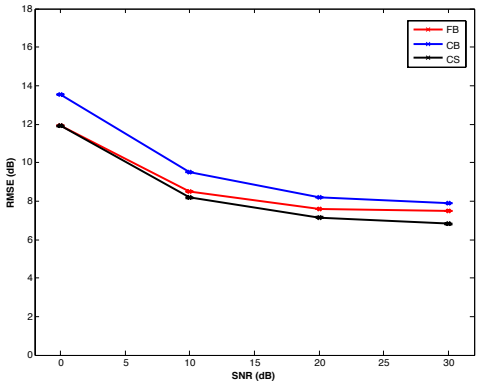

(a) Uniform spacing

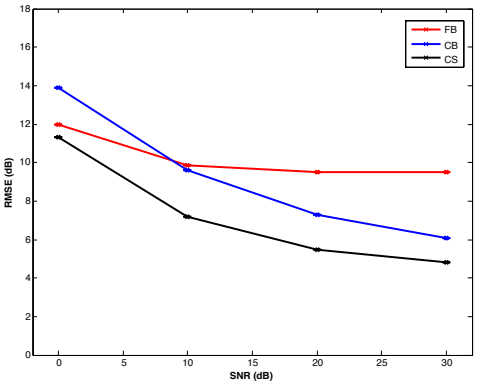

(b) Nonredundant spacing

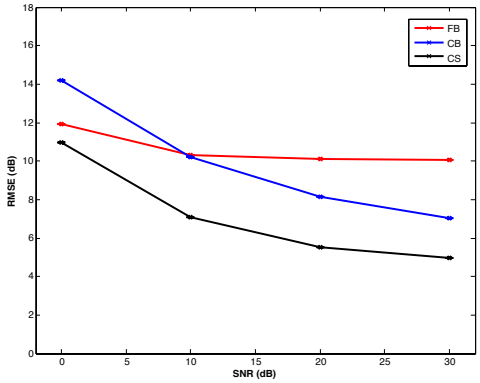

(c) Random spacing

Figure 4.18: The mean of RMSE as function of SNR for CS (black), CB (blue), and FB (red) for ARPS model reflectivity estimation. The number of receivers is 33 and the number of samples is 1024.

Further, CS performs better using NRS and RS than US, for different SNR and given the same number of receivers. For FB, lower RMSE is obtained with the US configuration than with NRS and RS configurations, because higher sidelobes in FB receiving patterns can be observed with RS and NRS as shown in Fig. 4.2. On the other hand, CB with NRS configuration can produce lower RMSE if the SNR is greater than 10 dB.

Further, the improvement of CS with increasing SNR is similar to the ones from CB in all three configurations. Note that the estimation of CB and FB is the total power, which includes both the contributions from signals and noise, and no attempt was made in this work for noise removal. However, in CS, the amount of noise is considered by the beta term in the minimization, and the estimation result consists mainly of signal contribution. Also, the inclusion of Laplace in the minimization enforces adjacent pixels to have similar values. In other words, CS is less susceptible to noise for the given cases.

Examples of CS, CB, and FB retrievals from one realization of the SNR of 0, 10, and 20 dB cases for US, NRS, and RS receiver configurations are provided in Fig 4.19, 4.27, and 4.21, respectively. Note that the model reflectivity is presented in Fig. 4.17. It is clear that the reflectivity structures are grossly reconstructed using CS, CB, and FB for all three receiver configurations and SNR=10 and 20 dB. However, some detailed structures are not recovered accurately, especially at low SNR of 0 dB. For example, the large errors in the vicinity of strong reflectivity gradient, such as in Region I and III, can be observed for all three methods. Additionally, the degradation of CB and FB from SNR=20 dB to SNR=10 dB can be clearly observed in the NRS and RS receiver configurations and is more evident than the degradation of CS, as indicated in Fig. 4.21. The noise will increase the estimated total power from CB and FB and also limits the performance of CB and FB. It is also true for CS. This

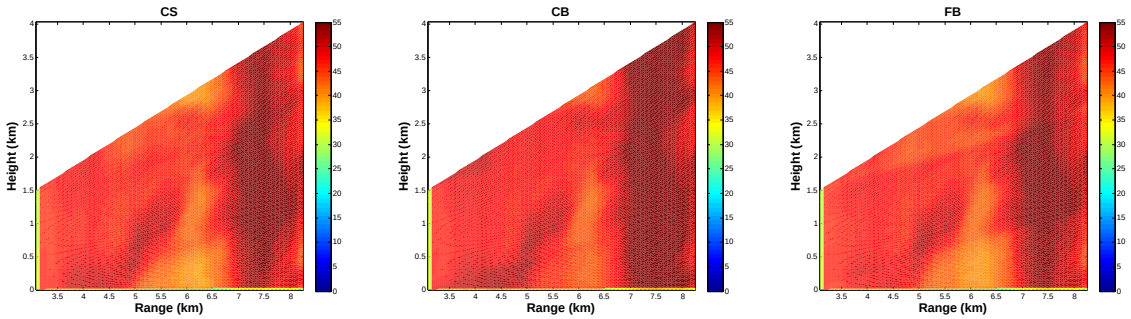

(a) SNR =0 dB

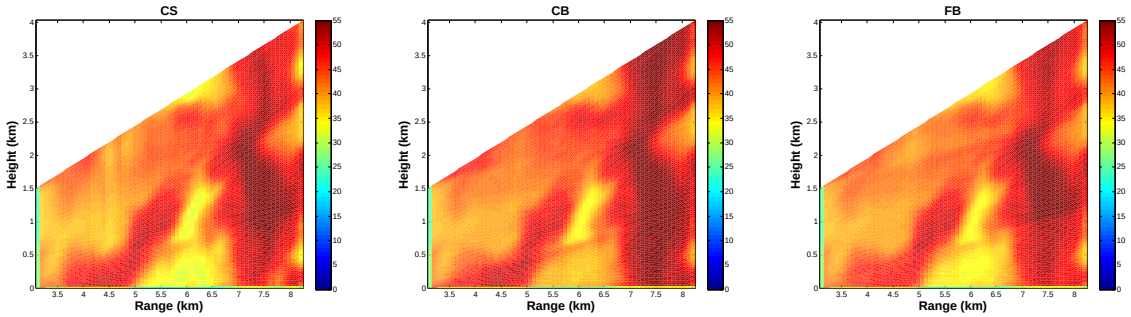

(b) SNR =10 dB

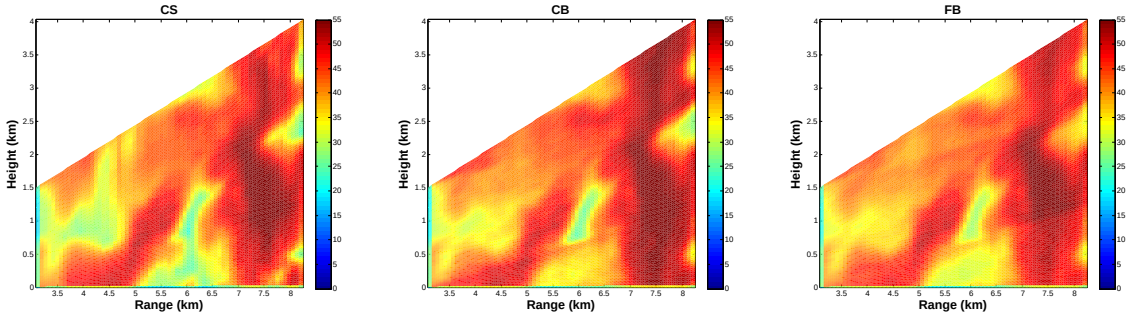

(c) SNR =20 dB

Figure 4.19: CS (left), CB (middle), and FB (right) reflectivity reconstruction with 33 receivers and 1024 samples using US configuration for SNR=0 dB (first row), SNR=10 dB (second row), and SNR=20 dB (last row)

fact can be clearly observed in estimated reflectivity profiles from CS, CB, and FB for the given SNR cases in Fig. 4.22 and 4.23.

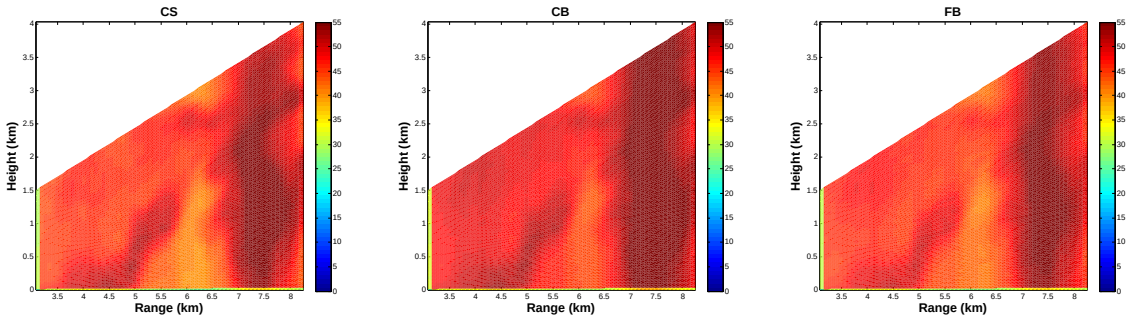

(a) SNR =0 dB

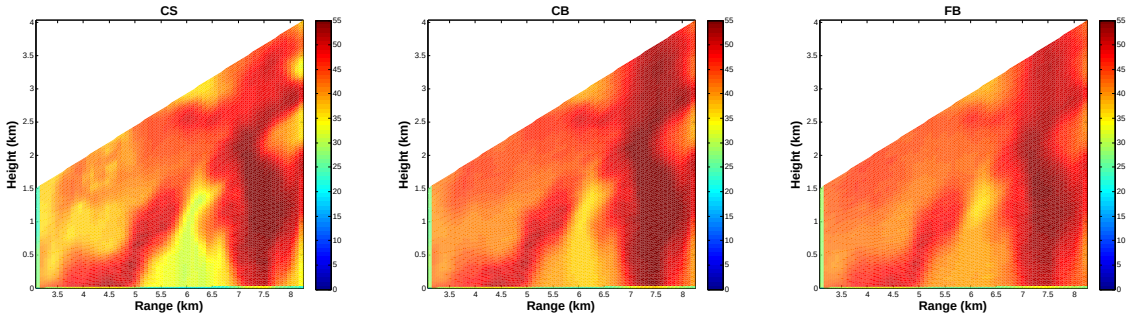

(b) SNR =10 dB

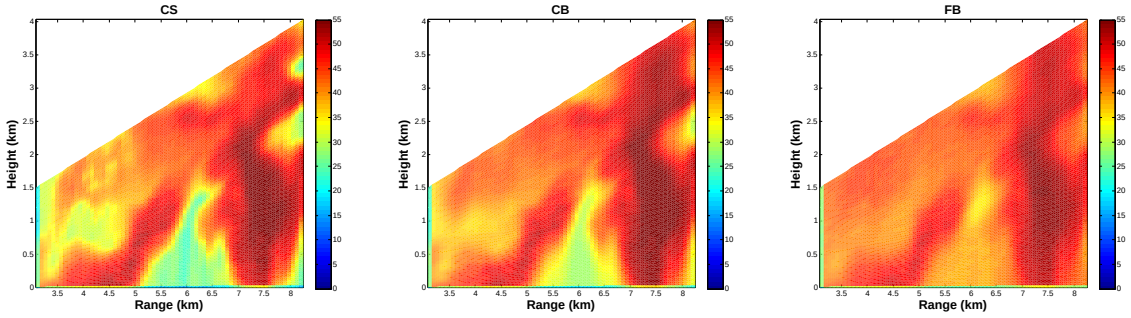

(c) SNR =20 dB

Figure 4.20: CS (left), CB (middle), and FB (right) reflectivity reconstruction with 33 receivers and 1024 samples using NRS configuration for SNR=0 dB (first row), SNR=10 dB (second row) and SNR=20 dB (last row)

In the US configuration, the reflectivity structures in Regions II and III are reasonably reconstructed from CS, CB, and FB for all SNR cases. However, Regions I, IV, and V are not well-estimated by the three estimation methods at SNR=0 dB.

The reflectivity in all regions from I to V are well-retrieved using CS at SNR=20 dB, and the reconstruction of reflectivity in Regions I and III is better than CB. Also, the reconstruction of CS for Regions I and IV is better than FB. Reconstruction of reflectivity in Regions III and V for CS can be similar to FB. It is clear that when the SNR decreases, the performance of CS, CB, and FB is degraded in Regions I, III, IV, and V where the reflectivity in those regions is lower than the reflectivity in Region II. Due to the noise, the methods are not capable of estimating low reflectivity values.

Further, in the NRS configuration, CS is capable of recovering all the regions better than those from CB and FB at SNR=20 dB, and CB performs better than FB. It is clear that CS can reconstruct Region V grossly at SNR=10 dB in contrast to CB and FB. Further, the indication of Region I can be seen only from CS at SNR=10 dB. Similarly, the in RS configuration, CS has the indication of Regions I, IV, and V, where CB and FB do not. At SNR=20 dB, CS reconstruction is much better than CB and FB, manifested by the success of reconstructing low reflectivity with CS in Regions I, IV, and V. As a result, CS performs better in NRS and RS configurations than in US.

Two example profiles at a range of 7.42 and 6.2 km are shown in Fig. 4.22 and 4.23 for CS, CB, and FB for SNR=0, 10, and 20 dB and three different configurations. It is clear that the recovery of the valley of the dual Gaussian 3 km in height is improved for CS, CB, and FB as SNR increases, as demonstrated in Fig. 4.22.

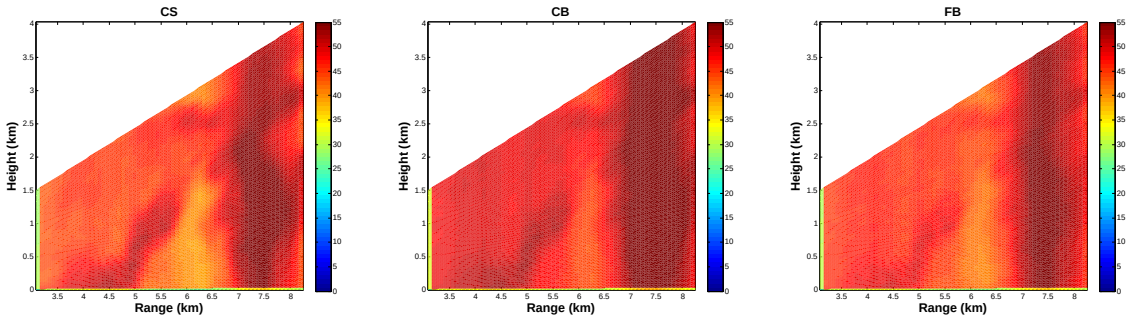

(a) SNR=0 dB

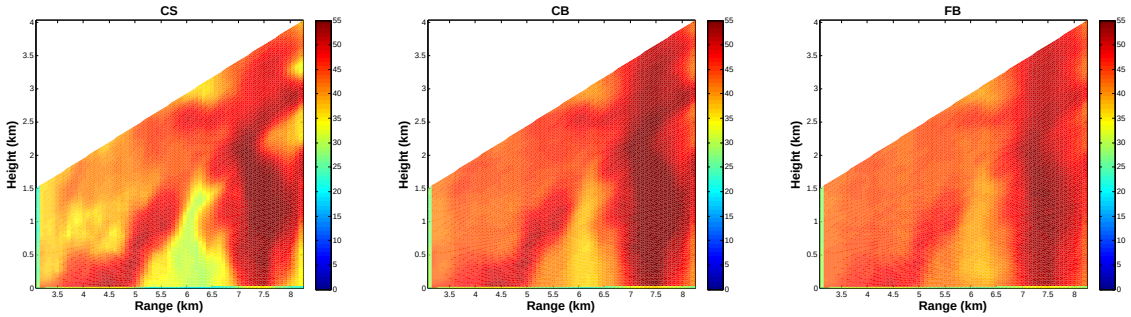

(b) SNR=10 dB

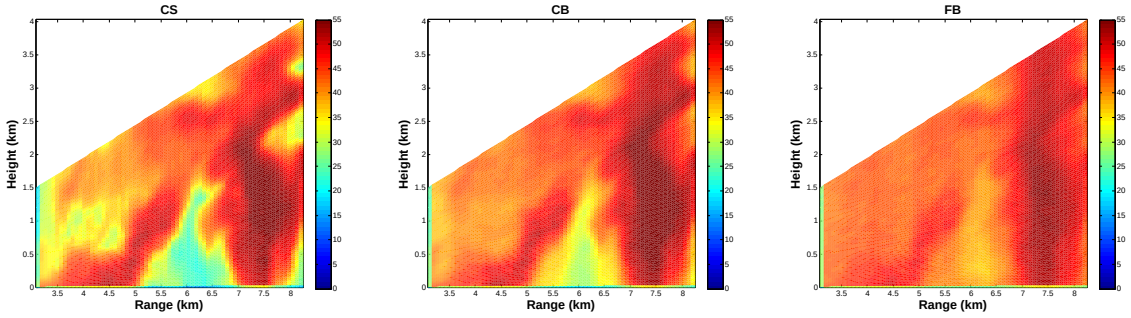

(c) SNR=20 dB

Figure 4.21: CS (left), CB (middle), and FB (right) reflectivity reconstruction with 33 receivers and 1024 samples using RS configuration for SNR=0 dB (first row), SNR=10 dB (second row), and SNR=30 dB (last row)

Additionally, as shown in Fig. 4.23, the reflectivity with a similar Gaussian shape at 1 km height can be better reconstructed with CS than CB and FB for NRS and RS as SNR increases. The improvement is more evident in CS than in CB and FB

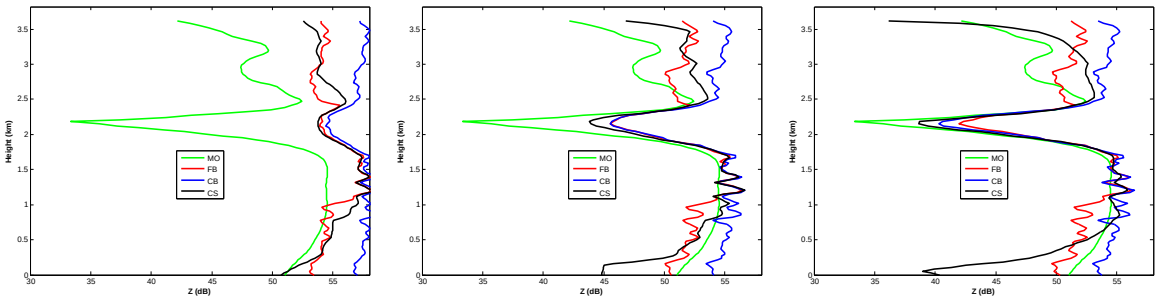

(a) Uniform spacing

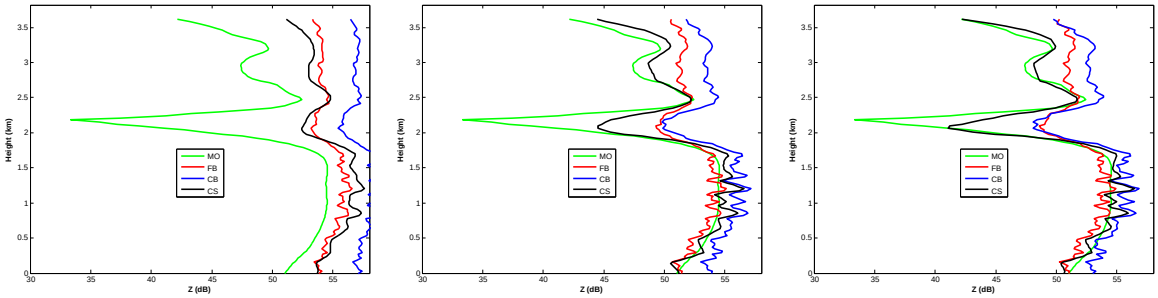

(b) Nonredundant spacing

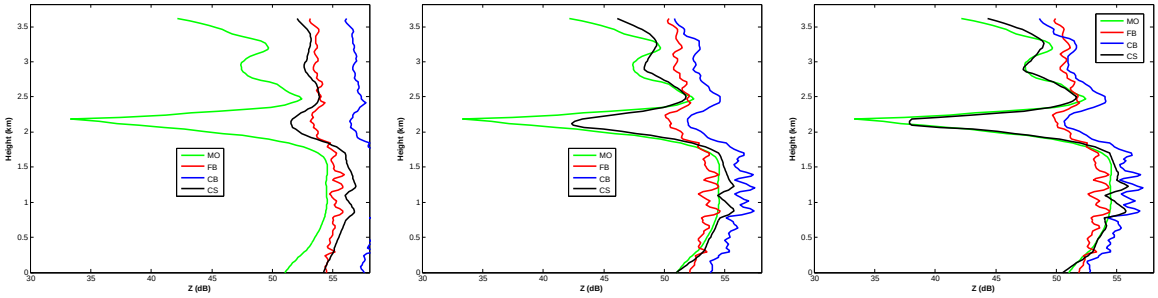

(c) Random spacing

Figure 4.22: CS (black), CB (blue), and FB (red) reflectivity reconstruction profile with SNR=0 dB (left panel), SNR=10 dB (middle panel), and SNR=20 dB (right panel). The number of receivers is 33 and the number of samples is 1024. The range of the profile is 7.42 km.

using NRS and RS configurations in both figures. Moreover, the model reflectivity similar to a dual Gaussian shape appearing at a height of 2.5 and 3.2 km height as shown in Fig. 4.22 is recovered from CS in all three configurations at SNR=0 dB,

where CB and FB are not capable of resolving them. The reconstruction of dual Gaussians becomes more clear when using CS with NRS and RS configurations, especially if SNR is greater than 0 dB. FB does not clearly resolve the dual Gaussians in all three configurations for the given SNRs in Fig. 4.22. CB is able to resolve the dual Gaussians using RS and NRS configurations when SNR equal and greater than 10 dB, where the estimation from RS is slightly better than NRS. Additionally, it is important to point out that CS provides a larger dynamic range than CB and FB for the three receiver configurations when SNR is larger than 0 dB.

Similarly, in Fig. 4.23, CS provides a larger dynamic range than CB and FB using NRS and RS configurations for all the SNRs considered. At SNR=20 dB, CS reconstructs reflectivity with good agreement with high reflectivity in the model. CS, CB and FB are not able to recover low reflectivity at 0.4 km height, where the peak difference is 25 dB from the single Gaussian at 1 km. As the SNR decreases, the performance of CS, CB, and FB becomes limited, and they are not able resolve large reflectivity variations well.

Noise impact on velocity estimation

The impact of noise on CS, CB, and FB velocity estimation is studied by using the ARPS model velocity, which is shown in Fig. 4.17. In order to avoid unreasonably high RMSE of velocity estimates, the estimated velocities are dealiased by using a simple approach defining a threshold of 10 ms^{-1} for the velocity difference between elevation angles as well as the true velocity profile. Subsequently, RMSE

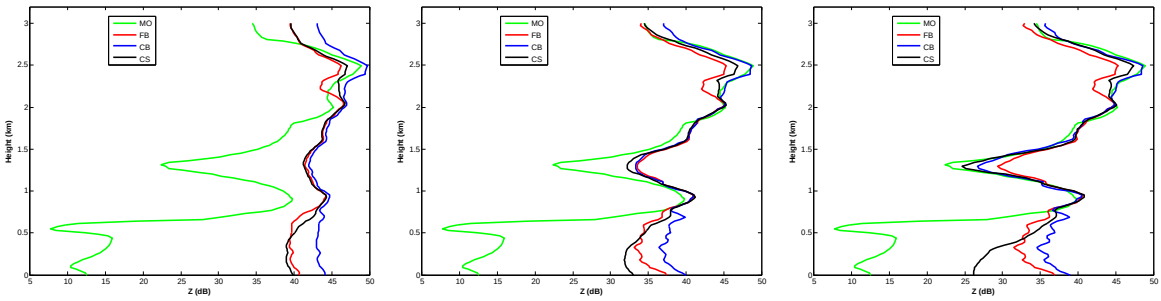

(a) Uniform spacing

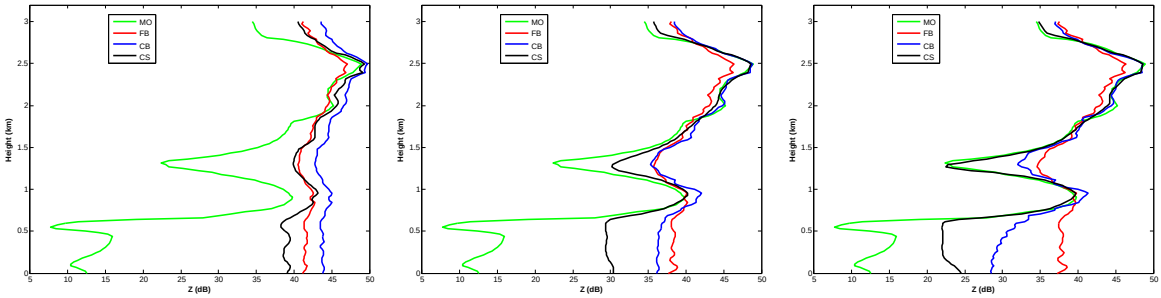

(b) Nonredundant spacing

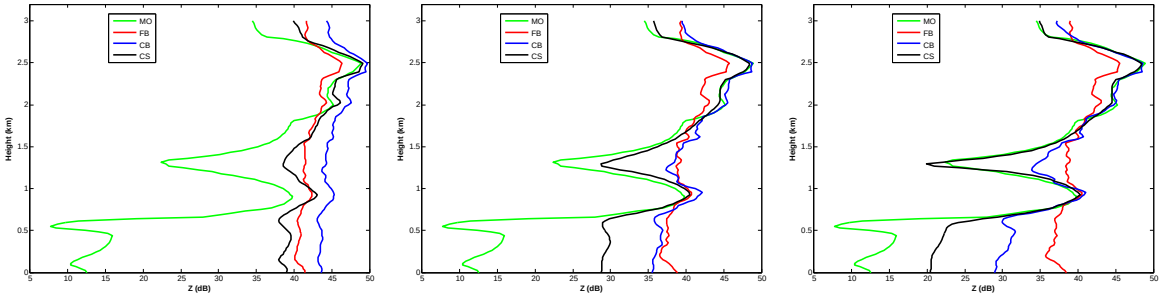

(c) Random spacing

Figure 4.23: The same as Fig. 4.22 but for the profile range of 6.2 km.

is calculated from the dealiased velocity. The mean of RMSE for CS, CB, and FB velocity estimation with 33 receivers is shown in Fig. 4.24. The improvement of CS and CB as a function of SNR can be observed for three receiver configurations. The improvement of FB velocity estimates as SNR increases can only be observed for the US receiver configuration.

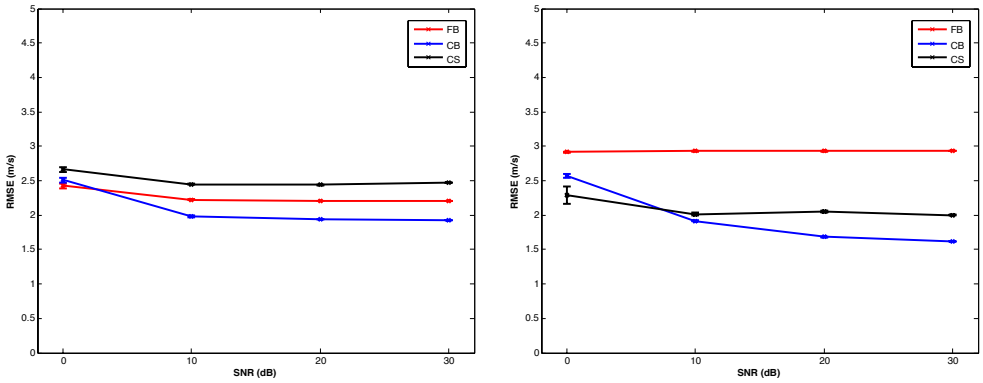

(a) Uniform spacing

(b) Nonredundant spacing

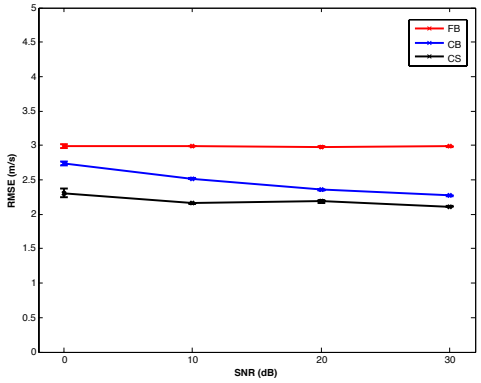

(c) Random spacing

Figure 4.24: The mean of RMSE as function of SNR for CS (black), CB (blue), and FB (red) for ARPS model velocity estimation. The number of receivers is 33, and the number of samples is 1024.

The mean RMSE of CS and FB velocity estimation is higher than 2 ms^{-1} in the three configurations. CB has the minimum RMSE in NRS at an SNR of 30 dB, which is about 1.5 ms^{-1}. On the other hand, CS has lower RMSE than CB and FB in the RS configuration for all the SNRs, however, CS is slightly better if NRS rather than the RS configurations are used.

The reconstruction of velocity for CS, CB, and FB using 33 receivers in the US configuration is shown in Fig. 4.25 for one realization. It is clear that CS, CB, and FB

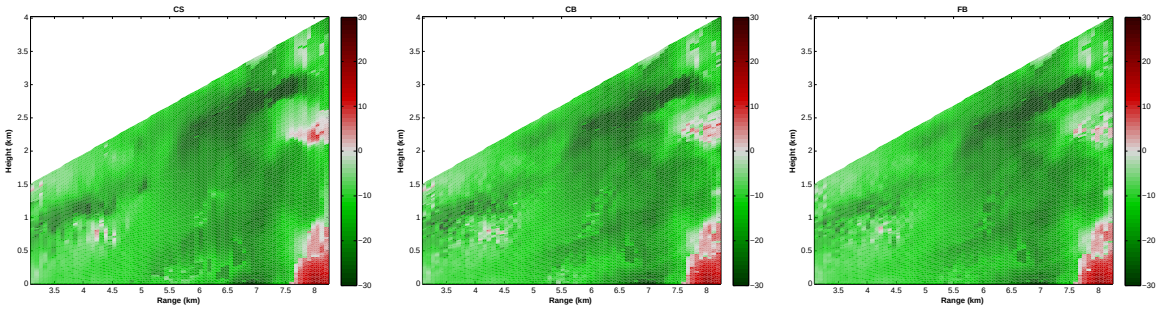

(a) SNR=0 dB

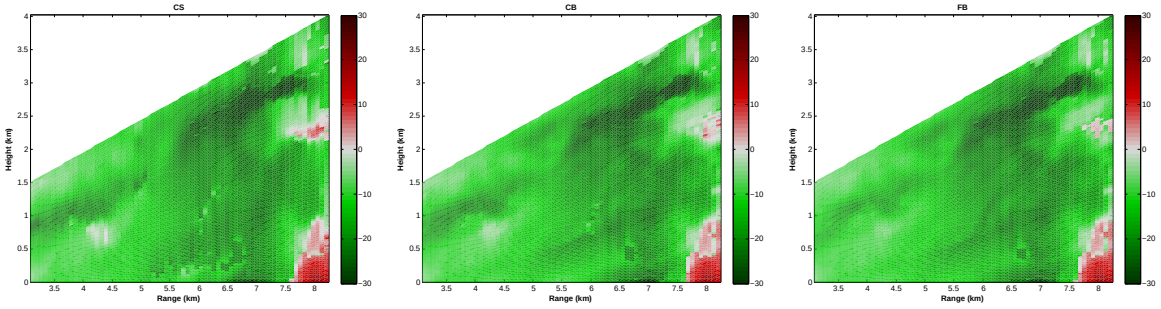

(b) SNR=10 dB

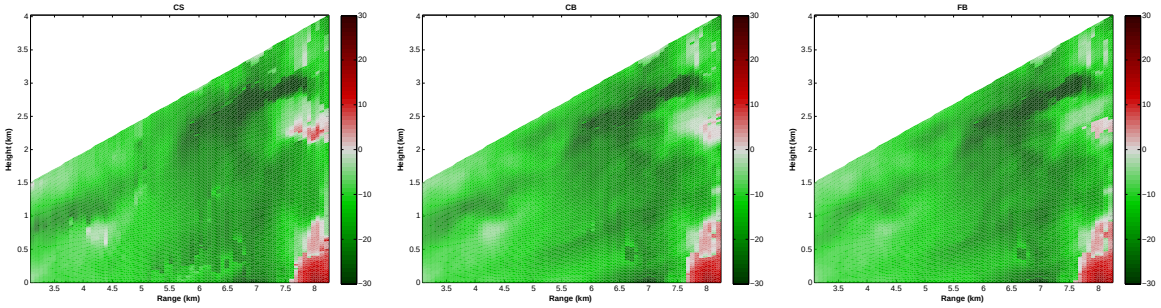

(c) SNR=20 dB

Figure 4.25: CS (left), CB (middle), and FB (right) velocity reconstruction with 33 receivers and 1024 samples using the US configuration for SNR=0 dB (first row), SNR=10 dB (second row), and SNR=20 dB (last row)

grossly reconstruct velocity in US for all the SNRs, and the performance is improved as SNR increases. The large errors come from the low reflectivity Regions of III and IV when SNR is relatively high, and from Region I and V when the SNR is low.

The velocity reconstruction of CS, CB, and FB is qualitatively similar for the given SNR case using the US configuration. However, CB and FB have better recovery of the upper side of the velocity structure between 5 and 7.5 km in range than CS at SNR=10 and 20 dB.

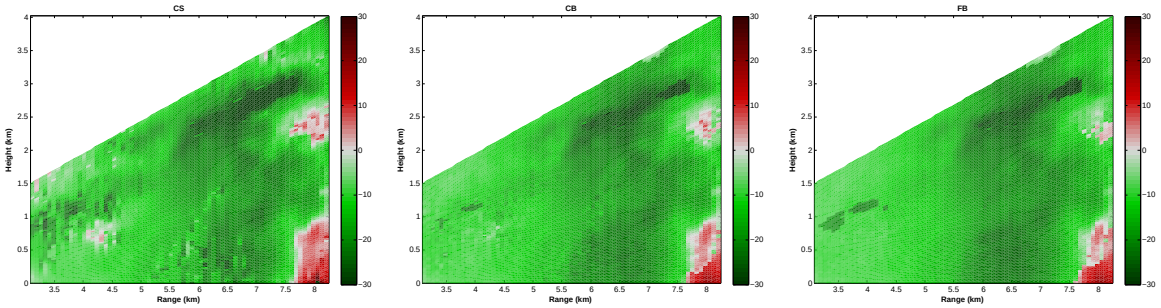

(a) SNR =0 dB

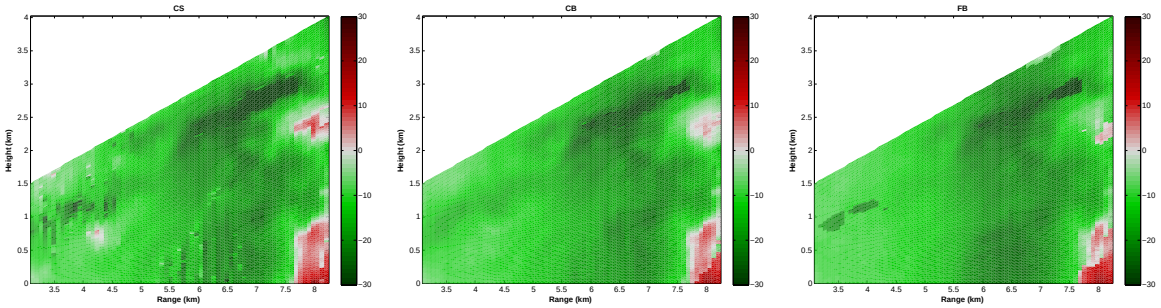

(b) SNR =10 dB

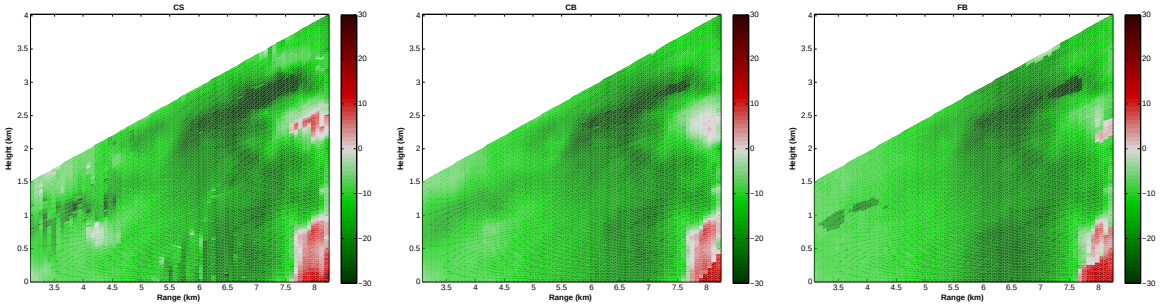

(c) SNR =20 dB

Figure 4.26: CS (left), CB (middle), FB (right) velocity reconstruction with 33 receivers and 1024 samples using NRS configuration for SNR is 0 dB (first row), SNR is 10 dB (second row) and SNR = 20 dB (last row)

On the other hand, CS has better performance than CB and FB using NRS configuration at SNR = 0 dB, for the range is less than 5 km in Fig. 4.26. As SNR increases, CB performance improves more than FB. Further, CB velocity estimation becomes better than CS at SNR = 20 dB. The velocity structure at range is less than 5 km (Regions I and II) is poorly reconstructed from FB using NRS configuration.

CS, CB, and FB grossly reconstruct velocity using the RS configuration with 33 receivers, but CS and CB estimations are better than FB. Further, CS performs better than CB using RS configuration, and the velocity in Regions I and II is recovered better using CS than using CB. In CS reconstruction there is not significant improvement as SNR increases from 0 to 20 dB. Example profiles of CS, CB, and FB velocity estimates from one realization of SNR=0, 10, and 20 dB for three different configurations is provided in Fig. 4.28. The velocity profile is at the same range of 6.2 km as the reflectivity profile in Fig. 4.23. It is clear that CS, CB, and FB grossly reconstruct velocity profile in the three configurations. CS and CB have velocity aliasing, and CS especially has sharp peaks on the reconstruction because of the imperfection of dealiasing process by using a 10 ms^{-1} threshold. It also indicates that CS has more aliasing in the reconstruction for this case, where low model reflectivity can be observed in Region III. CB and CS velocity reconstructions has more agreement with the velocity profile than FB in NRS and RS. Another velocity profile of CS, CB, and FB from one realization of the SNR=0, 10 and 20 dB for three different configuration is provided in Fig 4.29. Again, the range location of the velocity profile is

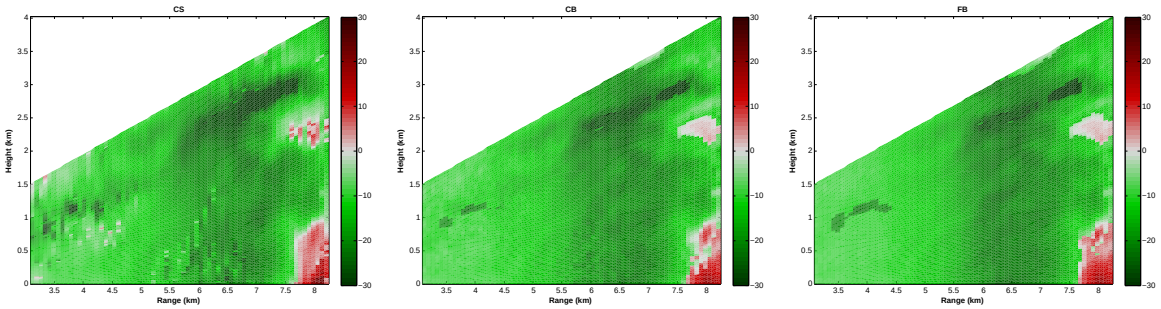

(a) SNR=0 dB

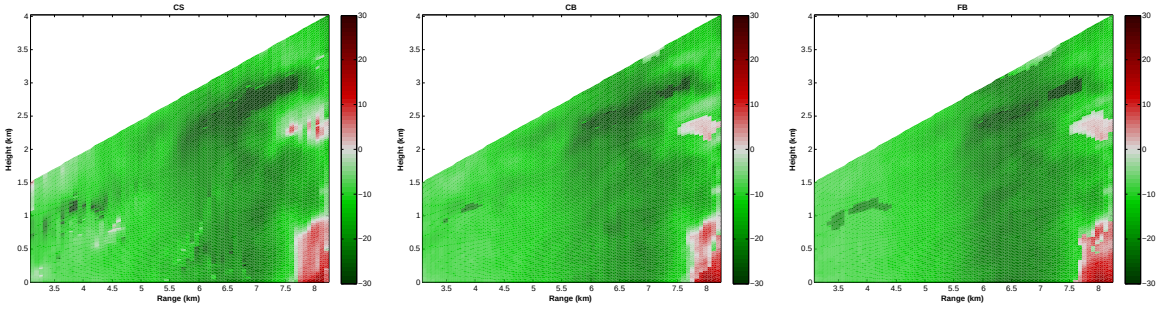

(b) SNR=10 dB

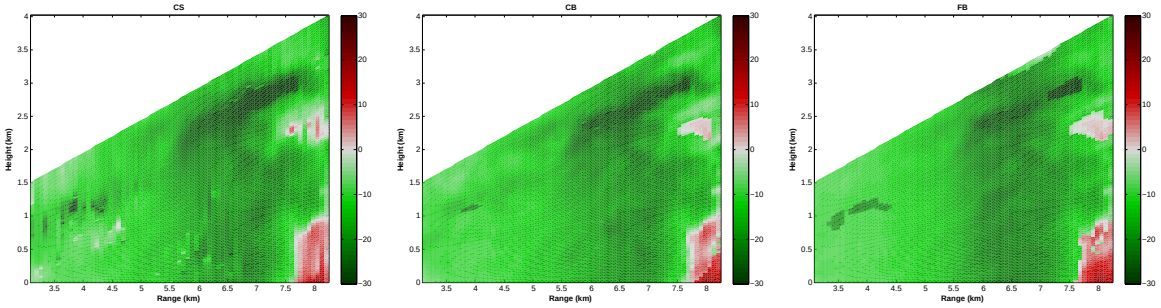

(c) SNR=20 dB

Figure 4.27: CS (left), CB (middle), and FB (right) reflectivity reconstruction with 33 receivers and 1024 samples using the RS configuration for SNR=0 dB (first row), SNR=10 dB (second row), and SNR=20 dB (last row)

the same as the reflectivity profile at range 7.42 km as shown in Fig. 4.22, where the reflectivity has relatively higher values at lower altitudes. CS, CB, and FB produce similar velocity estimation and the reconstructions have similar agreement with the

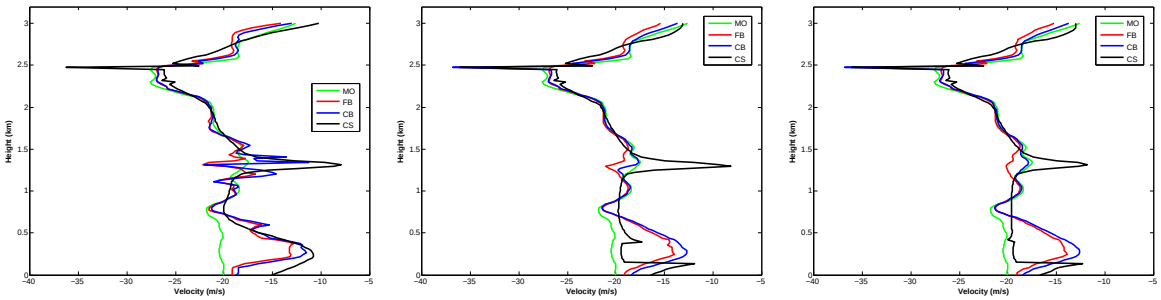

(a) Uniform spacing

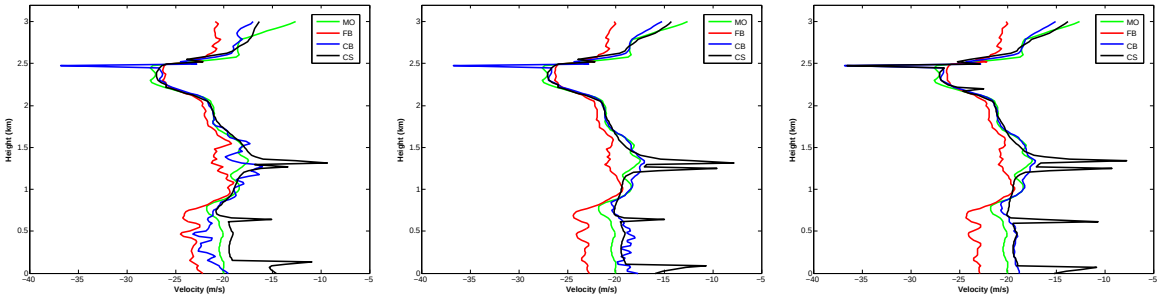

(b) Nonredundant spacing

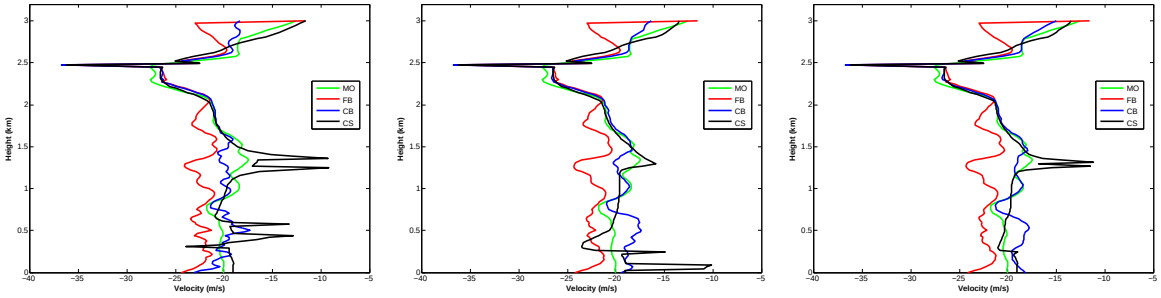

(c) Random spacing

Figure 4.28: CS (black), CB (blue), and FB (red) velocity reconstruction profile with SNR=0 dB (left panel), SNR=10 dB (midlle panel), and SNR=20 dB (right panel). The number of receiver is 33 and the number of samples is 1024.

true velocity profile given the SNR and receiver configuration. The velocity profile in Fig. 4.29 at 7.42 is estimated more accurately compared to the velocity profile in Fig. 4.28 at range 6.2. It can be said that the recovered velocity structure for CS, CB, and FB are not affected much especially for the regions of high reflectivity when

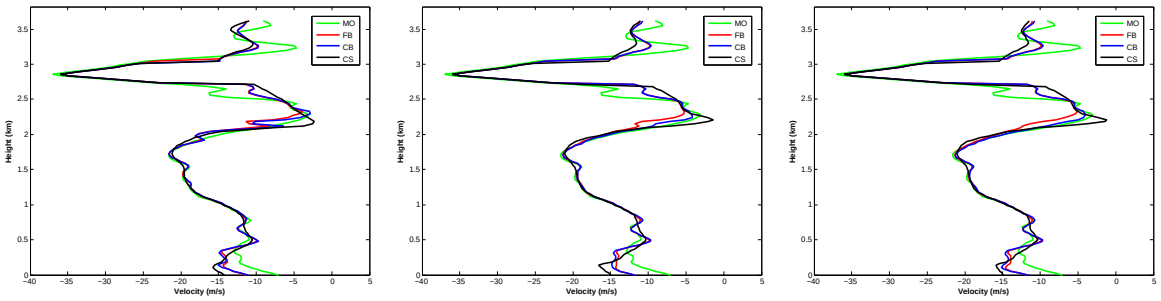

(a) Uniform spacing

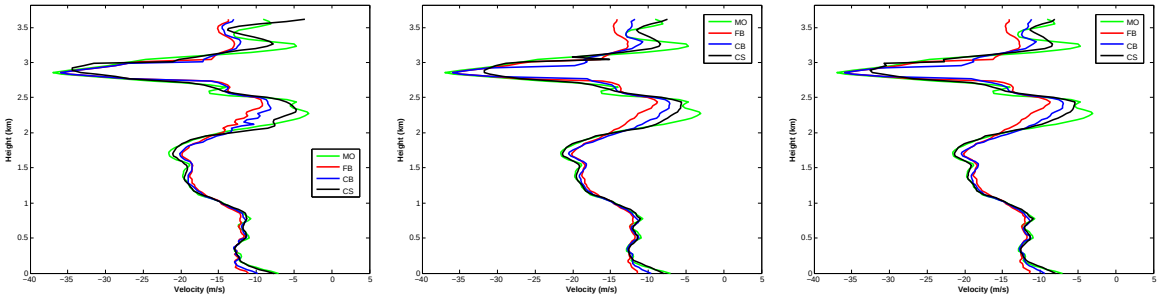

(b) Nonredundant spacing

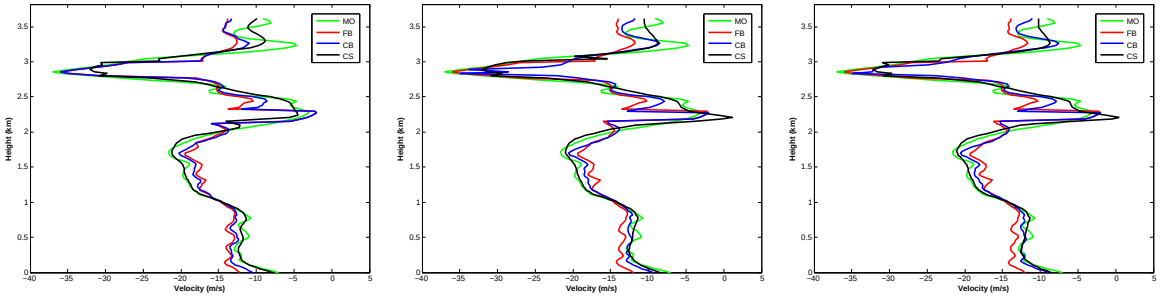

(c) Random spacing

Figure 4.29: CS (black), CB (blue), and FB (red) velocity reconstruction profile with SNR=0 dB (left panel), SNR=10 dB (midlle panel), and SNR=20 dB (right panel). The number of receivers is 33 and the number of samples is 1024.

SNR decreases, since the noise is theoretically uncorrelated from sample to sample at lag 1.

4.7.3.2 Impact of number receivers

The impact of the number of receivers on reflectivity and velocity reconstruction are studied by using receiver numbers of 17, 33, and 65. The mean of RMSE as function of number of receivers for CS, CB, and FB reflectivity estimation is shown in Fig. 4.30.

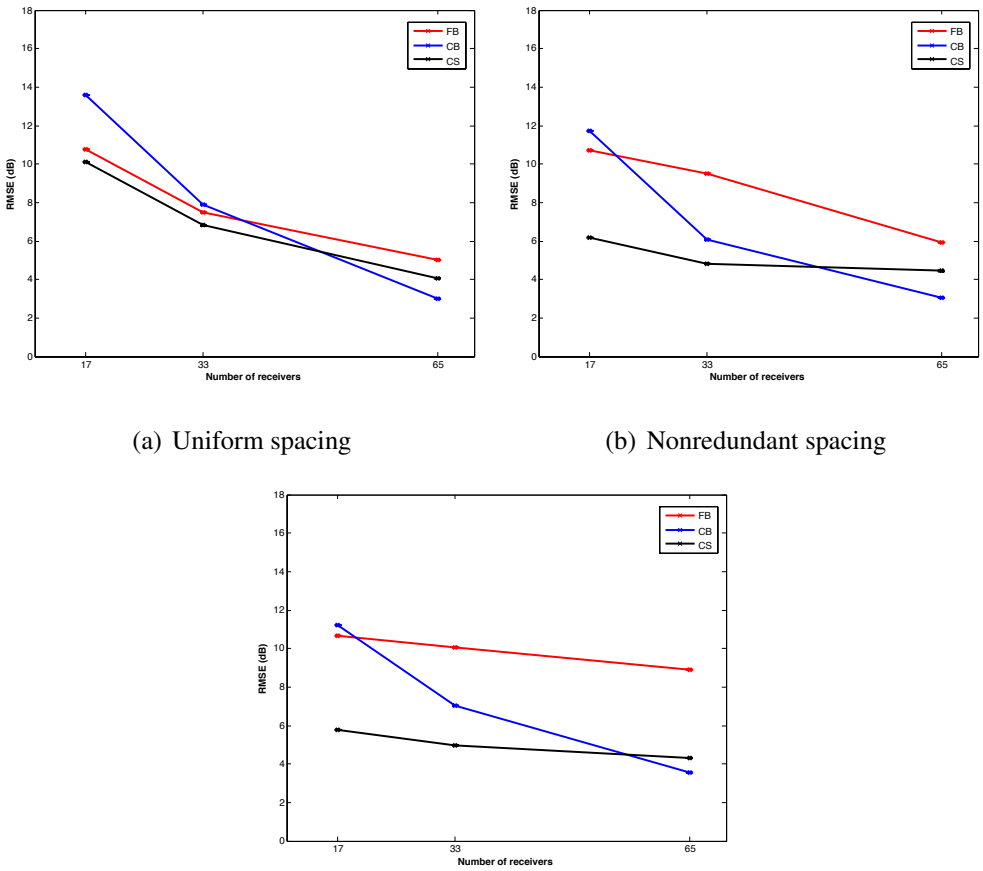

(a) Uniform spacing

(b) Nonredundant spacing

(c) Random spacing

Figure 4.30: The mean of RMSE as function of number of receivers for CS (black), CB (blue), FB (red) for the ARPS model reflectivity estimation. 33 receivers, SNR = 30 dB and the number of samples 1024.

The improvement of CS, CB, and FB as a function of number of receivers can be observed for three receiver configurations. It can be observed that the improvement of CB performance as the receiver number increases is more significant than both FB and CS for all three receiver configurations. For CS, the improvement with the NRS and RS configurations is not as evident as the one with US configuration. In NRS and RS, the rank of measurement matrix $\mathbf{H_p}$ from 17 to 65 receivers are almost the same. Additionally, the coherence for 17, 33, and 65 receivers is quite similar as shown in Table 4.2. In the US configuration, the rank of $\mathbf{H_p}$ increases from 17 to 53 as the number of receivers increases from 17 to 65 receivers, due to the redundancy of measurement vectors in $\mathbf{H_p}$. In other words, given a smaller number of receivers like 17, CS has the potential to perform better with NRS and RS than US. In contrast to CS, FB has the lower RMSE in US than in the NRS and RS receiver configurations, because of higher sidelobes in RS and NRS. For 65 receivers, CB provides the best performance among the three methods for all three configurations given the high SNR and the large number of samples in this case. Additionally, CB performance for the NRS and US configurations is similar and is slightly better than with RS for 65 receivers.

Examples of CS, CB, and FB estimations from one realization of 17, 33, and 65 receivers for the US configuration are provided in Fig. 4.31. Note that the model of reflectivity is presented in Fig. 4.17. It is clear that the reflectivity structure is reasonably reconstructed using CS, CB, and FB with 33 and 65 receivers at an SNR

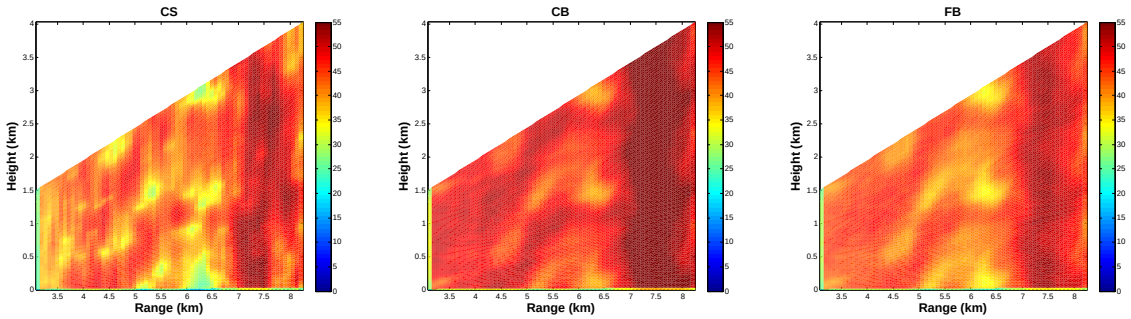

(a) N = 17

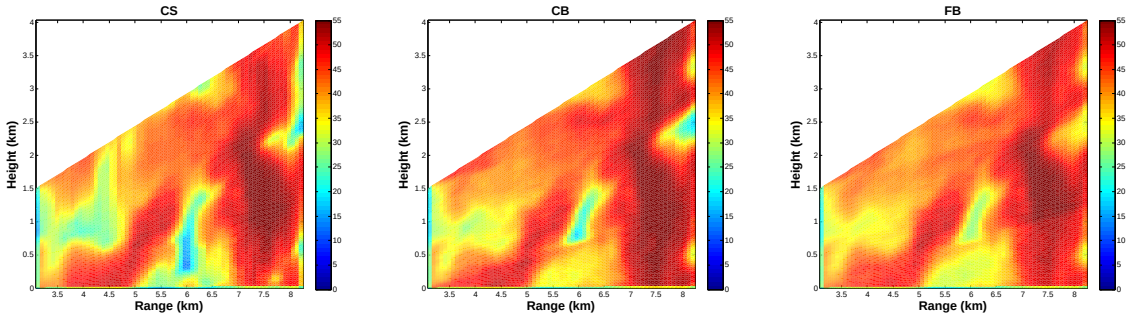

(b) N = 33

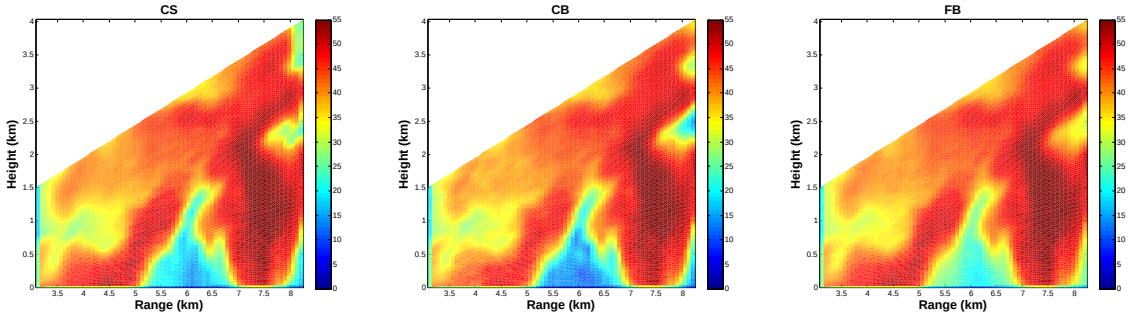

(c) N= 65

Figure 4.31: CS (left), CB (middle), and FB (right) reflectivity reconstruction profile with 17, 33, and 65 receivers using US configuration. SNR=30 dB and the number of samples is 1024.

of 30 dB. By increasing the number of receivers, the recovery of Regions I to V is improved for CS, CB, and FB. Reconstruction of CS, CB, and FB using 17 receivers cannot distinguish the reflectivity structures clearly, where grating lobes occur at about 14^o. CS, CB, and FB have similar reconstruction with 65 receivers, and CB

produces lower reflectivity in Region III than CS or FB. Reflectivity in Regions I, II, and IV are reasonably estimated from three methods using US configuration. CS reconstructs Region III better than CB and FB using 33 receivers as shown in Fig. 4.31. However, CS cannot clearly distinguish the two regions of IV and V, while FB and CB provide better results.

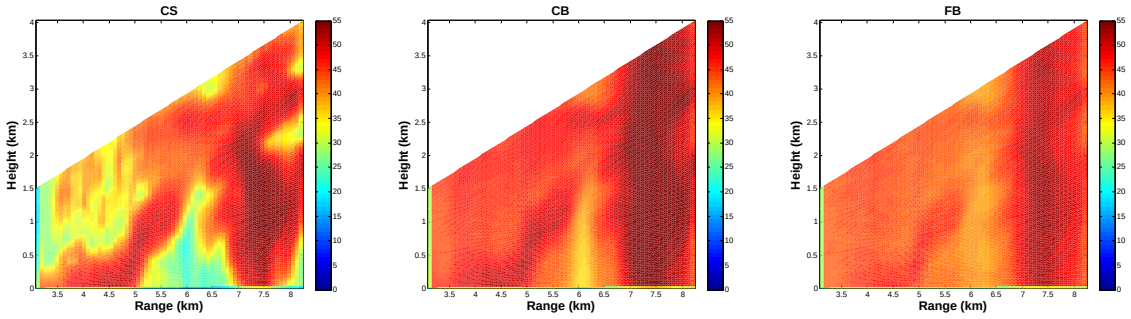

(a) N = 17

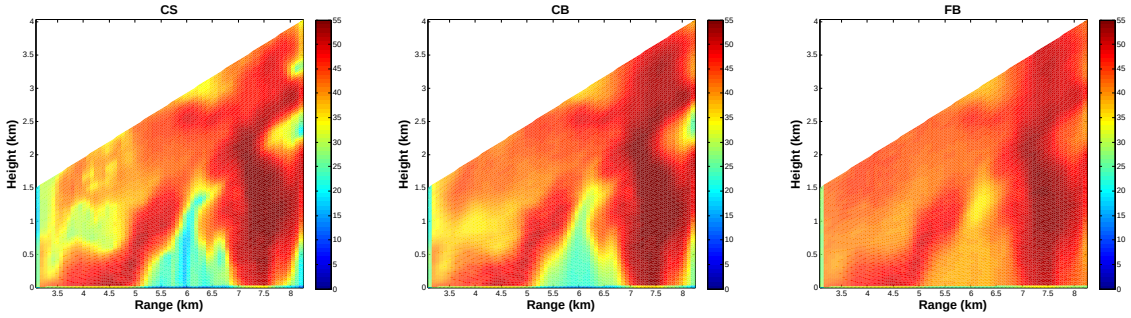

(b) N = 33

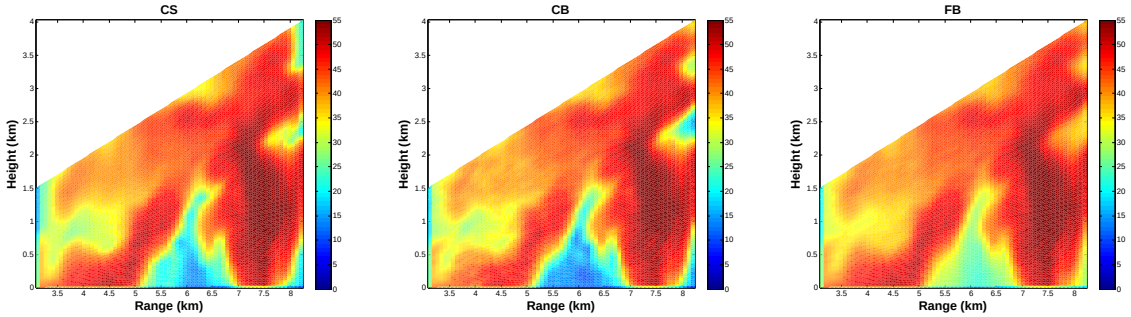

(c) N= 65

Figure 4.32: same as Fig. 4.31 but for NRS receiver configuration.

In the NRS configuration, CS is capable of reconstructing reflectivities reasonably well in all regions with only receivers, where CB and FB have indication of the structure of Region II and III in Fig. 4.32. The reconstructions of CS, CB and FB become qualitatively better as the receiver number increases. Five regions (I to V) are resolved accurately using CS with 33 receivers, whereas CB did not resolve Region V and has slightly indication of the structure of Region I. FB is not capable of resolving regions clearly using 33 receivers in the NRS configuration in Fig. 4.32. Using 65 receivers, CS, CB, and FB are able to recover five regions, where the regions are more obvious in CS and CB reconstructions than FB.

Similarly, CS with RS and 17 receivers can resolve the reflectivity grossly, but not the detail structures. CB and FB have a slight indication of structures only in Regions II and III. As the number of receivers increases from 17 to 65, the reconstruction of CS and CB improves qualitatively, and the regions become more obvious. The reconstruction of CS using 33 receivers is better than CB and FB, where Regions I, IV, and V are resolved more clearly in CS in Fig. 4.33. CS and CB reconstruction with 65 receivers is similar in the RS configuration. Note that the additional receivers can provide better reconstruction for the three methods. It is important to point out that CS performs better than CB and FB by using 17 and 33 receivers in the NRS and RS receiver configurations.

Examples of CS, CB, and FB reflectivity reconstruction profiles from 17, 33, and 65 receivers for three configurations are provided in Fig. 4.34 and Fig. 4.35, where

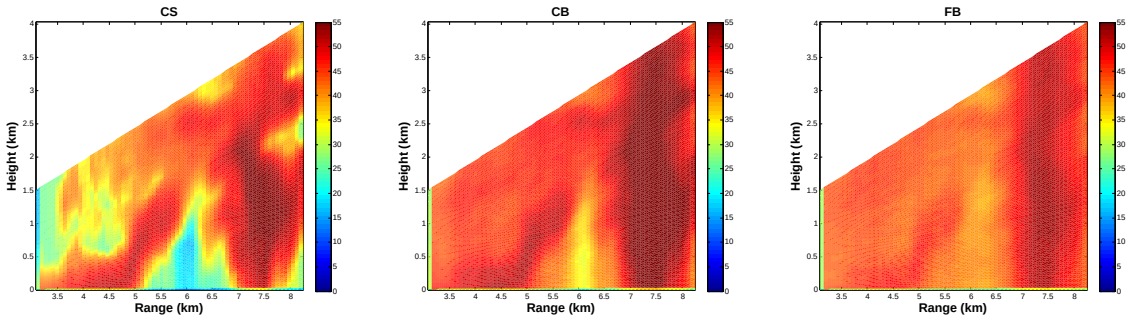

(a) N = 17

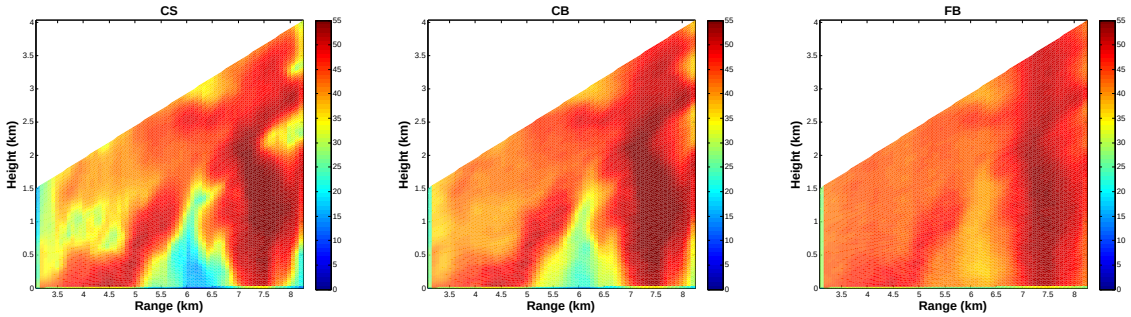

(b) N = 33

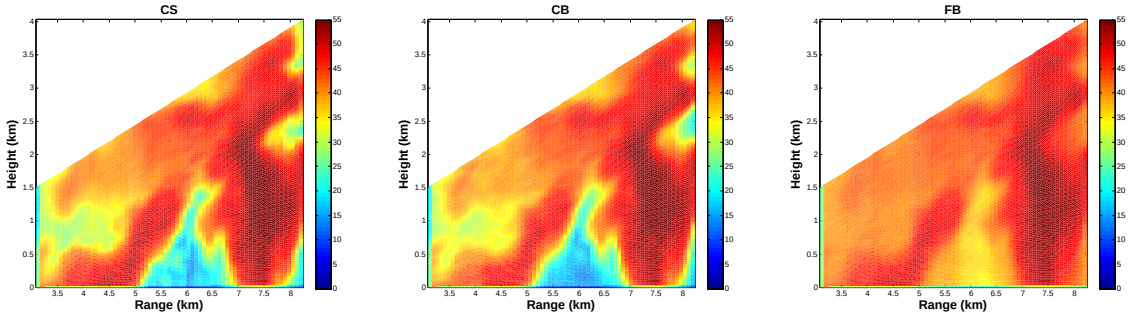

(c) N = 65

Figure 4.33: same as Fig. 4.31 but for RS receiver configuration

the profiles are obtained at a range of 6.15 km and 7.42 km, respectively. The improvement on the reconstruction of the reflectivity with a Gaussian shape centered at a height of 1 km is obvious for CS and CB in the three configurations as the receiver numbers increase in Fig. 4.34. The improvement on FB reconstruction can be observed in US and NRS more clearly. The single Gaussian reflectivity at 1 km is

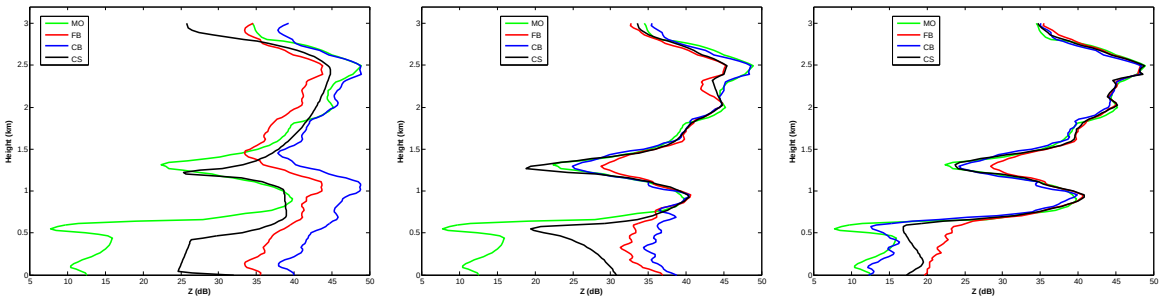

(a) Uniform spacing

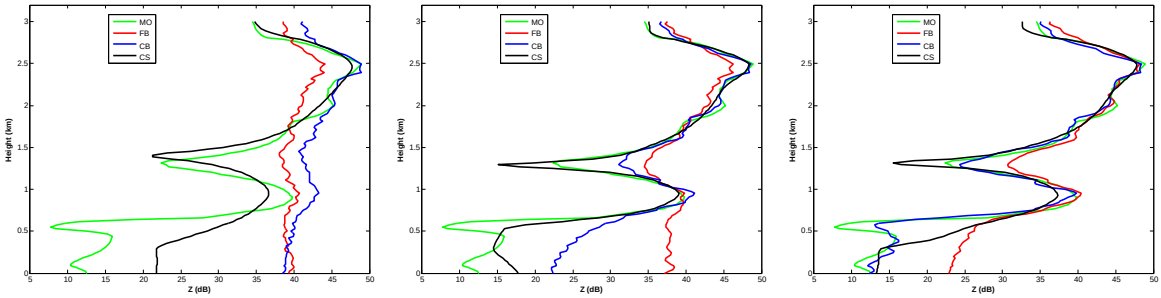

(b) Nonredundant spacing

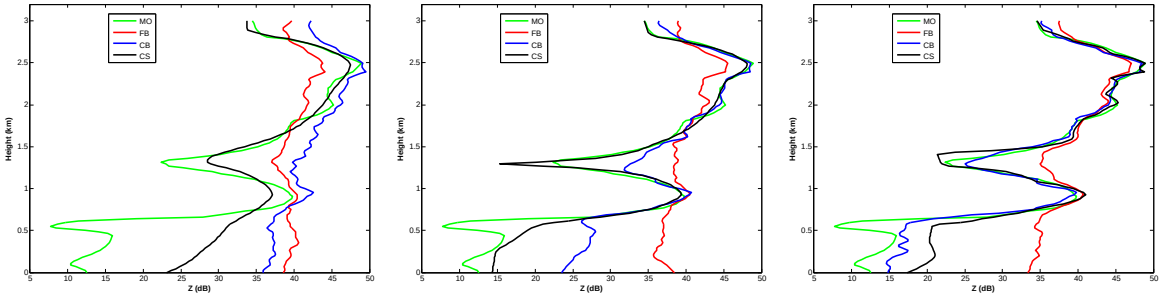

(c) Random spacing

Figure 4.34: CS (black), CB (blue), and FB (red) reflectivity reconstruction profile with 17 (left panel), 33 (middle panel), and 65 (right panel) receivers. The number of samples is 1024 and SNR=30 dB.

resolved better with CS than with CB and FB using 33 receivers in the three configurations. On the other hand, CB can resolve the small single Gaussian reflectivity at a height of 0.4 km using 65 receivers in US and NRS, where CS can only resolve it in US and RS configurations. FB does not show any indication for resolving the small

single Gaussian at 0.4 km. The grating lobe effect can be observed easily in the US configuration with 17 receivers in both Figs. 4.34 and 4.35, where the reflectivity between 1.5 and 3 km is exactly repeated from 0 to 1.5 km in CB and FB. However, in CS, the single Gaussian at 1 km is estimated with a wide width and are able to be separated from the reflectivity structure between 1.5 and 3 km, where CB and FB are not.

Similarly, the repetition in the reflectivity structures can be observed for CB and FB in Fig. 4.35 using the US configuration of 17 receivers, where CS produces a totally different estimation. It is clear that the reconstruction of the small valley at a height of 3 km is better resolved using CS than CB or FB, where the reconstruction difference is more evident in 17 receivers in NRS and RS than US. It is important to point out that CS is able to provide a larger dynamic range than CB and FB in all three configurations of 17, 33, and 65 receivers. Note that CS is also able to recover the dual Gaussians at the 2.5 and 3 km height by using NRS with 17 receivers, and the recovery becomes more accurate by increasing the number of receivers. However, CB and FB can reconstruct them accurately using 65 receivers in all three configurations. The CB result shows an indication of the dual Gaussians in the NRS and RS configurations with 33 receivers. CS, CB, and FB do not resolve the dual Gaussians for the US configuration of 33 receivers.

Error analysis in range for compressibility of reflectivity structures

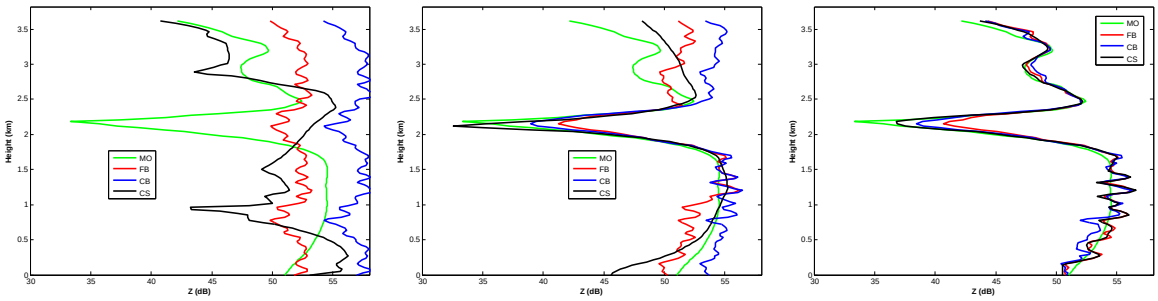

(a) Uniform spacing

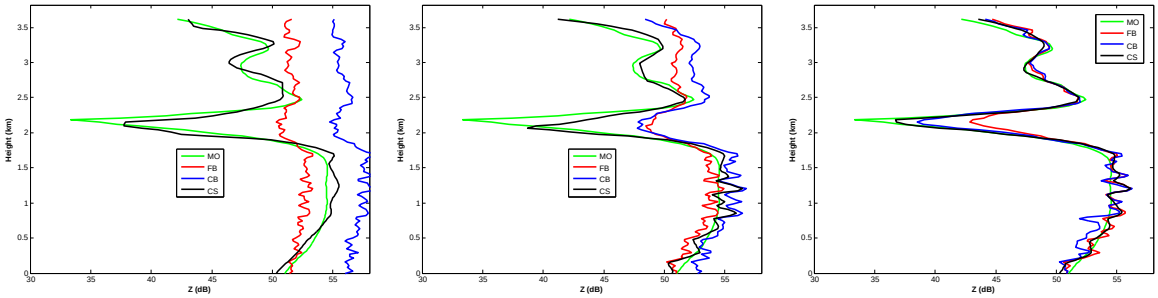

(b) Nonredundant spacing

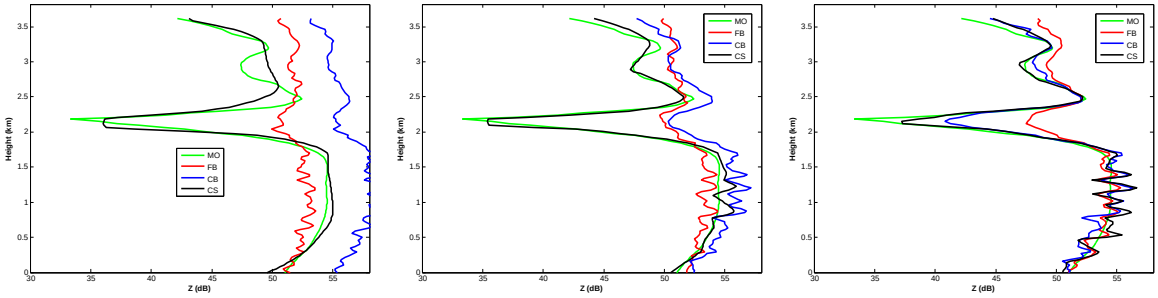

(c) Random spacing

Figure 4.35: CS (black), CB (blue), and FB (red) reflectivity reconstruction profile with 17 (left panel), 33 (middle panel), and 65 (right panel) receivers. The number of samples is 1024 and SNR=30 dB. The location of the reflectivity profile is at 7.42 km in range.

In order to show the impact of compressibility on the CS reflectivity estimation, the mean RMSE of CS reconstruction as a function of range is shown in Fig. 4.36 for the three receiver configurations of 17, 33, and 65 receivers. The mean RMSE is calculated over each height profile. The compressibility index of reflectivity profiles

was shown in Fig. 4.4(c). Note that the higher compressibility index indicates a low compressible image. Furthermore, the coherence values for the three receiver configurations and for the number of receivers 17, 33, and 65 is shown in Table 4.2 for reflectivity estimation. The coherences for the given cases were close and around approximately 0.5, given the theoretical value between 0 and 1. Since the coherence for all conditions is similar, the performance of CS is expected to largely depend on the compressibility index.

The mean RMSE of CS increases as the compressibility index increases in Fig. 4.36 for all three configurations. A large RMSE value obtained between 5 - 7 km and 8 - 9 km ranges, where the reflectivity profiles are more compressible relatively ranging from 3 - 5 km and 7 - 8 km than the reflectivity models in the 5 - 7 km and 8 - 9 km ranges. Interestingly, CB and FB have a RMSE curve trend similar to CS. Generally, when the number of receivers increases the variation on RMSE over a range decreases for CS and CB for the three receiver configurations. The mean RMSE of CS and CB in NRS and RS is similar for the given number of receivers. Another comparison can be made between the receiver configurations by considering the rank differences. For example, if we compare the mean error between 5.3 km - 6.5 km in US, NRS, and RS, the computed errors are 8.18 for US, 6.72 for NRS, and 5.47 for RS for 33 receivers. The rank of $\mathbf{H_p}$ was 33, 54, and 53 for US, NRS, and RS respectively for 33 receivers. Additionally, the computed coherence was 0.51, 0.48, and 0.46 for US, NRS, and RS respectively for 33 receivers. As the rank increases

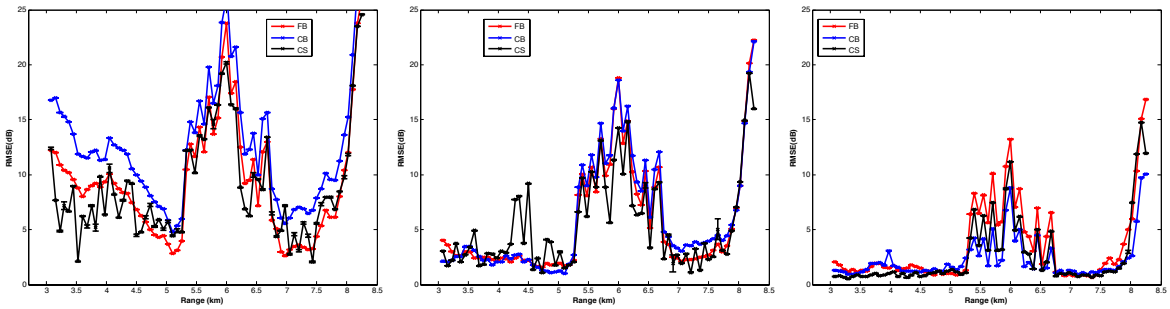

(a) Uniform spacing

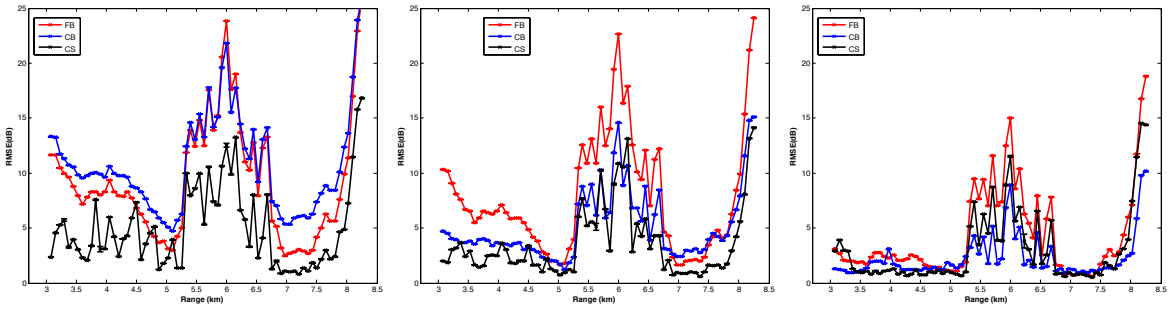

(b) Nonredundant spacing

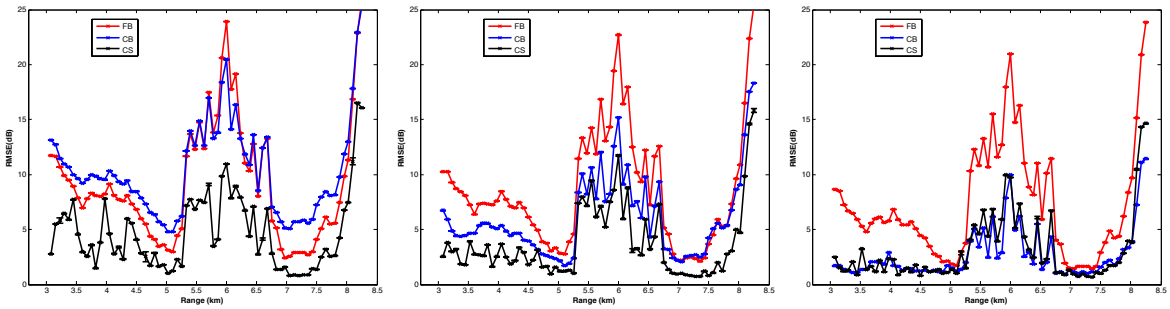

(c) Random spacing

Figure 4.36: The mean of RMSE for CS (black), CB (blue), and FB (red) with the number of receivers as 17 (left panel), 33 (middle panel), and 65 (right panel) using SNR=30 dB and 1024 samples.

from the US to RS configurations, the mean RMSE decreases. It suggests that the performance of CS also depends on the rank for the same sparsity image, but since the coherence value is quite similar, it is difficult to assess.

Number of receivers impact on velocity estimation

The impact of the receiver number on velocity estimation is studied using ARPS model velocity. Here again, the velocity is dealiased by using a 10 ms^{-1} threshold if the velocity aliasing is detected. The mean of RMSE as a function of receiver numbers for CS, CB, and FB velocity estimation is shown in Fig. 4.37. All three methods with US, NRS, and RS can be improved as the number of receivers increases. It is

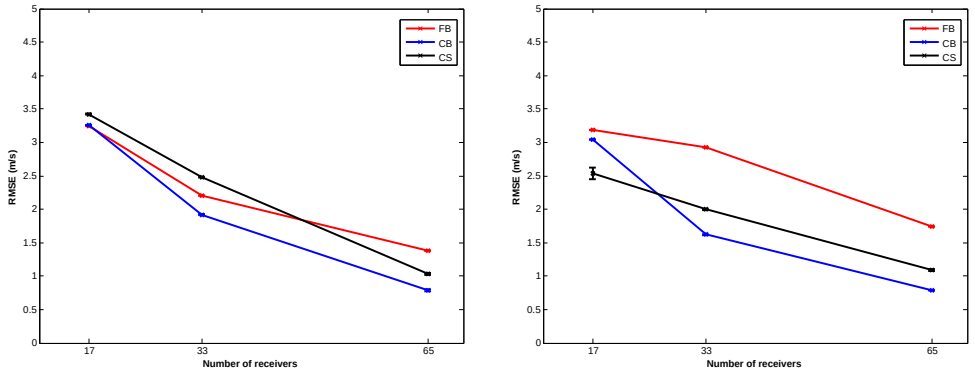

(a) Uniform spacing

(b) Nonredundant spacing

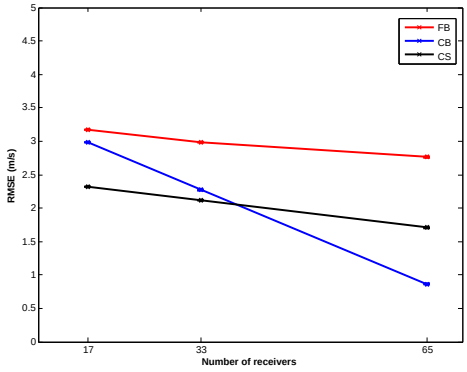

(c) Random spacing

Figure 4.37: The mean of RMSE as function of number of receivers for CS (black), CB (blue), FB (red) for the ARPS model velocity estimation. SNR = 30 dB and the number of samples 1024.

obvious that CB is capable of achieving a RMSE of less than 1 ms^{-1} for 65 receivers in all three configurations. The RMSE for CS with 65 receivers is about 1 ms^{-1}.

The performance of CS is better than FB, but worse than CB with 65 receivers in all three configurations for this case of high SNR=30 dB and a large number of samples (1024). In the RS configuration, CS performance is better than CB and FB using 17 and 33 receivers. Additionally, CS has better performance than CB and FB in NRS using 17 receivers. However, CB performs better than CS with 33 receivers in US and NRS configurations. FB performs better in US than NRS and RS configurations and achieves a RMSE of less than 2 ms^{-1} with 65 receivers.

Examples of CS, CB, and FB retrievals from one realization with the number of receivers 17, 33, and 65 for the US configuration is provided in Fig 4.38. Note that the reconstructed reflectivity is presented in Fig. 4.31. It is clear that the velocity structures are grossly reconstructed using CS, CB, and FB with all the given numbers of receivers at SNR = 30 dB. By increasing the number of receivers, the estimation of velocity in Regions I to V is improved for CS, CB, and FB. Additionally, even though all three methods have similar reconstruction results with 33 and 65 receivers, CB produces better estimation in Regions II and IV than CS or FB. CS has aliasing artifacts in Regions I and II, and the estimation in Region III is not clear as those using CB and FB in Fig. 4.38. CS has relatively large errors in Region IV using the US configuration of 33 and 65 receivers.

In the NRS configuration, CS is capable of resolving velocity in Regions I and II with 17 receivers, where CB and FB has only a slight indication of Region I in Fig. 4.39. The reconstructions of CS, CB, and FB become qualitatively better as

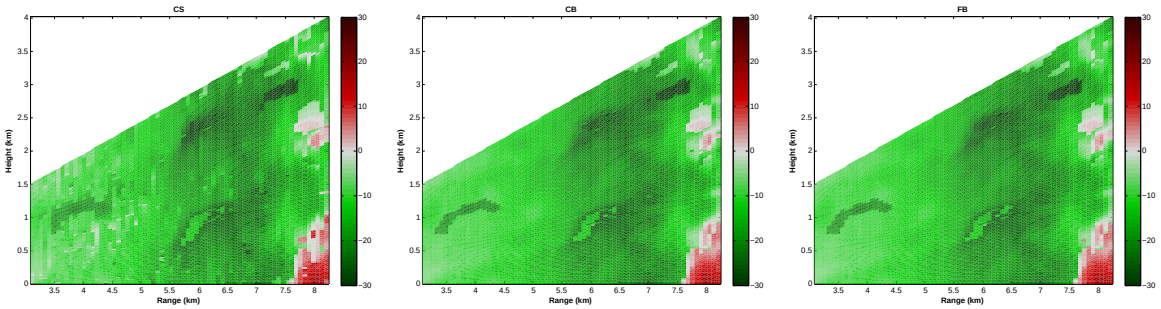

(a) N = 17

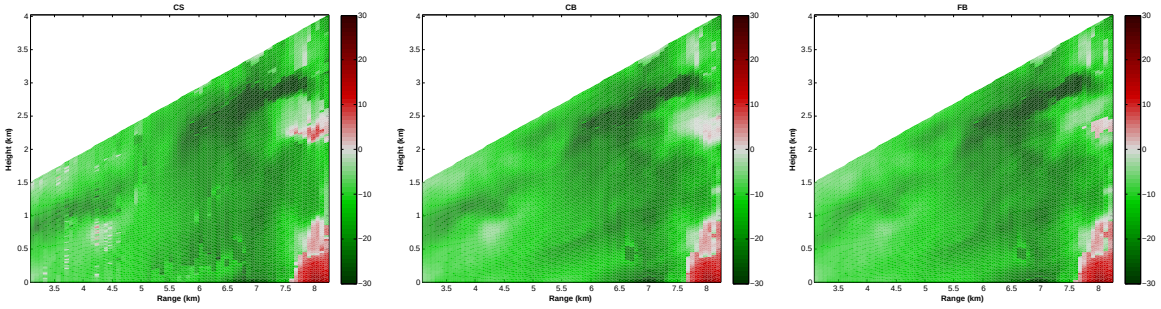

(b) N = 33

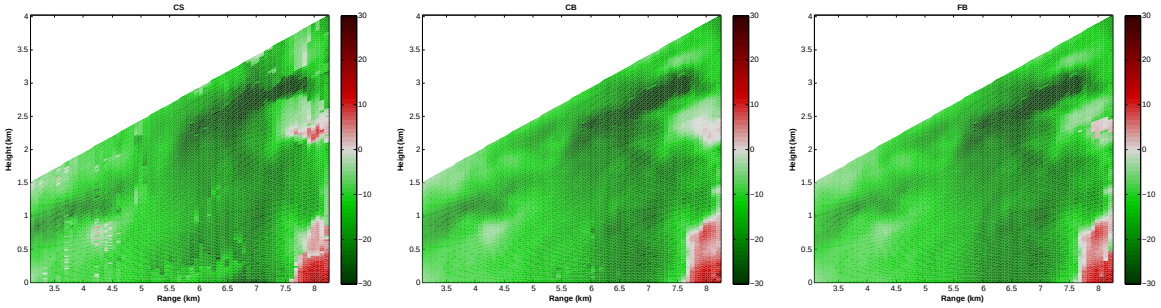

(c) N = 65

Figure 4.38: CS (left), CB (middle), and FB (right) reflectivity reconstruction profile with 17, 33, and 65 receivers using US configuration. SNR = 30 dB and the number of samples is 1024.

the receiver numbers increase. CS has large artifacts with 33 receivers at Region I, where CB provides a smoother result and FB is not able to resolve it. CS, CB, and FB have similar reconstruction with 65 receivers, where Region II has better agreement

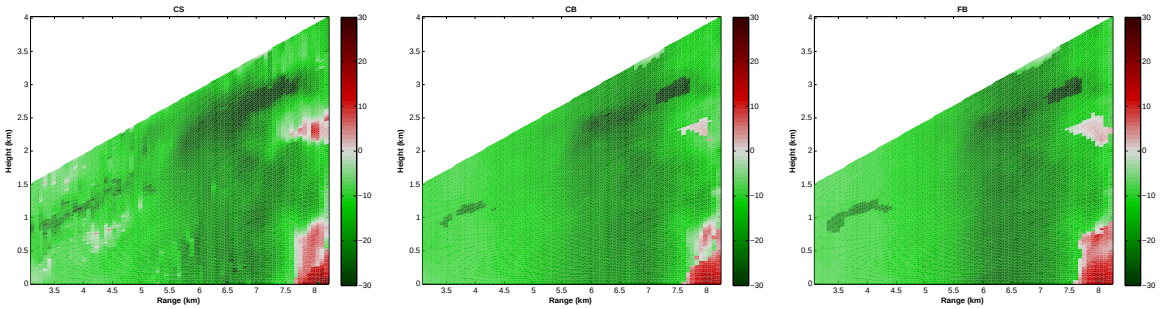

(a) N = 17

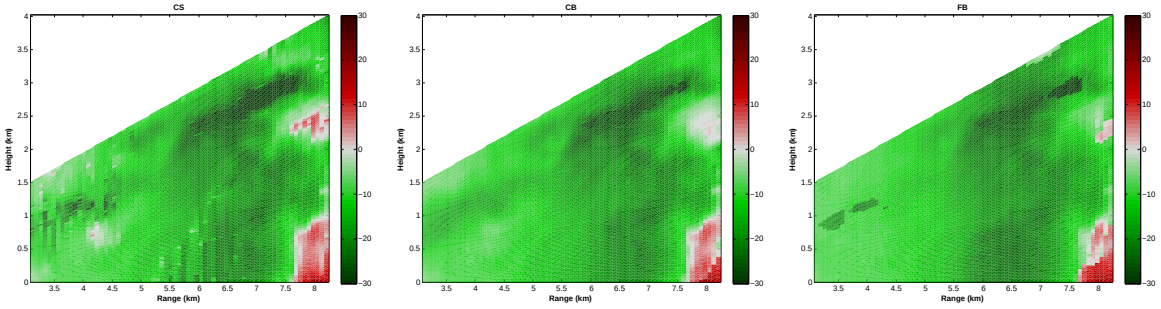

(b) N = 33

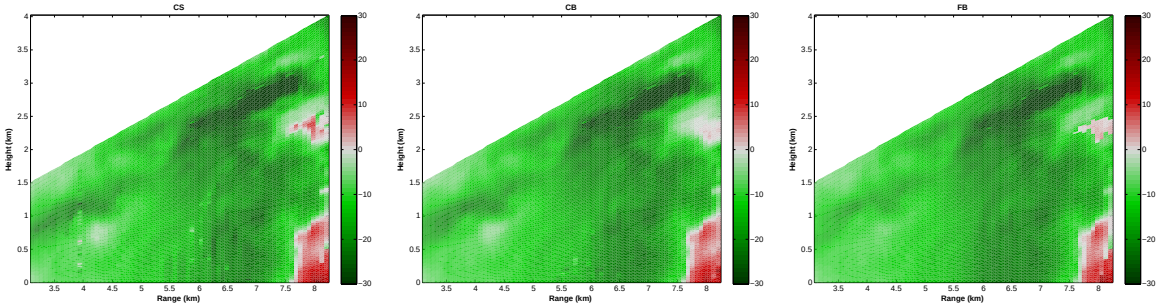

(c) N = 65

Figure 4.39: same as Fig. 4.38 but for NRS receiver configuration

with the model velocity. In CS, large errors occurs at Regions I, III and IV, which are associated with the low reflectivity values.

CS, CB, and FB grossly reconstruct velocity using the RS configuration with 17 and 33 receivers at SNR=30 dB, but CS and CB estimations are better than FB in Fig. 4.40. CS is able to recover velocity in Regions I and IV with 17 receivers,

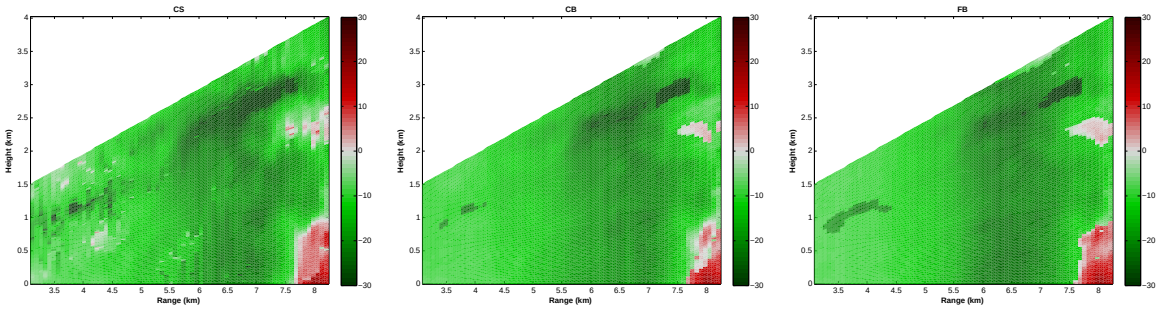

(a) N = 17

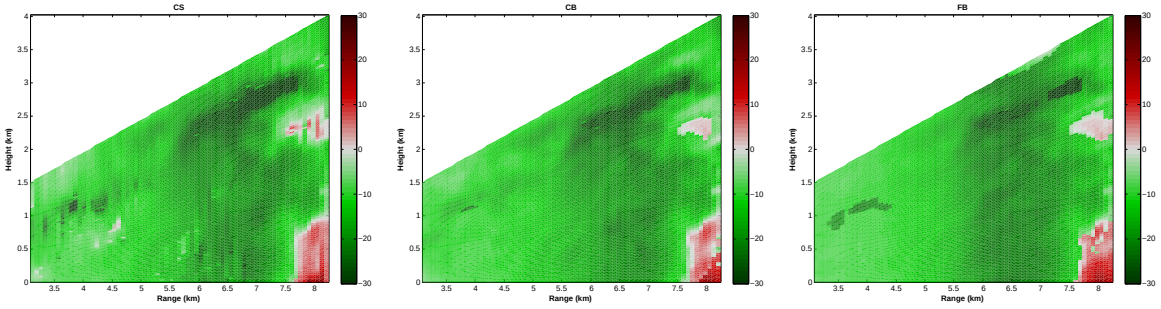

(b) N = 33

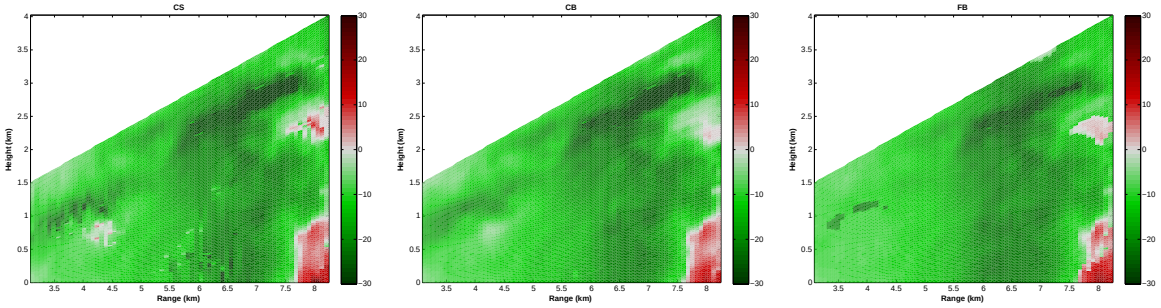

(c) N = 65

Figure 4.40: the same as Fig. 4.38 but for RS configuration.

although Region I looks noisy. CB and FB performed poorly in Regions I and IV; the details are not visually detectable. Additional receivers increase CB performance significantly in the RS configuration. The velocity estimation of CB is better than CS with 65 receivers, especially at Regions I, III and IV in Fig. 4.40.

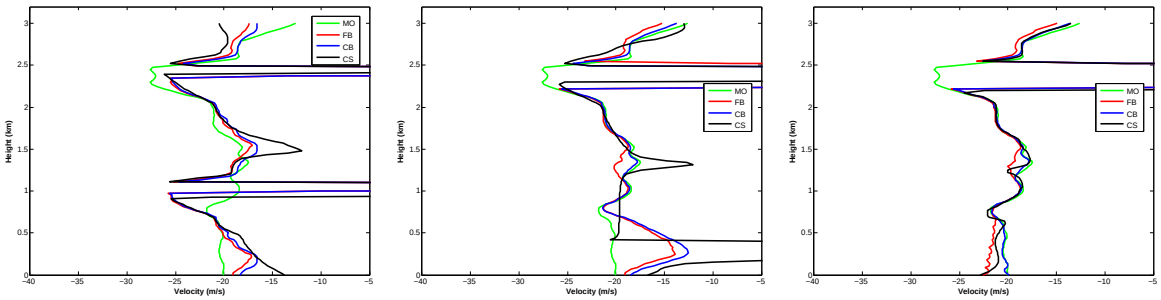

(a) Uniform spacing

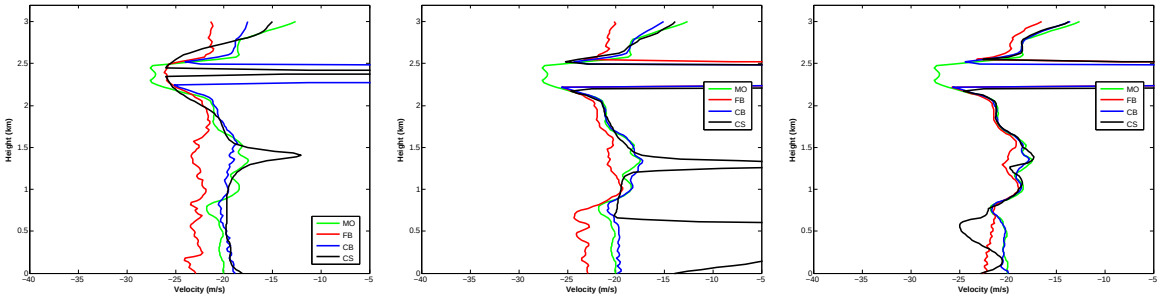

(b) Nonredundant spacing

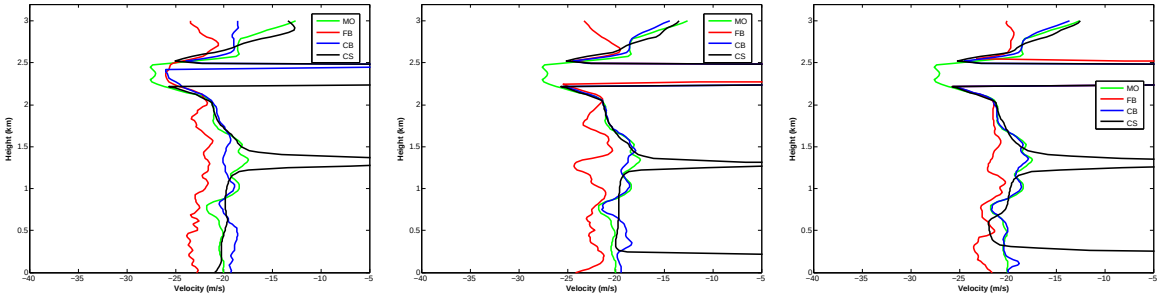

(c) Random spacing

Figure 4.41: CS (black), CB (blue), and FB (red) velocity reconstruction profile before dealiasing with SNR=30 dB. The numbers of receivers are 17 (left column), 33 (middle column), and 65 (right column), and the number of samples is 1024.

Example profiles of CS, CB, and FB velocity reconstruction from one realization of number of receivers 17, 33, and 65 at SNR=30 dB for three different configuration are provided before and after dealiasing process in Figs. 4.41 and 4.42, respectively. The velocity profile is at the same range with the reflectivity profile in Fig. 4.34 from

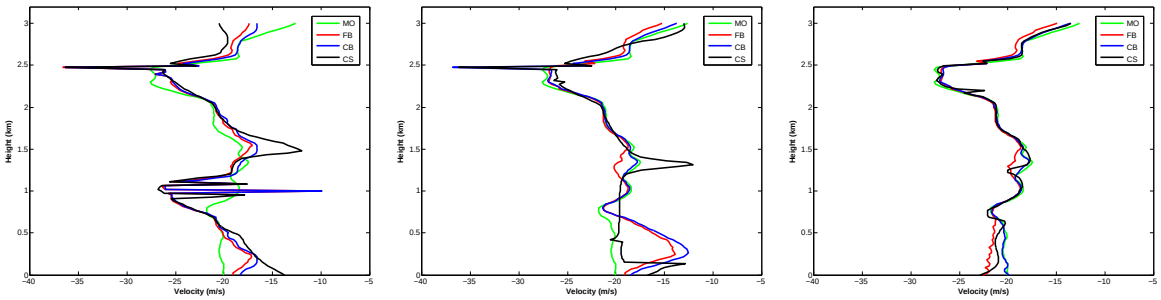

(a) Uniform spacing

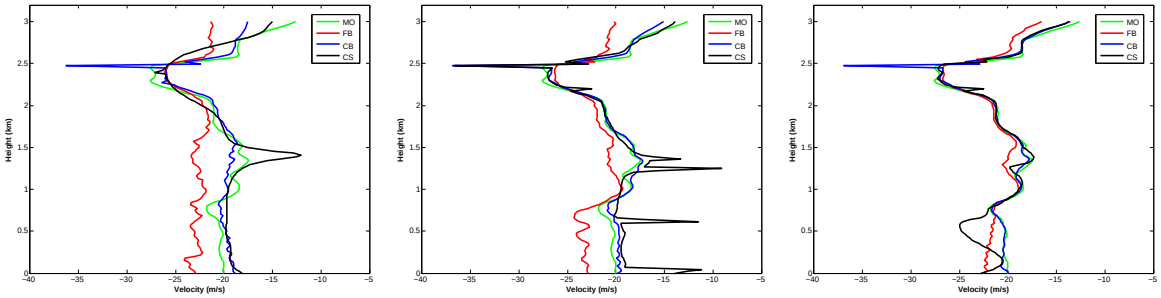

(b) Nonredundant spacing

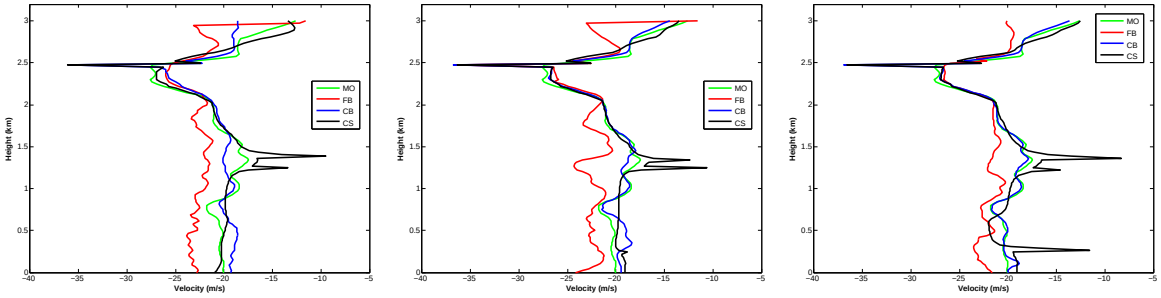

(c) Random spacing

Figure 4.42: CS (black), CB (blue), and FB (red) velocity reconstruction profile with SNR=30 dB. The numbers of receivers are 17 (left column), 33 (middle column), and 65 (right column), and the number of samples is 1024.

Region III. CS and CB have velocity aliasing issues and the sharp peaks remain on the reconstruction because of the imperfection of the dealiasing process by using a 10 ms^{-1} threshold. It is more obvious in RS for all number of receivers at 1.4 km and also in NRS with 33 receivers at 0.6 km and 1.4 km heights. CB and CS grossly

reconstruct velocity, even though aliasing velocity exists in all three configurations. CB has more agreement with the velocity profile than FB and CS in NRS and RS in this case.

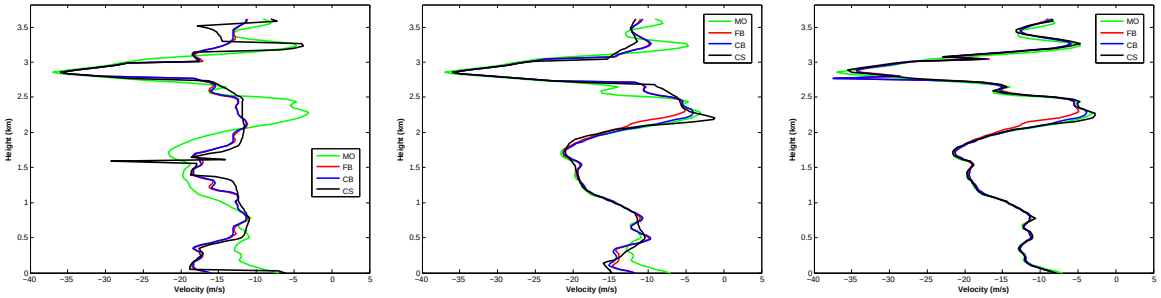

(a) Uniform spacing

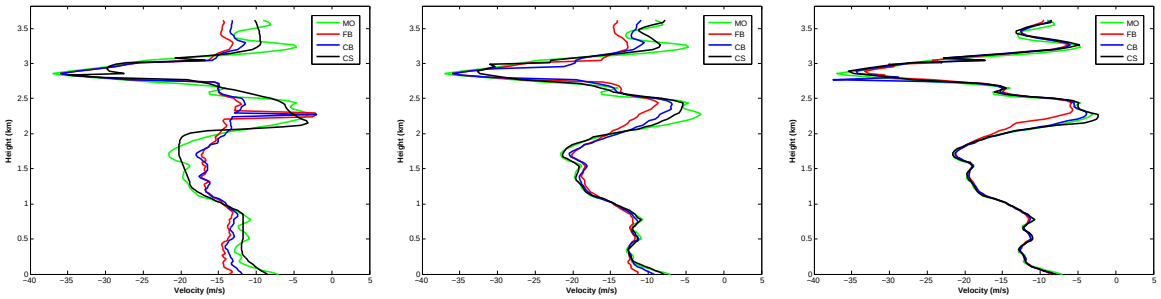

(b) Nonredundant spacing

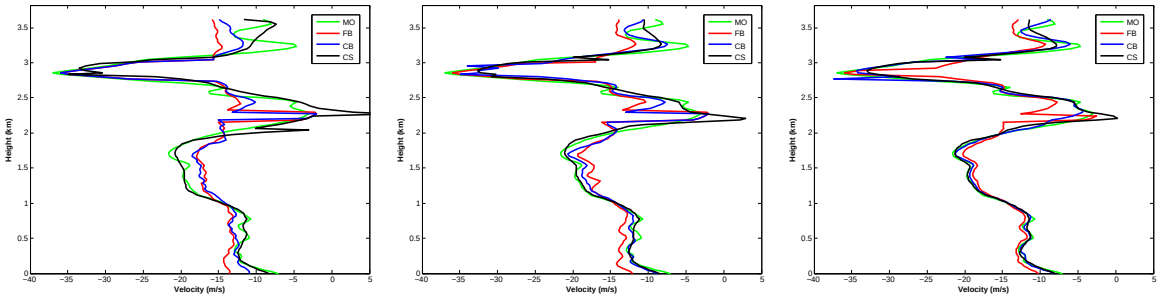

(c) Random spacing

Figure 4.43: CS (black), CB (blue), and FB (red) velocity reconstruction profile with SNR=30 dB. The numbers of receivers are 17, 33, and 65, and the number of samples is 1024.

Another velocity profile of CS, CB, and FB from one realization with 17, 33, and 65 receivers for three different configurations is provided in Fig. 4.43. Again, the

range location of the velocity profile is the same as the reflectivity profile as shown in Fig. 4.35, where the reflectivity has relatively higher values at lower altitudes. In the US configuration, the reconstruction of velocity for CS, CB, and FB is similar with 17, 33, and 65 receivers. In NRS, CS has a distinct difference at 1.5 and 2.3 km from CB and FB, and the estimation is better. In RS and other cases in Fig 4.43, the difference between the estimation of CS, CB, and FB is small and they have similar agreement with the model velocity at 30 dB SNR.

4.7.3.3 Impact of number of samples

The impact of the number of samples on reflectivity and velocity reconstruction is studied by increasing the number of samples from 64 to 1024 using 33 receivers in three receiver configurations and SNR = 30 dB. The "log2" base is used to plot the RMSE as a function of number of samples due to the large gap between the numbers. The mean of the RMSE as a function of sample numbers for CS, CB, and FB reflectivity estimation is shown in Fig. 4.44. The improvement of CS and CB as a function of number of samples can be observed for three receiver configurations. It is obvious that the improvement in CB and CS performance is comparable in NRS and RS receiver configurations as the number of samples increases for 33 receivers. Unlike CB and CS, the improvement in FB performance is very small for the three configurations. Note that CS produces a lower RMSE than CB and FB for all the receiver configurations and numbers and all the numbers of samples, except at 64

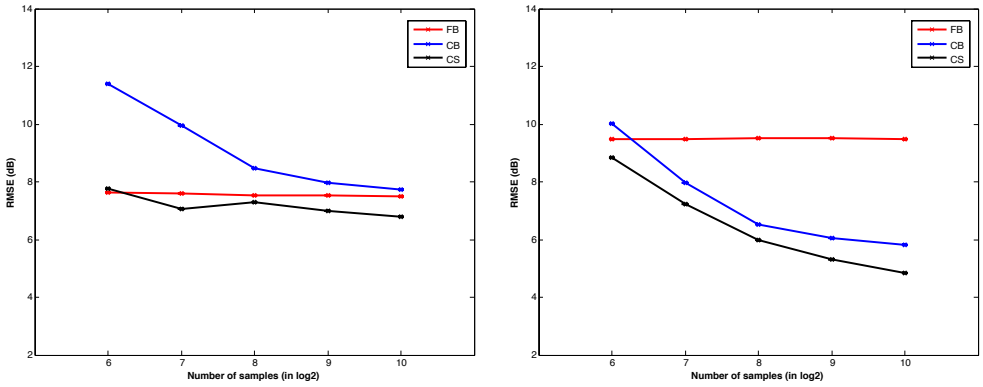

(a) Uniform spacing

(b) Nonredundant spacing

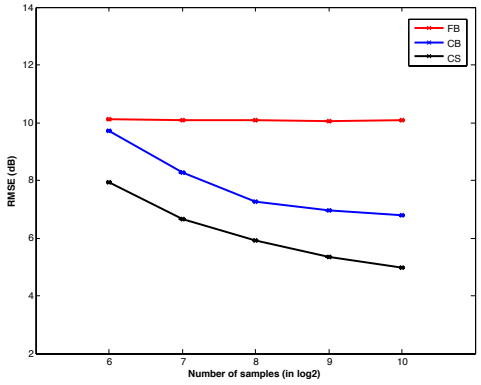

(c) Random spacing

Figure 4.44: The mean of RMSE as function of number of samples for CS (black), CB (blue), FB (red) for the ARPS model reflectivity estimation. SNR = 30 dB and the number of receivers 33.

samples in the US configuration as shown in Fig. 4.44. The performance of FB in the NRS and RS configurations is insignificant as the number of samples increases. CB performance is better than FB in the NRS and RS configurations when using a number of samples greater than 64.

Examples of CS, CB, and FB reflectivity retrievals from one realization by using 64, 128 and 256 samples for three configurations with 33 receivers are shown in Fig. 4.45. CS and FB are able to reconstruct reflectivity structure grossly using three

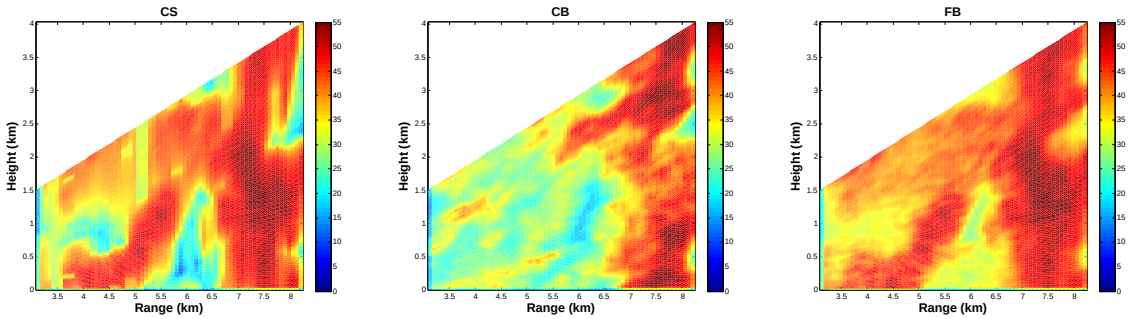

(a) Number of samples = 64

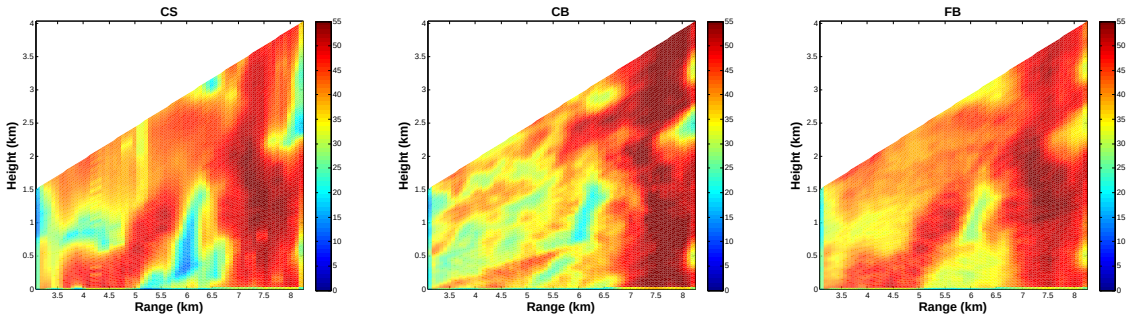

(b) Number of samples = 128

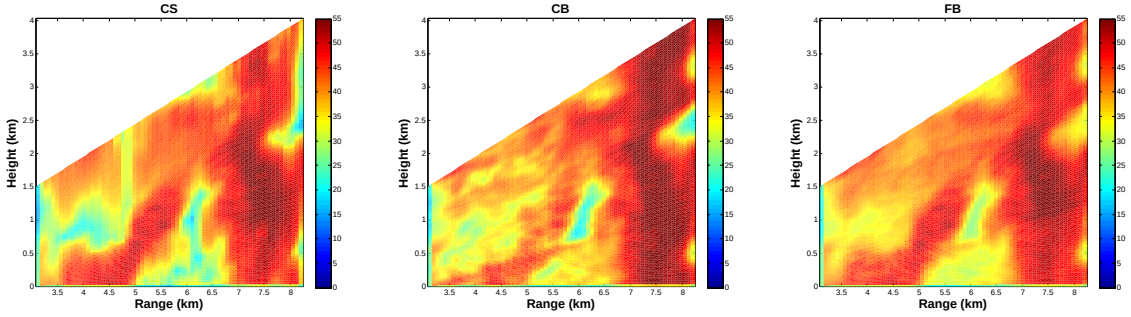

(c) Number of samples = 256

Figure 4.45: CS (left), CB (middle), and FB (right) reflectivity reconstruction profile with numbers of samples 64, 128 and 256, using US configuration. SNR = 30 dB and the number of receivers is 33.

different number ofs samples with 33 receivers in the US configuration. It is clear that CB is not able to estimate reflectivity structures accurately using 64 samples with 33 receivers in Regions I, II, and III. The reflectivity structures in Regions I, II,

and III are recovered with more detailed in CS and FB estimation than in CB with 64 samples and 33 receivers in the US configuration. The reconstruction of CS, CB, and FB improves generally as the number of samples increases.

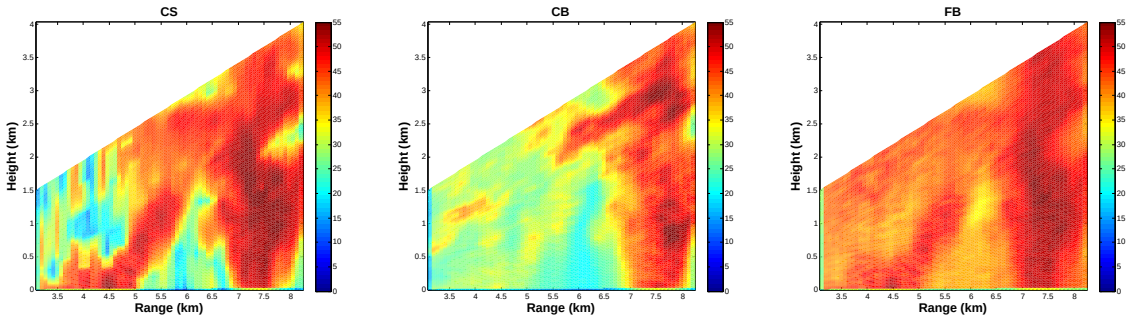

(a) Number of samples = 64

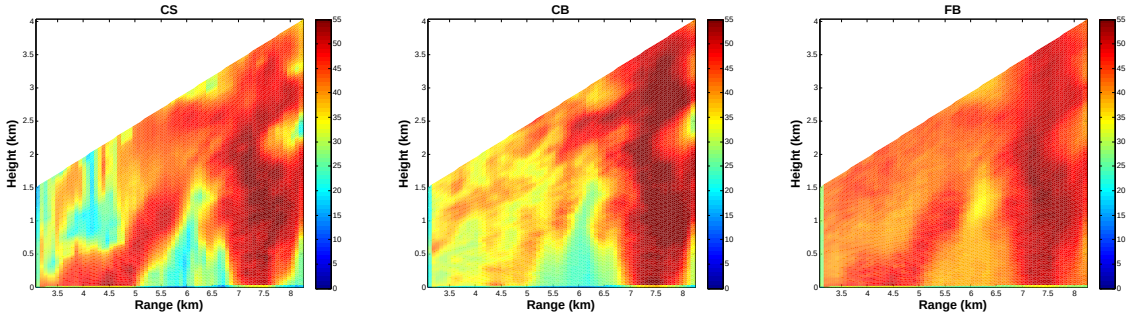

(b) Number of samples = 128

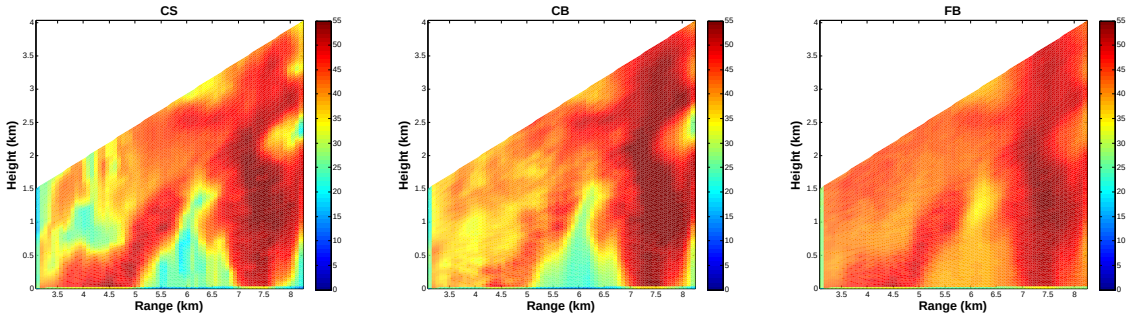

(c) Number of samples = 256

Figure 4.46: same as Fig. 4.45 but for NRS configuration

In the NRS configuration, CS and CB have better estimation in Region III, but FB's worse than in the US configuration in Fig. 4.46. In the CS estimation, the upper

portion of Region I is reconstructed poorly in NRS compared to US for 64 samples. On the other hand, reflectivity in Regions IV and V are recovered better in NRS. As the number of samples increases, estimation in Region I improves in CS and becomes better with the detailed structures. However, CB and FB are not capable of resolving Regions I and II clearly in NRS, even using 128 samples. There is a small indication of Region I and II using 256 samples in CB and FB in Fig. 4.46.

The reconstruction of CS has more detailed structures than CB and FB using 33 receivers and 64 samples in the RS configuration in Fig. 4.47. In RS, CS is capable of resolving reflectivity structures in Regions II, III, IV, and V with 33 receivers and 64 samples; also Region I is recovered, but the accuracy is less than in other regions. CB has indication of Region III only, and other regions are not resolved in RS with 33 receivers. As the number of samples increases, Region I in CS and Region III in CB become more clear. However, Region I is not distinguishable in CB and FB using 256 samples in the RS configuration. The reconstruction of FB is poor in RS, and did not improve much by increasing the number of samples to 256.

Examples of reflectivity profiles from one realization of the 64, 128, and 256 samples with 33 receivers are shown in Fig. 4.48 for the three receiver configurations. CS is able to recover two wide Gaussians at 1 km and 2.5 km with a similar width of the model reflectivity using 64 samples and 33 receivers for all three configurations. CB has a narrower width than the true one at 64 samples, and the reflectivity between 0.5 - 1.5 km is 10 dB down in all three configurations. FB has similar estimations at

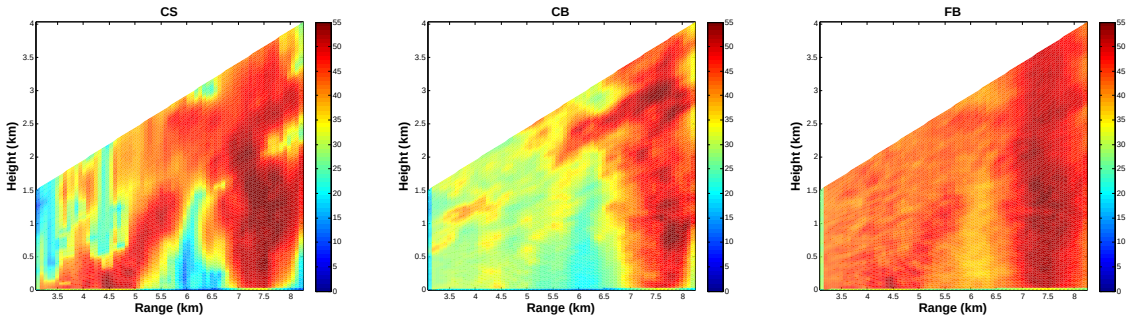

(a) Number of samples = 64

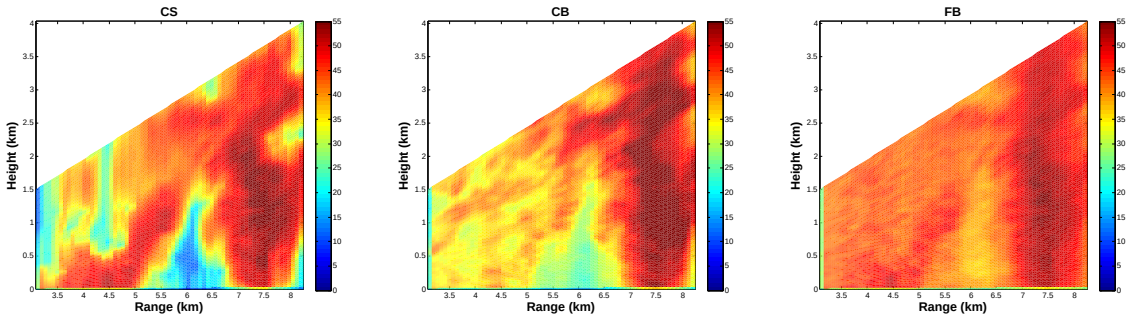

(b) Number of samples = 128

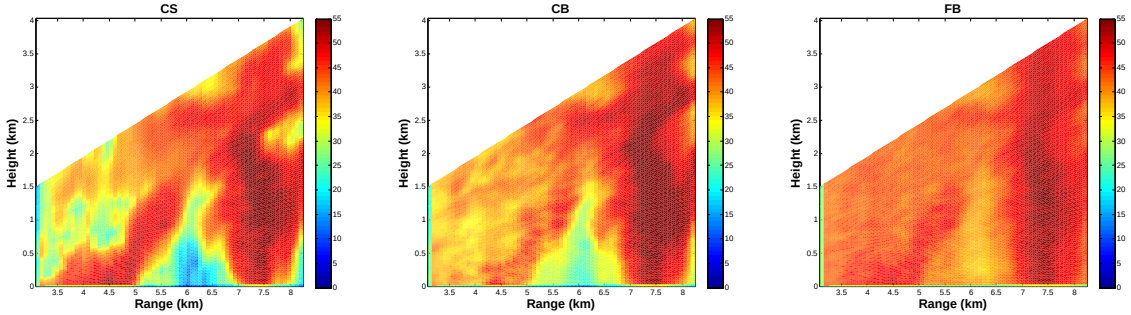

(c) Number of samples = 256

Figure 4.47: same as Fig. 4.45 but for RS configuration.

64 samples. CB has better agreement with the model reflectivity using 256 samples rather than 64 samples.

Another example profile of CS, CB, and FB reconstruction profiles for 64, 128, and 256 samples and the three different configurations is provided in Fig. 4.49. Similar to Fig. 4.48, CB produces poor estimation using 64 samples with 33 receivers in

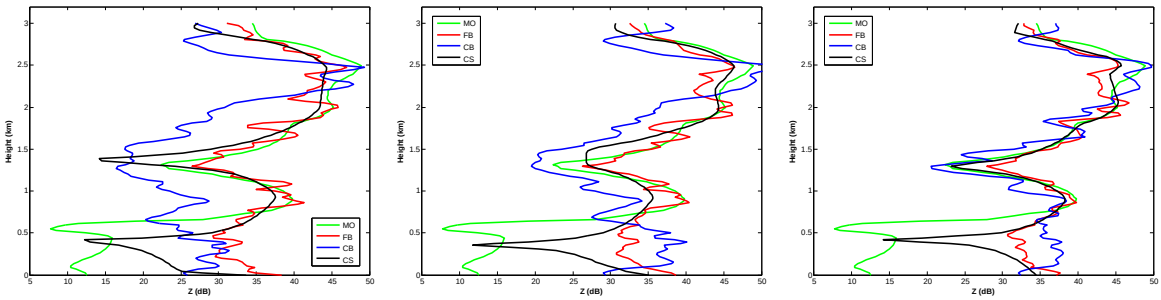

(a) Uniform spacing

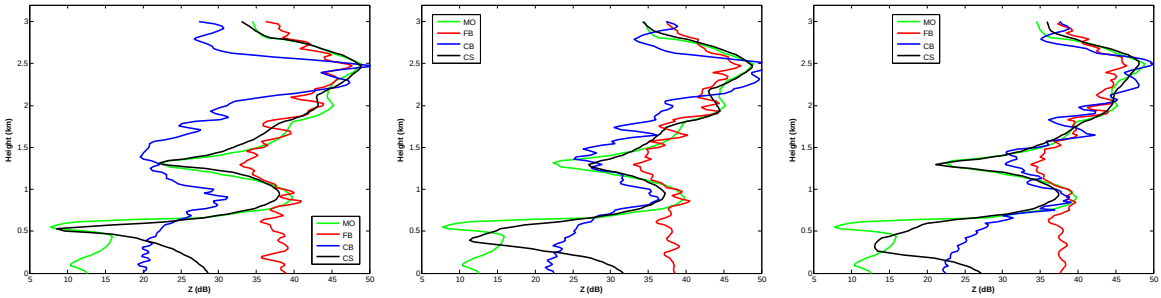

(b) Nonredundant spacing

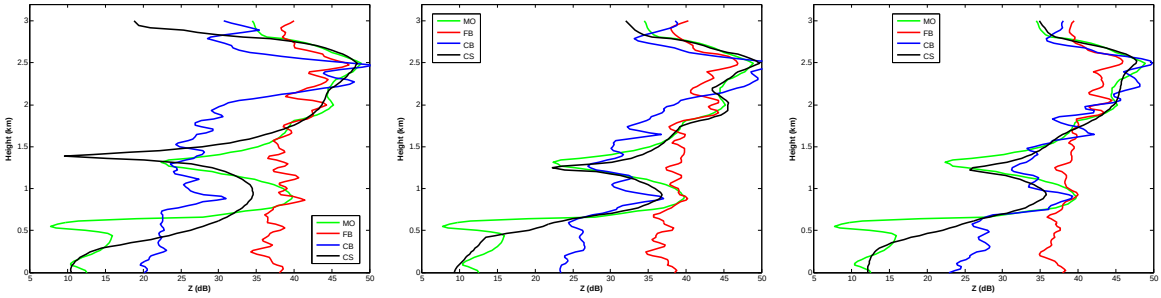

(c) Random spacing

Figure 4.48: CS (black), CB (blue), and FB (red) reflectivity reconstruction profile with the number of samples 64 (left panel), 128 (middle panel), 256 (right panel). The number of receivers is 33 and SNR=30 dB. The location of the reflectivity profile is at 6.2 km in Region III

all three configurations in Fig. 4.49. The valley structure at a height of 3 km can be resolved much better with CS than with FB and CB for 64, 128, and 256 samples and the NRS and RS configurations. However, the location of the valley reflectivity in the

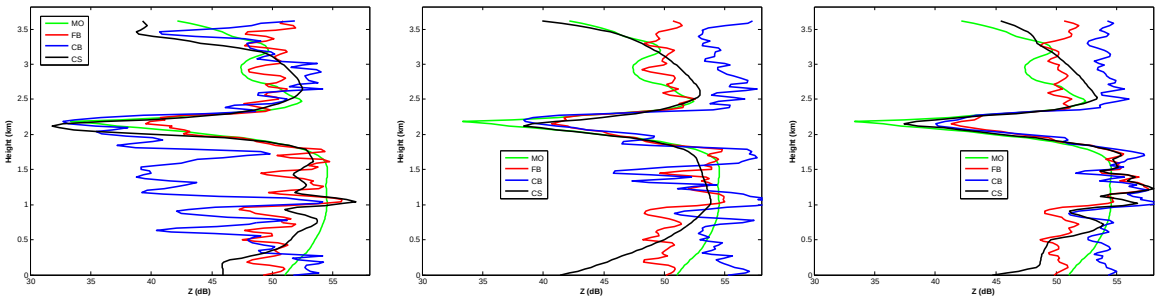

(a) Uniform spacing

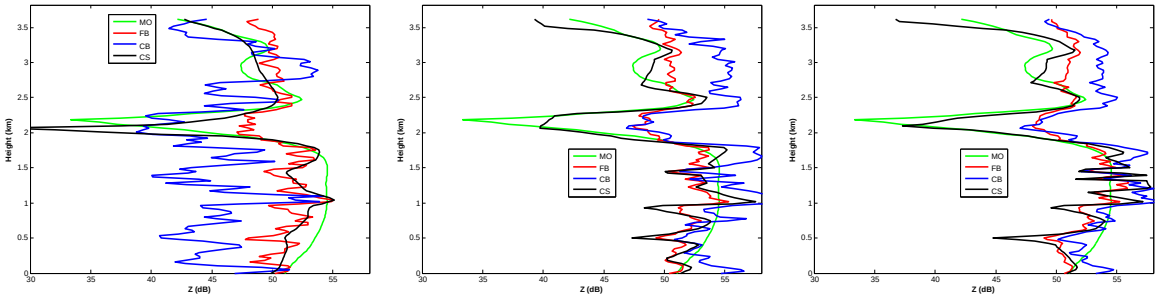

(b) Nonredundant spacing

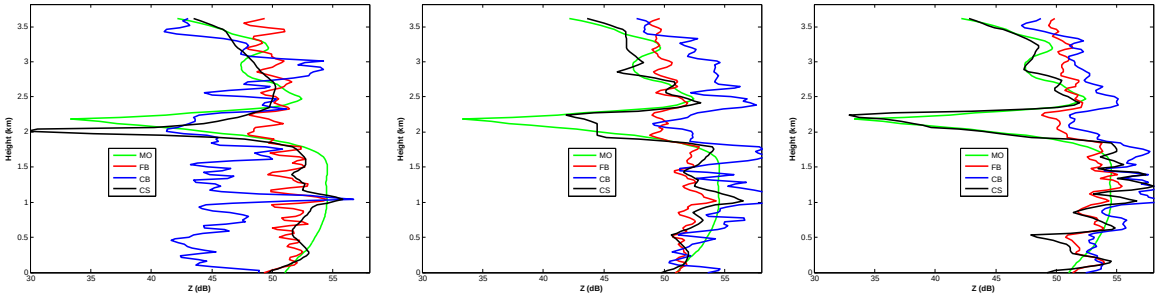

(c) Random spacing

Figure 4.49: CS (black), CB (blue), and FB (red) reflectivity reconstruction profile with the number of samples 64 (left panel), 128 (middle panel), 256 (right panel). The number of receivers is 33 and SNR=30 dB. The location of the reflectivity profile is at 7.4 km in Regions IV and V.

CS reconstruction is slightly shifted using 64 samples. Note that the additional samples can provide better reconstruction for the three methods. It is important to point out that CS performance becomes better by increasing the number of samples to 128

and 256, and the valley and dual Gaussians at 3 km are recovered using NRS and RS configurations, where CB and FB do not resolve these structures, as demonstrated in Fig. 4.49.

Number of samples impact on velocity estimation

The impact of the number of samples on velocity estimation is investigated in this section using 64, 128, 256, 512, and 1024 samples. The velocity is dealiased if the velocity aliasing is detected based on the threshold. For the threshold value, 20 ms^{-1} is used for 64 samples, due to the large oscillations in the velocity. The RMSE is calculated based on the dealiased velocity as shown in Fig. 4.50. The x-axis is scaled by using log2 base to plot the result for better demonstration. The performance of CS, CB, and FB increases as the number of samples increases. It is clear that CB performs better than CS and FB for a large number of samples and US and NRS. The CS and CB performance is comparable in the RS configuration as the number of samples increases. In NRS, the RMSE of the CB estimation is less than 2 ms^{-1} when the number of samples is greater than 128. FB performs better using US than NRS and RS in Fig. 4.50. CS shows similar performance in RS and NRS when the number of samples is greater than 128.

Examples of CS, CB, and FB velocity retrievals from one realization by using 64, 128 and 256 samples with 33 receivers for three different configurations are shown in Fig. 4.51. CS, FB, and CB reconstruct velocity structure grossly using three numbers of samples with 33 receivers in the US configuration. It is clear that the CB velocity

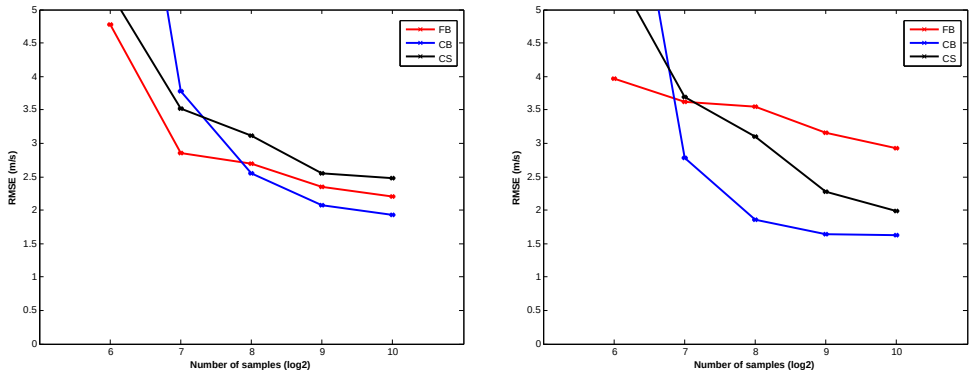

(a) Uniform spacing

(b) Nonredundant spacing

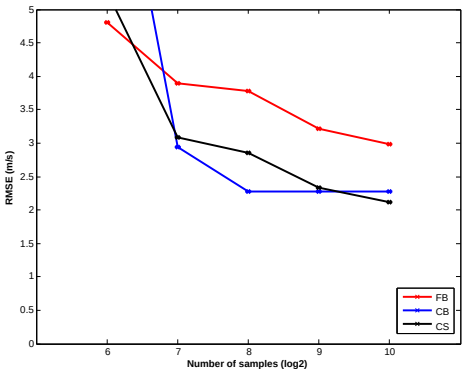

(c) Random spacing

Figure 4.50: The mean of RMSE as function of number of samples for CS (black), CB (blue), and FB (red) for the ARPS model velocity estimation. SNR = 30 dB and the number of receivers is 33.

estimate has more velocity oscillations using 64 samples and 33 receivers. CS and FB perform better than CB using 64 samples in the US configuration. CS aliases velocity artifacts, but less severely than CB. Regions I, II and III are recovered with cleaner and more detailed structures in CS and FB than CB with 64 samples and 33 receivers in the US configuration as shown in Fig. 4.51. The reconstruction of CS, CB and FB improves generally by increasing the number of samples. CB produces good velocity estimation using 256 samples.

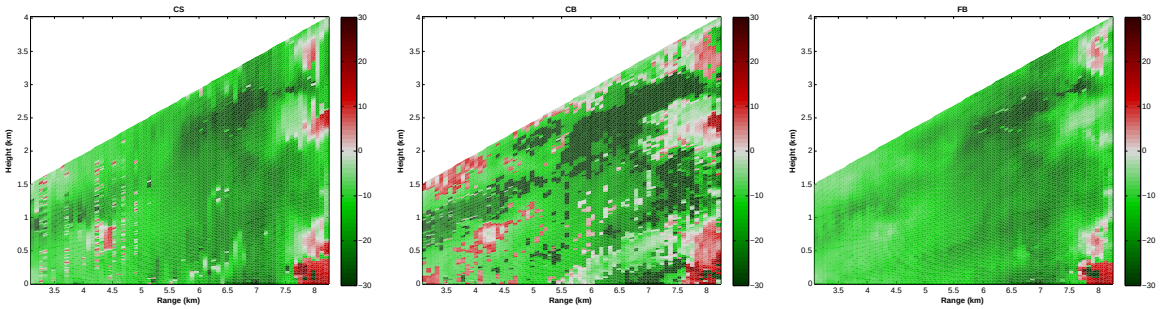

(a) Number of samples = 64

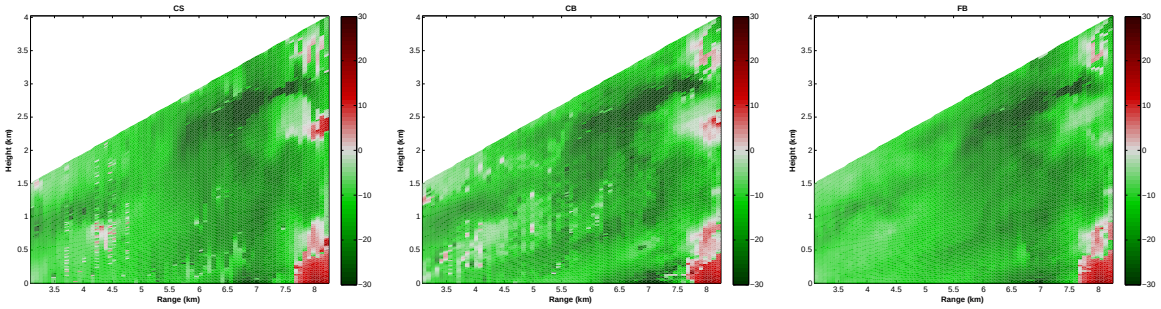

(b) Number of samples = 128

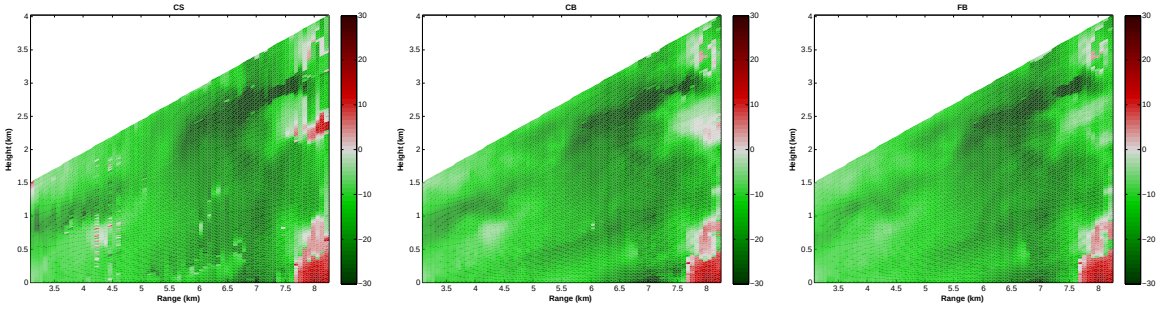

(c) Number of samples = 256

Figure 4.51: CS (left), CB (middle), and FB (right) velocity reconstruction with the number of samples 64, 128 and 256 using US configuration. SNR = 30 dB and the number of receivers is 33.

In the NRS configuration, the CB estimation using 64 samples looks noisy and has more oscillations than using 128 and 1256 samples in Fig. 4.52. CS and FB have more clean reconstruction compared to CB using 64 samples with 33 receivers.

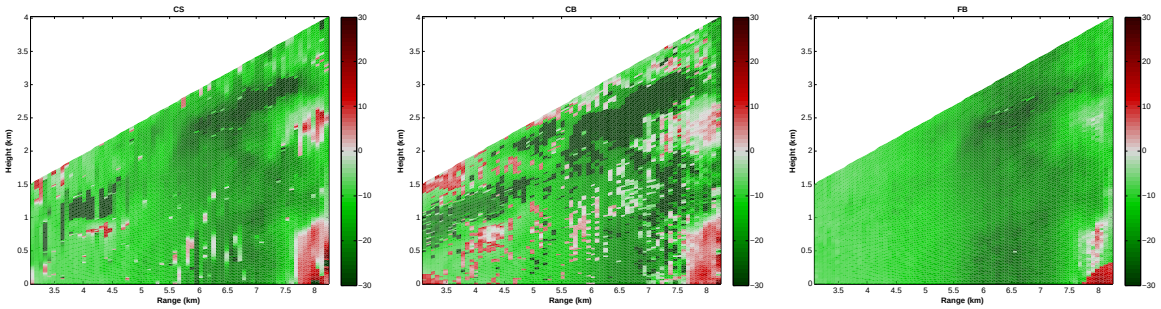

(a) Number of samples = 64

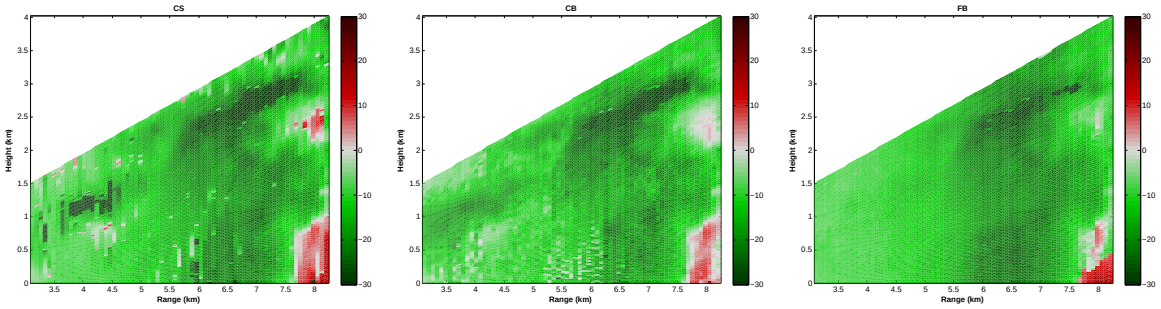

(b) Number of samples = 128

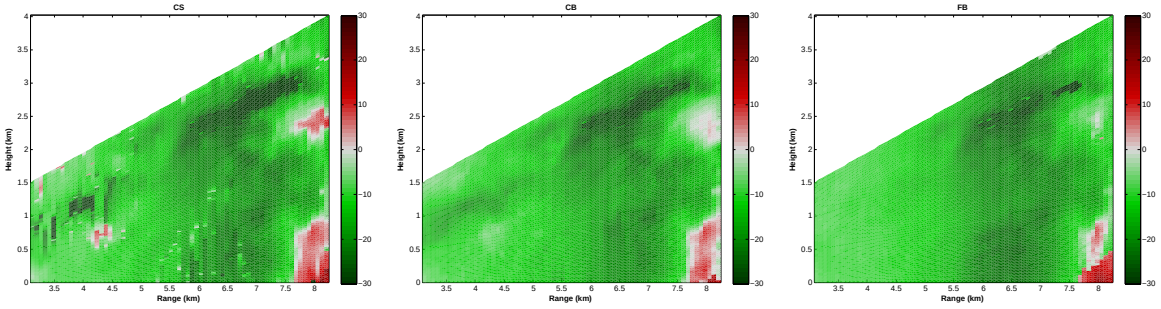

(c) Number of samples = 256

Figure 4.52: same as Fig. 4.51 but for NRS receiver configuration.

However, CB has a velocity structure in Region I, that is better than FB and slightly better than CS in Fig. 4.52. Increasing the number of samples did not improve the estimation qualitatively for CS and FB in Region I.

Moreover, the velocity structures in Region I were also not recovered accurately in CS and FB using 64 and 256 samples in the RS configuration in Fig. 4.53. The

velocity reconstruction of CB using NRS is similar to RS in Fig. 4.53. The difference between the FB velocity estimation using 64 and 256 samples in RS is indistinguishable. Further, CS has more errors in Regions I and IV in the RS configuration, which the low reflectivity is associated with.

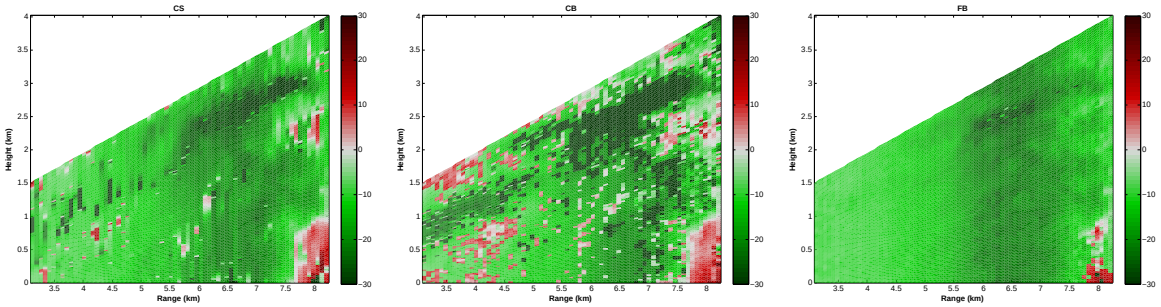

(a) Number of samples = 64

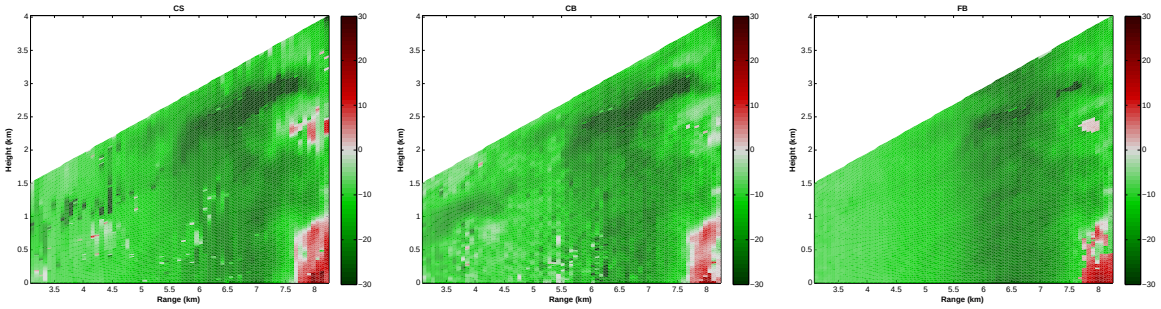

(b) Number of samples = 128

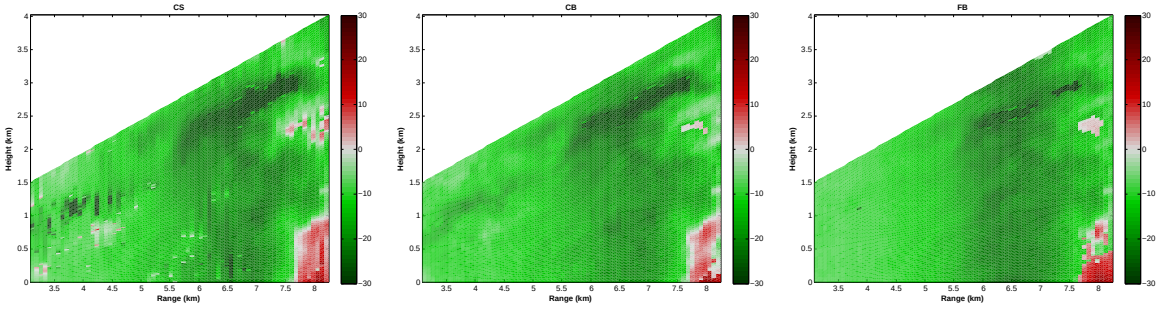

(c) Number of samples = 256

Figure 4.53: the same as Fig. 4.51 but for RS receiver configuration.

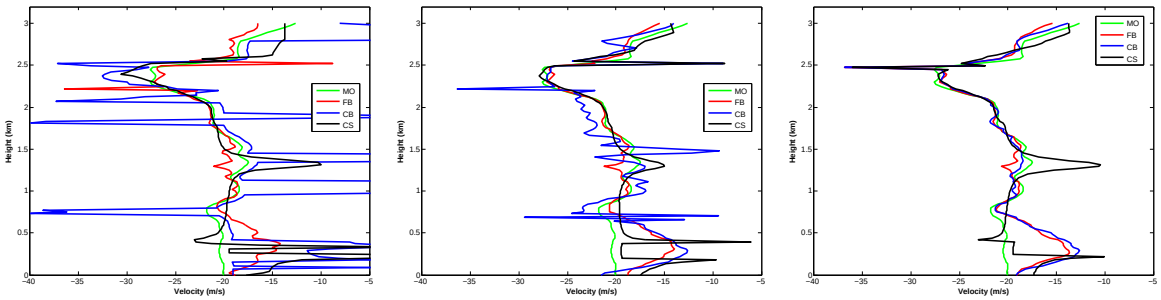

(a) Uniform spacing

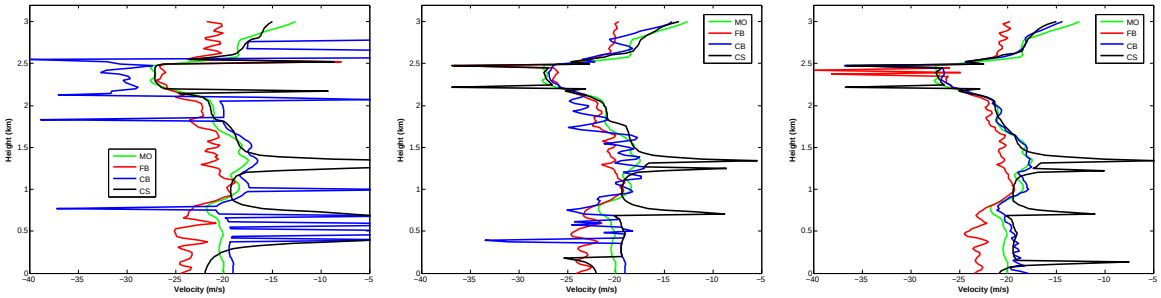

(b) Nonredundant spacing

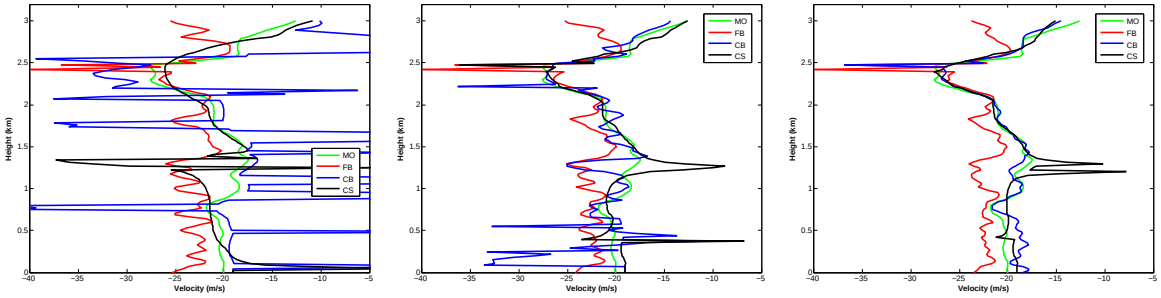

(c) Random spacing

Figure 4.54: CS (black), CB (blue), and FB (red) reflectivity reconstruction profile with the number of samples 64 (left panel), 128 (middle panel), 256 (right panel). The number of receivers is 33 and SNR=30 dB. The location of the reflectivity profile is at 6.2 km in Region III.

Examples of velocity profiles for CS, CB, and FB from one realization of the 64, 128 and 256 samples with 33 receivers are shown in Fig. 4.48 for the three receiver configurations. It is clear that CS and FB have relatively fewer oscillations than CB

using 64 samples with 33 receivers for all three configurations. By increasing the number of samples, the oscillations on CB estimation is significantly reduced. CS has peaks still remaining after the dealiasing process. CB is capable of resolving the velocity changes using 256 samples better than FB and CS, and has better agreement with model velocity.

Another example profile of CS, CB, and FB velocity reconstruction from one realization of 64, 128 and 256 samples for three different configurations is provided in Fig 4.55. Similar to Fig. 4.54, CB produces poor estimation and has many oscillations using 64 samples with 33 receivers in all three configurations in Fig. 4.55. Increasing the number of samples to 128 significantly reduces the oscillations on the CB estimation. CS, CB, and FB have similar velocity reconstruction with 128 and 256 samples in all three receiver configurations. The velocity profile in Fig. 4.55 is grossly estimated using 128 and 256 samples, using CS, CB, and FB with three configurations.

4.8 Experimental results from AIR radar

In order to further demonstrate and verify CS reconstruction of reflectivity and velocity profiles, CS is implemented using the data from the Atmospheric Imaging Radar (AIR) collected on April 15, 2012. The AIR has 36 receivers with equal spacing of 1.8λ and 25^o transmitted beamwidth in elevation, mechanical azimuth scanning, where the detailed specifications are provided by Isom et al. (2013). The data were

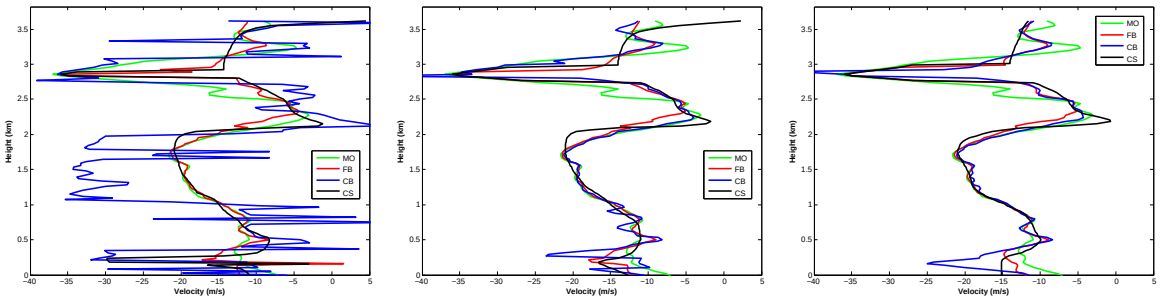

(a) Uniform spacing

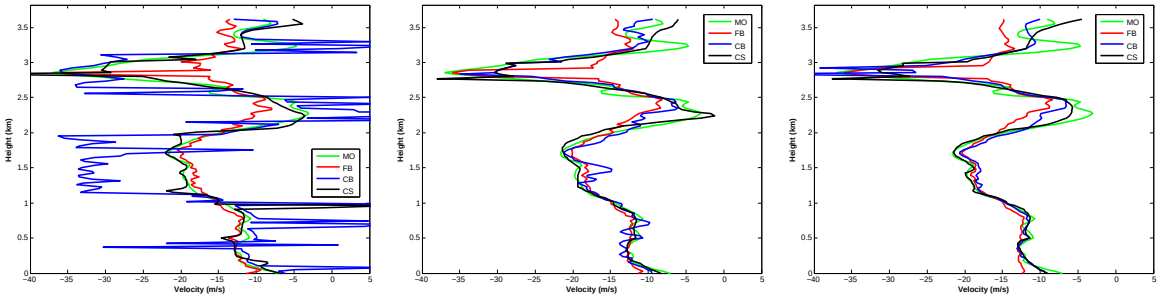

(b) Nonredundant spacing

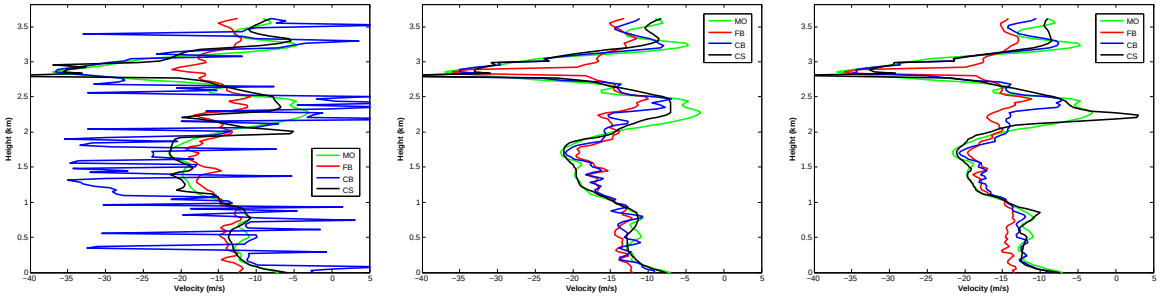

(c) Random spacing

Figure 4.55: CS (black), CB (blue), and FB (red) reflectivity reconstruction profile with the number of samples 64 (left panel), 128 (middle panel), 256 (right panel). The number of receivers is 33 and SNR=30 dB. The location of the reflectivity profile is at 6.2 km in Region III.

obtained using staggered PRT, PRT1 = 0.409 and PRT2 = 0.614 ms, which leads to the aliasing velocity of 38.3 ms^{-1}. The wavelength of the operational frequency is

3.14 cm and range resolution in 30 m. Using the data from the AIR, the reconstruction of FB, CB, and CS is obtained from correlations of received signals at lag 0 from 53 samples. The velocity is obtained by processing the data separately for each PRT, and then the estimated velocities from two different PRTs are combined based on the difference between the two estimates. The reconstructed reflectivity image is normalized to the maximum value of the image to plot them with the same colorbar, since the estimated power is not calibrated. A comparison of CS, CB, and FB reflectivity estimation is provided in Fig. 4.56 for a range of 15 km - 16.5 km and 0 - 7 km in height. The reconstructed image from AIR will be in RHI format with the range resolution of 30 m. Additionally, in CB, diagonal loading is used, and signal power of 0.15 dB is added to the spatial autocorrelation matrix $\mathbf{R}(0)$. Otherwise, the result was too noisy.

It is clear that three reflectivity layers can be observed by all three methods in Fig 4.56. The two relatively narrow and horizontally-oriented layers are located at a height of approximately 0.2 and 1.8 km, respectively. The third layer is wider and exhibit an upward feature extending from 3 km to 4.2 km in height over the entire range of interest. Moreover, the separation between the three layers is more distinct with the CS estimation compared to CB. As shown previously in Fig. 4.45 in simulation, the performance of CS with the US receiver configuration is limited for a small number of samples (53 in this case). Also, the estimations of CS and FB were similar, and CS was capable of resolving the structures slightly better than FB.

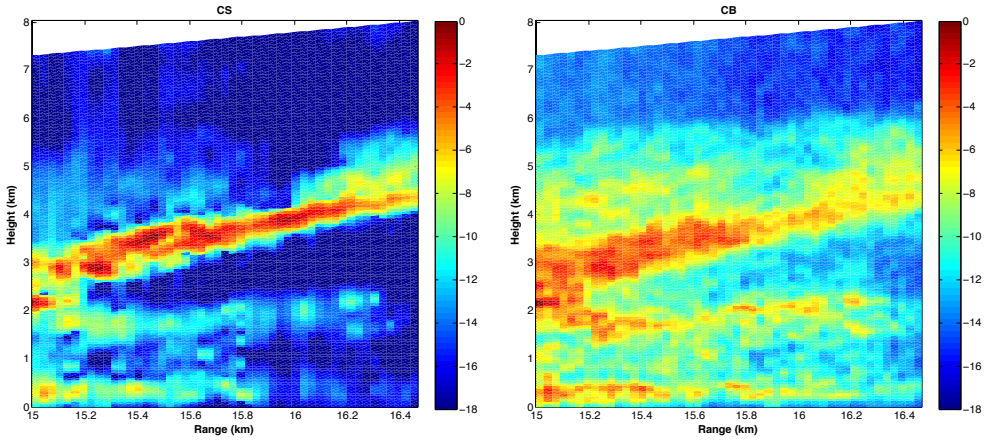

(a) CS (b) CB

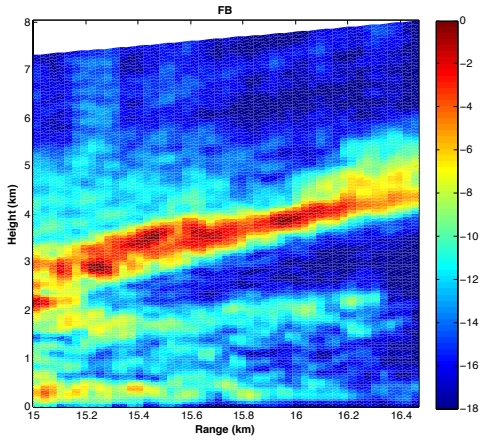

(c) FB

Figure 4.56: CS (left), CB (middle), and FB (right) reflectivity reconstruction using 36 receivers and 53 samples.

Example profiles of CS, CB, and FB reflectivity estimates from ranges of 15, 15.8, and 16.4 km are shown in Fig. 4.57. It can further verify that CS and FB produce similar reflectivity structures, while CS has a slightly larger dynamic range and fewer fluctuations than FB. A structure similarity between CS and CB can be observed in Fig. 4.57(a). Based on the reflectivity profile in the simulation with 33 receivers and 64 samples, CS produces a larger dynamic range than FB, and the agreement of the

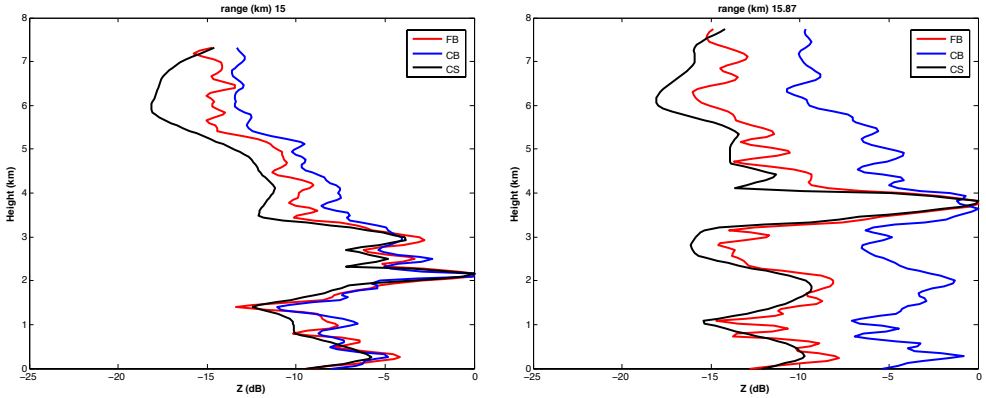

(a) Range at 15 km

(b) Range at 15.8 km

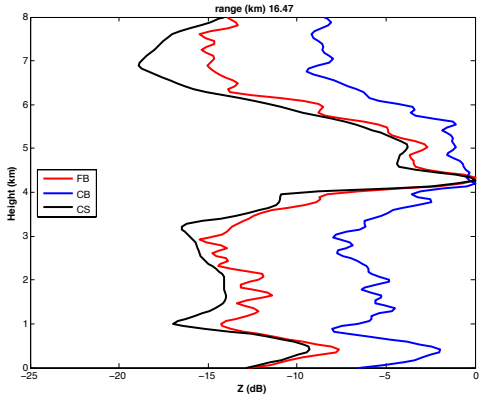

(c) Range at 16.4 km

Figure 4.57: CS (left), CB (middle), and FB (right) reconstructed reflectivity profiles using 36 receivers and 53 samples.

CS estimation is better than FB in Fig 4.49. A similar observation can be obtained from the simulation in Fig 4.48. Unfortunately, there is no quantitative measure for the verification of the estimations. Based on the simulation result, CS can provide DR of 25 dB under similar conditions.

The RHIs of velocity reconstructions using CS, CB, and FB are shown in Fig. 4.58. Similar to the simulation result in Section 4.7.3.3, owing to the smaller number of samples, CB fails to estimate velocity accurately, and the image looks noisy due

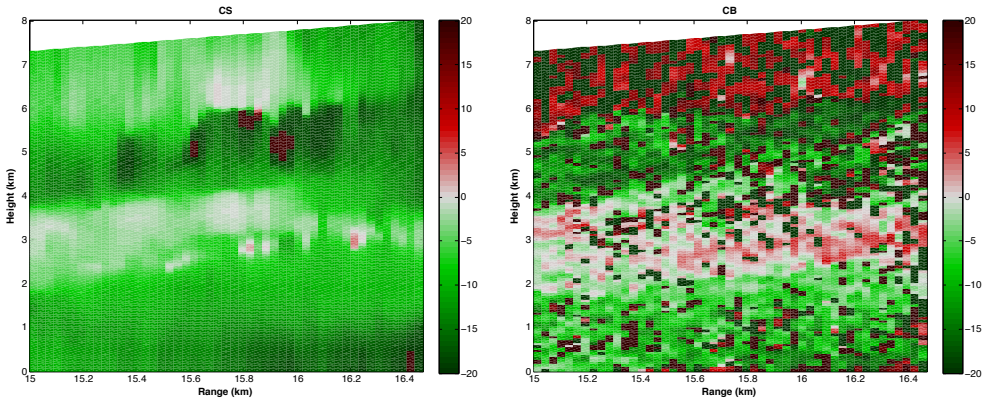

(a) CS (b) CB

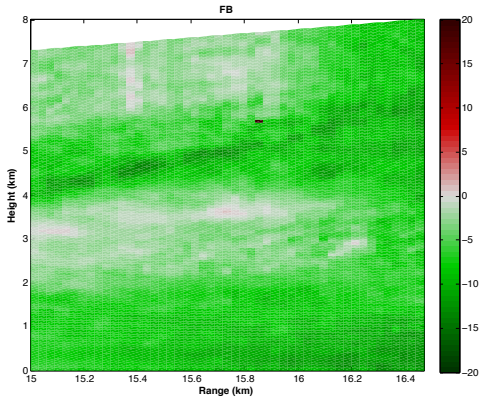

(c) FB

Figure 4.58: CS (left), CB (middle), and FB (right) velocity reconstruction using 36 receivers and 53 samples.

to oscillations from aliasing velocity. On the other hand, FB and CS produce similar velocity estimates, where CS seems to produce aliased velocity at 5 km in height and 15.6, 15.8, and 16 km in range. In the region between 3 - 4 km in height and 15 - 16 km in range, a velocity estimation of 0 ms^{-1} can be observed for CS, FB, and CB. This region also corresponds to the low reflectivity value region between the two layers of the reflectivity structure. Vertical profiles of velocity estimation of CS, CB, and FB are exemplified in Fig. 4.59. Again, the velocity estimates from

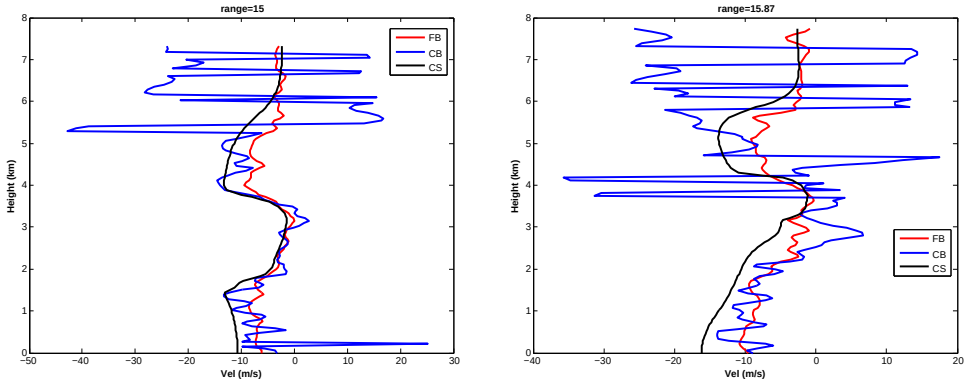

(a) Range at 15 km

(b) Range at 15.8 km

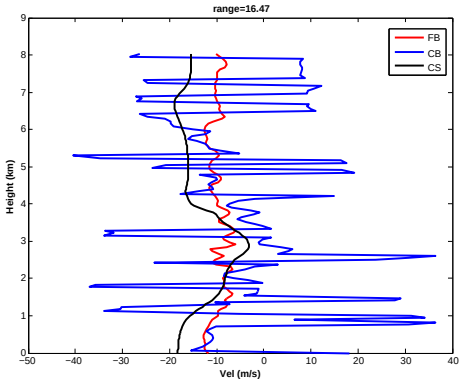

(c) Range at 16.4 km

Figure 4.59: CS (left), CB (middle), and FB (right) reconstructed velocity profiles using 36 receivers and 53 samples.

CS are similar to those from FB, but CS has larger DR than FB in Fig 4.59(c). CB has a similar velocity estimation to CS and FB, but with relatively large oscillations at an altitude lower than 5 km as shown in Fig. 4.59(a) and lower than 3 km in Fig. 4.59(b). It is clear that CB velocity has large fluctuations when using only 53 samples and 36 receivers in the US configuration. Similar results were observed for CB in the simulation by using 64 samples and 33 receivers in the US configuration in Fig. 4.55 and 4.54, where CS and FB had fewer oscillations, and their velocity estimation better agrees with the true velocity.

Another example of CS, CB, and FB from an AIR experiment on April 15, 2012 is shown in Fig. 4.60 at a range of 9 km to 16.5 km. The radar parameters were the same as in the previous experiment. It is obvious that similar reflectivity structures

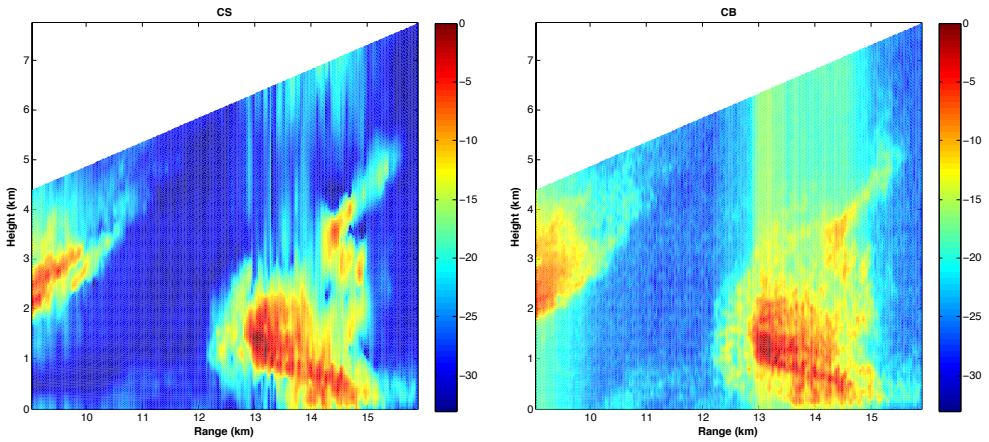

(a) CS

(b) CB

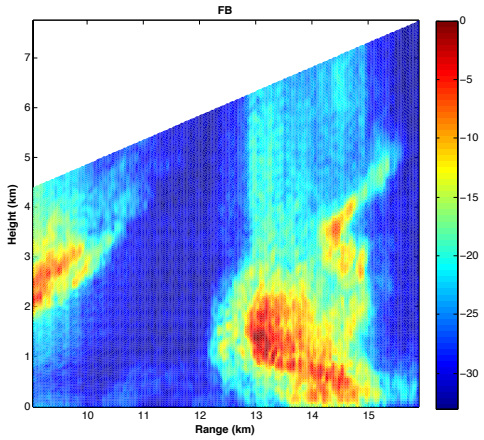

(c) FB

Figure 4.60: CS (left), CB (middle), and FB (right) reflectivity reconstruction using 36 receivers and 53 samples.

are reconstructed by all three methods. The separation of relatively high reflectivity structures between 8-10 km, 13-15 km, 14.5-15 km, and 2-3 km in range, and 0-2 km and 2.5 -4 km in height, respectively, is slightly better from CS and FB than

from CB. Additionally, CS has a lower reflectivity estimation than FB and CB in the region above 3 km in height and 13-15 km in range.

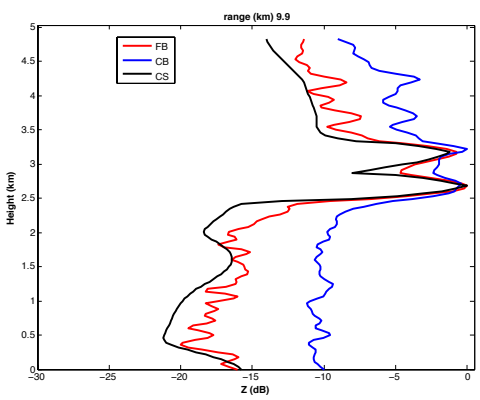

(a) Range at 15 km

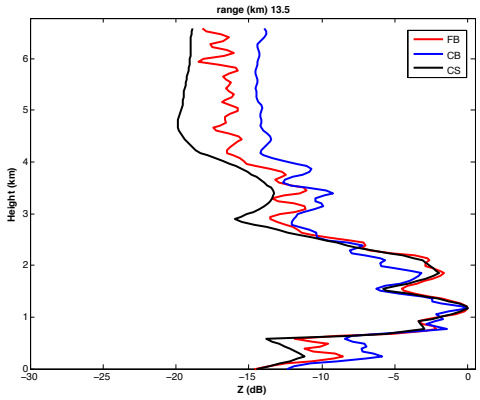

(b) Range at 15.8 km

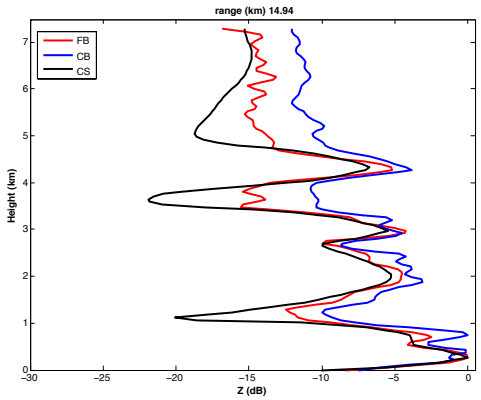

(c) Range at 16.4 km

Figure 4.61: CS (left), CB (middle), FB (right) reconstructed reflectivity profiles using 36 receivers and the number of samples 53.

Three example profiles of reconstructed reflectivity using CS, CB, and FB are shown in Fig. 4.61. The dual Gaussian-like structure with the peak locations at a height of 2.5 and 3.2 km has relatively equal amplitude that can be reasonably reconstructed using all three methods (ie, likely to be real) in Fig 4.61(a). CS provides deeper valley between the dual peaks than FB and CB. Further, CS has 22 dB DR

of reflectivity, which is larger than the DR from FB and CB estimated reflectivity (approximately 19 dB and 11 dB, respectively). Additionally, the fluctuation in the CS estimation is less than than in FB and CB. Similar results are obtained in the simulation that CB and FB can produce fluctuation in reflectivity estimates given smooth reflectivity in the simulation, using 64 samples and 33 receivers in Fig. 4.55. In Fig. 4.61(b), the small wide peak at between 3 - 4 km height, where the peak amplitude difference is about 15 dB, is recovered more clearly using CS than CB or FB. Additionally, the reflectivity reconstruction is similar for CS, FB, and CB in Fig. 4.61(b).

Moreover, the reconstruction of CS, CB, and FB is similar for the reflectivity structure, which has three Gaussians peaks at 4.4, 3, and 2 km height with similar width in Fig. 4.61(c). However, CS has deeper separation between the peaks than FB and CB, and DR of 20 dB. As shown in the simulation, CS is capable of resolving peak separation, for example, valley structure DR of about 20 dB in Fig. 4.55 and 4.54. In all three subfigures, CS has a larger dynamic range than CB and FB.

The RHI of velocity estimation using the three methods is shown in Fig. 4.62. CS and FB have similar velocity reconstruction between 12 - 15 km in range and 0 - 4 km in height. For the velocity structure at 0 - 4 km height and at 9 - 10 km, range is varied by CS, CB, and FB estimation. Again, CB velocity estimation looks noisy using 53 samples and 36 receivers, and it is consistent with the simulation result using 64 samples and 33 receivers in the US receiver configuration.

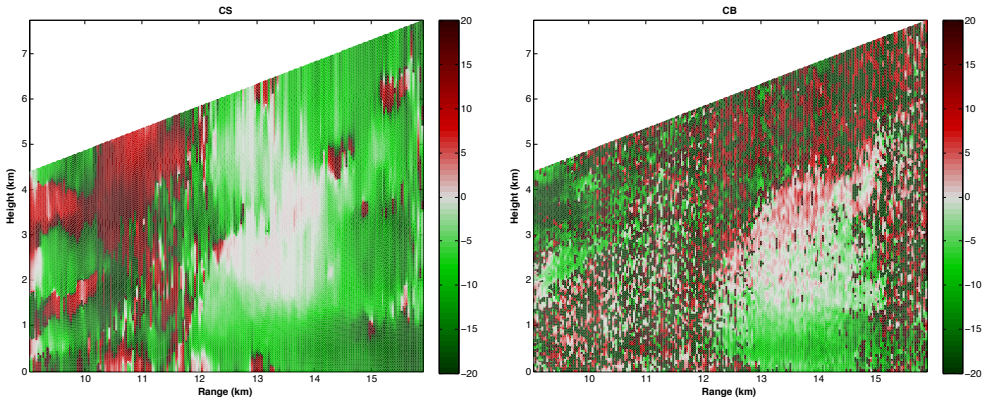

(a) CS

(b) CB

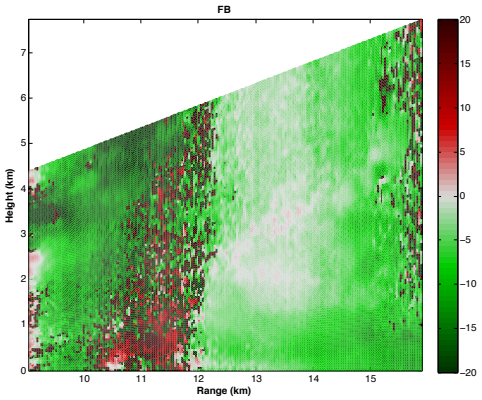

(c) FB

Figure 4.62: CS (left), CB (middle), and FB (right) velocity reconstruction using 36 receivers and 53 samples.

Profiles of velocity estimates from the three methods at the ranges of 9.9, 13.5, and 15 km are shown in Fig. 4.63. CB has large fluctuations in velocity estimation in different regions. For example, the velocity estimation of CS and FB has a small variation in Fig. 4.63(c), whereas CB is not able to estimate velocity in any region at this profile using 53 samples and 36 receivers. Further, CB partially estimates the velocity at the lower height in Fig 4.63(b), where FB and CS can produce reasonable

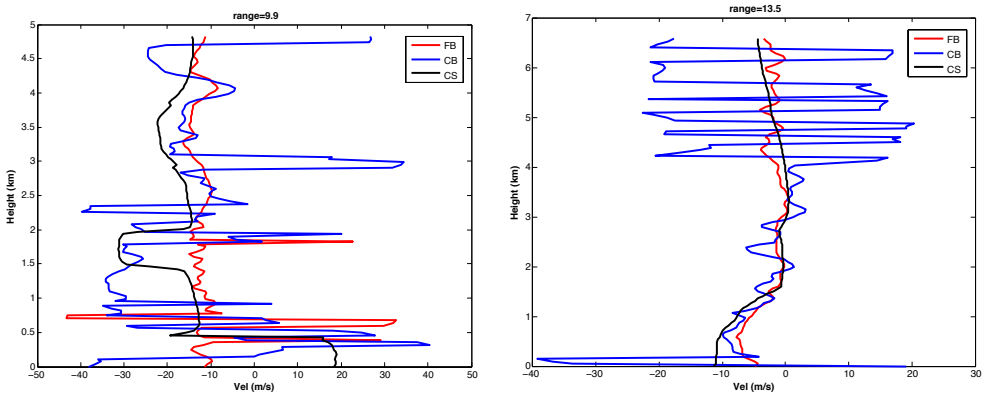

(a) Range at 9.9 km

(b) Range at 13.5 km

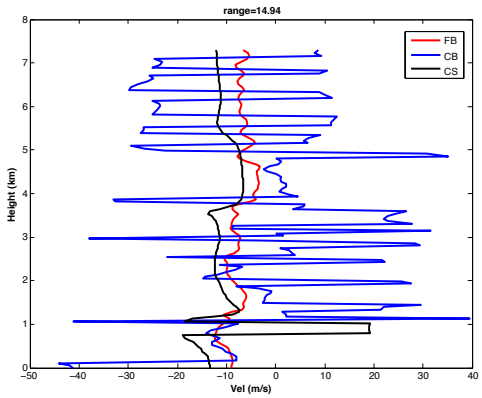

(c) Range at 15 km

Figure 4.63: CS (left), CB (middle), and FB (right) reconstructed velocity profiles using 36 receivers and 53 samples.

velocity estimates for the entire profile. The result indicates that CB needs more samples to better estimate velocity structure accurately in the whole region. As shown in the simulation, by increasing the number of samples, CB is capable of estimating velocity better in Fig. 4.51, and CB performance improves significantly as the number of samples increases. Further, FB estimates velocity reasonably using 64 samples with 33 receivers in the US configuration in Fig. 4.51.

4.8.1 Undersampling AIR receivers

Further, in order to demonstrate the CS reconstruction of reflectivity and velocity profiles using fewer number of receivers, the AIR receivers are undersampled. 17 receivers are selected randomly from the uniformly distributed 36 receivers by keeping the same aperture size and receiver spacing of 1.8λ at least for one of the receiver pairs. A comparison of CS, CB, and FB reflectivity estimation with 17 receivers using RS is provided in Fig. 4.64 and the result can be compared to result with 36 receivers in Fig. 4.56. For CB, signal power of 0.15 dB is diagonally added to the spatial autocorrelation matrix $\mathbf{R}(0)$.

The separation between the three layers is more distinct with the CS estimation compared to CB and FB in Fig 4.64. In FB and CB, the three reflectivity layers using 17 receivers becomes less clear comparing to result in Fig 4.56 with 36 receivers. Especially in FB, more reflectivity structures at the above of 4-km height can be observed due to high sidelobes using RS. The performance of FB dramatically reduced qualitatively from 36 to 17 receivers. The similar degradation can be observed in CB estimation as decreasing the number of receivers 36 to 17. CS can still provide larger dynamic range of reflectivity with 17 receivers than CB and FB. As shown in simulation in Fig. 4.33, where CS had better reconstruction than CB and FB using 17 in RS receiver configuration. Further the improvement in CS from 17 to 33 was less significant than CB, since CS had most of the reflectivity structures in the reconstruction.

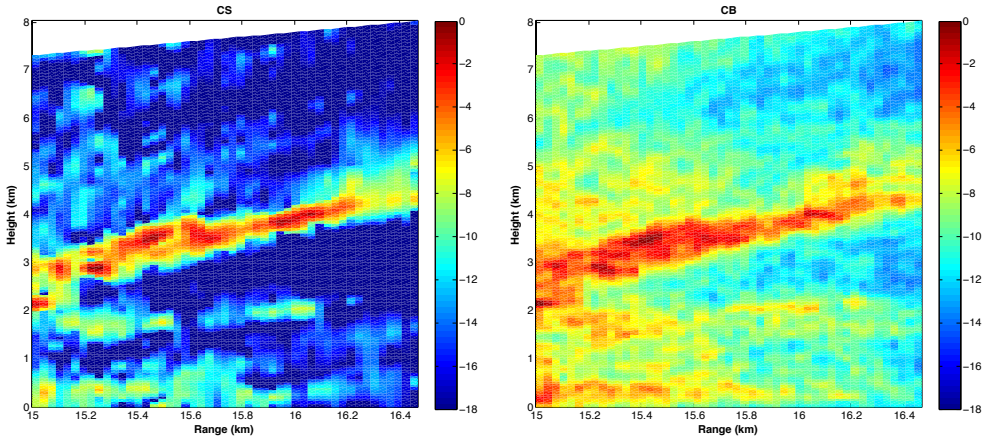

(a) CS (b) CB

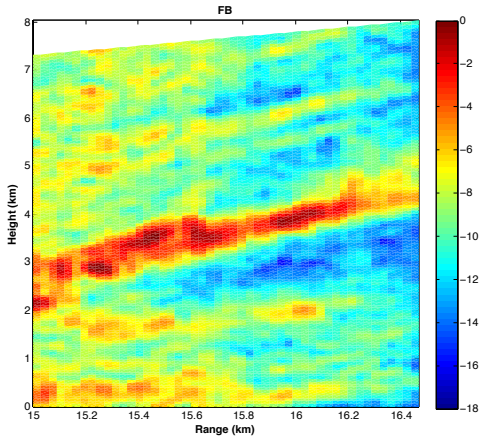

(c) FB

Figure 4.64: CS (left), CB (middle), and FB (right) reflectivity reconstruction using 36 receivers and 53 samples.

Example profiles of CS, CB, and FB reflectivity estimates from ranges of 15, 15.8, and 16.4 km are shown in Fig. 4.65 using 17 receivers. It is clear that CB and FB have similar reflectivity profiles, while CS has a larger dynamic range. In CS, the fluctuations in the profile using 17 receivers in Fig. 4.65 are increased compared to reconstructed profile with 36 receivers in Fig. 4.57. It is observed that by reducing the weights of wavelet, the fluctuations can be reduced in CS estimation.

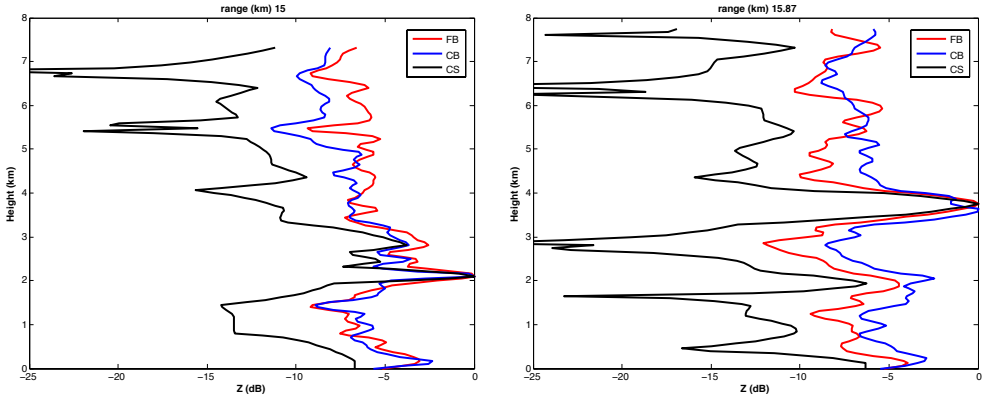

(a) Range at 15 km

(b) Range at 15.8 km

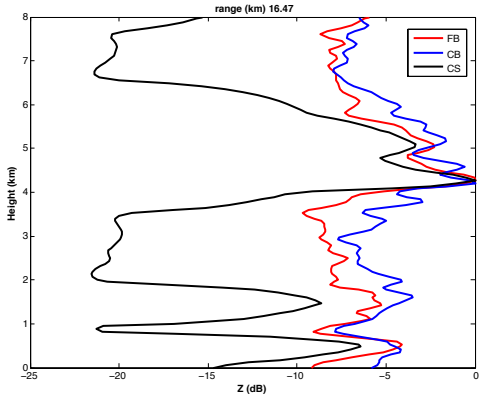

(c) Range at 16.4 km

Figure 4.65: CS (left), CB (middle), and FB (right) reconstructed reflectivity profiles using 36 receivers and 53 samples.

On the other hand, velocity estimation of CS, CB, and FB using 17 receivers are visually similar to estimation from 36 receivers and the RHIs of velocity reconstructions using CS, CB, and FB are shown in Fig. 4.66. Again, CB fails to estimate velocity accurately, and the image looks noisy due to oscillations from aliasing velocity. FB and CS produce similar velocity estimates, where CS seems to produce aliased velocity approximately at 5.5 km in height and 15.8 km in range. A similar observation is made in simulation in Fig. 4.40, where CS had similar performance

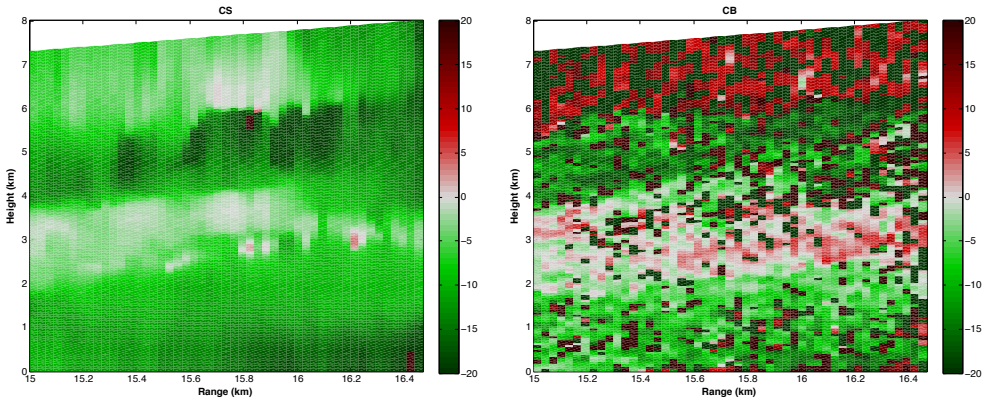

(a) CS (b) CB

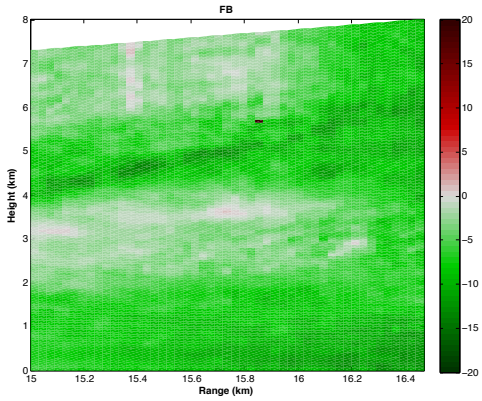

(c) FB

Figure 4.66: CS (left), CB (middle), and FB (right) velocity reconstruction using 36 receivers and 53 samples.

with 17 and 33 receivers in RS receiver configuration while CB velocity estimation improved more than CS as increasing the number of receivers 17 to 33.

Similarly, vertical profiles of velocity estimation of CS, CB, and FB are exemplified in Fig. 4.67 using 17 receivers. Again, the velocity estimates of CS, CB, and FB with 17 receivers are similar to those with 36 receivers in Fig 4.59. Interestingly, CS velocity profile becomes more similar to FB with 17 receivers than 36 receivers

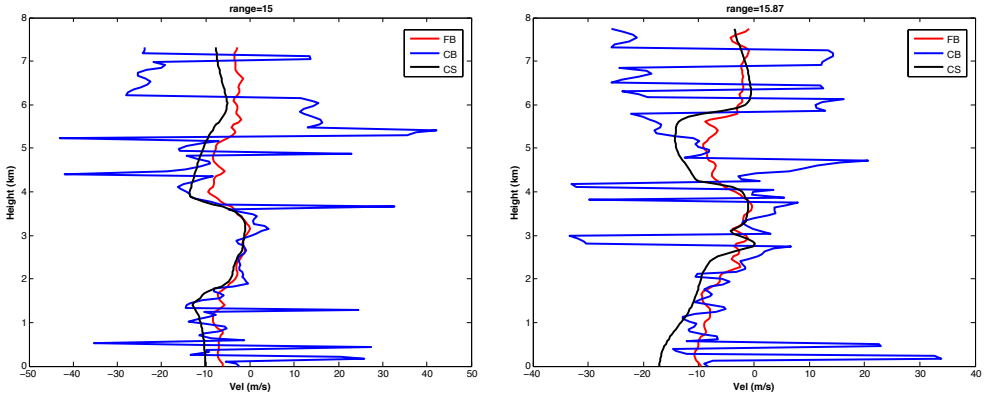

(a) Range at 15 km

(b) Range at 15.8 km

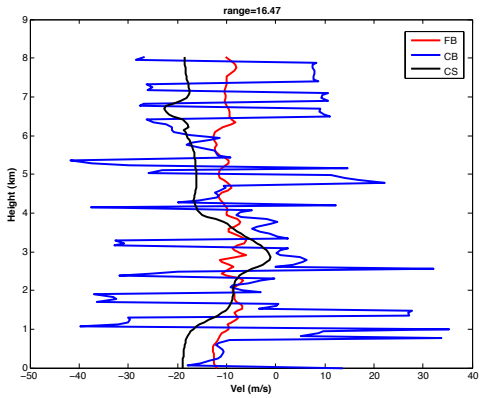

(c) Range at 16.4 km

Figure 4.67: CS (left), CB (middle), and FB (right) reconstructed velocity profiles using 36 receivers and 53 samples.

in Fig. 4.67. The oscillations in CB relatively increased as decreasing the number of receivers and CB has large oscillations compared to CS and FB with 17 receivers.

4.9 Summary and Conclusions

In this work, CS was proposed to improve the reconstruction of reflectivity and velocity structure for imaging radar, as an alternative to DBF techniques. The application of CS to DBF was formulated using a linear model for both reflectivity and velocity

estimation and subsequently demonstrated using two parts of simulations. In the first part of the simulation, user-defined and simplified reflectivity and velocity profiles were used to test dynamic range and resolution for high SNR and large number of samples. In the second part of the simulation, realistic reflectivity and velocity directly derived from ARPS were used to test the feasibility of CS. In both parts of the simulations, three receiver configurations of US, NRS, and RS are considered, where the minimum receiver spacing is selected to be half-wavelength to avoid grating lobes. The performance of CS, CB, and FB was quantified using RMSE, RES, DR, and velocity interval and subsequently studied statistically as a function of SNR, number of receivers, number of samples and reflectivity models. Note that CS relies on the linear model and can be applied to two dimensional beamforming. It is obvious that CS, CB, and FB can grossly reconstruct the reflectivity and velocity profiles in most cases. Moreover, CS can provide better reconstruction for reflectivity and velocity than both FB and CB when the amount of noise is increased, the dynamic range of reflectivity is relatively small, or using a smaller number of samples, for example. Specifically, the results show that CS is less susceptible to noise contamination.

Increasing the number of receivers, the performance of CS, CB, and FB is improved. Moreover, CS and CB take advantage of nonredundant and random spacing receiver configurations, where the redundancy in the receiver pairs is reduced significantly and so the number of independent measurements increases. CS is able to

recover reflectivity structure accurately by using 17 receivers with NRS and RS for the cases considered in this work. The shape of the reflectivity structures preserved in CS and CB is comparable for the larger number of receivers and samples. CS overestimates the resolution when the dynamic range of reflectivity becomes larger; however, it still provides reasonable results compared to CB and FB. The impact of reflectivity on velocity estimation is studied. Again, when the dynamic range of reflectivity becomes larger, the interval of valid velocity estimates (defined by error less than 3 ms^{-1}) for CS becomes narrower. This is also true for FB velocity estimates. However, CB can provide a reasonable velocity interval by using high number of samples and receivers.

For a smaller number of samples and receivers, CS is able to provide better estimation than CB using the NRS and RS receiver configurations. One difficulty in CS estimation is the beta value selection. The beta value controls the tolerance of noise or error in the algorithm and CS is sensitive to the beta value. An inappropriate value of beta could lead to inaccurate estimation. Additionally, the CS algorithm performance can be improved by carefully choosing penalty parameters between the wavelet and Laplace. Based on the cases presented in this work, CS has potential to perform better reconstructions than CB or FB for the given SNR, number of receivers, number of samples, calibration, etc. In the present study, SVD was used to reduce the size of the measurement matrix and potentially reduce the redundancy in the measurements. The beta value for the noise and statistical imperfections in the data is

estimated by defining a threshold on the measurements associated with the smaller singular values. It is important to note that incoherence and sparsity are fundamental for evaluating the quality of reconstruction; however, in this work, incoherence is not very strong (5.5 in the range of 1 to 11.3) for three receiver configurations due to the use of wavelet transformation. The incoherence value was too high with DCT, therefore, wavelet transformation was selected for the study. In this work, the time series signals are generated by using a three dimensional radar simulator. Thousands of scatters are randomly located within the simulation domain. The calibration of CS and FB power estimates was made by considering the transmitting and receiving antenna pattern in the simulation. It is important that CS can be calibrated by using uniform reflectivity or a point target structure for the three receiver configurations based on the simulation results.

Chapter 5

Conclusions and Future Work

5.1 Summary

In this dissertation, the emerging technology of compressive sensing is applied to refractivity retrieval with a network of weather radars and reconstruction of reflectivity and velocity angular profile with imaging radar, where the number of measurements are limited. Due to the small number of measurements and noise contamination, compressive sensing is an attractive method for the estimation, since it is robust to noise and well suited for underdetermined problems. CS has been applied to other fields and has shown promising image reconstruction with much fewer measurements than those used in the conventional sampling scheme.

In the first study, CS was proposed to improve the refractivity retrieval using a network of radars since the performance of CLS for refractivity retrieval can be restricted by the limited number of high-quality ground returns and noise. The application of CS to refractivity retrieval was formulated using a linear model and subsequently demonstrated using simulations in Chapter 3. The modeled refractivity fields were obtained from the Advanced Regional Prediction System (ARPS) model. ARPS is a compressible nonhydrostatic storm-scale numerical weather prediction

model developed at the Center for Analysis and Prediction of Storms (CAPS). The performance of CS and CLS was quantified using RMSE and was tested statistically as a function of noise, number of radars, and refractivity models with different levels of compressibility and smoothness. Note that both CS and CLS rely on the same linear model and can be implemented for a single radar. It is evident that both CS and CLS can generally reconstruct the refractivity difference most of the time. Moreover, in the cases investigated, CS always provides better reconstruction than CLS, manifested by the lower RMSE. In addition, the results have shown that CS is also less susceptible to noise contamination, especially when the image for reconstruction is more compressible.

Furthermore, by taking advantage of networked radars, both CS and CLS performances can be improved as the number of measurements and the viewing angles increase. However, the shape of the refractivity difference is better reconstructed with CS than CLS. The CS algorithm can be further improved by more carefully choosing regularization parameters between the DCT and TV terms. In CLS, the selection of the threshold level for the singular values may not be optimal. Based on the cases presented in this work, CS performs better than CLS given the same conditions such as noise, number of radars, etc.

The second topic is the application of CS to imaging radar to reconstruct reflectivity and velocity profiles within the field of view, defined by the wide transmitted

beam. The time series signals are generated by using a three dimensional radar simulator. The problem of DBF is posed as an inverse problem and formulated using a linear model for both reflectivity and velocity estimation. CS is implemented by using wavelet and Laplace transformations in the l_1-norm minimization. The calibrations of CS and FB power estimates are made by using uniform reflectivity considering the transmitting and receiving antenna pattern for three receiver configurations in the simulation. It is important that CS can be calibrated by a point target structure for three receiver configurations based on the simulation results (the results for point targets was not demonstrated).

The application of CS to DBF was demonstrated using simulations, where the model reflectivity is obtained from Gaussian models and ARPS model in chapter 4. The US, NRS and RS receiver configurations with a fixed aperture size of 2 m are studied. The performance of CS, CB, and FB was quantified using DR and was tested as a function of dynamic range by using a single Gaussian model. A high SNR and high number of samples are used to demonstrate capability of CS compared to CB and FB. For the tested cases, CS can produce larger DR than CB and FB using all three receiver configurations with better agreement with the true DR by using 33 receivers. CB and FB using the US configuration produced slightly higher DR than NRS and RS. Increasing the number of receivers to 65, the performance of CS and CB improves and produces similar DR. Note that CB underestimates DR for all the

cases using the three configurations, while CS overestimates DR especially when DR becomes larger than 25 dB.

The impact of reflectivity on velocity was studied, and the performance of CS, CB, and FB was measured using VI as a function of DR. CS performed better using NRS than RS and US, while the performance of CB was better using RS than NRS using 33 receivers. The performance of CS and CB was similar when DR is less than 20 dB. When DR is greater than 20 dB, CB performed better than CS and FB using RS. When the number of receivers is increased to 65, VI of CB become the same using all three configurations. CS performance using the NRS and US configuration becomes similar to CB. Additionally, CB was able to estimate full velocity interval by using the RS configuration with 17 receivers.

Further, the resolution of CS, CB, and FB estimations for dual Gaussian models is quantified by using RES. The performance of the methods was tested as a function of peak separation using a SNR of 30 dB and 1024 samples with 33 receivers. The performance of CS was better than CB or FB using all three configurations when the peak separation was less than 10 degrees. CS overestimates the RES when the separation of peaks is larger than 10 degrees, while CB underestimates it. The RES of CB was larger than FB using all three configurations. The RES of CS was still larger than CB and FB when the number of receivers increased to 65. CS and CB performed better using US and NRS than the RS configuration, and FB was better using US.

The resolution of velocity was studied by using uniform reflectivity at 30 dB and changing the slope of linear velocity. RMSE was used to quantify the resolution. The RMSE of CS was much lower than CB and FB using the NRS and RS configuration for all the velocity profiles with 33 receivers. However, the RMSE of CS, CB, and FB was similar using the US configuration. When the number of receivers increased to 65, the performance of CB and FB becomes similar to CS using US and NRS.

Moreover, the modeled reflectivity and velocity field are obtained from the ARPS model. The performance of CS, CB, and FB was quantified using RMSE for both reflectivity and velocity and was tested as a function of SNR, number of receivers, and number of samples. CS performed better than CB and FB for reflectivity estimation using all three configurations with 33 receivers for all the given SNRs and number of samples. However, the performance of CB becomes better than CS when using 65 receivers for all the receiver configurations. By increasing the number of receivers, the performance of CS, CB, and FB was improved. It is observed that CS produces relatively large errors for the low compressible reflectivity images compared to high compressible images. Further, CS performed better using NRS and RS than the US configuration for the reflectivity estimation, which is indicated by the RMSE. CS is able to reconstruct the reflectivity field grossly for most cases and detail structures are more obvious in the CS estimation than CB and FB using the NRS and RS configurations. In addition, results have shown that CS is less susceptible to noise compared to CB and FB. Further, CS is able to reconstruct the reflectivity field

grossly with 17 receivers using the NRS and RS configurations. The shape of the reflectivity structures preserved in CS and CB is comparable with 65 receivers and 1024 samples.

The performance of CB for velocity estimation was better than CS using the US configurations with 33 and 65 receivers. However, CS performed better using the RS configuration with 33 receivers for the velocity estimation for all the given SNR cases. CS is able to reconstruct velocity field grossly for most of the cases. CS has velocity aliasing especially at the low reflectivity region and due to the imperfect dealiasing process, the RMSE of CS becomes high. Especially at a low SNR, CS is capable of reconstructing most of the velocity structure. It is important to point out that one difficulty in CS estimation is the beta value selection. The CS performance can be improved by choosing β carefully in the l_1-norm minimization.

Further, two experimental data from imaging radar AIR were used to demonstrate the feasibility of CS in radar imaging. The data was obtained on April 15, 2012. CS and FB qualitatively produced similar reflectivity and velocity estimation, where the reconstructed reflectivity from CB was noisy because of the use of 53 samples and 36 receivers.

The coherence condition was studied to assess the probability of exact reconstruction using l_1-norm minimization on sparse images. It is important to note that, while coherency is fundamental in evaluating quality of sparse approximation, the

satisfaction of the restricted isometry property (RIP) enables more robust and stable reconstruction of sparse signals (Duarte and Eldar 2011). RIP ensures that two sparse images with the same transform coefficients at different locations cannot produce the same measurement vector and thus guarantees a unique solution (Duarte and Eldar 2011). However, it is computationally expensive to check the RIP condition (Baraniuk et al. 2010). On the other hand, coherency provides an alternative way to check the probability of robust recovery (Tropp 2006). Additionally, coherency can be conservatively used to bound RIP and enables stable recovery via l_1-norm minimization (Potter et al. June 2010). Furthermore, it is also important to note that compressible images can be reconstructed by approximating most significant transform coefficients, even when RIP is not satisfied (Zhang 2008; Candès and Tao 2007). While under such conditions the recovery of images might not be exact, they are still valuable in solving practical problems. In the refractivity retrieval study, while the computed coherence is relatively low (10 in a range of 1 to 60), such a value cannot be used to guarantee exact recovery (similar to conditions with unsatisfied RIP) unless the sparsity property of signals to be recovered and transformation matrix are also considered (Candès and Romberg 2006). On the other hand, the present simulation results demonstrate that the proposed method based on the CS theory indicates better performance than CLS in reconstructing refractivity. Moreover, in the DBF study, the coherence is computed for the three receiver configurations (US, NRS, and RS) with the wavelet transformation and the values are similar at about 5.5 in

the range of 1 to 11.3. The coherence value was not too low as in refractivity study. However, the present simulation results demonstrate that CS can still achieve better performance than CB and FB in reconstructing reflectivity and in some cases for velocity.

5.2 Suggestions for future research

In the radar refractivity retrieval study, the radar locations are selected to be at the corners, and target locations are random for simplicity. Note that ground targets are sparsely distributed and likely to group together, which makes it even more challenging to estimate the phase. This work is just the first step in tackling the problem, so a more general and convenient setup was used. As such, the improvement in the overlap region of refractivity from additional radar can be easily observed and quantified. For future study, a realistic radar configuration and target locations can be considered. One difficulty in refractivity retrieval is to unwrap the received signal phase accurately in the case of sparse and missing target distributions in the radar field of view. The phase-unwrapping algorithm can be tested and implemented for refractivity field experimentation. The implementation of CS on real data should be tested and verified with surface stations. A common region can be scanned by creating a network of radars using mobile radars and a fixed site radar.

Another important issue in CS application is the choice of parameters for the combination of multiple transformation matrix in the l_1-norm minimization. Further,

the selection of the parameters can be effected by the choice of β value based on the discrepancy principle in the inverse problems and of the l_1- norm solver. Another research direction is the selection of β value for the error tolerance under various amounts of noise and numbers of measurements. A good choice of β will lead to a good choice of regularization parameters and calibration value in chapter 4. The optimum β value can be obtained based on the minimum RMSE by searching for β within a large interval by assuming the calibration value is known. Then by using a polynomial fitting, the parameters for the β estimation can be obtained. On the other hand, in order to find the calibration value, a β value is needed. By using a large number of samples and high SNR, the calibration value can be guessed from uniform reflectivity. It is also worth noting that the condition of incoherence can be further improved by designing a better transformation matrix, which can result in better sparsity of signals in the transformed domain and incoherence to measurement matrices.

For the digital beamforming study, the spatial continuity is considered only in one dimension (vertical direction) for CS estimation. Cross-range spatial continuity can be considered between the successive range gates. In other words, another possible way to estimate reflectivity in two dimensions (estimation of RHI image at once) by concatenating the measurements in a vector form and creating a new combined measurement matrix. However, the computational time will be increased significantly, since the size of measurement matrix and transformation matrix increase

proportionally with the number of measurements and number of pixels to be reconstructed. Further, CS can be applied to range imaging which is a similar concept to DBF. CS can be applied to waveform design for weather radar by using random sampling procedure with coded pulses.

References

Aybat, N. S. and A. Chakraborty, 2008: Reconstruction of ct images from parsimonious angular measurements via compressed sensing.

Baer, D. and J. H. W. Company, 1978: *Building Losses from Natural Hazards: Yesterday, Today and Tomorrow*. J.H. Wiggins Company.

Baraniuk, R. G., 2007: Compressive sensing [lecture notes]. *Signal Processing Magazine, IEEE*, **24**, 118–121.

Baraniuk, R. G., V. Cevher, M. F. Duarte, and C. Hegde, 2010: Model-based compressive sensing. *Information Theory, IEEE Transactions on*, **56**, 1982–2001.

Bean, B. R. and E. J. Dutton, 1968: *Radio Meteorology*, Dover Publications. 435.

Besson, L. and J. Parent du Châtelet, 2013: Solutions for improving the radar refractivity measurement by taking operational constraints into account. *J. Atmos. Oceanic Technol.*, **30**, 1730–1742.

Bluestein, H. B., M. M. French, I. PopStefanija, R. T. Bluth, and J. B. Knorr, 2009: A mobile, phased-array doppler radar for the study of severe convective storms. *Bull. Amer. Meteor. Soc.*, **91**, 579–600.

Bluestein, H. B., W.-C. Lee, M. Bell, C. C. Weiss, and A. L. Pazmany, 2003: Mobile doppler radar observations of a tornado in a supercell near bassett, nebraska, on 5 june 1999. part ii: Tornado-vortex structure. *Monthly Weather Review*, **131**, 2968–2984.

Bodine, D., P. Heinselman, B. L. Cheong, R. D. Palmer, and D. Michaud, 2008: Convection initiation and storm evolution forecasting using radar refractivity retrievals. *24th Conf. on Severe Local Storms*.

Bodine, D., D. Michaud, R. D. Palmer, P. L. Heinselman, J. Brotzge, N. Gasperoni, B. Leng Cheong, M. Xue, and J. Gao, 2011: Understanding radar refractivity: Sources of uncertainty. *J. Appl. Meteor. Climatol.*, **50**, 2543–2560.

Boyd, S. and L. Vandenberghe, 2004: *Convex Optimization*. Cambridge University Press.

Brandes, E. A., G. Zhang, and J. Vivekanandan, 2002: Experiments in rainfall estimation with a polarimetric radar in a subtropical environment. *J. Appl. Meteor.*, **41**, 674–685.

Braun, J., C. Rocken, and R. Ware, 2001: Validation of line-of-sight water vapor measurements with gps. *Radio Science*, **36**, 459–472.

Bunting, W. and B. Smith, 1993: A guide for conducting convective windstorm surveys. *NOAA Tech. Memo. NWS SR- 146*, Scientific Services Division, Southern Region, Fort Worth, TX, number 44.

Candès, E. and T. Tao, 2007: Rejoinder: The dantzig selector: Statistical estimation when p is much larger than n. *Annals of Statistics*, **35**, 2392–2404.

Candès, E. J., 2006: Compressive sampling. *Proc. Int. Congr. Math. (ICM)*, volume 3, 1433–1452.

Candès, E. J. and J. Romberg, 2005: Practical Signal Recovery from Random Projections. volume 5914.

Candès, E. J. and J. Romberg, 2006: Sparsity and incoherence in compressive sampling.

Candès, E. J. and T. Tao, 2005: Decoding by linear programming. *IEEE Trans. Inf. Theory*, **51**, 4203–4215.

Candès, E. J. and M. B. Wakin, 2008: An introduction to compressive sampling. *IEEE Signal Process. Mag.*, **25**, 21–30.

Capon, J., 1969: High-resolution frequency-wavenumber spectrum analysis. *Proc. of the IEEE*, **57**, 1408–1418.

Carbone, R. E., M. J. Carpenter, and C. D. Burghart, 1985: Doppler radar sampling limitations in convective storms. *J. Atmos. Oceanic Technol.*, **2**, 357–361.

Cheong, B. L., M. W. Hoffman, R. D. Palmer, S. J. Frasier, and F. J. Lopez-Dekker, 2004: Pulse pair beamforming and the effects of reflectivity field variations on imaging radars. *Radio Science*, **39**.

Cheong, B. L., M. W. Hoffman, R. D. Palmer, S. J. Frasier, and F. J. López-Dekker, 2006: Phased-array design for biological clutter rejection: Simulation and experimental validation. *J. Atmos. Oceanic Technol.*, **23**, 585–598.

Cheong, B. L., R. D. Palmer, C. Curtis, T.-Y. Yu, D. Zrnic, and D. Forsyth, 2008a: Refractivity retrieval using the phased array radar: First results and potential for multi-function operation. *IEEE Trans. Geosci. Remote Sens.*, **46**, 2527–2537.

Cheong, B. L., R. D. Palmer, and M. Xue, 2008b: A time series weather radar simulator based on high-resolution atmospheric models. *J. Atmos. Oceanic Technol.*, **25**, 230–243.

Chi, Y., L. Scharf, A. Pezeshki, and A. Calderbank, 2011: Sensitivity to basis mismatch in compressed sensing. *Signal Processing, IEEE Transactions on*, **59**, 2182–2195.

Crook, N. A., 1996: Sensitivity of moist convection forced by boundary layer processes to low-level thermodynamic fields. *Mon. Weather Rev.*, **124**, 1767—1785.

Dabberdt, W. F. and T. W. Schlatter, 1996: Research opportunities from emerging atmospheric observing and modeling capabilities. *Bull. Amer. Meteor. Soc.*, **77**, 305–323.

Davies-Jones, R., R. J. Trapp, and H. B. Bluestein, 2001: Tornadoes and tornadic storms. *Meteorological Monographs*, **50**, 167–222.

Ding, Y. and I. W. Selesnick, 2015: Artifact-free wavelet denoising: Non-convex sparse regularization, convex optimization. *IEEE Trans. Signal Process.*, **22**, 1364 –1368.

Donoho, D. L., 2006: Compressed sensing. *IEEE Trans. Inf. Theory*, **52**, 1289–1306.

Donoho, D. L. and M. Elad, 2003: Optimally sparse representation in general (non-orthogonal) dictionaries via l_1 minimization. *PNAS*, **100**, 2197–2202.

Duarte, M. F. and Y. C. Eldar, 2011: Structured compressed sensing: From theory to applications. *Signal Processing, IEEE Transactions on*, **59**, 4053–4085.

Edelmann, G. F. and C. F. Gaumond, 2011: Beamforming using compressive sensing. *J. Acoust. Soc. Am.*, **130**, EL232–EL237.

Eldar, Y. C. and G. Kutyniok, 2012: *Compressed Sensing Theory and Applications*. Cambridge University Press.

Emanuel, K., D. Raymond, A. Betts, L. Bosart, C. Bretherton, K. Droegemeier, B. Farrell, J. Fritsch, R. Houze, M. LeMone, D. Lilly, R. Rotunno, M. Shapiro, R. Smith, and A. Thorpe, 1995: Report of the first prospectus development team - u.s. weather research program. Technical Report NCAR/TN-415+STR, University Corporation for Atmospheric Research.

Emmanuel Candès, J. R., 2005: l_1-magic : Recovery of sparse signals via convex programming. Technical report, Caltech.

Fabry, F., 2004: Meteorological value of ground target measurements by radar. *J. Atmos. Oceanic Technol.*, **21**, 560–573.

Fabry, F., C. Frush, I. Zawadzki, and A. Kilambi, 1997: On the extraction of near-surface index of refraction using radar phase measurements from ground targets. *J. Atmos. Oceanic Technol.*, **14**, 978–987.

Feng, Y.-C., F. Fabry, and T. M. Weckwerth, 2016: Improving radar refractivity retrieval by considering the change in the refractivity profile and the varying altitudes of ground targets. *J. Atmos. Oceanic Technol.*, **33**, 989–1004.

Fritz, J. and V. Chandrasekar, 2009: Implementation and analysis of networked radar refractivity retrieval. *J. Atmos. Oceanic Technol.*, **26**, 2123–2135.

Gasperoni, N. A., M. Xue, R. D. Palmer, J. Gao, B. L. Cheong, and D. S. Michaud, 2009: Low-level moisture analysis from refractivity data derived from a network of s-band and x-band radars using arps 3dvar. *34th Conference on Radar Meteorology*, Amer. Meteor. Soc.

Giangrande, S. E. and A. V. Ryzhkov, 2008: Estimation of rainfall based on the results of polarimetric echo classification. *J. Appl. Meteor. Climatol.*, **47**, 2445–2462.

Grant, M. and S. Boyd, 2014: CVX: Matlab software for disciplined convex programming, version 2.1. `http://cvxr.com/cvx`.

Gurbuz, A. C., J. McClellan, and W. Scott, 2007: Compressive sensing for gpr imaging. *Signals, Systems and Computers, 2007. ACSSC 2007. Conference Record of the Forty-First Asilomar Conference on*, 2223–2227.

Hadamard, J., 1923: *Lectures on Cauchy's problem in linear partial differential equations*. New Haven Yale University Press.

Hansen, P. C., 1987: *Rank-deficient and discrete ill-posed problems: numerical aspects of linear inversion*. Society for Industrial and Applied Mathematics.

Hao, Y., D. Goeckel, R. Janawamy, and S. Frasier, 2006: Surface refractive index field estimation from multiple radars. *Radio Sci.*, **41**.

Harding, B. J. and M. Milla, 2013: Radar imaging with compressed sensing. *Radio Science*, **48**, 582–588.

Isom, B., R. Palmer, R. Kelley, J. Meier, D. Bodine, M. Yeary, B.-L. Cheong, Y. Zhang, T.-Y. Yu, and M. I. Biggerstaff, 2013: The atmospheric imaging radar:

Simultaneous volumetric observations using a phased array weather radar. *J. Atmos. Oceanic Technol.*, **30**, 655–675.

Jain, A. K., 1989: *Fundamentals of digital image processing*. Prentice-Hall, Inc. Upper Saddle River, NJ, USA.

Kudeki, E. and F. Sürücü, 1991: Radar interferometric imaging of field-aligned plasma irregularities in the equatorial electrojet. *Geophysical Research Letters*, **18**, 41–44.

Kurdzo, J. M., B. L. Cheong, R. D. Palmer, and G. Zhang, 2014: Optimized nlfm pulse compression waveforms for high-sensitivity radar observations. *2014 International Radar Conference*.

Kurdzo, J. M., F. Nai, D. J. Bodine, T. A. Bonin, R. D. Palmer, B. L. Cheong, J. Lujan, A. Mahre, and A. D. Byrd, 2016: Observations of severe local storms and tornadoes with the atmospheric imaging radar. *Bull. Amer. Meteor. Soc.*.

Li, J. and P. Stoica, 2006: *Robust Adaptive Beamforming*. Wiley-Interscience.

Liu, J., C. Han, X. Yao, and F. Lian, 2013: A novel coherence reduction method in compressed sensing for doa estimation. *Journal of Applied Mathematics*, **2013**.

Lustig, M., D. Donoho, and J. M. Pauly, 2007: Sparse MRI: The application of compressed sensing for rapid MR imaging. *Magn. Reson. Med.*, **58**, 1182–1195.

Mead, J. B., G. Hopcraft, S. J. Frasier, B. D. Pollard, C. D. Cherry, D. H. Schaubert, and R. E. McIntosh, 1998: A volume-imaging radar wind profiler for atmospheric boundary layer turbulence studies. *J. Atmos. Oceanic Technol.*, **15**, 849–859.

Metzger, R. Z., C. C. Weiss, and A. E. Reinhart, 2011: An examination of the structure of three tornadoes using high-frequency ka-band mobile doppler radar. *35th Conference on Radar Meteorology*.

Mir, H. and B. Carlson, 2012: On the definition of radar range resolution for targets of greatly differing rcs. *Instrumentation and Measurement, IEEE Transactions on*, **61**, 655–663.

Müller, J. L. and S. Siltanen, 2012: *Linear and nonlinear inverse problems with practical applications*. Society for Industrial and Applied Mathematics.

Nai, F., S. M. Torres, and R. D. Palmer, 2016: Adaptive beamspace processing for phased-array weather radars. *IEEE Trans. Geosci. Remote Sens.*, **54**, 5688–5698.

Naini, F. M., R. Gribonval, L. Jacques, and P. Vandergheynst, 2009: Compressive sampling of pulse trains: Spread the spectrum! *2009 IEEE International Conference on Acoustics, Speech and Signal Processing*, 2877–2880.

National Research Council, 1998: *The Atmospheric Sciences: Entering the Twenty-First Century*, The National Academies Press. 373.

—, 2002: *Weather Radar Technology Beyond NEXRAD*. The National Academies Press.

Needell, D. and J. Tropp, 2009: Cosamp: Iterative signal recovery from incomplete and inaccurate samples. *Applied and Computational Harmonic Analysis*, **26**, 301 – 321.

Nicol, J. C. and A. J. Illingworth, 2012: The effect of phase-correlated returns and spatial smoothing on the accuracy of radar refractivity retrievals. *J. Atmos. and Ocean. Technol.*, **30**, 22–39.

Ozturk, S., T.-Y. Yu, L. Ding, R. Palmer, and N. Gasperoni, 2014: Application of compressive sensing to refractivity retrieval using networked weather radars. *IEEE Trans. Geosci. Remote Sens.*, **52**, 2799–2809.

Palmer, R. D., S. Gopalam, T.-Y. Yu, and S. Fukao, 1998: Coherent radar imaging using Capon's method. *Radio Science*, **33**, 1585–1598.

Park, S. and F. Fabry, 2010: Simulation and interpretation of the phase data used by the radar refractivity retrieval algorithm. *J. Atmos. Oceanic Technol.*, **27**, 1286–1301.

Pazmany, A. L., J. B. Mead, H. B. Bluestein, J. C. Snyder, and J. B. Houser, 2013: A mobile rapid-scanning x-band polarimetric (raxpol) doppler radar system. *J. Atmos. Oceanic Technol.*, **30**, 1398–1413.

Polger, P. D., B. S. Goldsmith, R. C. Przywarty, and J. R. Bocchieri, 1994: National weather service warning performance based on the wsr-88d. *Bull. Amer. Meteor. Soc.*, **75**, 203–214.

Polo, Y. L., Y. Wang, A. Pandharipande, and G. Leus, 2009: Compressive wide-band spectrum sensing. *2009 IEEE International Conference on Acoustics, Speech and Signal Processing*, number 2337-2340.

Potter, L. C., E. Ertin, J. T. Parker, and M. Cetin, June 2010: Sparsity and compressed sensing in radar imaging. *Proceedings of the IEEE*, **98**, 1006–1020.

Roberts, R. D., E. Nelson, J. W. Wilson, N. Rehak, J. Sun, S. Ellis, T. Weckwerth, F. Fabry, P. C. Kennedy, J. Fritz, V. Chandrasekar, S. Reising, S. Padmanabhan, J. Braun, T. Crum, L. Mooney, and R. Palmer, 2008: REFRACTT 2006: Real-time retrieval of high-resolution, low-level moisture fields from operational NEXRAD and research radars. *Bull. Amer. Meteor. Soc.*, **89**, 1535–1548.

Rudin, L. I., S. Osher, and E. Fatemi, 1992: Nonlinear total variation based noise removal algorithms. *Physica D: Nonlinear Phenomena*, **60**, 259–268.

Ryzhkov, A. V., T. J. Schuur, D. W. Burgess, P. L. Heinselman, S. E. Giangrande, and D. S. Zrnic, 2005: The joint polarization experiment: Polarimetric rainfall measurements and hydrometeor classification. *Bull. Amer. Meteor. Soc.*, **86**, 809–824.

Shimose, K.-i., M. Xue, R. D. Palmer, J. Gao, B. L. Cheong, and D. J. Bodine, 2013: Two-dimensional variational analysis of near-surface moisture from simulated radar refractivity-related phase change observations. *Advances in Atmospheric Sciences*, **30**, 291–305.

Snyder, J. C., H. B. Bluestein, G. Zhang, and S. J. Frasier, 2010: Attenuation correction and hydrometeor classification of high-resolution, x-band, dual-polarized mobile radar measurements in severe convective storms. *J. Atmos. Oceanic Technol.*, **27**, 1979–2001.

Sun, J., 2005: Initialization and numerical forecasting of a supercell storm observed during steps. *Mon. Wea. Rev.*, **133**, 793–813.

Tikhonov, A. N., A. V. Goncharsky, V. V. Stepanov, and A. G. Yagola, 1995: *Numerical Methods for the Solution of Ill-Posed Problems*. Springer Netherlands.

Torres, S., R. Adams, C. Curtis, E. Forren, D. Forsyth, I. Ivić, D. Priegnitz, J. Thompson, and D. Warde, 2013a: A demonstration of adaptive weather-surveillance capabilities on the national weather radar testbed phased-array radar. *Phased Array Systems Technology, 2013 IEEE International Symposium on*, 460–463.

Torres, S., A. Ric, C. Christopher, F. Eddie, I. Igor, D. Priegnitz, T. John, and W. David, 2013b: 8.2 new weather-surveillance capabilities for nssl's phased-array radar. *29th Conf. on Environmental Information Processing Technologies, Austin, TX, Amer. Meteor. Soc., Paper 8.2*.

Tropp, J. A., 2006: Just relax: convex programming methods for identifying sparse signals in noise. *Information Theory, IEEE Transactions on*, **52**, 1030–1051.

Wada, M., H. Goto, F. Mizutani, S. Shimamura, S. Yoshida, H. Hanado, S. Sato, T. Ushio, and S. Kawamura, 2013: Development of dual polarization phased array radar. *36th Conference on Radar Meteorology*.

Weckwerth, T. M., H. V. Murphey, C. Flamant, J. Goldstein, and C. R. Pettet, 2008: An observational study of convection initiation on 12 june 2002 during ihop_2002. *Mon. Weather Rev.*, **136**, 2283–2304.

Weckwerth, T. M., D. B. Parsons, S. E. Koch, J. A. Moore, M. A. LeMone, B. B. Demoz, C. Flamant, B. Geerts, J. Wang, and W. F. Feltz, 2004: An overview of the international H_2O project (IHOP-2002) and some preliminary highlights. *Bull. Amer. Meteor. Soc.*, **85**, 253–277.

Weckwerth, T. M., C. Pettet, F. Fabry, S. Park, M. A. LeMone, and J. Wilson, 2005: Radar refractivity retrieval: Validation and application to short-term forecasting. *J. Appl. Meteor.*, **44**, 285–300.

Wiaux, Y., J. L., P. G., S. A.M.M., and V. P., 2009: Compressed sensing imaging techniques for radio interferometry. *Monthly Notices of the Royal Astronomical Society*, **395**, 1733–1742.

Woodman, R. F., 1997: Coherent radar imaging: Signal processing and statistical properties. *Radio Science*, **32**, 2373–2391.

Xue, M., D. Wang, J. Gao, K. Brewster, and K. K. Droegemeier, 2003: The advanced regional prediction system (ARPS), storm-scale numerical weather prediction and data assimilation. *Meteor. Atmos. Phys.*, **82**, 139–170.

Yu, T.-Y., M. B. Orescanin, C. D. Curtis, D. S. Zrnić, and D. E. Forsyth, 2007: Beam multiplexing using the phased-array weather radar. *J. Atmos. Oceanic Technol.*, **24**, 616–626.

Yu, T.-Y., R. D. Palmer, and D. L. Hysell, 2000: A simulation study of coherent radar imaging. *Radio Science*, **35**, 1129–1141.

Zhang, G. and R. J. Doviak, 2007: Spaced-antenna interferometry to measure cross-beam wind, shear, and turbulence: Theory and formulation. *J. Atmos. Oceanic Technol.*, **24**, 791–805.

Zhang, G., J. Vivekanandan, and E. Brandes, 2001: A method for estimating rain rate and drop size distribution from polarimetric radar measurements. *IEEE Trans. Geosci. Remote Sens.*, **39**, 830–841.

Zhang, Y., 2008: On theory of compressive sensing via l1-minimization: Simple derivations and extensions. *TR08-11, CAAM, Rice University*.

Zhu, J., D. Baron, and M. F. Duarte, 2015: Recovery from linear measurements with complexity-matching universal signal estimation. *IEEE Transactions on Signal Processing*, **63**, 1512–1527.

Zrnic, D. S., J. F. Kimpel, D. E. Forsyth, A. Shapiro, G. Crain, R. Ferek, J. Heimmer, W. Benner, T. J. McNellis, and R. J. Vogt, 2007: Agile-beam phased array radar for weather observations. *Bull. Amer. Meteor. Soc.*, **88**, 1753–1766.

Appendix A

Beta selection

The optimum β value in the constraint is found based on the minimum RMSE by searching for it within a large region of possible values for a given SNR case.

The RMSE between the reconstructed reflectivity and true reflectivity model is calculated in linear scale. The RMSE and optimum beta value plot is shown in Fig. 1 for a specific reflectivity case and a given SNR. It is obvious that there is one local minimum region for beta based on the RMSE values. The process is repeated for various reflectivity models and several realizations for the given SNR. Accordingly, the optimum β value is obtained as a function of SNR. Second order curve fitting is used to obtain polynomial parameter coefficients as a function of SNR. It is also found that a similar β value can be obtained by using the norm of measurements by defining a threshold value for calculation, such as $\beta = ||\mathbf{R_p}(30:128)||_{l_2}$ for reflectivity estimation with 128 pixels using 33 receivers with a threshold of 30.

The threshold value may vary with the number of receivers, but it is constant for various SNRs. Consequently, this new approach to estimate β makes it possible to avoid estimating SNR in the received signal. An inaccurate SNR estimation may lead to the wrong β value based on the curve fitting coefficients and thus lead to poor reconstruction.

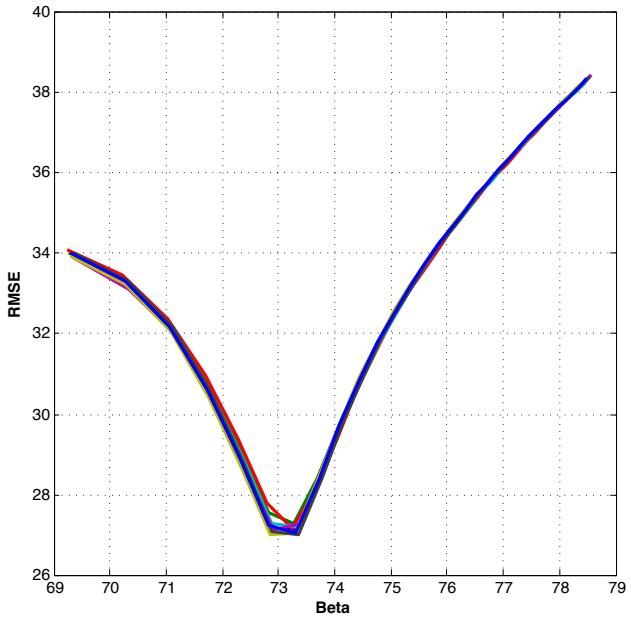

(a) Uniform reflectivity

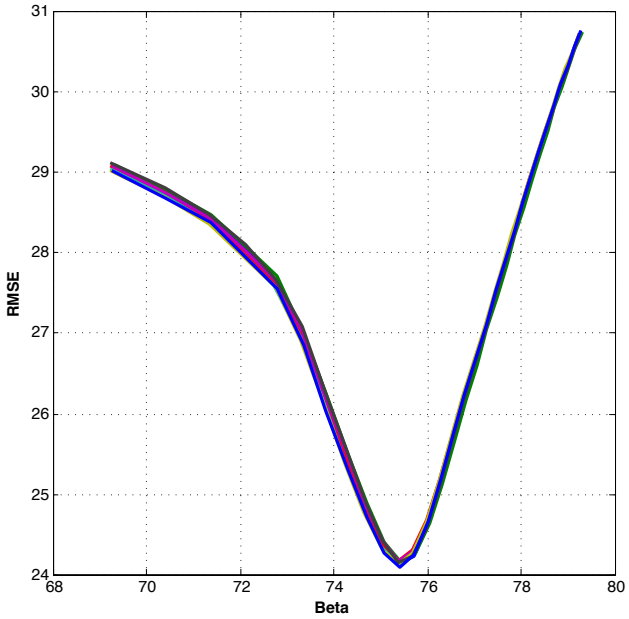

(b) Gaussian model std = 1.2 degree

Figure 1: RMSE as a function of beta for SNR=15 dB using uniform and Gaussian model reflectivity. The number of samples is 512 and number of receivers is 36 using uniform spacing receivers.

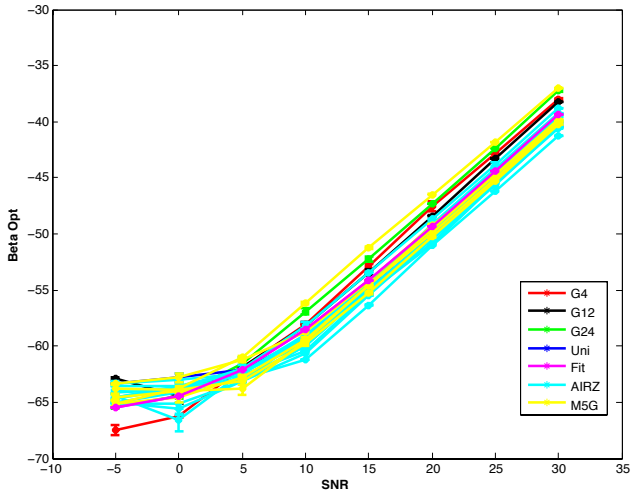

(a) Optimum beta from searching

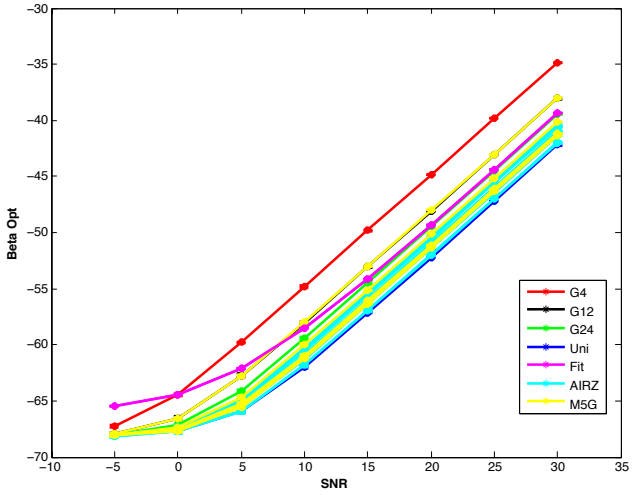

(b) Beta from norm of the signal

Figure 2: Optimum beta values as a function of SNR. Beta values are obtained from searching a large range and norm of the signal by setting the threshold = 33.

Appendix B

Calibration

Any weather radar requires a calibration process to establish a relationship between the collected data and the meteorological returns that are detected. Radar calibration determines the accuracy of the reflectivity value assigned to a given range gate, so therefore, it must be properly calibrated to ensure that the data collected accurately characterizes the meteorological returns. However, there can be uncertainties in the calibration value due to the complexity of estimation algorithm, resolution, noise, attenuation, loss, etc.

If we recall (4.25), it is clear that the received signal is a convolution of reflectivity and transmitted and received antenna pattern. The transmitted antenna pattern is much wider than the receiving antenna pattern, assuming that we can treat it as uniform. Further, if we assume that reflectivity Z is constant over the radar resolution volume and approximate the range with mean range from the transmitter to the center of volume r_0, then the received signal power can be written as a function of angle in the following,

$$P(z) = C\frac{Z_e(z)}{r_0^2}\sum_{z=1}^{P} w_{ar}(z) \tag{1}$$

where Z_e is equivalent reflectivity for the volume, which is a convolution of the true reflectivity with the transmitted antenna pattern, expressed as $Z_e(z) = Z(z)w_{at}(z)$. Then, the reflectivity angle can be expressed as

$$Z_e(z) = \frac{r_0^2 P(z)}{C\sum_{z=1}^{P} w_{ar}(z)} \tag{2}$$

The receiving antenna pattern in the denominator is a function of angle and also depends on the estimation method. For the FB, the receiving antenna pattern can be obtained from the spatial Fourier transform of the FB weights. Then the C value for

the FB can be found by dividing the FB power by the sum of the antenna pattern and reflectivity for each angle.

$$C(z) = \frac{r_0^2 P(z)}{Z_e(z) \sum_{z=1}^{P} w_{ar}(z)} \tag{3}$$

The same procedure is done for CB to obtain the C value; however, CB is data-dependent, and the found C value may not work for different reflectivity structures. It is important to note that CS does not have weighting functions and so there is no defined receiving antenna pattern. It is embedded in the inversion process. So, the C value for CS is expressed as

$$C(z) = \frac{r_0^2 P(z)}{Z_e(z)} \tag{4}$$

An example of the C value in angle is shown in Fig. 3 for CS, FB, and CB for the various number of receivers in US, NRS, and RS receiver configurations. The C value for CS, FB, and CB is obtained by using uniform reflectivity at 30 dB with high SNR and using 512 samples based on (3) and (4). It is clear that C values for CS, CB, and FB in angle for a given number of receivers seems to be constant, and variations are small compared to the mean value of C in angle. Further, the C value obtained by using different numbers of receivers is overlapped for CS and FB, unlike CB. It indicates that we can use the same C value for various numbers of receivers and different receiver configurations. The mean value of C over angle is obtained as 0.5 for CS, 0.37 for FB and is shown as a function of number of receivers for CS, FB, and CB in Fig. 4. The mean C value for CB varies with the number of receivers, but it is the same for different receiver configurations using the uniform reflectivity. However, the mean C value for CB varies with different reflectivity models.

In order to verify the calibration procedure, a Gaussian reflectivity model with std of 3 degree using a fixed base value at 25 dB is used. The reconstructed reflectivity profile of CS, FB, and CB using the mean C value is shown in Fig. 5 by using 64 receivers with SNR at 30 dB and 512 number of samples.

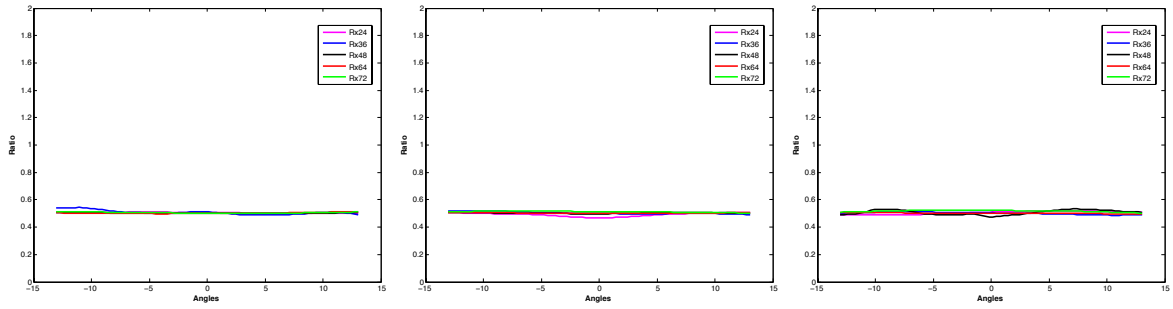

(a) CS

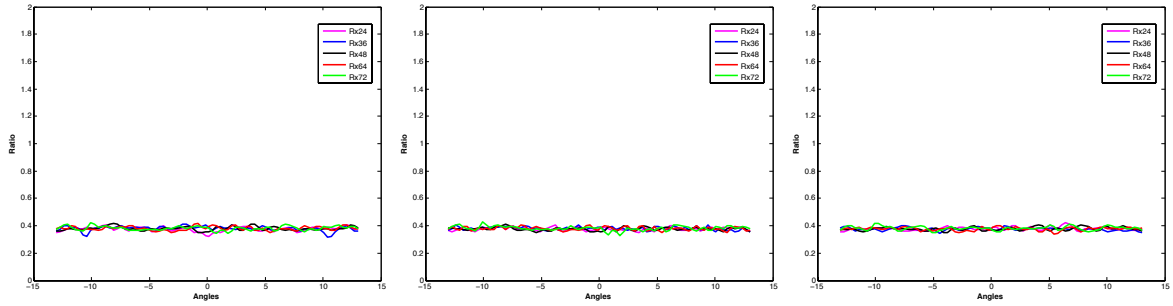

(b) FB

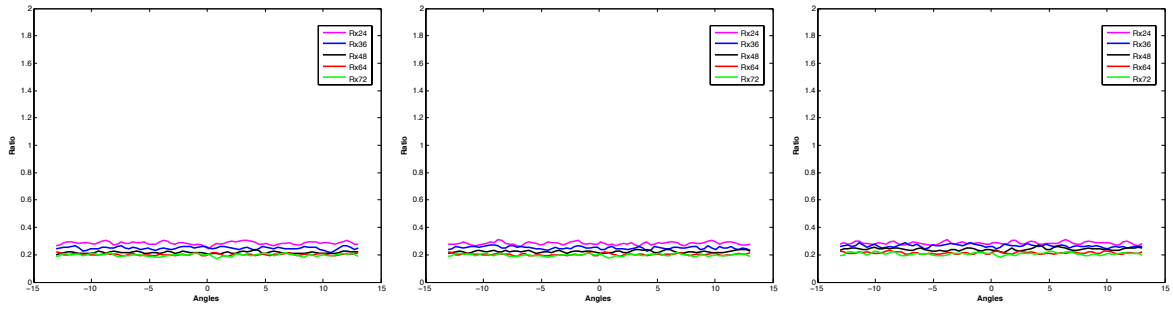

(c) CB

Figure 3: The C value as a function of angle for CS, FB, and CB using US (left panels), NRS (middle panels), and RS (right panels). The C value is obtained by using uniform reflectivity at 30 dB with high SNR and using 512 samples.

It is clear that CS reconstructed reflectivity overlaps with the model reflectivity by using the mean C value of 0.5 in three receiver configurations. Similarly, FB estimated reflectivity overlaps with the model reflectivity in US and NRS and slightly in US using the mean C value of 0.37. Good resolution is required for the calibration

procedure. In random spacing, FB has higher sidelobes and so limits the FB resolution. Note that the calibration value for CB did not work properly for the three receiver configurations.

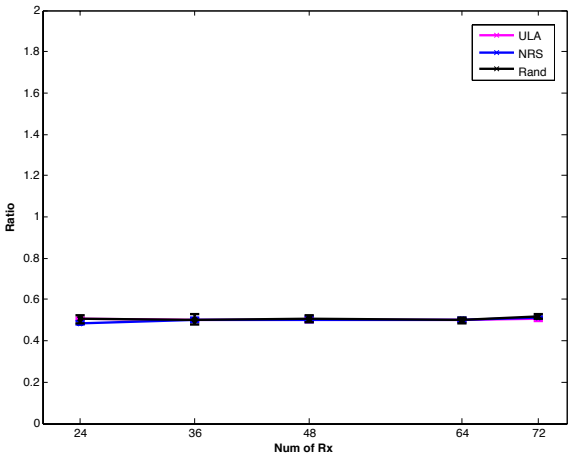

(a) CS

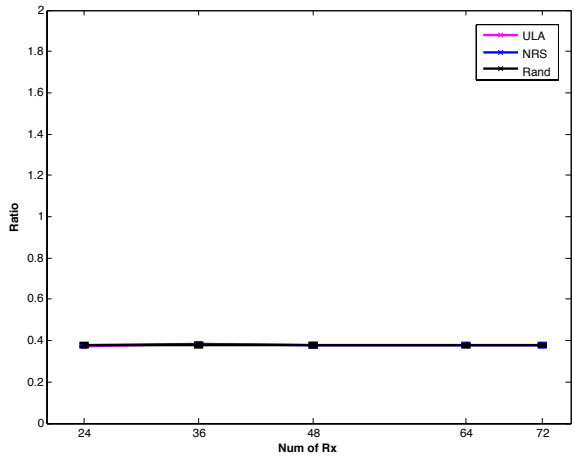

(b) FB

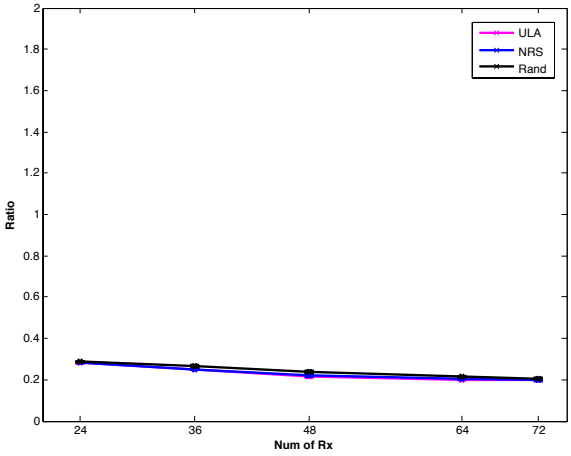

(c) CB

Figure 4: The mean C value as function of number of receivers for CS, FB, and CB is shown.

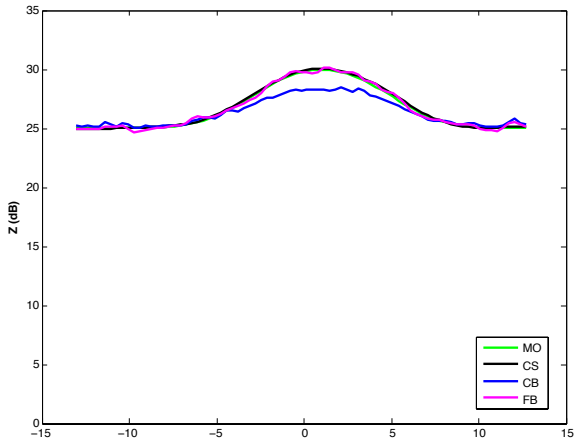

(a) US

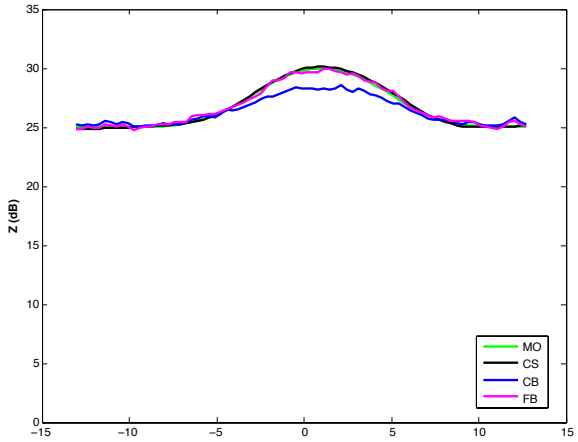

(b) NRS

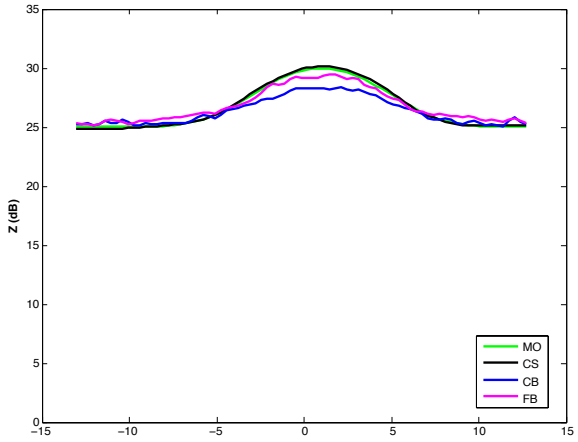

(c) RS

Figure 5: The reconstructed reflectivity profile of CS(black), FB (magenta), and CB (blue) using the mean C value is obtained by using 64 receivers. The model reflectivity is shown in green.